Neoproterozoic to middle Palaeozoic evolution of the Central Asian Orogenic Belt in south-central Mongolia: chronological and geochemical perspectives

Dissertation
zur Erlangung des Grades
“Doktor der Naturwissenschaften”
im Promotionsfach Geologie/Paläontologie

am Fachbereich Chemie, Pharmazie und Geowissenschaften
der Johannes Gutenberg-Universität Mainz

Antoine Demoux
geb. in Mâcon

Mainz, 2009

Erklärung

Ich versichere hiermit, die vorliegende Arbeit selbständig und nur unter Verwendung der angegebenen Quellen und Hilfsmittel verfasst zu haben.

All views and results presented in this thesis are those of the author, unless otherwise stated.

Mainz, May 2009

Abstract

Mongolia occupies a central position within the eastern branch of the large accretionary Central Asian Orogenic Belt (CAOB) or Altaids. The present work aims to outline the geodynamic environment and possible evolution of this part of the eastern CAOB, predominantly from the Cambrian to the middle Palaeozoic. The investigation primarily focussed on zircon geochronology as well as whole-rock geochemical and Sm–Nd isotopic analyses for a variety of metaigneous rocks from the southern Hangay and Gobi-Altai regions in south-central Mongolia.

The southern slope of the Hangay Mountains in central Mongolia exposes a large NW–SE-trending middle Neoproterozoic ophiolitic complex (c. 650 Ma), which is tectonically integrated within an accretionary complex developed between the Precambrian Baydrag and Hangay crustal blocks. Formation of the entire accretionary system along the north-eastern margin of the Baydrag block mainly occurred during the early Cambrian, but convergence within this orogenic zone continued until the early Ordovician, because of on-going southward subduction-accretion of the Baydrag block.

An important discovery is the identification of a late Mesoproterozoic to early Neoproterozoic belt within the northern Gobi-Altai that was reworked during the late Cambrian and throughout the late Ordovician/Devonian. Early Silurian low-grade mafic and felsic metavolcanic rocks from the northern Gobi-Altai display subduction-related geochemical features and highly heterogeneous Nd isotopic compositions, which suggest an origin at a mature active continental margin. Early Devonian protoliths of granodioritic and mafic gneisses from the southern Gobi-Altai display geochemical and Nd isotopic compositions compatible with derivation and evolution from predominantly juvenile crustal and mantel sources and these rocks may have been emplaced within the outboard portion of the late Ordovician/early Silurian active continental margin. Moreover, middle Devonian low-grade metavolcanic rocks from the southwestern Gobi-Altai yielded geochemical and Nd isotopic data consistent with emplacement in a transitional arc-backarc setting.

The combined U–Pb zircon ages and geochemical data obtained from the Gobi-Altai region suggest that magmatism across an active continental margin migrated oceanwards through time by way of subduction zone retreat throughout the Devonian. Progressive extension of the continental margin was associated with the opening of a backarc basin and culminated in the late Devonian with the formation of a Japan-type arc front facing a southward open oceanic realm (present-day coordinates).

Zusammenfassung

Die Mongolei nimmt eine zentrale Position innerhalb des östlichen Teils des großen Zentralasiatischen Orogens (CAOB), auch Altaiden genannt, ein. Die vorliegende Arbeit beschreibt das geodynamische Umfeld und die Entwicklung dieses Teils des CAOB vom Kambrium bis ins mittlere Paläozoikum. Die Untersuchungen konzentrieren sich auf Zirkondatierungen sowie die Geochemie und Sm–Nd-Isotopie von Gesamtgesteinsproben einer breiten Palette von metamorphen Orthogesteinen der südlichen Hangay und Gobi-Altai Region im südlichen Teil der Mongolei.

An der südlichen Flanke des Hangay-Gebirges ist ein umfangreicher NW–SE streichender Ophiolitkomplex aus dem mittleren Neoproterozoikum aufgeschlossen (c. 650 Ma). Dieser wurde tektonisch in einen Akkretionskeil zwischen den präkambrischen Baydrag und Hangay Krustenblöcken integriert. Die Hauptphase der Akkretion im gesamten System liegt im frühen Kambrium, jedoch hält die konvergente Tektonik aufgrund der andauernden südwärts gerichteten Akkretion des Baydrag-Grundgebirges bis ins frühe Oberordovizium an.

Von besonderer Bedeutung ist die Entdeckung eines Krustensegmentes innerhalb des nördlichen Altai aus dem späten Mesoproterozoikum bis frühen Neoproterozoikum der im oberen Kambrium und Ordovizium/Devon tektonisch und metamorph überprägt wurde. Untersilurische niedriggradige mafische und felsische Metavulkanite aus dem nördlichen Gobi-Altai zeigen subduktionstypische geochemische Eigenschaften und stark heterogene Nd-Isotopie, die auf eine Entstehung an einem reifen aktiven Kontinentalrand hinweisen. Frühdevonische Protolithe aus granodioritischen und mafischen Gneisen des südlichen Gobi-Altai legen auf Grund ihrer Geochemie und Nd-Isotopie eine Herkunft und Entwicklung aus hauptsächlich juveniler Kruste und Mantel nahe. Die Platznahme dieser Gesteine könnte innerhalb der Randbereiche des spätordovizisch/frühsilurischen aktiven Kontinentalrandes stattgefunden haben. Darüber hinaus deuten Geochemie und Nd-Isotopie mitteldevonischer niedriggradiger Metavulkanite aus dem südwestlichen Gobi-Altai auf eine Platznahme in einem “transitional back-arc” hin.

U–Pb Zirkonalter kombiniert mit geochemischen Daten aus der Gobi-Altai-Region legen nahe, dass durch Zurückschreiten der Subduktionszone während des Devons der Magmatismus über den aktiven Kontinentalrand in Richtung Ozean migrierte. Progressive Extension des Kontinentalrandes war mit der Öffnung eines Back-Arc-Beckens verbunden und gipfelte im späten Devon in der Ausbildung einer “Japan-type arc front” in Richtung eines nach Südwesten offenen Ozeans (nach heutigen Koordinaten).

Table of Contents

Preface

Central Asia is build up of a vast and curved accretionary system, known as the Central Asian Orogenic Belt (CAOB) or Altaids. The origin and evolution of the CAOB is still controversial and either explained by (1) oroclinal bending and strike-slip duplication of a single or two parallel volcanic arc systems between the late Cambrian and early Permian, or (2) by punctuated accretion of multiple magmatic arc systems and intervening ocean basins, from the late Mesoproterozoic to the late Permian/early Triassic.

Mongolia occupies a central position within the eastern branch of the CAOB and is generally interpreted in terms of a tectonic collage of lithostratigraphic units, or terranes (magmatic arcs, accretionary prism, ophiolitic complexes, microcontinents). Simplified, Mongolia is traditionally subdivided into a predominantly Precambrian/early Palaeozoic northern domain and a predominantly Palaeozoic southern domain. These domains are separated by the Main Mongolian Lineament (MML) regarded as a stabilized margin by the end of the Ordovician, facing a southward open realm. The south-central area of Mongolia is of particular interest because it overlaps the northern and southern Mongolian domains and therefore provides the opportunity to examine (1) the possible amalgamation of the northern domain prior to the early Ordovician and (2) the geodynamic environment(s) prevalent in the southern domain during the Palaeozoic.

This doctoral thesis deals with the geological, geochronological and geochemical evolution of rocks from south-central Mongolia with the intention to contribute to the knowledge about the Cambrian to middle Palaeozoic geodynamic evolution of this part of the eastern CAOB. Emphasis was placed on metaigneous rocks sampled in several key areas located S of the Hangay Mountains and in the Gobi-Altai region, which are separated by the MML. The research focussed on field investigations coupled with (1) precise U–Pb zircon dating predominantly obtained by Sensitive High-Resolution Ion Microprobe (SHRIMP II) and subordinately by thermal ionisation mass-spectrometry (TIMS) in order to clarify temporal constraints, (2) chemical characterization of the magmatic sequences based on whole-rock major and trace element analyses acquired by XRF and LA-ICP-MS, respectively, and (3) Sm–Nd isotopic systematics obtained by TIMS to provide information on the sources and petrogenesis of the magmatic sequences. The thesis is organized into four chapters in which the results are presented and discussed within the regional geological framework proposed by past studies. The various analytical methods are described in detail within each chapter, whereas a sample list (with geographical coordinates) and associated analytical data are given in the Appendix.

Chapter 1 presents a geochronological study of granitoid gneisses from the Baga Bogd Massif, located at the northern boundary of the Gobi-Altai region. The results of SHRIMP II zircon dating reveals three groups of protolith emplacement ages for these granitoid gneisses: (1) Late Palaeoproterozoic to early Mesoproterozoic, (2) early Neoproterozoic, and (3) late Cambrian. This study provides the first record of early Neoproterozoic granitic crust in this area and particularly emphasizes the involvement of pre-existing crustal fragments during the Palaeozoic accretionary history of the eastern CAOB. This issue is further discussed in Chapter 3 and supplemented by geochemical and isotopic data for low-grade metaigneous rocks from an area located immediately to the S of this massif. Chapter 1 is largely identical to a manuscript entitled “Precambrian crystalline basement in southern Mongolia as revealed by SHRIMP zircon dating” accepted in April 2008 for publication in *International Journal of Earth Sciences*, doi: 10.1007/s00531-008-0321-4. Co-authors are A. Kröner (Institut für Geowissenschaften, Universität Mainz, Germany), D.Y. Liu (Beijing SHRIMP Centre, Institute of Geology, Chinese Academy of Sciences, Beijing, China) and G. Badarch (Institute of Geology and Mineral Resources, Ulaanbaatar, Mongolia, deceased in June 2006). Three samples dated by SHRIMP were analysed by A. Kröner. All other analyses, data interpretations, and preparation of the manuscript were performed by A. Demoux.

Chapter 2 deals mainly with zircon ages obtained for high- and low-grade metamorphic rocks from the Bayankhongor/Baydrag orogenic zone located on the southern slope of the Hangay Mountains in central Mongolia. The field investigations combined with geochronological results permit to (1) refine the tectonothermal evolution of the Precambrian Baydrag block prior to 1.8 Ga and elucidate its southeastern extension, and (2) reconstruct the late Neoproterozoic to Cambrian accretion history of the mid-Neoproterozoic Bayankhongor ophiolite zone with the northeastern active margin of the Baydrag block. This chapter is largely identical to a manuscript entitled “Zircon ages from the Baydrag block and the Bayankhongor ophiolite zone: time constraints on late Neoproterozoic to Cambrian subduction- and accretion-related magmatism in central Mongolia”, accepted in February 2009 for publication in *Journal of Geology*. Co-authors are A. Kröner (Institut für Geowissenschaften, Universität Mainz, Germany), G. Badarch (Institute of Geology and Mineral Resources, Ulaanbaatar, Mongolia, deceased in June 2006), P. Jian (Beijing SHRIMP Centre, Institute of Geology, Chinese Academy of Sciences, Beijing, China), D. Tomurhuu

(Institute of Geology and Mineral Resources, Ulaanbaatar, Mongolia), and M.T.D. Wingate (Tectonics Special Research Centre, University of Western Australia). A. Kröner provided Pb–Pb zircon evaporation data as well as the data for two samples dated by SHRIMP II. P. Jian, Beijing, provided the data for one high-grade sample dated by SHRIMP II. Data interpretations, preparation of the manuscript as well as all other analyses were performed by A. Demoux.

Chapter 3 presents zircon ages (obtained by SHRIMP II and TIMS) and geochemical and Nd isotopic data for middle Palaeozoic metaigneous rocks from three localities within the Gobi-Altai area (i.e. S of the MML). The data emphasize rejuvenation of a Precambrian basement from the late Ordovician/early Silurian to the Devonian, likely within a active margin setting. The combined U–Pb zircon ages and geochemical data suggest that magmatism migrated toward the outboard portion of the active margin through time likely in response to subduction zone retreat. Progressive extension of the active margin throughout the Devonian resulted in formation of a Japan-type arc front associated with a back-arc basin. This latter issue is further discussed in chapter 4. Chapter 3, entitled “Middle Palaeozoic evolution of an active continental margin in southern Mongolia: zircon ages and geochemical characteristics of igneous rocks of the Gobi-Altai region”, is under consideration to be submitted as manuscript in the near future. Co-authors are E. Hegner (Institut für Geo- und Umweltwissenschaften, Universität München, Germany), A. Kröner (Institut für Geowissenschaften, Universität Mainz, Germany) and G. Badarch (Institute of Geology and Mineral Resources, Ulaanbaatar, Mongolia, deceased in June 2006). Acquisition of all data, interpretations, and preparation of the manuscript were performed by A. Demoux.

Chapter 4 reports SHRIMP II zircon ages, whole-rock major and trace element analyses as well as Nd isotopic data for low- and high-grade metaigneous rocks from the Tseel terrane, located in the northwestern Gobi-Altai area. The geochemical and isotopic results for mafic metavolcanic rocks are consistent with an emplacement within a transitional arc/backarc setting from moderately depleted mantle sources. The Nd isotopic results for felsic metaigneous rocks support an origin from predominantly juvenile crustal sources with minor contribution of Precambrian recycled crustal components. The combination of field and geochemical/isotopic data suggest that the investigated transect belongs to a crustal domain, which forms a part of a Japan-like setting. This chapter is largely identical to a manuscript entitled “Devonian arc-related magmatism in the Tseel terrane of southwestern Mongolia: chronological and geochemical evidence”, which was published in the *Journal of the*

Geological Society, London in May 2009. Co-authors are A. Kröner (Institut für Geowissenschaften, Universität Mainz, Germany), E. Hegner (Institut für Geo- und Umweltwissenschaften, Universität München, Germany) and G. Badarch (Institute of Geology and Mineral Resources, Ulaanbaatar, Mongolia, deceased in June 2006). Two samples dated by SHRIMP were analysed by A. Kröner. All other data, interpretations, and preparation of the manuscript were performed by A. Demoux.

Chapter 1

Precambrian crystalline basement in southern Mongolia as revealed by SHRIMP zircon dating

Abstract

Single zircon ages determined by ion microprobe (SHRIMP II) for granitoid gneisses from the southern slope of the Baga Bogd Massif (Gobi-Altai, southern Mongolia) reveal several episodes of zircon growth, ranging from late Palaeoproterozoic to late Cambrian. The oldest events are documented by a zircon crystallization age for a gneiss protolith at 1519 ± 11 Ma and by a xenocrystic zircon from a dark grey augen-gneiss yielding an age of c. 1701 Ma. Discrete igneous events are recorded in granite gneisses with protolith emplacement ages of 983 ± 6, 956 ± 3 and 954 ± 8 Ma. These ages provide the first record of early Neoproterozoic magmatic activity in this region. A much younger and discrete magmatic event is recorded by several dioritic to granitic orthogneisses which are tectonically interlayered with the older gneisses and have protolith emplacement ages between 502 and 498 Ma. These late Cambrian granitoids of calc-alkaline affinity are likely to have been emplaced along an active continental margin and suggest that the Baga Bogd Precambrian crustal fragment was either docked against the southward (present-day coordinates) growing margin of the CAOB or was a large enough crustal entity to develop an arc along its margin. We speculate that the Precambrian gneisses of this massif may be part of a crustal fragment rifted off the Tarim Craton.

1. Introduction

The Central Asian Orogenic Belt (CAOB; Fig. 1), also termed the Altaid Tectonic Collage (Şengör et al. 1993), is a complex tectonic mosaic of subduction-related complexes, island arcs, ophiolitic assemblages and slivers or terranes of Precambrian crystalline basement. The development and amalgamation of these orogenic domains are related to subduction-accretion processes within the Palaeo-Asian Ocean from early Neoproterozoic to late Palaeozoic time (Şengör et al. 1993; Buslov et al. 2001; Badarch et al. 2002; Khain et al. 2003; Kröner et al. 2007; Windley et al. 2007).

A striking feature of the CAOB is the predominantly juvenile character of the newly formed crust as revealed by Nd isotopic studies from Palaeozoic arc-related magmatic rocks (e.g. Jahn et al. 2000b; Kovalenko et al. 2004; Helo et al. 2006). However, the concept of juvenile crust defined exclusively by Nd isotopic data may not always be correct as suggested by Hargrove et al. (2006) from a study of granitoids in the Arabian-Nubian Shield. These authors demonstrated that isotopically juvenile magmas assimilated significant amounts of old crustal material as revealed by large proportions of inherited zircon within these rocks. In a similar way, Precambrian ages documented by xenocrystic and detrital zircons from Palaeozoic felsic volcanic rocks and arc-related clastic sediments in northern and central Mongolia (Kröner et al. 2007) suggest a substantial involvement of old material during the generation of these rocks.

Within most parts of the CAOB, and in particular Mongolia, terrains composed of high-grade metamorphic rocks were usually assumed to be Precambrian in age, though reliable radiometric ages are frequently missing (e.g. Mitrofanov et al. 1981; Badarch et al. 2002). These crystalline rocks were either interpreted as remnants of a single Precambrian microcontinent (Tuva-Mongolian; Şengör et al. 1993; Windley et al. 2007) or as individual microcontinents (e.g. Didenko et al. 1994 and references therein), namely Tuva-Mongolia, Dzabkhan and South Gobi. An alternative interpretation of the Tuva-Mongolia microcontinent (Kozakov et al. 1999a; Sal'nikova et al. 2001) is based on U–Pb zircon ages which demonstrate that the earliest metamorphic event occurred at c. 536 Ma, followed by a regional phase of upper amphibolite-facies metamorphism between c. 497 and 489 Ma. These authors therefore suggested that discrete crustal domains, with distinct pre-metamorphic histories (Kozakov et al. 2005), were tectonically juxtaposed prior to c. 497 Ma and then underwent a phase of high-grade metamorphism as part of the evolution of the CAOB.

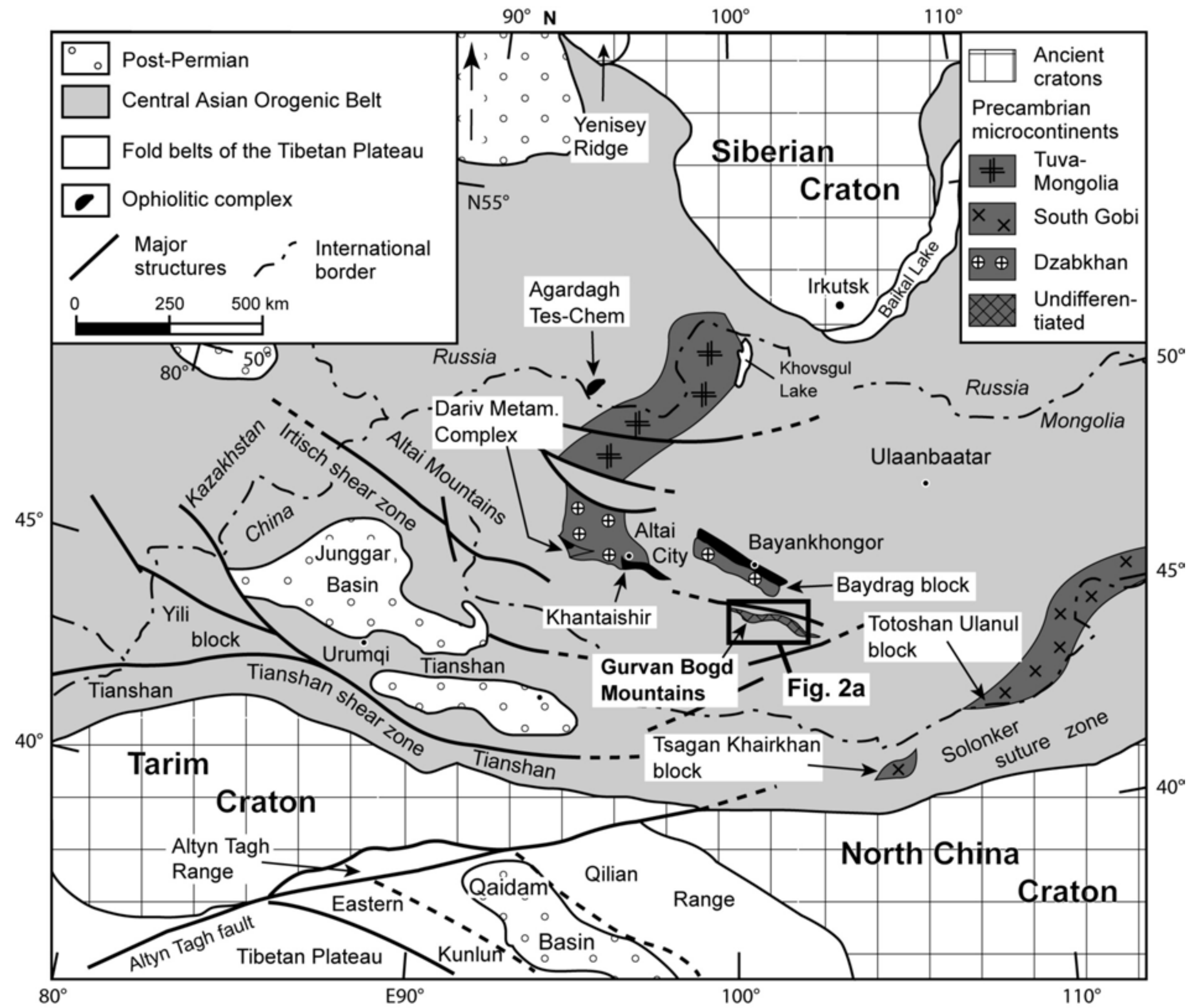

Fig. 1. Sketch map showing the position of Mongolia within the Central Asian Orogenic Belt (modified after Jahn et al. 2000b; Lu et al. 2008). The Central Asian Orogneic Belt (*light grey*) is predominantly composed of early Neoproterozoic to late Palaeozoic rock assemblages. The main identified Precambrian microcontinents, and their inferred extension, in Mongolia, northern China and southern Siberia are shown in dark grey (adapted from Kozakov et al. 2007b). The ophiolitic complexes mentioned in this paper are shown in black. Location of Fig. 2a is also shown.

The existence of undoubted Precambrian crystalline rocks in central and southern Mongolia is documented by zircon dating for a variety of gneisses from the Baydrag (central Mongolia) and the Totoshan-Ulanul (southern Mongolia) blocks which are parts of the Dzabkhan and South Gobi microcontinents, respectively (Fig. 1). Within the Baydrag block zircon dating yielded Archaean to Palaeoproterozoic emplacement ages of c. 2.80–1.82 Ga for orthogneiss protoliths (Mitrofanov et al. 1985; Kotov et al. 1995; Kröner et al. 2001; Kozakov et al. 2007b), whereas early Neoproterozoic intrusion ages of c. 0.95 Ga characterize granitic protolith of gneisses from the Totoshan-Ulanul block (Yarmolyuk et al. 2005).

We investigated the Baga Bogd Massif in southern Mongolia, which is part of the Gurvan Bogd Mountain range (Fig. 1). The occurrence of high-grade metamorphic rocks, including granitic gneisses and migmatites, led this range to be considered as Precambrian in age (Badarch et al. 2002). This study focusses on SHRIMP zircon dating of a variety of granitoid gneisses in order to identify pre-Palaeozoic magmatic events and to possibly correlate the above rocks with other Precambrian crustal fragments in southern Mongolia.

2. Geological framework

The Gurvan Bogd Mountain range is located at the eastern end of the Gobi-Altai in southwestern Mongolia and consists of three WNW–ENE striking massifs (Ih Bogd, Baga Bogd and Artz Bogd) with peaks up to 3957 m (Fig. 2a). The present-day topography of this mountain system (and the Altai and Gobi-Altai regions in general) resulted primarily from Cenozoic transpressive deformation in response to far-field stresses associated with the Indo-Eurasian collision (Tapponnier & Molnar 1979; Cunningham 2005). One of these massifs uplifted during this deformation is the Baga Bogd Massif (Vassallo et al. 2007), an asymmetric elliptic massif bounded in the north by the left-lateral strike-slip Bogd fault (Bayasgalan et al. 1999). It consists predominantly of variably deformed and metamorphosed Precambrian rocks, intruded by late Neoproterozoic granitoids as inferred from the 1:200,000 Geological Map (Zabotkin 1988; Fig. 2b). Permian granitoids and Jurassic intracontinental sediments are locally found, whereas the northeastern part of the massif is characterized by the occurrence of a late Palaeozoic volcano-sedimentary sequence, which is mostly in tectonic contact with the metamorphic rocks.

Three N–S valleys have been investigated along the southern slope of the Baga Bogd Massif, namely the Borbituutin and Tsagaanburgas Valleys and a third, unnamed valley to the east (Fig. 2b). The rocks exposed along these valleys were deformed under upper greenschist- to amphibolite-facies metamorphism, locally leading to incipient migmatization. A strong penetrative foliation and tight folding affected all metamorphic rocks, leading to parallelism of most lithological contacts. Along the Tsagaanburgas Valley, the predominant lithology is represented by strongly foliated dark augen-gneisses and layered migmatites of presumed igneous origin. These rocks are cut by undeformed dykes of mafic to intermediate composition, about one to several metres in width and consistently striking NE–SW and dipping from 45° to 75° NW or SE. The predominant rock types exposed along the

Borbituutin and unnamed valleys are light grey augen-gneisses (Fig. 3a), layered migmatites (Fig. 3b), biotite-quartz-feldspar gneisses, and a higher proportion of clastic metasedimentary rocks, including metaquartzite and quartz-biotite schist, as compared to the Tsagaanburgas Valley. Strongly foliated dioritic and granodioritic gneisses are also widespread in the unnamed valley. These rocks were, in turn, intruded by leucogranitic veins that locally display post-emplacement folding and boudinage; some veins contain a high proportion of garnet up

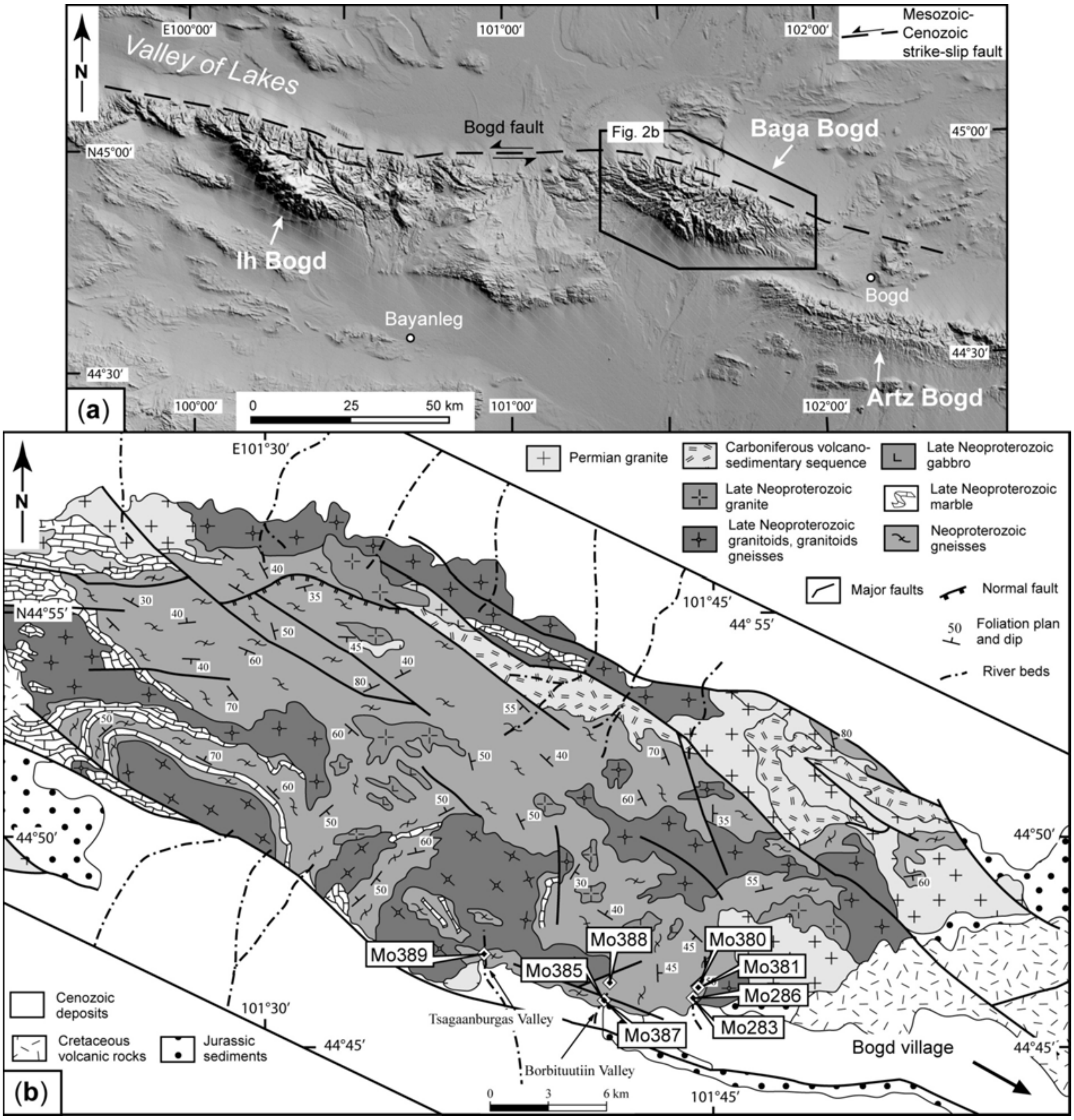

Fig. 2. (**a**) Grey-scaled digital topographic map of the Gurvan Bogd Mountains showing the massif of interest for this study (Baga Bogd). (**b**) Geological sketch map of the Baga Bogd Massif (modified after Geological Map L47-XXX, 1:200,000, Zabotkin 1988), with location of samples dated by SHRIMP.

to 1 cm in size (Fig. 3c). Undeformed dykes of mafic to intermediate composition (Fig. 3d), striking E–W and dipping S at 60–85°, also occur along these valleys.

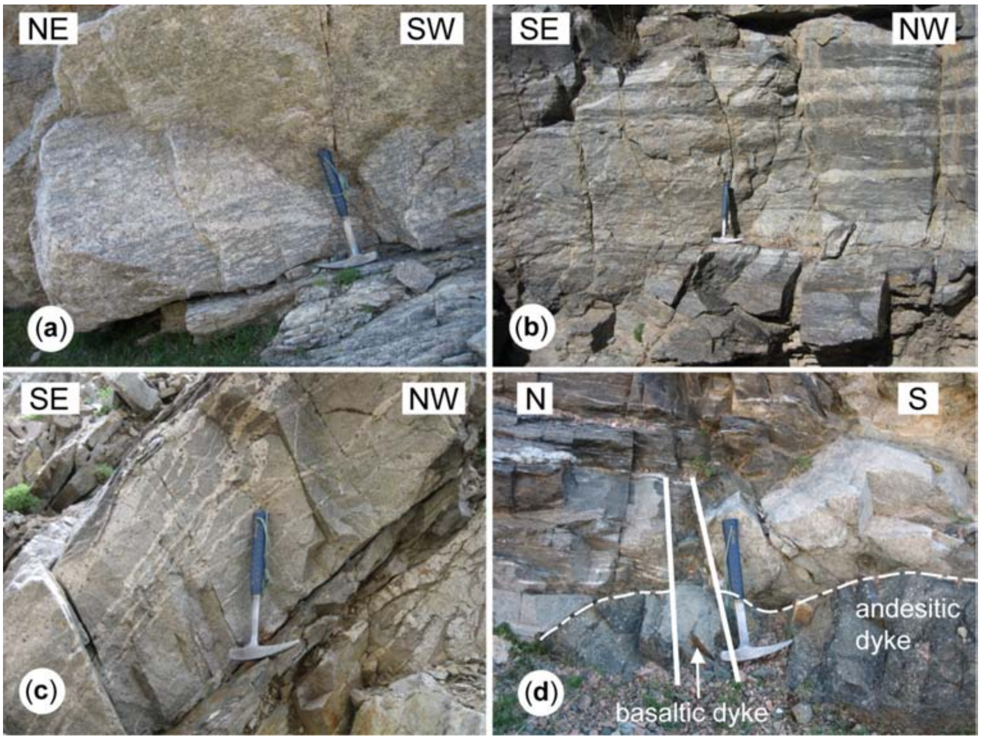

Fig. 3. Field photographs of selected rock types from the Baga Bogd Massif. (**a**) Strongly foliated light grey augen-gneiss (sample Mo385), Borbituutiin Valley. (**b**) Banded migmatite, Borbituutiin Valley. (**c**) Garnet-rich leucocratic veinlets cutting a fine-grained gneiss. (**d**) Cross-cutting relationship between basaltic/andesitic dykes and surrounding migmatitic country rock. Hammer for scale is 32 cm long.

3. Sample description and geochronological results

Eight samples representing different varieties of granitoid gneisses were collected for SHRIMP zircon dating on the southern slope of the Baga Bogd Massif (Fig. 2b). Separation of zircon grains followed standard procedures using heavy liquid and magnetic techniques. Representative zircons were hand-picked under a binocular microscope and mounted in epoxy resin together with chips of the reference zircons Temora 1 or CZ3. The resin disk was then polished to expose the interiors of the zircons. The internal structures of the grains were documented by cathodoluminescence (CL) images acquired with a JEOL JXA-8900 RL Superprobe in the Department of Geosciences, Mainz University (operating conditions were 15 kV accelerating voltage and 12 nA beam current on carbon-coated mounts). The U–Pb isotopic analyses on single zircons were carried out using the Sensitive High Resolution Ion Microprobe (SHRIMP II) at the Centre of Isotopic Research (CIR) in St. Petersburg (Russia) and in the Beijing SHRIMP Centre of the Chinese Academy of Geological Sciences. The instrumental characteristics are outlined by Larionov et al. (2004) and De Laeter & Kennedy (1998), respectively, and the analytical procedures are described in Claoué-Long et al. (1995), Nelson (1997) and Williams (1998). The uncertainty in the ratio $^{206}Pb^{*}/U$ during analysis of all CZ3 standard zircons during this study was 0.75% for the St. Petersburg instrument and 1.18% for the Temora 1 standard for the Beijing instrument. Sensitivity was about 56 cps/ppm/nA Pb for the standard CZ3 in St. Petersburg and about 23–24 cps/ppm/nA Pb for the Temora 1 standard on the Beijing instrument. The isotopic data and ages are reported in Appendix B-1. Errors on individual analyses are given at the 1σ level, based on counting statistics, and include the uncertainty in the standard U/Pb age (Nelson 1997). Errors for pooled analyses are given at the 95% confidence interval. The ages and errors of intercepts of the best-fit line with concordia were calculated using the Isoplot program (Ludwig 2003). These errors were not multiplied by the square root of the MSWD since the absolute value of the intercept error is strongly model dependent.

Sample Mo283 is a dark and well-foliated, medium-grained dioritic orthogneiss collected in the unnamed valley (N44°45’58.9”, E101°44’35.6”). It represents the most dominant rock type in this valley and is composed of large biotite flakes, plagioclase, recrystallized quartz showing undulose extinction, and relicts of clinopyroxene. Accessory minerals include apatite, zircon and epidote. The rock shows a strong penetrative foliation, defined by biotite flakes, which conforms to the foliation developed in the surrounding fine-grained biotite gneiss and quartzo-feldspathic layered gneiss. Field relationships suggest the dioritic gneiss to be intrusive into the above gneisses, but the strong ductile deformation has largely obliterated the original contacts. This sample contains a population of zircons dominated by clear, euhedral and long prismatic grains with short and slightly rounded terminations. The colour varies from slight yellowish to pinkish, and the grain size ranges from 150 μm up to 300 μm in length. The grains display oscillatory zoning in CL images (Fig. 4a) characteristic of igneous growth. A few smaller grains <150 μm in length are also present and are characterized by a dark colour, short prismatic and subhedral habit with slightly rounded faces. Nine grains were analysed on the St. Petersburg SHRIMP II. Eight grains yielded a tight cluster of concordant results (Fig. 4a) with a weighted mean $^{206}Pb/^{238}U$ age of 498 ± 3 Ma which is interpreted to reflect the time of crystallization of the gneiss protolith. One grain yielded a significantly older, concordant result (Fig. 4a) with a $^{206}Pb/^{238}U$ age of 656 ± 10 Ma and is interpreted as a xenocryst, probably inherited from the basement rock into which the gneiss protolith was emplaced.

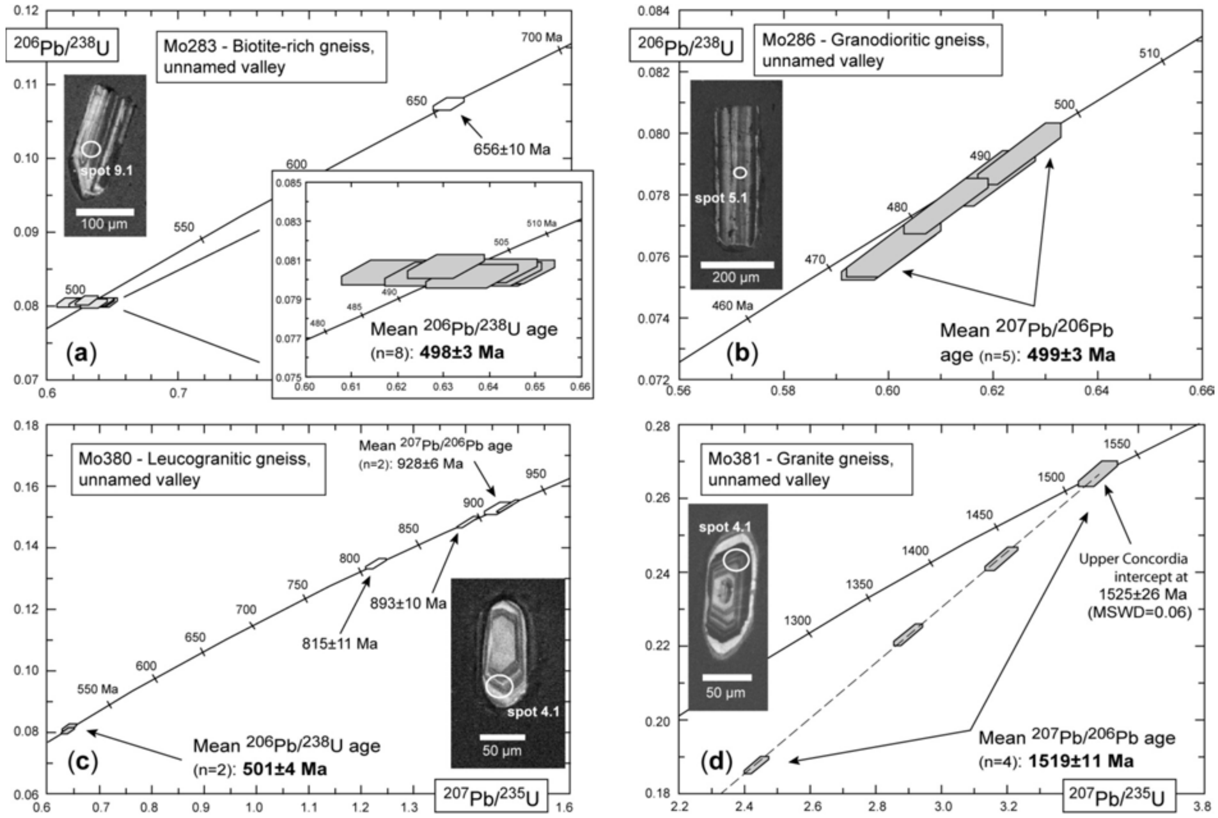

Fig. 4. Concordia diagrams showing SHRIMP analyses of single zircons for samples from the unnamed valley. Data boxes for each analysis are defined by standard errors in $^{207}Pb/^{235}U$, $^{206}Pb/^{238}U$ and $^{207}Pb/^{206}Pb$. Errors on pooled ages are given at 95% confidence level. Insets show CL images of zircon grains, white circles indicate SHRIMP analytical spots; spot numbers refer to those in Appendix B-1.

Sample Mo286 was collected some 15 m from sample Mo283 and is a strongly foliated, medium-grained biotite gneiss, originally a granodiorite, into which the above dioritic gneiss may originally have been intrusive. The texture is lepidoblastic, and the rock contains small biotite flakes mostly altered into chlorite, plagioclase with polysynthetic twinning, K-feldspar with a high degree of alteration and quartz showing undulose extinction. It contains accessory apatite, zircon, epidote and an oxide phase. The original relationship with the surrounding rocks is not clear since they now share the same foliation, and undoubted cross-cutting relationships are not preserved. The zircons from this sample are translucent, yellowish to slightly reddish in colour and predominantly long-prismatic or needle-like in shape and between 100 and 250 μm in length. Cathodoluminescence images reveal simple oscillatory zoning indicative of a magmatic origin and do not show inherited cores or metamorphic overgrowth (Fig. 4b). Five zircon grains were analysed on the St. Petersburg SHRIMP II, and these produced concordant or near-concordant results (Fig. 4b) with a weighted mean $^{207}Pb/^{206}Pb$ age of 499 ± 3 Ma. We interpret this to reflect the time of emplacement of the granodioritic protolith. Both samples Mo283 and Mo286 obviously reflect the same magmatic event and may represent one phase of late Cambrian granitoid plutonism in the Baga Bogd Massif.

Sample Mo380 is a leucocratic, fine-grained biotite granite gneiss cut by garnet-rich leucogranitic veins and was collected higher up in the unnamed valley (N44°46'11.7", E101°44'41.0"), some 400 m north of samples Mo283 and Mo286. It is composed of plagioclase, quartz, microcline, and small biotite flakes. The zircon grains are translucent, subhedral, long- to short-prismatic with a dominant brownish colour and vary in length between 100 and 250 µm. Cathodoluminescence images for the long-prismatic grains display simple igneous-related oscillatory zoning, whereas short-prismatic and more rounded grains tend to have partly recrystallized rims and convolute internal zoning (Corfu et al. 2003). Six grains were analysed on the Beijing SHRIMP II and produced concordant or near-concordant results which are spread along the concordia from 930 to 500 Ma (Fig. 4c). At the lowest end of the spread, two grains yielded concordant results, identical within error, with a mean $^{206}Pb/^{238}U$ age of 501 ± 4 Ma (Fig. 4c). The four remaining grains have ages between 930 and 815 Ma (Fig. 4c) with two grains at the end of the spread yielding similar results with a mean $^{207}Pb/^{206}Pb$ age of 928 ± 6 Ma. In view of the igneous origin of the zircons the age of 501 ± 4 Ma is interpreted as the time of emplacement of the gneiss precursor, whereas the remaining older grains suggest inheritance and involvement of Neoproterozoic basement material in the generation of the gneiss protolith. If this interpretation is correct, the gneiss protolith belongs to the same magmatic pulse as samples Mo283 and Mo286.

Sample Mo381 was collected in the same valley, about 600 m north of Mo380, and is a strongly foliated, fine-grained granite gneiss composed of biotite and muscovite flakes, quartz, K-feldspar and garnet. K-feldspar is moderately to intensely sericitized, and garnet is extensively replaced by chlorite. The rock has a lepidoblastic texture defined by alternation of quartzo-feldspatic and micaceous bands. The sample contains a small population of subhedral, translucent and brownish zircons, and CL images reveal oscillatory zoning as well as partially recrystallized rims for most of the grains (Fig. 4d). Four zircons from this sample were analysed on the Beijing SHRIMP II. One grain yielded a concordant analysis, and the three remaining grains produced discordant results (Fig. 4d). However, all analyses are aligned along a chord (MSWD = 0.06) yielding an upper intercept age of 1525 ± 26 Ma and a lower intercept at 60 ± 170 Ma reflecting recent lead-loss. All analyses have a weighted mean ^{207}Pb/^{206}Pb age of 1519 ± 11 Ma, identical within error to the upper intercept age, which we consider to best approximate the time of emplacement of the granitic protolith. Although sample Mo381 exhibits the same foliation as the other rocks described above, it is clearly much older and must be part of the basement into which the late Cambrian pluton was emplaced.

Sample Mo385 is a light grey augen-gneiss representing the main lithology in Borbituutiin Valley and was collected at N44°46’05.3”, E101°41’29.0”. The gneiss is strongly foliated, coarse-grained, and is composed of quartz, microcline and millimetre-size biotite that is mostly altered into chlorite. K-feldspar is extensively sericitized, and the augen are up to 5 cm in size. The zircons are translucent, long- to short-prismatic, with variable aspects ratios and rounded terminations. The length ranges from 100 to 280 µm, and the colour varies from light to dark brown. Cathodoluminescence images reveal oscillatory zoning (Fig. 5a), characteristic of magmatic growth, and the presence of inherited cores in some grains. Six zircons were analysed on the Beijing SHRIMP II and display variable degrees of discordance (Fig. 5a). All analyses, with one virtually concordant, are well aligned along a chord (MSWD = 0.13) (Fig. 5a) and define a weighted mean ^{207}Pb/^{206}Pb age of 954 ± 8 Ma. The above chord defines an upper concordia intercept age of 959 ± 23 Ma and a lower intercept at 89 ± 330 Ma. The upper intercept age is identical to the mean ^{207}Pb/^{206}Pb age but less precise because of the large error in the lower intercept. This lower intercept is geologically meaningless and clearly reflects recent lead-loss. We therefore consider the mean ^{207}Pb/^{206}Pb age of 954 ± 8 Ma to most closely approximate the time of emplacement of the gneiss precursor. Again, this sample is part of a Precambrian basement.

Sample Mo387 is a medium-grained dark grey augen-gneiss collected farther north in Borbituutin Valley at N44°46’12.0”, E101°41’33.5”. It is composed of strongly seriticized K-feldspar porphyroblasts, quartz, and biotite flakes with chloritized rims. It has a grano-lepidoblastic texture with a gneissic fabric underlined by biotite and quartz ribbons. The zircons are long-prismatic with a high aspect ratio, or short-prismatic and are translucent, mostly subhedral with rounded edges and light grey to brown colour. Cathodoluminescence images reveal well developed oscillatory zoning due to igneous growth (Fig. 5b) and core-rim relationships in some grains. Five zircon grains from this sample were analysed on the Beijing instrument. Four concordant and discordant analyses (Fig. 5b) are aligned along a Discordia line (MSWD = 0.02) which defines a lower intercept at 8 ± 190 Ma and an upper intercept age of 984 ± 27 Ma, identical within error to the weighted mean ^{207}Pb/^{206}Pb age of 983 ± 6 Ma of the four analyses. Thus, the age of 983 ± 6 Ma is considered to reflect the time of emplacement of the granitic protolith. The fifth grain yielded a much older ^{207}Pb/^{206}Pb age of 1701 ± 14 Ma (1σ) (Fig. 5b), which, as in previous samples, is interpreted as a xenocryst inherited from a late Palaeoproterozoic crustal source.

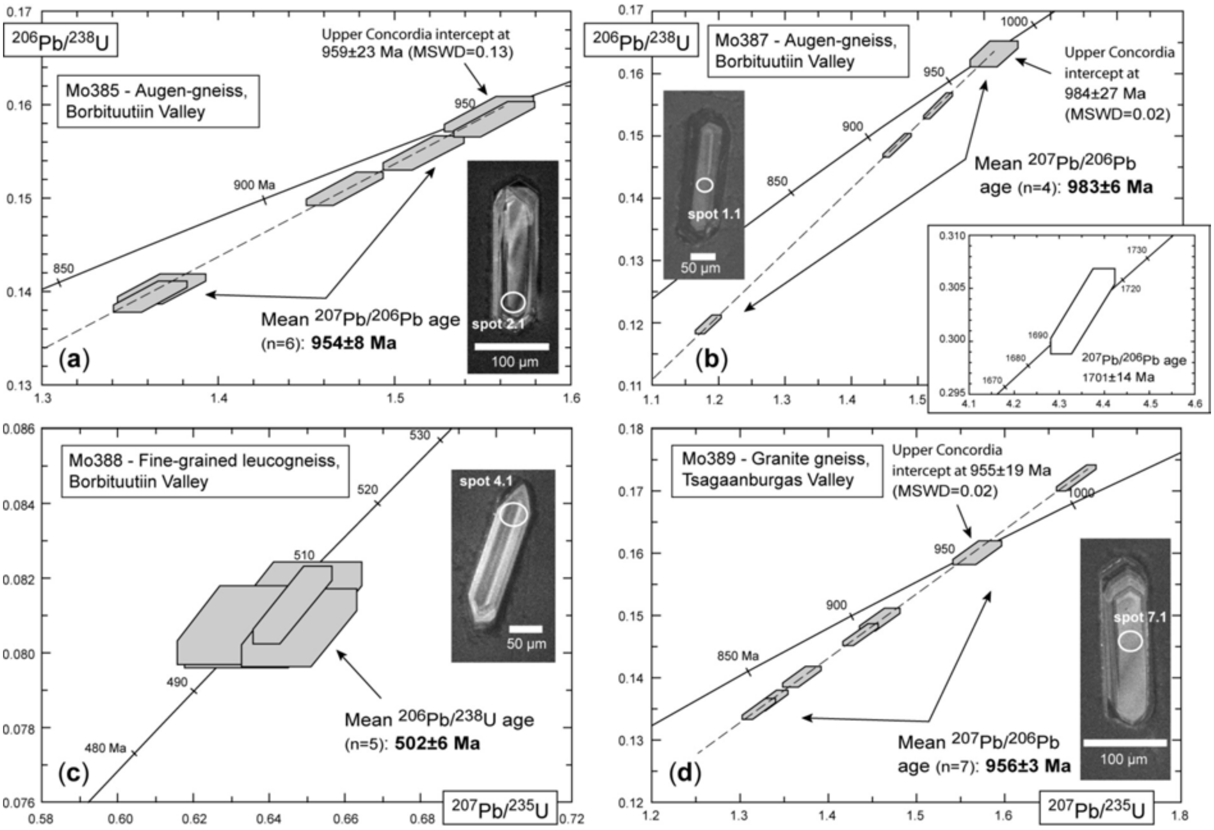

Fig. 5. Concordia diagrams showing SHRIMP analyses of single zircons for samples from the Borbituutiin and Tsagaanburgas Valleys. Data boxes for each analysis and errors on pooled ages as in Fig. 4. Insets show CL images of zircon grains, white circles indicate SHRIMP analytical spots; spot numbers refer those in Appendix B-1.

Sample Mo388 is a strongly deformed very fine-grained, laminated leucocratic gneiss, interlayered with the surrounding augen-gneiss and collected still farther north in Borbituutin Valley at N44°47’03.5”, E101°41’14.1”. The mineral assemblage consists of K-feldspar, quartz and minor biotite flakes. The zircons are of two types. Type 1 is represented by clear, transparent, long- to short-prismatic and euhedral grains, 100–150 μm in length and displaying typical magmatic growth features under cathodoluminescence (Fig. 5c). Type 2 grains are mostly short-prismatic, subhedral with rounded terminations and dark brown colour. They range in length between 100 and 250 μm and display complex internal growth structures as revealed by CL images. Five grains of type 1 grains were analysed on the Beijing SHRIMP II and yielded concordant results (Fig. 5c) with a weighted mean $^{206}Pb/^{238}U$ age of 502 ± 6 Ma which we interpret as the time of emplacement of the gneiss protolith.

Lastly, sample Mo389 is a coarse-grained, light grey granite gneiss collected in Tsagaanburgas Valley at N44°47'29.8", E101°37'16.9". This gneiss is composed of large K-feldspar, quartz, minor plagioclase, millimetre-size biotite and large idiomorphic garnet crystals altered into an assemblage of chlorite+quartz. K-feldspar is moderately sericitized and biotite is mostly transformed into chlorite. Quartz is mostly recrystallized. The zircons are mainly short-prismatic with rare long-prismatic and transparent grains. Most grains are euhedral to subhedral with slightly rounded terminations, vary in length from 80 to 250 μm, and are light yellowish to dark brownish in colour. Cathodoluminescence images reveal well-developed oscillatory zoning (Fig. 5d), characteristic of igneous crystallization, and do not show cores or overgrowth. Seven zircons were analysed on the Beijing instrument and yielded well-aligned results one of which is concordant, one reversely discordant and five exhibit variable degrees of discordance (Fig. 5d). All analyses define a weighted mean $^{207}Pb/^{206}Pb$ age of 956 ± 3 Ma, whereas linear regression (MSWD = 0.02) resulted in an upper concordia intercept age of 955 ± 19 Ma and a lower intercept at -13 ± 240 Ma which clearly reflects recent Pb-loss. As in the case of sample Mo385, both ages are identical, and we consider the more precise mean $^{207}Pb/^{206}Pb$ age as most closely reflecting the time of protolith emplacement.

4. Whole-rock major and trace elements chemistry

Major and trace element data for the dated samples were obtained by X-ray fluorescence spectrometry, using a Philips MagiXPro spectrometer in the Department of Geosciences, Mainz University. Loss on ignition (LOI) was determined by weight loss after heating at 1050 °C for 4 h. The results are listed in Appendix E-1.

Zircon geochronology revealed three groups of ages, one at around 500 Ma (samples Mo283, Mo286, Mo380 and Mo388), another with early Neoproterozoic ages ranging from 983 to 954 Ma (samples Mo385, Mo387 and Mo389) and one with a much older age of 1.52 Ga (sample Mo381). The distinction between the three groups was already suspected from field relationships although intrusive features displayed by the youngest group were partly obliterated during post-intrusion deformation. In the following, these samples will be treated as two separate groups: Precambrian (Meso- and early Neoproterozoic) gneisses on one side and the late Cambrian gneisses on the other side. The chemical indices of alteration (CIA) of 46–55 for all granitoid gneisses are comparable to those of unaltered granitic and mafic rocks (CIA for average fresh granite: 45–55; Nesbitt & Young 1982) except for the granite gneiss Mo381 which has a CIA index of 69 and the highest LOI value of 1.75 wt%. Nevertheless, the relatively high degree of alteration of K-feldspar and some biotite observed in thin section indicates that some elements and the alkaline elements in particular, may not reflect primary compositions.

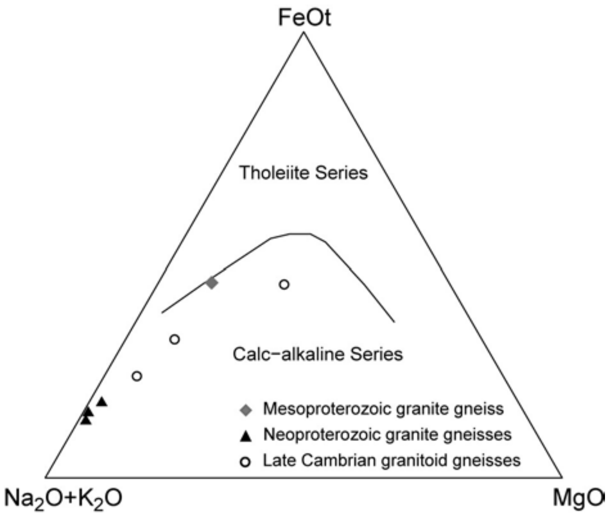

Fig. 6. AFM diagram for gneisses from the Baga Bogd Massif showing. FeOt, total iron as FeO; dividing line between tholeiitic and calc-alkaline series is from Irvine & Baragar (1971).

4.1. Major element chemistry

The early Neoproterozoic gneisses are granitic and calc-alkaline in composition (Fig. 6) and show limited variation in chemical composition with restricted SiO_2 contents of c. 71–79 wt%. They are characterized by homogeneous and low TiO_2, Fe_2O_3t, MgO and CaO contents and relatively high K_2O contents of 5.6–6.4 wt%, whereas significant scatter is observed for Al_2O_3, Na_2O and P_2O_5. These samples are all slightly peraluminous with A/CNK (Aluminium Saturation Index; molecular Al_2O_3/(CaO + Na_2O + K_2O) and A/NK values of 1.1 and 1.2–1.3, respectively (Fig. 7a). Compared to these samples, the Mesoproterozoic gneiss has lower SiO_2, CaO, Na_2O, K_2O, P_2O_5 contents and higher Al_2O_3, Fe_2O_3t, MgO and TiO_2 contents. This sample is clearly peraluminous (Fig. 7a) with A/CNK and A/NK values of 2.2 and 2.6, respectively, in agreement with its mineralogy. All samples with Precambrian ages are moreover characterized by low Na_2O/K_2O ratios (0.3-0.5) and an enrichment in iron as suggested by FeOt/(FeOt + MgO) ratios that are systematically higher than 0.8 at a given SiO_2 content (Fig. 7b).

The late Cambrian gneisses cover a wide compositional range with SiO_2 contents of c. 55–68 wt% and show dioritic to granodioritic compositions with calk-alkaline affinities (Fig. 1-6). They display crude correlations of decreasing TiO_2, Fe_2O_3t, MgO and CaO with increasing SiO_2. Most gneisses are slightly peraluminous with A/CNK and A/NK values of 1.1–1.2 and 1.5–1.7, respectively (Fig. 7a), whereas sample Mo283 with SiO_2 < 56 wt% is classified as metaluminous with A/CNK < 1 and A/NK > 1 (Fig. 7a). Moreover, these samples have higher Na_2O/K_2O ratios (0.6–1.2) and FeOt/(FeOt + MgO) ratios systematically lower than 0.8 (Fig. 7b) and are referred to as magnesian Cordilleran-type granitoids according to the classification of Frost et al. (2001).

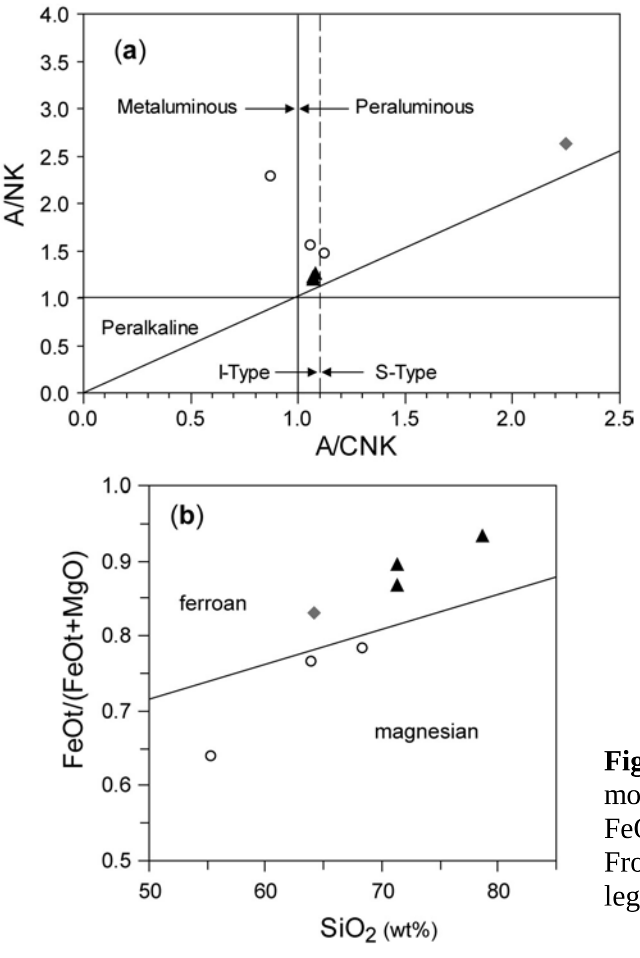

Fig. 7. (**a**) A/NK versus A/CNK diagram, modified after Shand (1951), and (**b**) FeOt/(FeOt+MgO) versus SiO_2 diagram after Frost et al. (2001). FeOt, total iron as FeO. For legend see Fig. 6.

4.2. Trace element chemistry

The Neoproterozoic granites gneisses have relatively low concentrations of Nb (4–9 ppm), Zr (85–151 ppm), Sr (87–96 ppm) and Ba (301–557 ppm). They show slight enrichments in large ion lithophile elements (LILE; Ba, Th, U) compared to high field strength elements (HFSE; Nb, Zr, Ti) and display Nb, Sr and Ti troughs on a bulk continental crust-normalized trace element patterns (Fig. 8a). The Mesoproterozoic gneiss Mo381 displays a slightly different picture with higher concentrations of Ba, Nb, Zr, Ni and Cr. Trace elements normalized to bulk continental crust show an overall good agreement with typical crustal values except for lower concentrations in Sr and P (Fig. 8a). Using the Nb–Y trace element discrimination diagram of Pearce et al. (1984), all Precambrian samples plot in the field of syn-collisional (syn-COLG)/volcanic arc-related granitoids (VAG, Fig. 9).

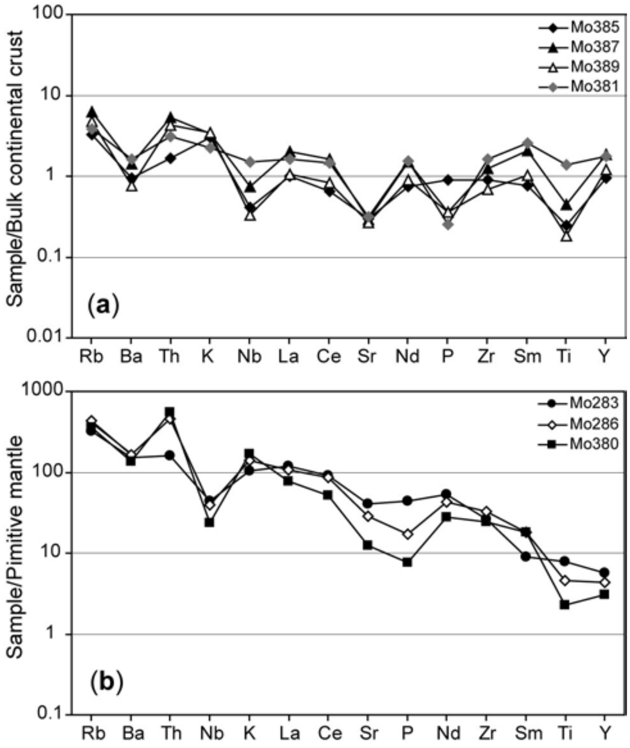

Fig. 8. Multi-element diagrams for (**a**) Meso- and early Neoproterozoic gneisses, and (**b**) late Cambrian gneisses from the Baga Bogd Massif. All elements were analysed by XRF; primitive mantle and bulk continental crust normalizing values are from Sun & McDonough (1989) and Rudnick & Fountain (1995), respectively.

Compared to the Precambrian samples, the late Cambrian rocks are more enriched in Nb, Zr, Sr and Ba.These samples are characterized by enrichment in LILE compared to HFSE when plotted in a primitive mantle-normalized spidergram (Fig. 8b). They display well pronounced negative Nb anomalies and slightly negative Ti anomalies. These gneisses display crude trends of decreasing contents of Nb, Sr, Ba and increasing Zr with increasing content of SiO_2. In the Nb-Y discrimination diagram (Pearce et al. 1984) these samples overlap the fields of syn-COLG/VAG and within-plate granitoids (WPG, Fig. 9), which suggests formation in an active continental margin environment or in a mature island arc.

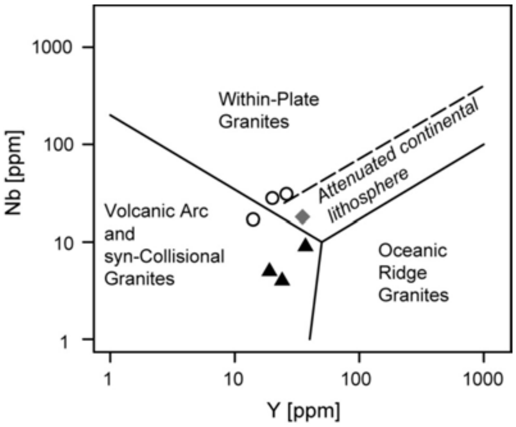

Fig. 9. Nb v. Y discrimination diagram for granites after Pearce et al. (1984). For legend see Fig. 6.

5. Discussion

Our SHRIMP zircon ages for granitoid protoliths of various orthogneisses from the Baga Bogd Massif in southern Mongolia confirm the Neoproterozoic and Cambrian age assessments inferred on the 1:200,000 Geological Map (Fig. 2b). We suspect that the Neoproterozoic gneisses experienced some structural and possibly metamorphic history prior to their incorporation into the early Palaeozoic arc terrane of southern Mongolia. However, strong ductile deformation during the Palaeozoic accretion event led to parallelism of structures in all metamorphosed rocks so that no distinction could be made in the field between Palaeozoic and older structures. No angular relationships between the Precambrian and early Palaeozoic orthogneisses were observed. This is unlike some of the low-strain domains of the large Baydrag block farther NE where Precambrian structures and a polymetamorphic Precambrian history are well preserved (Kozakov et al. 2007b).

5.1. Precambrian thermal events and possible link to identified crustal basement

The oldest dated event in the geological evolution of the study area was the intrusion of the granitic gneiss precursor of sample Mo381 at 1519 ± 11 Ma. An even older age of c. 1700 Ma is documented by a xenocrystic zircon grain from grey augen-gneiss sample Mo387. These ages document the presence of late Palaeoproterozoic to early Mesoproterozoic crust in the Baga Bogd Massif.

The existence of Precambrian crust of Archaean to Palaeoproterozoic age is well documented for the Baydrag block (Dzabkhan microcontinent; Kozakov et al. 1997) which is located to the northwest of the study area (Fig. 1). The Baydrag basement shows a complex and polyphase tectono-metamorphic evolution from late Archaean to late Palaeoproterozoic time (e.g. Kozakov et al. 1997, 2007b and references therein). The oldest rocks correspond to tonalitic and two pyroxene gneisses with protolith emplacement ages documented by conventional multigrain and SHRIMP single zircon ages of c. 2.80–2.65 Ga (Mitrofanov et al. 1985; Kozakov et al. 2007b). The last major thermal event experienced by these rocks reflects the peak of granulite-facies metamorphism with a minimum age of 1839 ± 1 Ma (Pb–Pb zircon evaporation age, Kröner et al. 2001), for metamorphic zircons from a metapelitic rocks. A post-tectonic granite with a U–Pb zircon age of 1825 ± 5 Ma (conventional method; Kotov et al. 1995) marks the final consolidation of this Precambrian crystalline block.

Other discrete Precambrian crustal domains are recognized in western Mongolia in the Dariv Metamorphic Complex and the Khantaishir Complex (Fig. 1), also assumed to be part of the Dzabkhan microcontinent (Badarch et al. 2002; Kozakov et al. 2002b), but display slightly different age patterns in comparison to the Baydrag block. Within the Dariv Metamorphic Complex there are unpublished zircon ages between 840 and 600 Ma with rare xenocrysts up to Archaean in age (Kozakov I.K., pers. comm., 2007). The minimum age of emplacement for the protolith of a dioritic gneiss is 1426 ± 1 Ma (Pb–Pb zircon evaporation age; Kröner et al. 2001). The Khantaishir Complex around Altai City contains a porphyritic granite gneiss with a crystallization age of 1127 ± 1 Ma and a 1715 Ma old xenocrystic zircon (Pb–Pb zircon evaporation ages; Kröner et al. 2001). Near Altai City, a migmatite yielded a SHRIMP zircon age of 840 ± 9 Ma and also contains inherited zircons ranging from 2445 to 1440 Ma in age (Zhao et al. 2006).

Compared to the crustal fragments discussed above, a distinctive feature of the Baga Bogd Massif are the early Neoproterozoic granitic intrusions documented by three samples (Mo387, Mo389, and Mo385) and yielding emplacement ages of 983 ± 6, 956 ± 3 and 954 ± 8 Ma respectively. Granitic protholiths with early Neoproterozoic ages have so far only been identified in one locality in southern Mongolia. A granite gneiss exposed in the Totoshan-Ulanul block of south-eastern Mongolia (Fig. 1) provided a protolith intrusion age of 952 ± 8 Ma (conventional U–Pb single and multigrain zircon age; Yarmolyuk et al. 2005). A similar event was documented to the W of the Totoshan-Ulanul block within the Tsagan-Khairkhan block of northern China (Fig. 1) where emplacement of a granite gneiss protolith was dated at 916 ± 16 Ma (U–Pb zircon age; Wang et al. 2001). These two blocks are usually considered as part of the South Gobi microcontinent.

The origin of these microcontinental crustal fragments is uncertain in most cases. They are interpreted either as fragments derived from the East Gondwana margin (Mossakovsky et al. 1994; Didenko et al. 1994; Filippova et al. 2001; Dobretsov et al. 2003; Dobretsov & Buslov 2007; Kheraskova et al. 2003) or from the Siberian Craton (Berzin et al. 1994; Kuzmichev et al. 2001; Yarmolyuk et al. 2006) or from both (Buslov et al. 2001). However, late Mesoproterozoic to early Neoproterozoic magmatic events have not been documented so far from the Siberian Craton margin (Pisarevsky & Natapov 2003; Gladkochub et al. 2006; Smelov & Timofeev 2007), and the distribution of sedimentary successions mainly record a passive margin environment (Pisarevsky et al. 2008). For example, the Teya granite pluton, part of the Yenisey Ridge and located at the south-western margin of the Siberian Craton (Fig. 1), has long been considered to reflect a Grenvillian-age collisional event. However, Vernikovsky et al. (2007) have now shown that the oldest phase of magmatism in this area occurred between 875 and 864 Ma, making a possible link with a Grenvillian-age event unlikely. On the other hand, discrete early Neoproterozoic magmatism is documented in north-western China. Southeast of the Tarim Basin, the Qilian and Qaidam blocks (Fig. 1) host granitoids, which are intrusive into shallow marine strata and ultramafic rocks and yielded emplacement ages of c. 930–920 Ma (conventional U–Pb zircon ages; Gehrels et al. 2003), whereas a zircon age of c. 969 Ma was reported for a granitoid gneiss in the Altyn Tagh range (Fig. 1)(ion microprobe analysis; Cowgill et al. 2003). Lu et al. (2008) listed numerous zircon ages between 1050 and 920 Ma for granitoids from the northern and eastern margin of the Tarim Craton. These authors interpret these early Neoproterozoic magmatic events as the result of what they term “Tarimian Orogeny”, leading to the final cratonization of the Tarim Craton.

The aforementioned magmatic ages compare well with our new zircon ages and suggest that the Baga Bogd Massif is unlikely to be related to the Baydrag basement block but shares greater similarities with crustal fragments in southern Mongolia and northwestern China. It is therefore unlikely that the Baga Bogd block was derived from the Siberian Craton. It may either be considered as a fragment of the South Gobi microcontinent, rifted off the northeastern Gondwana margin (Buslov et al. 2001) or as a fragment of the Tarim Craton. However, considering the poor correlation and the paucity of reliable ages, further data are required to draw definitive conclusions.

5.2. Late Cambrian plutonism and geodynamic implications

Finally, our results document a phase of late Cambrian magmatism with the emplacement of granitic, granodioritic and dioritic intrusions at 502 ± 6, 501 ± 4, 499 ± 3 and 498 ± 3 Ma.

Moreover, two of the late Cambrian gneisses contain xenocrystic zircons with ages of c. 928, 893, 815 and 656 Ma. These inherited grains provide further evidence for Neoproterozoic crustal material and suggest several Neoproterozoic zircon-forming events within the study area as also supported by early Neoproterozoic zircon ages recorded in samples Mo385, Mo387 and Mo389.

Evidence for an oceanic domain to the north of the Baydrag block is indicated by the large (300 km long) Bayankhongor ophiolite mélange recording ocean-crust formation at c. 665 Ma ago (SHRIMP zircon age; Kovach et al. 2005). A minimum age for the accretion of this oceanic remnant with the Baydrag block (Buchan et al. 2001) is bracket by syn-collisional granitoids intruding the ophiolite and its boundary fault between c. 547 and 539 Ma (U–Pb and Pb–Pb zircon evaporation ages; Buchan et al. 2002; Kozakov et al. 2006). Within this interval, the southwestern margin of the Siberian Craton faced the open Palaeo-Asian Ocean as indicated by a broad belt of c. 570 Ma old ophiolitic remnants. Slivers of oceanic crust are well exposed in the Khantaishir ophiolite south of Altai City (U–Pb zircon age of 568 ± 4 Ma for plagiogranite; Khain et al. 2003), in the Dariv Range farther W (Bayannor ophiolite, U–Pb zircon age of 571 ± 4 Ma for plagiogranite; Khain et al. 2003) and more to the north in the Tuva area of southern Siberia with the Agadagh Tes-Chem Massif (Pb–Pb zircon evaporation age of 570 ± 1 Ma; Pfänder & Kröner 2004). The accretion of these portions of oceanic lithosphere onto Precambrian crystalline massifs likely occurred in late Cambrian time and was accompanied by widespread magmatism and regional metamorphism. A minimum time for the accretion of the Bayannor ophiolite within the Dariv Metamorphic Complex is given by the intrusion of an undeformed quartz diorite at 515 ± 8 Ma (SHRIMP zircon age; Dijkstra et al. 2006). A phase of high-grade metamorphism in this complex is moreover recorded at 499 ± 3 Ma by a U–Pb zircon age for a hypersthene-garnet granulite (Kozakov et al. 2002b) and may reflect accretion of the ophiolitic sequence onto the crystalline basement. The post-tectonic intrusion of a "stitching granite" at 497 ± 1 Ma (Pb–Pb zircon evaporation age; Kröner et al. 2001) indicates that this phase of accretion was accomplished in the latest Cambrian.

Within this framework, and according to the chemistry of the dated samples, we consider that the late Cambrian phase of magmatism recorded in the Baga Bogd Massif occurred in an active continental margin environment and was related to the progressive closure of the Palaeo-Asian Ocean. Moreover, these data suggest that the Baga Bogd Precambrian crustal fragment was either docked against the southward (present-day coordinates) growing margin of the CAOB or was a large enough crustal entity to develop a magmatic arc along its margin.

The field relationships, combined with our new zircon ages, indicate that the different generations of granitoid gneisses underwent a common metamorphic and deformational event. This produced the regional penetrating fabric, leading to tectonic interlayering of Precambrian and late Cambrian gneisses, and most probably culminated in migmatization of the most fertile lithologies. This event occurred after the Cambrian, but our data are insufficient to constrain the time of post-Cambrian metamorphism. We speculate that this event may signify accretion of the Baga Bogd or South Gobi basement terrane onto the southward (present-day coordinates) growing margin of the CAOB or accretion of a Japan-style basement-core magmatic arc in the course of continuous closure of oceanic basins in the Palaeo-Asian Ocean.

6. Conclusions

Our new SHRIMP zircon ages for granitoid gneisses in the Baga Bogd Massif of southern Mongolia indicate the presence of Precambrian crystalline rocks and a late Cambrian phase of granitoid magmatism. The protolith emplacement of a granite gneiss (Mo381) is dated at 1519 ± 11 Ma and represents, up to now, the oldest rocks in this massif. A phase of magmatism is then documented by granite gneisses whose precursors were emplaced at 983 ± 6, 956 ± 3 and 954 ± 8 Ma. This is the second record in southern Mongolia of early Neoproterozoic granitoid magmatism. Finally, a late Cambrian subduction-related phase of magmatism is identified by several granitoid gneisses with homogeneous protolith intrusion ages at c. 500 Ma. Our results document the presence of an additional fragment of Precambrian crystalline basement in southern Mongolia and reinforce the idea that slivers of Precambrian crystalline domains are widespread in central and southern Mongolia as suggested by recent geological and isotopic studies (Yarmolyuk et al. 2005; Kozakov et al. 2007b).

Chapter 2

Zircon ages from the Baydrag block and the Bayankhongor ophiolite zone: time constraints on late Neoproterozoic to Cambrian subduction- and accretion-related magmatism in central Mongolia

ABSTRACT

Central Mongolia represents a heterogeneous crustal domain of the Central Asian Orogenic Belt and is composed of contrasting lithotectonic units with distinct pre-orogenic histories. We report single zircon evaporation and SHRIMP ages for high-grade rocks of the Neoarchaean-Palaeoproterozoic Baydrag block and for meta-igneous rocks of the junction between the late Neoproterozoic Bayankhongor ophiolite zone (BOZ) and the Baydrag block. Zircon ages for metamorphic rocks of the Baydrag block indicate a major tectonothermal event between 1840 and 1826 Ma, coeval with the emplacement of granitic rocks at mid-crustal level dated at 1839 Ma. A granite gneiss yielded a much younger crystallization age of 1051 Ma, the first Grenvillian age reported for this region. Together with predominantly Mesoproterozoic detrital zircon ages for a quartzite lens from the Burd Gol accretionary complex, these data attest to the heterogeneity and long Precambrian history of the Baydrag block. Crystallization ages for granite gneisses from the northeastern margin of the Baydrag block indicate prolonged plutonic activity between 579 and 537 Ma, probably related to southward subduction of the Bayankhongor oceanic crust. A syntectonic granite vein yielded a crystallization age of 519 Ma, likely linked to accretion of the BOZ onto the northeastern active margin of the Baydrag block. Lastly, a felsic meta-volcanic rock from the southeastern termination of the BOZ yielded a crystallization age of 472 Ma and suggests that punctuated

volcanic centres developed during the early Ordovician in response to protracted convergence.

1. Introduction

The Central Asian Orogenic Belt (CAOB; Jahn et al. 2000a), or Altaid Tectonic Collage (Şengör et al. 1993; Şengör & Natal'in 1996) is regarded as one of the largest areas on Earth of continental crust formation during the Phanerozoic (Şengör et al. 1993; Jahn et al. 2000a; Jahn 2004). It is bounded in the north by the Siberian Craton and in the south by the Tarim and Sino-Korean Cratons and extends from the Ural Mountains in the west to the Pacific cost in the east (Fig. 1a). This large orogenic system formed as a result of subduction-accretion processes within the Paleo-Asian Ocean and involved magmatic arc assemblages, ophiolitic complexes and subordinate microcontinents (Coleman 1989; Zonenshain et al. 1990; Şengör et al. 1993; Berzin et al. 1994; Mossakovsky et al. 1994; Yakubchuk 2004, 2008; Kröner et al. 2007; Windley et al. 2007). Besides its giant size, the CAOB had an unusually long orogenic history, beginning in the latest Mesoproterozoic (Khain et al. 2002) and terminating in late Permian to early Triassic (Xiao et al. 2003; Li 2006; Chen et al. 2008; Zhang et al. 2009).

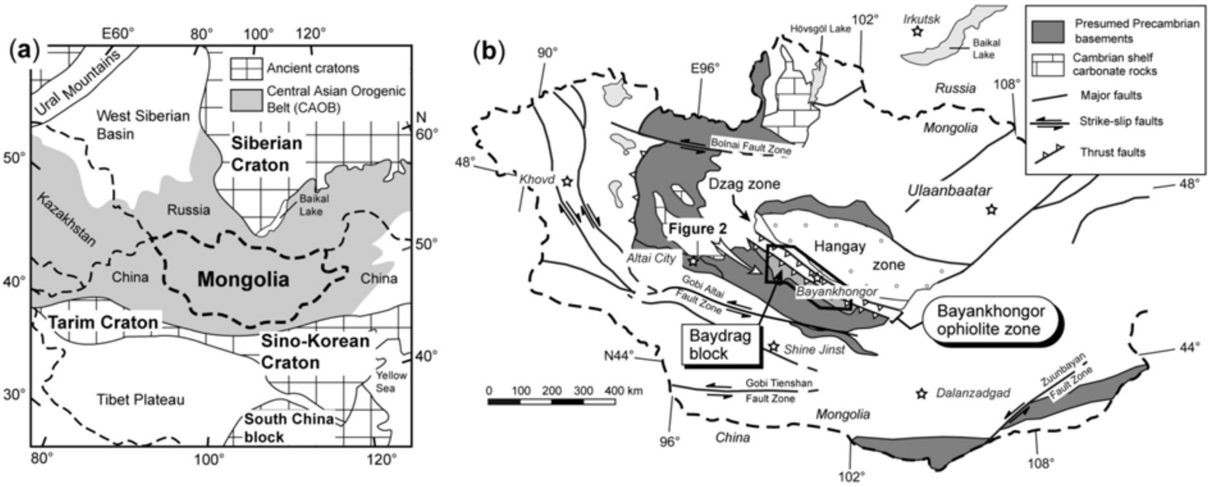

Fig. 1. (**a**) Outline of the Central Asian Orogenic Belt (CAOB) showing location of Mongolia (modified after Jahn et al. 2000a). (**b**) Simplified lithotectonic map of Mongolia (modified after Lamb et al. 1999; Badarch et al. 2002), showing the distribution and presumed extension of Precambrian basement and location of the Bayankhongor ophiolite zone, sandwiched between the Dzag zone and the Baydrag block. Location of Figure 2 is also indicated.

Several domains of high-grade rocks within the CAOB have long been interpreted as remnants of pre-orogenic microcontinents (Berzin et al. 1994; Mossakovsky et al. 1994).

These interpretations were mainly based on geological mapping, lithological correlations and metamorphic grade, and the paucity of precise geochronological constraints has led to many misconceptions and misinterpretations. For instance, high-grade gneisses in southern Tuva and western Mongolia, previously thought to be Precambrian in age, underwent granulite- to amphibolite-facies metamorphism between the Cambrian and the early Ordovician (Sal'nikova et al. 2001; Kozakov et al. 2002b) and are likely to have resulted from accretion/collision processes during the evolution of the CAOB. However, the presence of Precambrian magmatic rocks is relatively well documented for several high-grade crystalline complexes such as in southern Kazakhstan (Kröner et al. 2007) and southern Mongolia (Yarmolyuk et al. 2005; Demoux et al. 2009a), but the geographical extent of these domains remains uncertain. The best studied Precambrian complex occurs in central Mongolia within the Dzabkhan microcontinent (Mossakovsky et al. 1994) and is known as the Baydrag block or terrane (Fig. 1b; Kozakov et al. 2007b; Badarch et al. 2002), which consist of a c. 1000 km^2 nucleus, where Neoarchaean to Palaeoproterozoic magmatic and tectono-metamorphic events are well defined by reliable radiometric ages. Considering the uncertain geographic extend and tectonic boundaries of the Baydrag crystalline complex we use the original descriptive term Baydrag block (Mitrofanov et al. 1981) instead of Baydrag "terrane" as recently proposed by Badarch et al. (2002).

Determining the timing of tectonothermal events during juxtaposition of lithotectonic units is of critical importance in establishing the amalgamation history of the CAOB. Central Mongolia is an ideally suited region to scrutinize this problem because it contains contrasting lithotectonic units (Fig. 1b) composed of a metamorphosed turbidite-like sequence (Dzag zone), a late Neoproterozoic ophiolite (Bayankhongor ophiolite zone, BOZ) and a Precambrian basement complex (Baydrag block). We present new single zircon evaporation and sensitive high-resolution ion microprobe (SHRIMP) ages for high-grade rocks from the Baydrag block and for metaigneous rocks from a transect across the southeastern termination of the Bayankhongor ophiolite zone and Baydrag block in central Mongolia. These ages enable us (1) to refine the tectonothermal evolution of the Baydrag block prior to 1.8 Ga and to elucidate its eastern extension, and (2) to reconstruct the late Neoproterozoic to Cambrian accretion history of the BOZ with respect to that of the Baydrag block.

2. Regional geology and geochronological background of the Baydrag block and Bayankhongor ophiolite zone

In central Mongolia, the southern flank of the Hangay highland is occupied by an orogenic zone that contains the late Neoproterozoic Bayankhongor ophiolite (Buchan et al. 2001; Tomurtogoo 2002; Kovach et al. 2005). This ophiolite forms a NW–SE trending sub-linear zone (Fig. 1b) and is tectonically integrated within an accretionary complex developed between the Baydrag block and the Dzag zone (Fig. 2a; e.g. Osozawa et al. 2008 and references therein). Previous lithological and structural studies have shown that the overall regional structural pattern is dominated by NW-striking and NE-vergent thrust faults (Fig. 2a; Buchan et al. 2001; Osozawa et al. 2008), which enable distinguishing six major lithotectonic units described below from south to north; earlier geochronological results are summarized in Table 1.

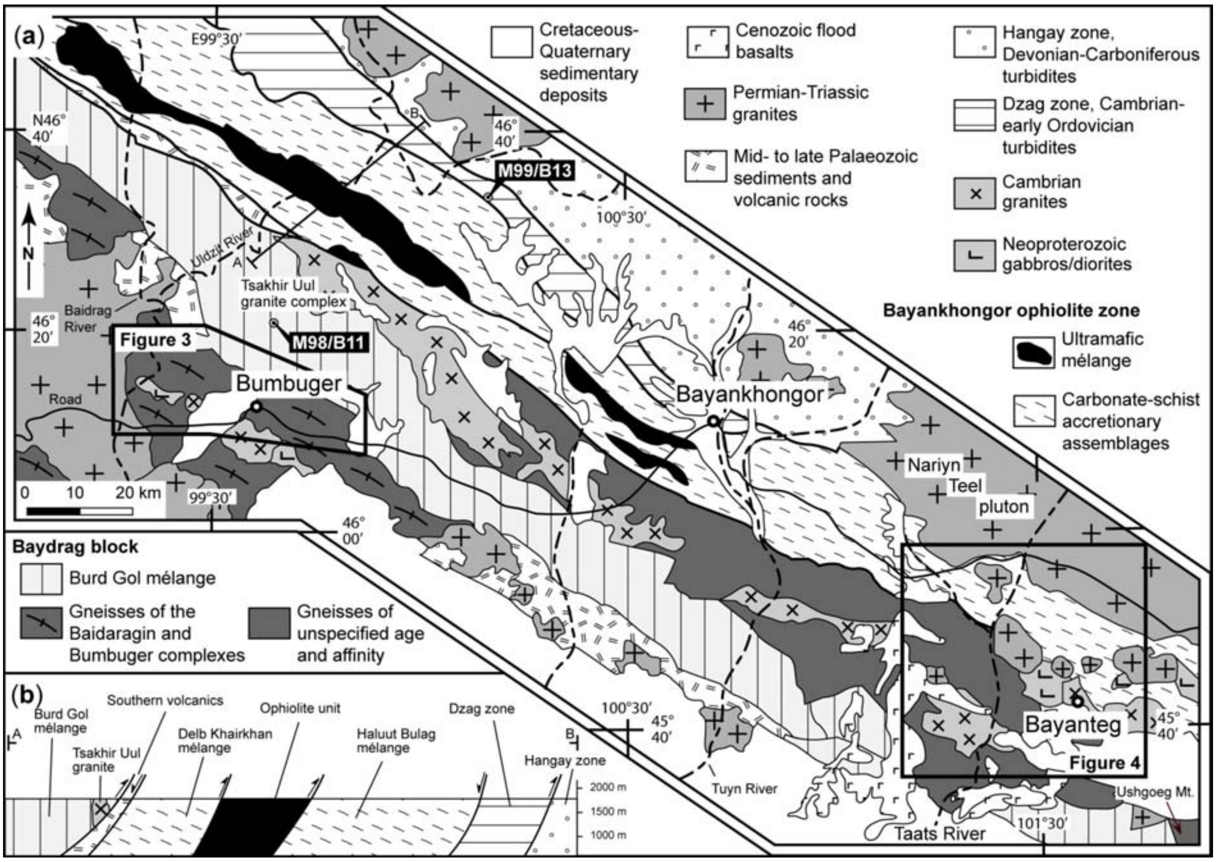

Fig. 2. (**a**) Simplified geological map of the Bayankhongor area and Baydrag block (modified after 1:500,000 Geological Map of western Mongolia); also indicated are areas investigated in this study (Figures 3 and 4) and the location of samples M98/B11 and M99/B13 from the Burd Gol mélange and Dzag zone, respectively. (**b**) Simplified cross section showing tectonic contacts between the Burd Gol mélange, the Bayankhongor ophiolite zone and the Dzag zone (modified after Buchan et al. 2002; Osozawa et al. 2008).

Table 1. Compilation of isotopic ages obtained in previous studies for rock assemblages of the Baydrag block, the Burd Gol mélange, the Bayankhongor ophiolite zone, the Dzag zone, and the Hangay batholith

Unit	Rock type[a]	Age (Ma)	Isotopic system	Mineral[a]	Method[b]	Significance[c]	Reference
Baydrag block							
Baidaragin	Opx-Cpx gneiss and tonalitic gneiss	~1800	U–Pb	Zrn	SHRIMP	Zrn rims and recryst. domains, HT metam., TTE-3	Kozakov et al. 2007b
Bumbuger	Grt-bearing gneiss	~2000–1700	U–Pb	Zrn	SHRIMP	Zrn rims and recryst. domains, HT metam., TTE-3	Kozakov et al. 2007b
Bumbuger	Granosyenite	1825 ± 5	U–Pb	Zrn	TIMS	Emplacement, TTE-3	Kotov et al. 1995
Bumbuger	Granodiorite	1854 ± 5	U–Pb	Zrn	TIMS	Emplacement, TTE-3	Kozakov 1993
Bumbuger	Bt-rich granite	2308 ± 4	U–Pb	Zrn	TIMS	Emplacement, TTE-2	Kotov et al. 1995
Bumbuger	Opx quartz diorite	2364 ± 6	U–Pb	Zrn	TIMS	Emplacement, TTE-2	Kotov et al. 1995
Bumbuger	Bt plagiogneisses	2370 ± 20	U–Pb	Zrn	TIMS	High-grade metam., TTE-2	Bibikova et al. 1990
Bumbuger	Grt-bearing gneiss	2501 ± 33	U–Pb	Zrn	SHRIMP	Detrital zrn cores	Kozakov et al. 2007b
Baidaragin	Opx-Cpx gneiss and tonalitic gneiss	~2650–2500	U–Pb	Zrn	SHRIMP	Plutonic activity, TTE-1	Kozakov et al. 2007b
Baidaragin	Tonalitic gneiss	2650 ± 30	U–Pb	Zrn	TIMS	Emplacement, TTE-1	Mitrofanov et al. 1985
Baidaragin	Opx-Cpx gneiss	~2890–2804	U–Pb	Zrn	SHRIMP	Zrn cores, emplacement	Kozakov et al. 2007b
Taats River	Grt metagranite	532 ± 9	U–Pb	Zrn	TIMS	Protolith emplacement	Kozakov et al. 2008
Taats River, east	Granodiorite, gneissic	546 ± 5	U–Pb	Zrn	TIMS	Protolith emplacement	Kozakov et al. 2008
Taats River	Granodiorite, gneissic	547 ± 4	U–Pb	Zrn	TIMS	Protolith emplacement	Kozakov et al. 2006
Taats River	Ky-bearing pegmatite	562 ± 2	U–Pb	Zrn	TIMS	Syntectonic emplacement?	Kozakov et al. 2006
Taats River	Granosyenite, gneissic	564 ± 5	U–Pb	Zrn	TIMS	Protolith emplacement	Kozakov et al. 2008
Burd Gol mélange							
Burd Gol mélange	Pelitic schist	699 ± 35	K–Ar	Mu		Deformation	Teraoka et al. 1996
Burd Gol mélange	Bt-Grt gneiss	533 ± 3	Ar–Ar	Bt		Deformation	Höck et al. 2000
Tsakhir Uul pluton	Leucogranite	539 ± 5	Pb–Pb	Zrn	Evap.	Emplacement,	Buchan et al. 2002
Tsagaan Nuruu	Monzogranite	514 ± 10	U–Pb	Zrn	SHRIMP	intrusive into Burd Gol mélange	Jahn et al. 2004
Tsakhir Uul pluton	Kfs granite	505 ± 22	K–Ar	Bt		Cooling age	Osozawa et al. 2008
Tsakhir Uul pluton	Kfs granite	510 ± 22	K–Ar	Bt		Cooling age	Osozawa et al. 2008
Tsakhir Uul pluton	Kfs granite	494 ± 22	K–Ar	Bt		Cooling age	Osozawa et al. 2008
Tsakhir Uul pluton	Kfs granite	487 ± 22	K–Ar	Bt		Cooling age	Osozawa et al. 2008
Tsakhir Uul pluton	Granite	469 ± 9	K–Ar	Bt		Crystallization?	Takahashi et al. 2000
Southern volcanics	Rhyolite dyke	474 ± 8	Pb–Pb	Zrn	Evap.	Island arc magmatism	Buchan et al. 2002
Bayankhongor ophiolite zone							
Ophiolite unit	Anorthosite	665 ± 21	U–Pb	Zrn	SHRIMP	Oceanic crust form.	Kovach et al. 2005
Ophiolite unit	Gabbro	569 ± 21	Sm–Nd	Pl, Cpx, Hbl, WR	Isochron	Oceanic crust form. or amphibolite-facies metam.?	Kepezhinskas et al. 1991
Ophiolite unit	Pillow basalt	485 ± 6	Ar–Ar	Hbl		Low-grade metam.	Delor et al. 2000
Ulaan Uul granite	Red granite	539 ± 1	Pb–Pb	Zrn	Evap.	Granite emplacement,	Buchan et al. 2002
Ulaan Uul granite	Red granite	545 ± 2	Pb–Pb	Zrn	Evap.	cutting thrust fault	Buchan et al. 2002

[a] Mineral abbreviations after Kretz (1983); WR: whole-rock.

[b] Evap.: evaporation; TIMS: thermal ionisation mass spectrometry; SHRIMP: sensitive high resolution ion microprobe.

[c] TTE: tectonothermal event; metam.: metamorphism ; form.: formation; recryst.: recrystallized.

Table 1. *(Continued)*

Dzag zone							
Dzag zone	Pelitic schist	395 ± 20	K–Ar	Mu		Deformation ages related to Ordovician low-grade metam.	Teraoka et al. 1996
Dzag zone	Pelitic schist	440 ± 22	K–Ar	Mu			Teraoka et al. 1996
Dzag zone	Pelitic schist	454 ± 9	K–Ar	Mu			Kurimoto et al. 1998
Dzag zone	Pelitic schist	447 ± 9	K–Ar	Mu			Kurimoto et al. 1998
Hangay batholith							
Nariyn Teel pluton	Syenogranite	229 ± 6	U–Pb	Zrn	SHRIMP	Emplacement	Jahn et al. 2004
KhoitTamir Massif	Granodiorite	255 ± 1	U–Pb	Zrn	TIMS	Emplacement	Yarmolyuk et al. 2008b
Tsetserleg Massif	Granite	255 ± 1	U–Pb	Zrn	TIMS	Emplacement	Yarmolyuk et al. 2008b
Bu-Tsagan Massif	Monzodiorite	253 ± 2	U–Pb	Zrn	TIMS	Emplacement	Yarmolyuk et al. 2008b
Baidarik Massif	Qtz monzodiorite	242 ± 2	U–Pb	Zrn	TIMS	Emplacement	Yarmolyuk et al. 2008b
Uszekhiin Massif	Qtz diorite	261 ± 2	U–Pb	Zrn	TIMS	Emplacement	Yarmolyuk et al. 2008b

2.1. Baydrag block

The gneissic basement making up most of the Baydrag block is subdivided into two complexes according to their lithological characteristics, namely Baidaragin and Bumbuger (Fig. 3; e.g. Kozakov et al. 2007b). The Baidaragin complex is primarily composed of migmatitic tonalitic gneisses, which contain lenses of amphibolite and pyroxene-bearing mafic gneisses. The Bumbuger complex is dominated by metasediments and includes an alternation of pyroxene-bearing crystalline schists and leucocratic gneisses as well as forsterite-bearing marbles, quartzites, garnet-biotite schists and leucocratic pyroxene-bearing gneisses. All rocks underwent amphibolite- to granulite-facies metamorphism and record a polyphase tectono-metamorphic evolution. The structural relationship between both complexes is uncertain due to strong reworking of lithological contacts during a c. 1.8 Ga tectonothermal event (Kozakov et al. 2007b). However, Kozakov et al. (1997) speculated on the basis of Nd model ages that the Bumbuger metasediments were most likely derived from the Neoarchaean Baidaragin complex.

Previous geochronological studies within the Baydrag block led to recognition of three major tectonothermal events summarized as follows: (1) a Neoarchaean event between 2890 and 2650 Ma related to protolith emplacement of metaigneous rocks of the Baidaragin complex (Mitrofanov et al. 1985; Kozakov et al. 2007b); (2) an early Palaeoproterozoic event between 2370 and 2308 Ma related to the emplacement of two-pyroxene granodiorite, quartz diorite and biotite granite veins (Bibikova et al. 1990; Kotov et al. 1995); and (3) a late Palaeoproterozoic event between 1854 and 1825 Ma related to the emplacement of enstatite-bearing garnet granodiorite and amphibole granosyenite veins (Kozakov 1993; Kotov et al. 1995). The third tectonothermal event produced the dominant present-day structural grain recognized within both the Baidaragin and Bumbuger complexes and was previously interpreted as the final phase of stabilization of the Baydrag block (Kotov et al. 1995). However, Kozakov et al. (2007b) reported SHRIMP ages of c. 2.0 to 1.7 Ga for homogeneous rims and recrystallized domains of zircons from rocks of both the Baidaragin and Bumbuger complexes, suggesting that at least part of the Baydrag block underwent post-Palaeoproterozoic reworking.

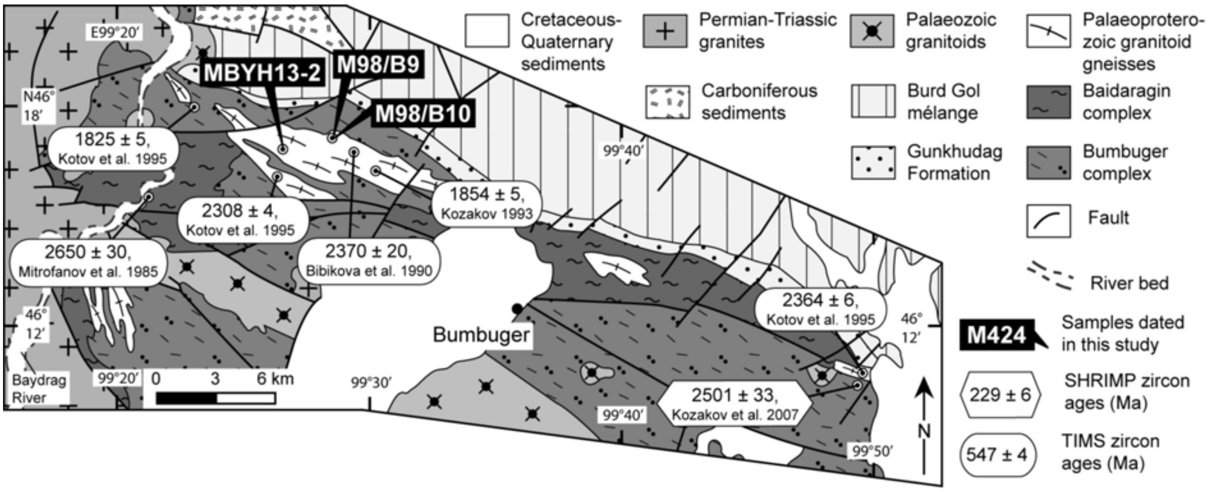

Fig. 3. Geological sketch map of the Baydrag block (modified after Tomurtogoo et al. 1998). Previous geochronological results and location of dated samples are also indicated.

Northwest of Bumbuger village (Fig. 2a), gneisses of the Baydrag block are overlain unconformably by the unmetamorphosed Gunkhudag Formation (Tomurtogoo & Gerel 1999), a shelf-like sedimentary sequence about 250 metre-thick. The lower part contains NE-dipping coarse-grained quartzite and conglomerate beds, overlain upsection by pebbly sandstone and stromatolite-bearing dolomite of early Mesoproterozoic age (Dergunov et al. 1997).

2.2. Burd Gol mélange

To the NE of the Gunkhudag Formation, the Burd Gol mélange forms a NW–SE elongated trough (Fig. 2a). The mélange is composed of phyllites and graphite-rich chlorite-biotite schists that contain lenses of meta-igneous and -sedimentary rocks cross-cut by abundant quartz veins (Buchan et al. 2001). Microfossils from black shales suggest Mesoproterozoic to Neoproterozoic ages (Mitrofanov et al. 1981). Mineral assemblages within the mélange indicate Barrovian metamorphic conditions and point to a general northward increase of the metamorphic grade towards the thrust contact with the BOZ (Buchan et al. 2001). The lithological characteristics and structural patterns of the Burd Gol mélange suggest that it constitutes an accretionary complex built up against the Baydrag block (Buchan et al. 2001; Windley et al. 2007). Metamorphic white micas from pelitic schists yielded a K-Ar age of 699 ± 35 (Teraoka et al. 1996), whereas a biotite-garnet gneiss from the southeastern termination of the mélange (Ushgoeg Mt.; Fig. 2a) yielded a ^{40}Ar/^{39}Ar biotite plateau age of 533 ± 3 Ma (Höck et al. 2000). Carbonaceous phyllites and pelitic schists yielded initial ε_{Nd}-values of -16.1 to -11.5 and Nd mean crustal residence ages of 2.7 to 2.5 Ga (Kovalenko et al. 2005; Kozakov et al. 2007b), suggesting that gneisses of the Baydrag block constitute a potential source area. The mélange is intruded along its northern margin by the Tsakhir Uul granite complex (Fig. 2a), from which a leucogranite and a monzogranite body yielded zircon crystallization ages of 539 ± 5 and 514 ± 10 Ma, respectively (Buchan et al. 2002; Jahn et al. 2004).

2.3. Southern volcanics

To the north of the Burd Gol mélange, this lithotectonic unit consists of a narrow belt of Carboniferous marine sediments (Dergunov et al. 1997), which unconformably overlies a sequence of island arc-related volcanic rocks (Buchan et al. 2002). The time of island arc magmatism is uncertain, but a minimum age is provided by a zircon crystallization age of 474 ± 8 Ma for a rhyolite dyke cross-cutting the volcanic sequence (Buchan et al. 2002).

2.4. Bayankhongor ophiolite zone (BOZ)

The BOZ (Fig. 2a) consists of a central ophiolite unit tectonically bounded by the Delb Khairkhan and Haluut Bulag mélanges (Fig. 2b; Buchan et al. 2001; Osozawa et al. 2008). The Delb Khairkhan mélange contains lenses of igneous and sedimentary rocks, distributed in a matrix of pelitic schists. Carbonate rocks contain Neoproterozoic stromatolites and early to middle Cambrian fossils (Dergunov et al. 1997). Along its northern side, the lithological characteristics of mafic igneous lenses (gabbro, dolerite, pillow basalt) are similar to those in the ophiolite unit to the north (Buchan et al. 2001). The ophiolite unit contains virtually all typical ophiolite lithologies, but the original sequence is tectonically dismembered into blocks enclosed within a matrix of serpentinite. Based on a Sm–Nd mineral/whole rock isochron age for a gabbro, the ophiolite has long been considered to have formed c. 569 Ma ago (Kepezhinskas et al. 1991). However, Kovach et al. (2005) obtained a SHRIMP zircon age of 665 ± 15 Ma for an anorthosite from a layered gabbro sequence and challenged the significance of the former Sm–Nd age. Pillow basalts locally exhibit a mineral lineation defined by metamorphic amphiboles with a $^{40}Ar/^{39}Ar$ plateau age of 485 ± 6 Ma (Delor et al. 2000). The fault-bounded contact between the Delb Khairkhan mélange and the ophiolite unit is stitched by the undeformed Ulaan Uul red granite, which yielded zircon crystallization ages of 545 ± 2 and 539 ± 1 Ma (Buchan et al. 2002). The Haluut Bulag mélange shows a block-in-matrix structure and is predominantly composed of sedimentary lenses embedded in a matrix of low-grade phyllite (Buchan et al. 2001). Slate-carbonate rocks of the matrix yielded initial ε_{Nd}-values of -4.2 to -3.2 with Nd mean crustal residence ages of 1.64 to 1.57 Ga (Kovalenko et al. 2005).

Based on the dominant NE-vergence of thrusts faults (Fig. 2b), Buchan et al. (2001) proposed that the Bayankhongor ophiolite crust was subducted to the southwest with the Burd Gol mélange representing an accretionary prism build up against the northeastern margin of the Baydrag block. In addition to the phase of accretion and northeastward thrust stacking, Osozawa et al. (2008) recognized a superimposed phase of brittle deformation associated with two detachment faults bounding the BOZ (Fig. 2b). These authors related this event to terminal Devonian collision between the Baydrag block and the Dzag zone to the northeast.

2.5. Dzag zone

This lithotectonic unit consists of asymmetrically folded chlorite-rich psammitic and pelitic schists of grenschist-facies and less deformed fine-grained siltstone and sandstone beds. Relicts of sedimentary structures suggest a deep-sea turbiditic origin and deposition on a passive margin (Buchan et al. 2001). Metamorphic white micas from pelitic schists yielded K–Ar ages of 454 ± 9 to 395 ± 20 Ma (Teraoka et al. 1996; Kurimoto et al. 1998) which were interpreted to reflect regional low-grade metamorphism. Pelitic schists yielded initial ε_{Nd}-values of -3.3 and -3.1 with Nd mean crustal residence ages of 1.58 to 1.47 Ga (Jahn et al. 2004). Rocks of the Haluut Bulag mélange and Dzag zone display much younger Nd model ages than sediments of the Burd Gol mélange, suggesting an origin from distinct sources.

2.6. Hangay zone

This unit is predominantly composed of unmetamorphosed and gently folded middle to late Palaeozoic turbidite-dominated sediments intruded by undeformed early Permian to late Triassic granitoids (Takahashi et al. 2000; Jahn et al. 2004; Orolmaa et al. 2008; Yarmolyuk et al. 2008b). Kovalenko et al. (2004) speculated that sediments of this zone cover an unexposed Precambrian microcontinental block because of Mesoproterozoic Nd model ages of c. 1.4–1.1 Ga for late Palaeozoic and Mesozoic granitoids. This hypothesis is supported by late Archaean to early Neoproterozoic detrital zircons in arc-derived sediments of the Hangay-Hentey basins (Kelty et al. 2008) and by Re–Os data from mantle xenoliths, which together suggest the presence of Mesoproterozoic subcontinental lithospheric mantle (Wang et al. 2006).

3. Field relationships along the Taats River

The rocks exposed along the N–S trending Taats River are primarily composed of high- and low-grade metamorphic lithologies, intruded by undeformed granitoids of Cambrian to Permian age (Fig. 4). These rocks are presumed to constitute the eastern extension of the Baydrag block (Fig. 2a), and most “stratigraphic” ages used in the following description are taken from the 1:200,000 Geological Map (Fig. 4; Zabotkin 1988), unless stated otherwise.

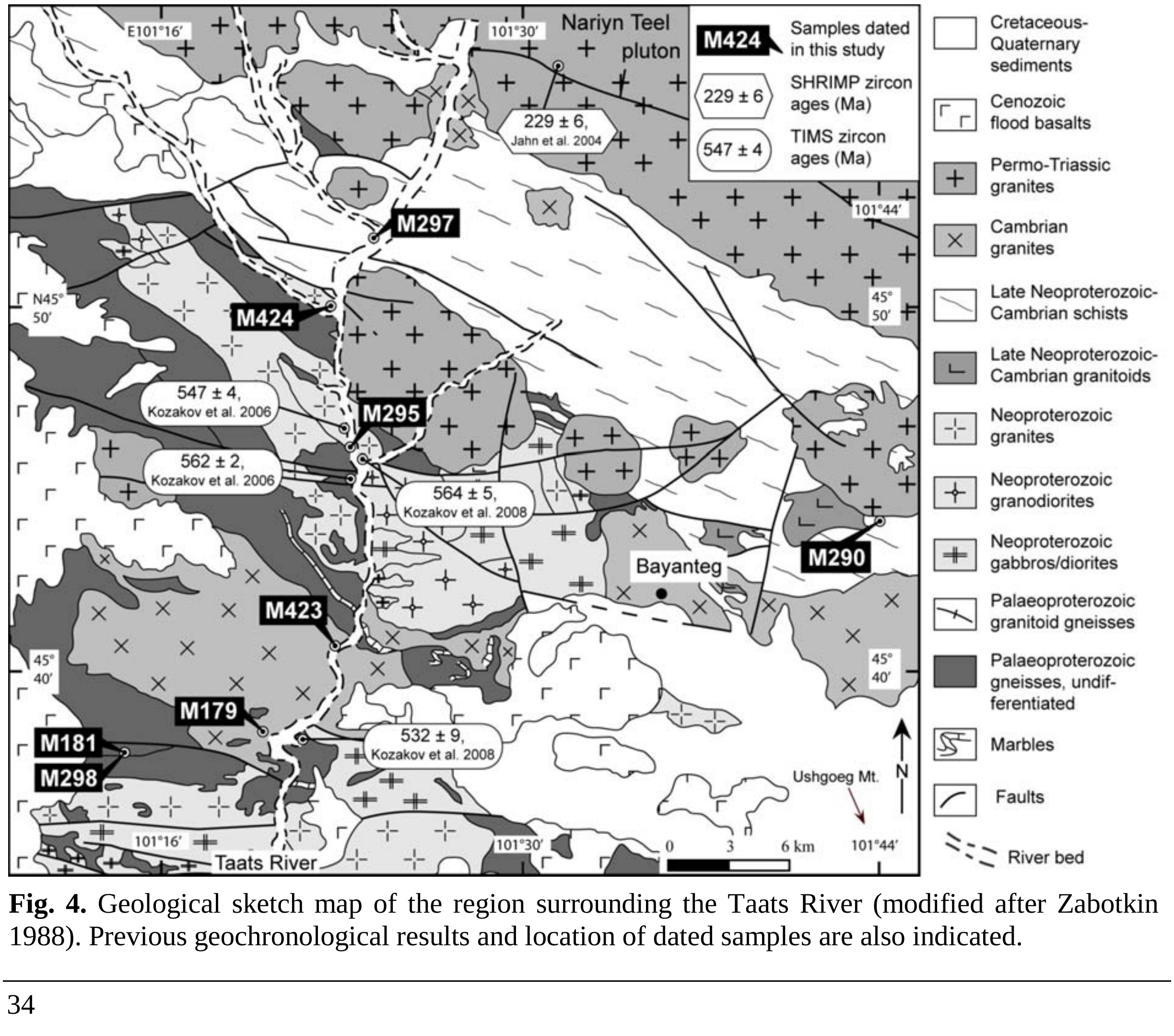

Fig. 4. Geological sketch map of the region surrounding the Taats River (modified after Zabotkin 1988). Previous geochronological results and location of dated samples are also indicated.

The section is described from south to north and is based on our own field observations. The southern termination is composed of presumed Palaeoproterozoic gneisses (Fig. 4; Zabotkin 1988). Among these are strongly foliated and layered, fine-grained granite gneisses with a penetrative subvertical foliation striking E–W and steeply dipping N or S. This foliation is locally folded into tight isoclinal folds with steeply dipping fold axes and stretching lineation. These gneisses contain several metre-wide tectonic lenses of foliated garnet-bearing metagabbro and amphibolite, wrapped around by the surrounding foliation and probably representing a phase of mafic magmatism that occurred prior to the deformation of the entire package. Towards the north, the gneisses predominantly consist of interlayered quartzite, metagraywacke, biotite-rich gneisses, calc-silicate schists and minor garnet-bearing amphibolite bands. These lithologies are intruded by a large granite pluton of Cambrian age. Close to the southern margin of this pluton is a gently folded S-verging sequence of metagraywacke with conformable granitic pegmatite sills and cross-cut by undeformed aplite dykes (Fig. 5a). A garnet-bearing metagranite interlayered with the surrounding metasediments yielded a TIMS zircon age of 532 ± 9 Ma (Kozakov et al. 2008). Foliation in the metasediments generally strikes NW–SE and dips between 30 to 60 degrees SW. Elongate biotite aggregates in biotite-rich gneisses define a mineral lineation plunging between 20 to 30 degrees WSW. Close to the northern margin of this pluton, the metasediments are deformed into several metre-scale S-verging recumbent folds. Syntectonic granite veins emplaced conformably to the foliation in the metasediments occur locally and are folded together with the entire pile and boudinaged in some places (Fig. 5b).

Rocks north of the granite pluton predominantly consist of strongly deformed clastic metasediments, including mostly felsic schists and metagraywacke with interlayered metre-thick beds of garnetiferous metapelite, marble, calc-silicate rocks and quartzite. The structural grain is defined by a penetrative foliation striking NW–SE and dipping steeply NNE (Fig. 5c). This sequence is locally migmatitic with leucocratic veinlets or melt patches of gabbroic to granodioritic composition. Rare ptygmatic folds with subvertical axes indicate local coaxial deformation (Fig. 5d). The entire sequence is cut by randomly distributed pegmatite veins. The relationship between the steeply N-dipping metasediments and the aforementioned flat-lying and folded metasediments to the south is obscured by the Cambrian pluton and was not observed along this transect.

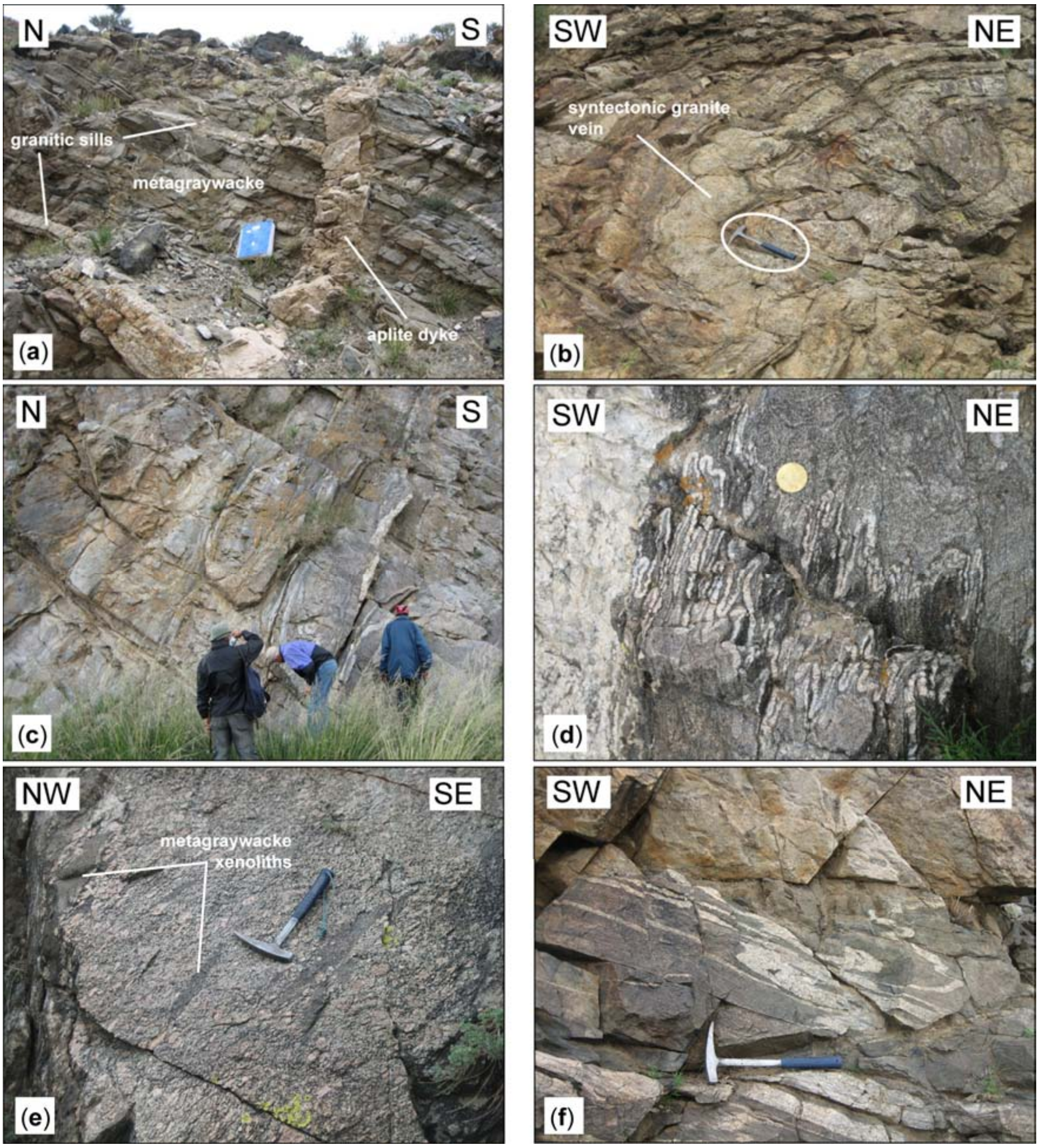

Fig. 5. Field photographs of rocks exposed along the Taats River. (**a**) Gently folded metagraywacke and pegmatite sills cut by aplite dyke. (**b**) S-verging recumbent fold and syntectonic granite vein (sample M423) showing boudinage. (**c**) Steeply N-dipping sequence of partly migmatitic metasediments. (**d**) Ptygmatic folds with subvertical fold axes. (**e**) Porphyritic granite with flattened and aligned metagraywacke xenoliths (sample M295). (**f**) Isoclinally folded and partly disrupted leucosomes in migmatitic metasediment.

About 1.5 km north of the Cambrian pluton, there is a 15 metre-wide zone of sheared marble with a NW–SE striking foliation steeply dipping NE. C–S fabrics, the asymmetric shape of marble boudins as well as slickensides and an associated shallow-dipping striation suggest a top-to-the-SE dextral sense of movement. Farther north, there is a coarse-grained and foliated porphyritic granite of presumed Neoproterozoic age (Fig. 4) with K-feldspar porphyroblasts that reach several cm long and show a preferred orientation. This granite contains flattened xenoliths of metagraywacke (Fig. 5e) with a consistent orientation. The intrusive relationship between the pluton and surrounding metasediments is poorly preserved because contacts are generally sheared and lie parallel to the foliation observed in the granite and the surrounding metasediments. Kozakov et al. (2006, 2008) reported TIMS zircon ages of 547 ± 4 Ma and 564 ± 5 for foliated granodiorite and granosyenite bodies, respectively. About 1 km south of the porphyritic granite, a syntectonic kyanite-bearing pegmatite vein yielded a TIMS zircon age of 562 ± 2 Ma (Kozakov et al. 2006). Towards the north, the sedimentary lithologies are still partly migmatitic and show an E–W striking foliation gently dipping NNE and axial planar to isoclinally folded and rootless leucosomes (Fig. 5f).

The northern termination of the transect is composed of a thick sequence of greenschist-facies quartz-chlorite-epidote schists of presumed late Neoproterozoic-Cambrian age (Fig. 4). The schistosity generally strikes NW–SE and dips between 45 to 65 degrees NE. This sequence is intruded in the north by the Nariyn Teel pluton, assumed to be Permian in age (Fig. 4). However, Jahn et al. (2004) obtained a SHRIMP zircon age of 229 ± 6 Ma for a syenogranite from this pluton. The entire schist sequence is assumed to constitute the southeastern extension of the BOZ as shown on the 1:500,000 Geological Map (Fig. 2a). In contrast to the metasediments in the south, these low-grade schists do not show evidence of migmatization.

4. Geochronological results

4.1. Analytical methods

Zircons were separated at the University of Mainz using conventional procedures including magnetic separation and heavy liquid (methylene iodide). Representative zircons were handpicked under a binocular microscope according to their morphological habits and crystallographic quality. Internal zircon structures were documented with transmitted and reflected light photomicrographs and cathodoluminescence (CL) images. CL imaging was performed on a JEOL JXA-8900 RL Superprobe at the University of Mainz (operating conditions were 15 KV accelerating voltage and 12 nA beam on carbon-coated mounts). CL images reveal internal structures by imaging high-U (dark) and low-U (bright) domains (Corfu et al. 2003).

Single zircon evaporation. Our laboratory procedures as well as comparisons with conventional and ion-microprobe zircon dating are detailed in Kröner et al. (1991) and Kröner & Hegner (1998). Isotopic measurements were carried out on a Finnigan-MAT 261 mass spectrometer at the Max-Planck-Institut für Chemie in Mainz. The calculated ages and uncertainties are based on the means of all ratios and their 2σ mean errors. Mean ages and errors for several zircons from the same sample are presented as weighted means of the entire population. During the course of this study we repeatedly analysed fragments of large, homogeneous zircon grains from the Palaborwa Carbonatite, South Africa. Conventional U–Pb analyses of six separate grain fragments from this sample yielded a $^{207}Pb/^{206}Pb$ age of 2052.2 ± 0.8 Ma (2σ, W. Todt, unpublished data), whereas the mean $^{207}Pb/^{206}Pb$ ratio for 19 grains, evaporated individually over a period of 12 months, was 0.126634 ± 0.000027 (2σ error of the population), corresponding to an age of 2051.8 ± 0.4 Ma, identical to the U-Pb age. The above error is considered the best estimate for the reproducibility of our evaporation data and corresponds approximately to the 2σ (mean) error reported for individual analyses in this study (Appendix C-1). In the case of combined data sets the 2σ (mean) error may become very low, and whenever this error was less than the reproducibility of the internal standard, we have used the latter value (that is, an assumed 2σ error of 0.000027). Analytical results are listed in Appendix C-1. The $^{207}Pb/^{206}Pb$ spectra are shown in histograms that permit visual assessment of the data distribution from which the ages are derived. The evaporation technique provides only Pb isotopic ratios, and there is no *a priori* way to determine whether a measured ratio reflects a concordant age. Thus, all $^{207}Pb/^{206}Pb$ ages determined by this method are necessarily *minimum* ages. However, many studies have demonstrated that there is a very strong likelihood that these data represent true zircon crystallization ages when (1) the $^{207}Pb/^{206}Pb$ ratio does not change with increasing temperature of evaporation and/or (2) repeated analyses of grains from the same sample at high evaporation temperatures yield the same isotopic ratios within error. Comparative studies by evaporation, conventional U–Pb dating, and ion-microprobe analysis have shown this to be correct (see Kröner et al. 1999 for summary and additional references).

SHRIMP II analyses. Representative zircon grains were handpicked under a binocular microscope, mounted in epoxy resin together with chips of the zircon standard TEMORA 1 or the Perth Consortium standard CZ3 and then polished to about half of their thickness. Isotopic analyses were performed on the sensitive high-resolution ion microprobes (SHRIMP II) in Beijing SHRIMP Centre of the Chinese Academy of Geological Sciences and the Perth

Consortium, Australia. The instrumental characteristics were outlined by De Laeter & Kennedy (1998) and the analytical procedures are described in Claoué-Long et al. (1995), Nelson (1997) and Williams (1998). For data collection, six scans through the critical mass range were made on both instruments. Primary beam intensity was about 6.4 nA in Beijing and about 2.2 nA in Perth The measured $^{206}Pb/^{238}U$ ratios for the TEMORA 1 standard were normalized to 0.0668, equivalent to an age of 417 Ma (Black et al. 2003) and those for CZ3 to 0.0914, equivalent to an age of 564 Ma (Pidgeon et al. 1994). Mass-resolution was about 5000 at both instruments, and thus allowed a clear elimination of isobaric interferences. The uncertainty in the ratio of radiogenic ^{206}Pb over U calculated for all measurements of TEMORA 1 in Beijing was 1.2% and 1.0% for the standard CZ3 in Perth. Sensitivity for ^{206}Pb on TEMORA 1 and CZ3 was about 25 and 22 cps/ppm/nA, respectively. Analyses of unknown samples and standards were alternated to asses the extent of Pb^+/U^+ discrimination. Raw data reduction followed the method described by Nelson (1997, 2006). Corrections for common Pb were made using the ^{204}Pb method, assuming, that for low counts of ^{204}Pb, common Pb is mainly surface-related (Kinny 1986, Nelson 1997) and has the composition of the Broken Hill lead. In the case of higher ^{204}Pb counts, the age-related common Pb was corrected following the model Pb composition of Cumming & Richards (1975). Errors on individual analysis are based on counting statistics and are given at the 1σ level, and include the uncertainty of the standard. Stern (1997) provided a detailed account of the counting error assessment for SHRIMP analyses. Errors for pooled ages are reported at $2\ \sigma$ (95% confidence interval). The ages and 2σ errors of intercepts of the best-fit lines were calculated using the Isoplot program of Ludwig (2003). Analytical results are listed in Appendix B-2.

4.2. Baydrag block, Burd Gol mélange and Dzag zone.

Sample M98/B9 (N46°16’59’’, E99°28’40’’; Fig. 3) is a massive and foliated enderbitic gneiss of dioritic composition intruding a sequence of banded metapelite in the Bumbuger complex. Zircons are dark-red in colour, predominantly long-prismatic with rounded terminations. Evaporation of three grains yielded a mean $^{207}Pb/^{206}Pb$ age of 2409.1 ± 0.4 Ma (Fig. 6a) that we consider to reflect the time of dioritic protolith emplacement.

Sample M98/B10 is a granulite-facies banded garnetiferous metapelite collected about 100 m southwest of sample M98/B9 (Fig. 3). This rock shows many anatectic features and diffuse contacts, grading into more homogeneous charnockites and enderbites. Our sample contains metamorphic zircons of dark red-brown colour with spherical and multifaceted habits. Evaporation of four grains yielded a mean $^{207}Pb/^{206}Pb$ age of 1839.8 ± 0.6 Ma (Fig. 6b) that we interpret to reflect the time of high-grade metamorphism in the Baydrag block.

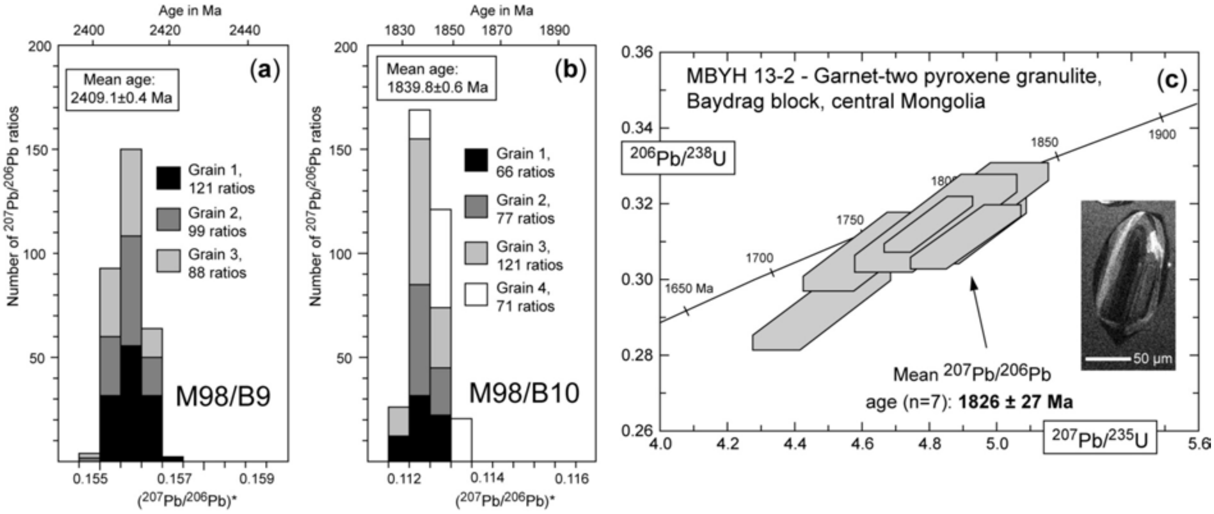

Fig. 6. (**a, b**) Histograms showing distribution of radiogenic lead isotope ratios derived from evaporation of single zircons from high-grade rocks of the Baydrag block. Mean ages are given with 2σ (mean) error. (**a**) Spectrum for three zircons from enderbitic gneiss sample M98/B9, integrated from 308 ratios (Appendix C-1). (**b**) Spectrum for four zircons from metapelite sample M98/B10, integrated from 335 ratios (Appendix C-1). (**c**) Concordia diagram showing SHRIMP analyses of single zircons for garnet-two pyroxene granulite sample MBYH 12-3. Data boxes for each analysis are defined by standard errors in the $^{207}Pb/^{235}U$, $^{206}Pb/^{238}U$ and $^{207}Pb/^{206}Pb$ ratios. Error for pooled age is at 95% confidence level. Inset shows CL image of an analysed zircon.

Sample MBYH 13-2 is a garnet-two pyroxene granulite collected within the Bumbuger complex (N46°16’51’’, E99°26’35’’; Fig. 3). Zircons are spherical or long-prismatic and subhedral with smooth terminations related to metamorphic growth. CL images show sector-zoned domains and wide and structureless metamorphic rims that mantle older igneous cores in some grains. Metamorphic rims of six grains were analysed on the SHRIMP II in Beijing and yielded a cluster of near-concordant data points (Fig. 6c) with a weighted mean $^{207}Pb/^{206}Pb$ age of 1826 ± 26 Ma (MSWD = 0.69). This age is identical, within error, to the evaporation age obtained for sample M98/B9 and reflects a major late Palaeoproterozoic metamorphic event in the Baydrag block.

Sample M98/B11 is a fine-grained, whitish-blue quartzite lens, several metres thick and embedded within cleaved phyllites of the Burd Gol mélange (N46°20’57’’, E99°38’31’’; Fig. 2). It contains a heterogeneous population of zircons with clear to yellow-brown colours, short- to long-prismatic habits with well-rounded terminations and pitted surfaces. Thirteen zircons were evaporated and produced highly variable isotopic ratios with $^{207}Pb/^{206}Pb$ ages ranging between 2032 and 1017 Ma (Fig. 7). This age pattern suggests a maximum earliest Neoproterozoic depositional age and a heterogeneous sedimentary source dating back to the Palaeoproterozoic.

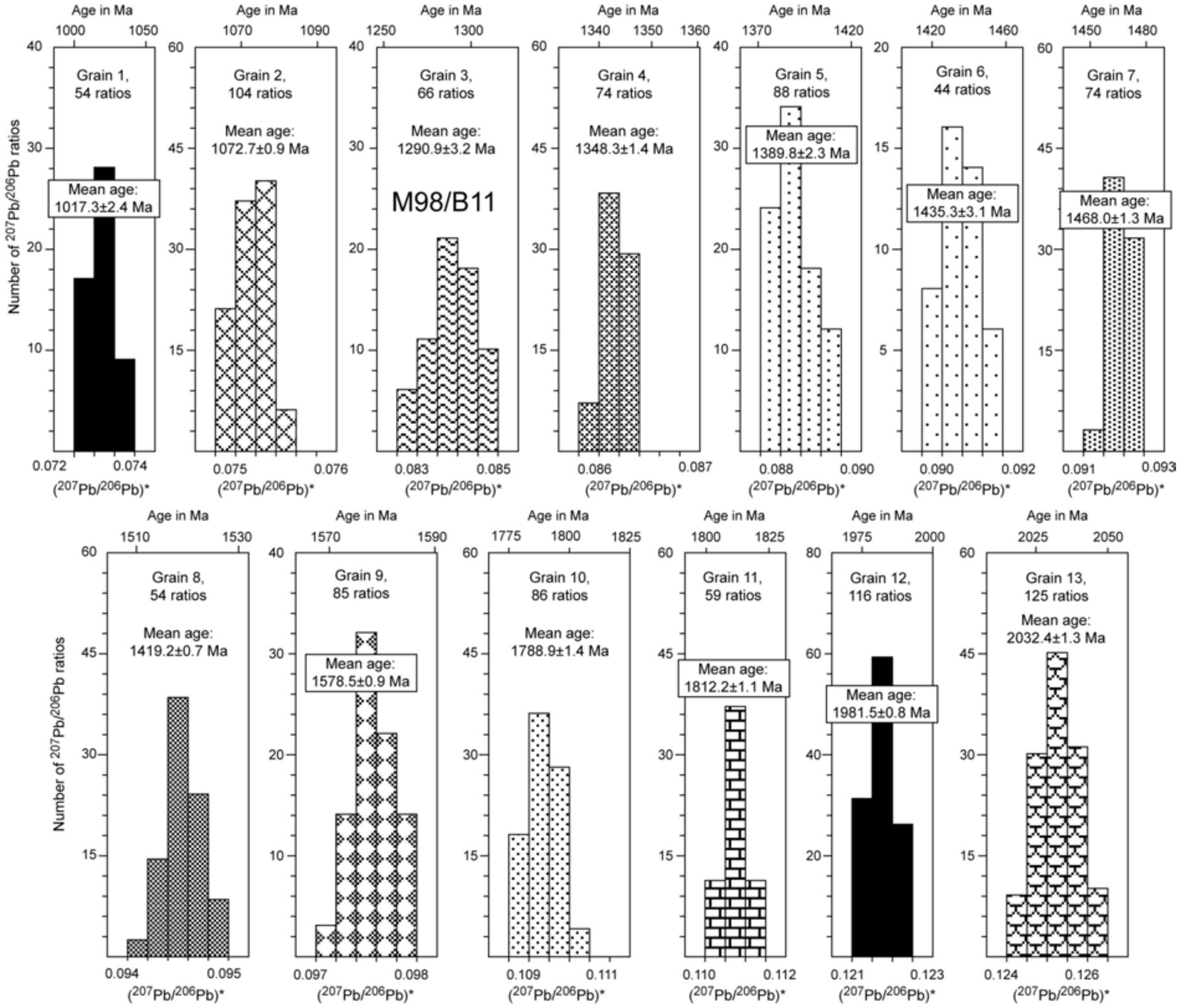

Fig. 7. Histograms as in Fig. 6a for detrital zircons from quartzite sample M98/B11 from Burd Gol mélange. The spectra have been integrated from ratios as shown. For analytical data see Appendix C-1.

Sample M99/B13 is a volcanic sandstone from the Dzag zone (N46°33’38’’, E100°09’21’’; Fig. 2a). Zircons are mostly composed of dark red-brown, oval to ball-rounded grains indicating long-distance sedimentary transport, and a few stubby, near idiomorphic grains indicating detrital input from proximal sources. Eight zircons were evaporated and produced variable ^{207}Pb/^{206}Pb ages ranging from 2143 to 1771 Ma (Fig. 8). This suggests detrital input into the Dzag sediments from a source terrane that contains Palaeoproterozoic rocks. The range of detrital ages is most likely not representative of the entire population in this sample, and nothing definite can be said about the time of deposition of the Dzag sediments. However, the pattern of detrital zircon ages supports the previous assumption of the existence of a Palaeoproterozoic basement (Kovalenko et al. 2004), now present at depth and covered by the Palaeozoic Hangay sediments.

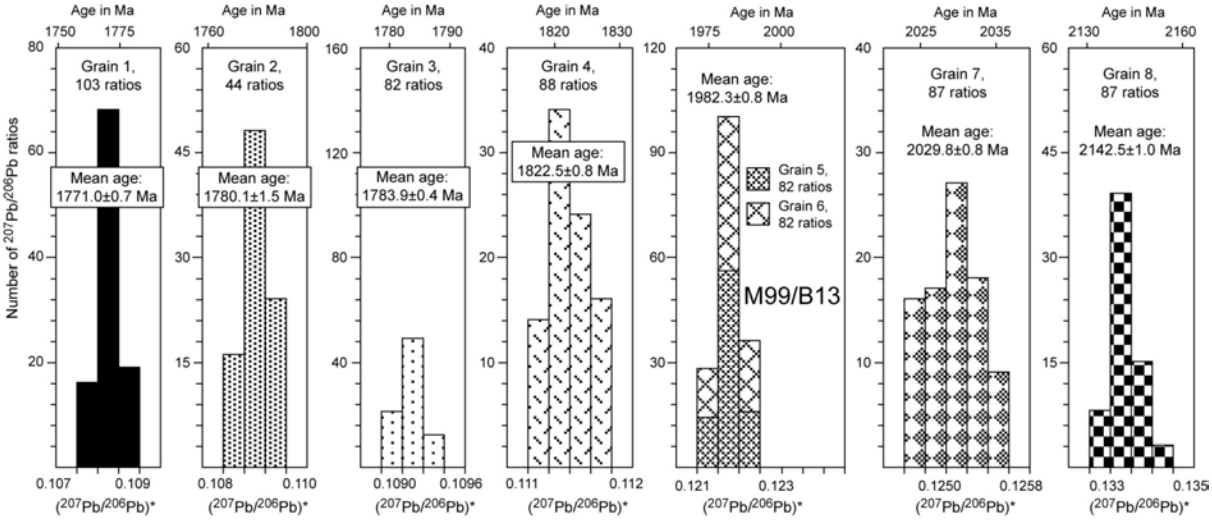

Fig. 8. Histograms as in Fig. 6a for detrital zircons from volcanic sandstone sample M99/B13 from the Dzag zone. The spectra have been integrated from ratios as shown. For analytical data see Appendix C-1.

4.3. Taats River and Bayanteg areas.

Sample M181 is a strongly foliated and layered fine-grained biotite gneiss collected at the southern end of the transect (N45°37’47’’, E101°14’52’’; Fig. 4). It is composed of quartz with undulose extinction, fresh biotite flakes, K-feldspar mostly altered into fine-grained sericite, plagioclase and minor secondary white mica. Zircons are subhedral with smooth edges, subrounded terminations and pitted surfaces. In CL images, most grains have dark (high-U) cores and brightly luminescent (low-U), narrow and structureless rims, presumably reflecting metamorphic overgrowth. Cores of fifteen grains were analysed on the SHRIMP II in Perth and yielded a complex array of predominantly discordant results. Seven analyses are aligned along a chord (MSWD = 0.004) yielding an upper Concordia intercept age of 1839 ± 11 Ma and a lower intercept at -3 ± 120 Ma (Fig. 9a). These analyses have a weighted mean ^{207}Pb/^{206}Pb age of 1839 ± 8 Ma (MSWD = 0.003), identical to the upper intercept age, which we consider to best approximate the time of emplacement of the granitic protolith. Three additional grains display a crude alignment and have a weighted mean ^{207}Pb/^{206}Pb age of 1992 ± 14 Ma. The remaining analyses yielded much older and discordant results with minimum ^{207}Pb/^{206}Pb ages of 3119, 2936 and 2664 Ma (Fig. 9a). These grains reflect inheritance from Archaean to Palaeoproterozoic sources.

Sample M298 is a strongly foliated granite gneiss collected some 150 metres southwest of sample M181 (N45°37’45’’, E101°14’48’’; Fig. 4). Both samples display a similar foliation indicating that they underwent a common phase of deformation. Zircons are light to dark brown in colour and are mostly long-prismatic with slightly rounded terminations that we ascribe to partial dissolution and recrystallization during a metamorphic overprint. CL images show oscillatory zoning related to igneous growth. Some grains have a few μm-thick rims overgrowing the primary igneous texture. Five zircon cores were analysed on the Beijing SHRIMP II of which one result is concordant and the four remaining data are discordant (Fig. 9b). The five analyses are aligned along a chord (MSWD = 0.002) with an upper Concordia intercept age of 1053 ± 28 Ma and a lower intercept age at 21 ± 330 Ma, suggesting recent Pb-loss. The concordant grain has a ^{207}Pb/^{206}Pb age of 1053 ± 20 Ma, and all analyses define a weighted mean ^{207}Pb/^{206}Pb age of 1051 ± 10 Ma (MSWD = 0.01), identical, within error, to the upper intercept age. We therefore consider the latter age to approximate the time of crystallization of the granite protolith.

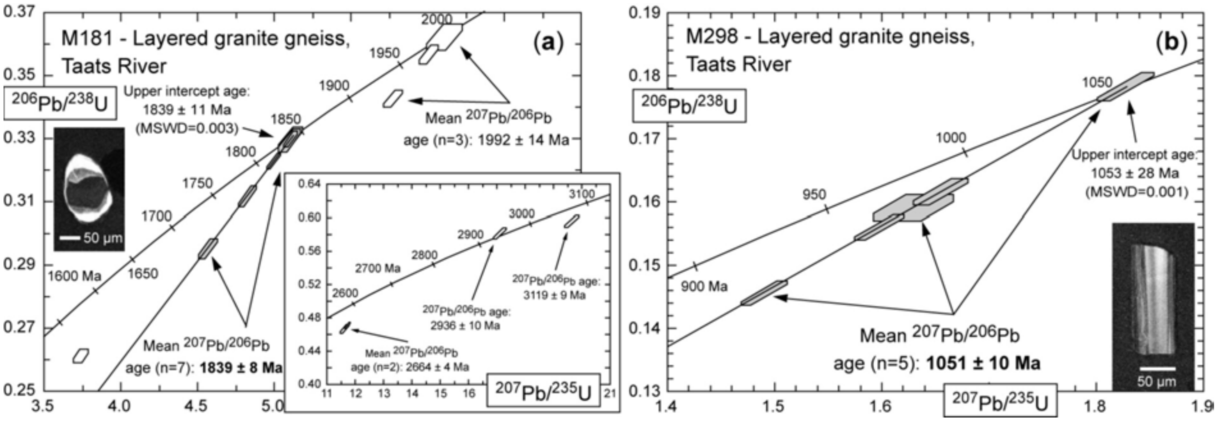

Fig. 9. Concordia diagrams showing SHRIMP analyses of single zircons for granite gneisses from the Taats River. Data boxes for each analysis are defined by standard errors in the ^{207}Pb/^{235}U, ^{206}Pb/^{238}U and ^{207}Pb/^{206}Pb ratios. Pooled and intercept errors are at 95% confidence level. Insets show CL images of analysed zircons.

Sample M179 (N45°38’19’’, E101°20’04’’; Fig. 4) is a peraluminous leucocratic granite vein, about 1 m wide and interlayered with the surrounding metagraywacke. It consists of quartz, K-feldspar, biotite, muscovite, and minor plagioclase, euhedral small garnet and secondary sericite. Quartz often shows undulose extinction, K-feldspar is altered into fine-grained sericite, and biotite is partly replaced by chlorite. Myrmekite is locally developed along K-feldspar grain boundaries. Only a few zircons of poor crystallographic quality were recovered, which show igneous-related internal structures as well as inherited rounded cores in CL images. Only two grains could be analysed on the Perth instrument, and three analyses yielded concordant and similar results (Fig. 10a) with a weighted mean $^{206}Pb/^{238}U$ age of 537 ± 6 Ma (MSWD = 0.15) that we interpret to reflect the time of crystallization of the granite vein. A further analysis from the core of a grain yielded a much older and concordant $^{206}Pb/^{238}Pb$ age of 793 ± 12 Ma that we interpret as a xenocryst assimilated from the surrounding host rocks.

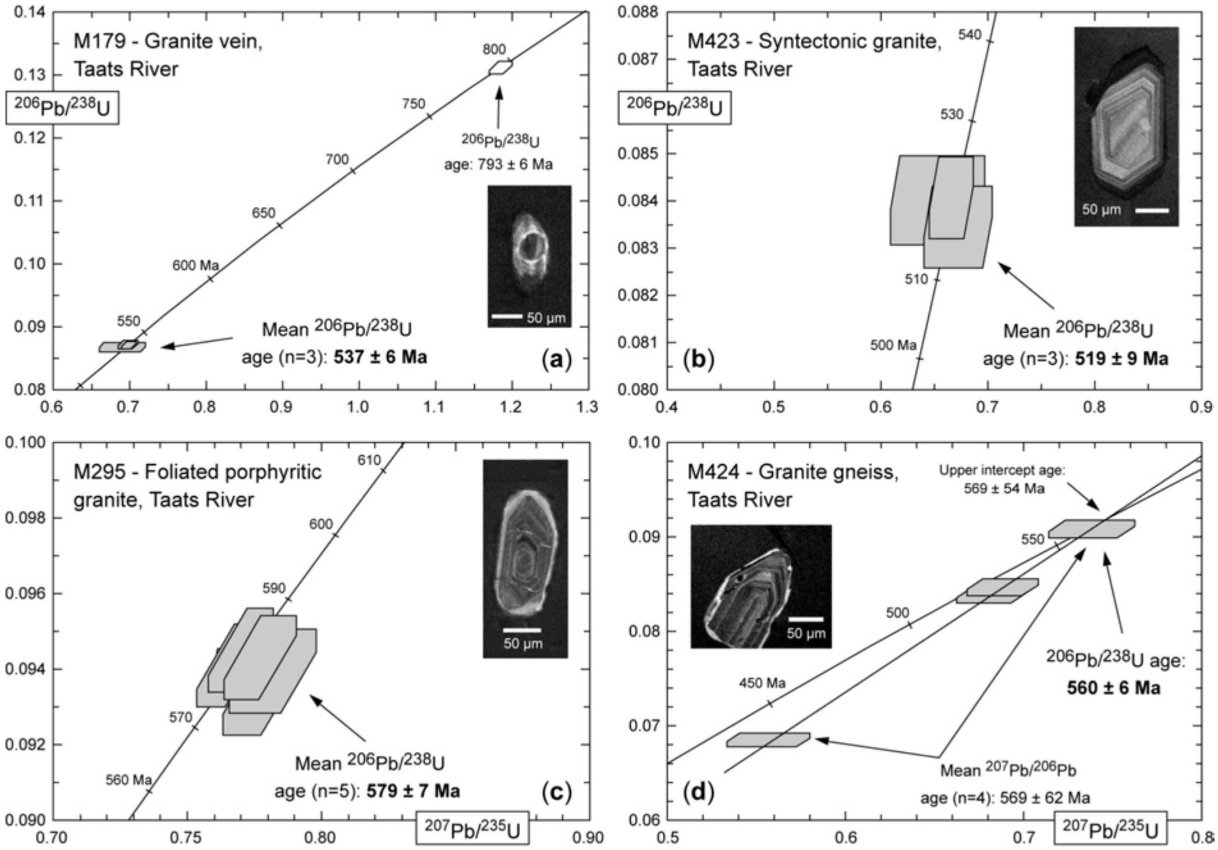

Fig. 10. Concordia diagrams showing SHRIMP analyses of single zircons from granites and granite gneisses of the Taats River. Data boxes and errors on pooled ages and intercepts as in Fig. 9. Insets show CL images of analysed zircons.

Sample M423 (N45°40’45’’, E101°22’53’’; Fig. 4) is a medium-grained syntectonic granite vein, about 40 cm-wide, and deformed together with the surrounding metasediment (Fig. 5c). This sample is composed of quartz, plagioclase, K-feldspar variably altered into fine-grained sericite, and biotite mostly replaced by chlorite. Zircons are predominantly clear, pale yellow, short-prismatic and idiomorphic, but some are subrounded and dark coloured. The idiomorphic grains have typical magmatic internal zoning, whereas the subrounded grains tend to have higher luminescence and structureless cores. Three idiomorphic zircons were analysed on the Beijing SHRIMP II and produced similar and concordant results (Fig.

10b) with a weighted mean ^{206}Pb/^{238}U age of 519 ± 9 Ma (MSWD = 0.11). This is interpreted to reflect the time of emplacement of the syntectonic granite and the last tectono-metamorphic event undergone by the enclosing meta-sediments.

Sample M295 (N45°46’05’’, E101°23’31’’; Fig. 4) is a coarse-grained porphyritic granite that intrudes a sequence of meta-sediments and contains numerous enclaves of metagraywacke. The rock is composed of orthoclase phenocrysts set in a fine-grained matrix of recrystallized quartz and plagioclase. Zircons are translucent, faintly yellow, short-prismatic and subhedral with slightly rounded terminations. CL images reveal oscillatory zoning, typical of igneous growth. All grains display a narrow and strongly luminescent overgrowth that truncates and corrodes the primary internal zoning. Five zircon cores were analysed on the Beijing instrument and produced a tight cluster of results (Fig. 10c) with a weighted mean ^{206}Pb/^{238}U age of 579 ± 7 Ma (MSWD = 0.15), which we interpret as the time of granite emplacement.

Sample M424 (N45°50’07’’, E101°23’04’’; Fig. 4) is a fine-grained layered granite gneiss consisting of K-feldspar, biotite, quartz and plagioclase. Secondary minerals include chlorite, white mica and minor calcite. Zircons are translucent, short-prismatic and mostly subhedral with smooth edges and have oscillatory-zoned internal structure. All grains display a narrow (few μm-wide) high luminescent rim, and some have dark and rounded inherited cores. Igneous domains of four zircons were analysed on the Beijing instrument, of which one grain yielded a concordant result with a ^{206}Pb/^{238}U age of 560 ± 12 Ma, whereas the three other results are discordant (Fig. 10d). When forced through the origin, the four analyses are aligned along a chord (MSWD = 0.0003) with an upper Concordia intercept age of 569 ± 54 Ma. All analyses have a mean ^{207}Pb/^{206}Pb age of 569 ± 62 Ma, identical to the upper intercept and the concordant age. We consider the latter as the best estimate for the time of emplacement of the granite gneiss protolith.

Sample M297 (N45°51’54’’, E101°24’17’’) is a strongly sheared felsic schist, most likely derived from a volcaniclastic protolith, and was collected within the presumed late Neoproterozoic-Cambrian sequence bordering the northern part of the study area (Fig. 4). The rock is composed of quartz, K-feldspar, biotite, and secondary white mica, clinozoisite and calcite. Quartz is often found as ribbons and shows undulose extinction. The zircon population is heterogeneous and consists of rare short-prismatic and idiomorphic grains and abundant subhedral and long- to short-prismatic grains, usually dark-coloured. Most grains have well-developed oscillatory zoning. Ten zircons were analysed on the Beijing SHRIMP

II, and six results are aligned along a chord (MSWD = 0.06) with an upper Concordia intercept age of 606 ± 39 Ma and a lower intercept at 21 ± 330 Ma. All six analyses have a weighted mean ^{207}Pb/^{206}Pb age of 601 ± 7 Ma (MSWD = 0.06), identical, within error, to the upper intercept age (Fig. 11a). We therefore consider the latter age to best approximate the time of emplacement of the felsic volcanic protolith. Three other grains yielded much older and concordant ^{207}Pb/^{206}Pb ages of 950, 912 and 823 Ma. The remaining grain yielded a concordant and much younger ^{206}Pb/^{238}U age of 196 ± 5 Ma (Fig. 11a) for which we do not have a satisfactory explanation. The zircon morphology and internal structure is identical to the 601 Ma old grains, and the analysis represents the centre of the grain and is unlikely to reflect a metamorphic overprint. No Jurassic thermal event has previously been reported from this area.

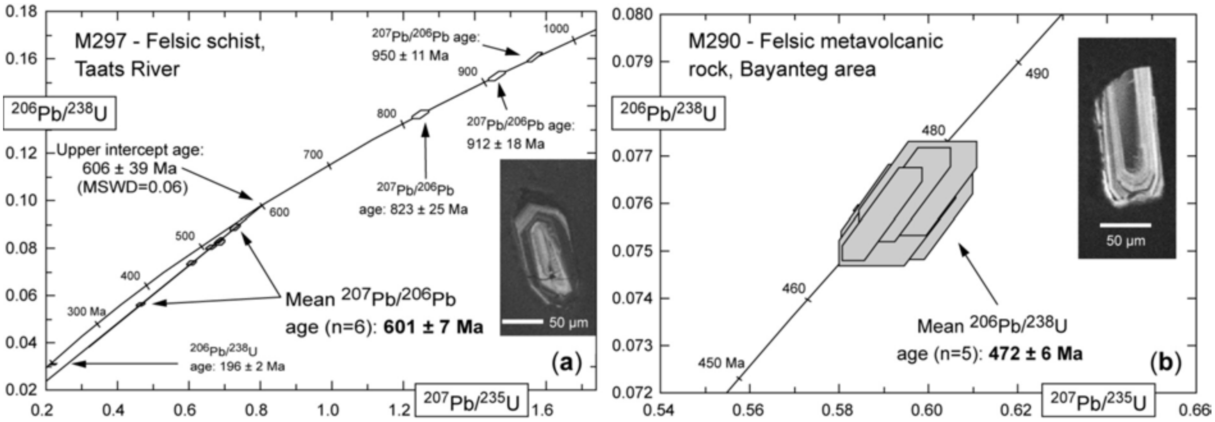

Fig. 11. Concordia diagrams showing SHRIMP analyses of single zircons for felsic schists from the Taats River and Bayanteg area. Data boxes and errors on pooled ages and intercepts as in Fig. 9. Insets show CL images of analysed zircons.

Finally, sample M290 (N45°44'15'', E101°43'32'') is a strongly sheared felsic metavolcanic rock collected about twelve km northeast of Bayanteg village (Fig. 4). This sample also belongs to the presumed late Neoproterozoic-Cambrian sequence and is composed of K-feldspar, quartz, and rare relicts of amphibole and secondary sericite. Zircons are clear, colourless, short-prismatic and euhedral to subhedral. CL images reveal typical igneous oscillatory zoning and rare and small subrounded inherited cores. Igneous domains of five zircons were analysed on the Beijing instrument, and the results define a cluster of concordant results (Fig. 11b) with a weighted mean ^{206}Pb/^{238}U age of 472 ± 6 Ma (MSWD = 0.08) that we interpret as the time of emplacement of the felsic volcanic protolith. This age is much younger than the age obtained for sample M297, presumed to be part of the same lithological unit, and therefore raises the question whether these rocks really belong to the same lithostratigraphic sequence.

5. Discussion

5.1. Tectonothermal evolution of the Baydrag block prior to 1.8 Ga.

The tectonothermal evolution of the Baydrag block is characterized by three distinct events, namely Neoarchaean magmatic activity between c. 2.80 and 2.65 Ga and two Palaeoproterozoic tectonothermal episodes at 2.37–2.31 Ga and 1.85–1.82 Ga. Our zircon ages provide a more accurate timing for the upper age limit of the second event and for the peak of metamorphism related to third thermal event.

A metadiorite intrusive into a high-grade metapelitic sequence of the Bumbuger complex has a crystallization age of 2409 ± 1 Ma. This date is slightly older than the timing of magmatism previously reported at 2370 and 2364 Ma (Bibikova et al. 1990; Kotov et al. 1995) and is ascribed to the beginning of the second tectonothermal event. We suggest that the upper age limit of this event should be extended to 2.41 Ga. In addition, deposition of the metapelite protolith must have occurred prior to 2.41 Ga, and the sequence underwent high-grade metamorphism dated by metamorphic zircons at 1840 ± 1 Ma. Another sample that underwent granulite-facies metamorphism contains metamorphic zircons with a SHRIMP age of 1826 ± 26 Ma. We interpret these ages to reflect a major high-grade metamorphic event at 1.84–1.83 Ga related to the third tectonothermal episode that resulted in regional metamorphism and deformation of the Baydrag block.

The granite gneiss M181 from the southern part of the Taats River transect has a SHRIMP zircon age of 1839 ± 8 Ma. This sample also contains inherited zircon cores with ages between c. 3.12 and 1.99 Ga, suggesting that the granitic protolith was formed by melting of Archaean to Palaeoproterozoic sources. These results suggest that the Palaeoproterozoic gneisses exposed at the southern termination of the Taats River transect should be considered as a part of the Baydrag block. The 3.12 Ga old zircon core is the oldest record of crust-formation in this crystalline complex. We note that the crystallization age for the granite gneiss protolith is identical, within error, to the age of high-grade metamorphism at 1.84–1.83 Ga recorded in the Bumbuger complex. This may be explained by the emplacement of the gneiss protolith at mid-crustal level, whereas rocks of the northwestern domain of the Baydrag block represent a deeper crustal section.

5.2. Evidence for Meso- and Neoproterozoic episodes of zircon growth and heterogeneity of the Baydrag block.

One interesting aspect of our study is the occurrence of granite gneiss M298, interlayered with the c. 1.84 Ga old granite gneiss M181 but derived from a much younger granitic protolith with a crystallization age of 1051 ± 10 Ma. This is the first Grenvillian magmatic crystallization age reported from the Baydrag block. Since both granite gneisses record the same ductile deformation they most likely experienced a common phase of deformation and metamorphism after 1.05 Ga. Moreover, this age provides further evidence for late Grenvillian-age igneous activity in south-central Mongolia as recently recognized within the Gurvan Bogd Mountains located about 80 km southeast of the Baydrag block (Fig. 14; Demoux et al. 2009a).

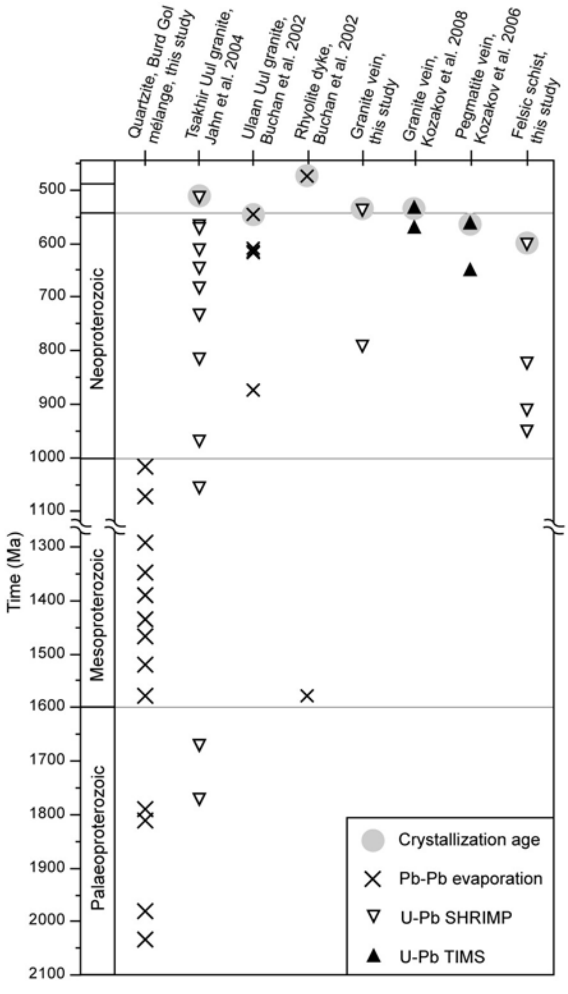

Fig. 12. Synoptic diagram showing pattern of inherited zircon ages for rocks of the Bayankhongor ophiolite zone, the Burd Gol mélange and the Taats River transect. The data indicate inheritance from predominantly Neoproterozoic sources for igneous rocks, whereas the quartzite from the Burd Gol mélange displays considerable detrital input from Mesoproterozoic sources.

The pattern of inherited zircons in late Neoproterozoic to Cambrian granitic rocks intrusive into the rock assemblages of the BOZ, the Burd Gol mélange and the Taats River transect indicates substantial inheritance from Neoproterozoic sources (Fig. 12). These results are moreover supported by geochronological data for the quartzite lens from the Burd Gol mélange, which most likely formed through erosion of the Baydrag gneisses. This sample contains an array of detrital zircons ranging in ages from 2032 to 1017 Ma (Fig. 12), which suggests that Palaeoproterozoic and late Mesoproterozoic rocks were exposed at the surface at the time of sediment deposition. The geological evolution of the Baydrag block has previously been restricted to the Neoarchaean and late Palaeoproterozoic, but the data presented here attest to considerable lithological heterogeneity and a long Precambrian history of this crustal domain, the details of which still need to be unravelled.

Lastly, felsic schist sample M297 of volcaniclastic origin, collected on the southeastern side of the BOZ, yielded a SHRIMP zircon age of 601 ± 7 Ma. Regarding its composition and position within the BOZ, we suggest that this sample belongs to the Delb Khairkhan mélange. The late Neoproterozoic age agrees with previous paleontological ages reported for carbonate rocks from this unit (Dergunov et al. 1997). This sample suggests that the northern margin of the Baydrag block was the site of sporadic volcanic activity during the late Neoproterozoic, likely developed in response to southward subduction of the Bayankhongor oceanic crust. We therefore speculate that the Delb Khairhan mélange represents an accretionary complex, developed in front of the Burd Gol mélange, and which received volcanic products shed from the Baydrag margin as well as igneous and sedimentary material scraped off the subducting Bayankhongor oceanic crust. The felsic schist contains zircon xenocrysts with early Neoproterozoic ages (Fig. 12), which again supports the heterogeneous composition of the Baydrag block.

5.3. Late Neoproterozoic-Cambrian magmatism and regional implications.

Along strike, to the northwest of the Taats River, the Tsakhir Uul granite intrudes the Burd Gol mélange and yielded zircon crystallization ages of 539 and 514 Ma (Buchan et al. 2002; Jahn et al. 2004). This granite is only deformed on its northern margin where a weak foliation is developed along a thrust fault (Buchan et al. 2002). Our protolith crystallization ages of 579 and 560 Ma for two granite gneiss samples suggest that plutonic activity began at least in late Neoproterozoic times. These dates are moreover comparable to the crystallization ages of 562 and 564 Ma obtained for a syntectonic kyanite-bearing granitic vein and a granosyenite from the Taats River area (Kozakov et al. 2006, 2008). The occurrence of kyanite, which we could not substantiate, suggests that magmatism occurred contemporaneously with a phase of medium-pressure metamorphism.

The fault-bounded contact between the Delb Khairkhan mélange and the ophiolite unit is stitched by the undeformed 545–539 Ma old Ulan Uul granite (Buchan et al. 2002), which suggests that both units were juxtaposed prior to 545 Ma. This pluton shows a pattern of inherited zircons (Fig. 12) and Nd isotopic data similar to those reported for the Tsakhir Uul granite (Buchan et al. 2002). This may suggest that both granite complexes were produced during the same magmatic event, possibly related to the early stage of accretion of the BOZ onto the Burd Gol accretionary complex (Buchan et al. 2002). Our zircon age of 537 ± 6 Ma obtained for granite vein M179 is comparable to the emplacement ages of the Ulaan Uul and Tsakhir Uul granites (Fig. 13) and may have been produced during the same magmatic event.

In summary, our data together with previous ages from the BOZ and the Taats River area indicate protracted granitoid activity from late Neoproterozoic to early Cambrian times between 579 and 537 Ma (Fig. 13). We speculate that this phase of magmatism was developed at the northeastern (present-day coordinates) active margin of the Baydrag block in response to southward subduction of the Bayankhongor oceanic crust (Buchan et al. 2001).

A zircon age of 519 ± 9 Ma obtained for syntectonic granitic vein M423 reflects a mid-Cambrian tectono-magmatic event that produced S-verging recumbent folds and asymmetric drag folds. We suggest that this event corresponds to the ‘peak’ of accretion of the BOZ onto the Baydrag block, which began at about 540 Ma (Buchan et al. 2002). The ductile fabrics were then overprinted by brittle deformation as exemplified by a dextral strike-slip shear zone developed within a marble horizon. We propose that dextral shearing postdates the N–S ductile deformation and is related to a transpressive tectonic regime during terminal collision. However, we do not have a reliable time constraint for this contractional event.

The mid-Cambrian tectono-magmatic event identified in the Taats River area is significantly younger than the biotite Ar–Ar age of 533 ± 6 Ma (Fig. 13; Höck et al. 2000) obtained for a garnet-biotite gneiss from the Ushgoeg Mt. (Fig. 2a). This may be attributed to different levels of exposure of crustal blocks with different exhumation histories. The Taats River crustal domain was probably still at depth when rocks of the Ushgoeg Mt. area already occupied a higher crustal level.

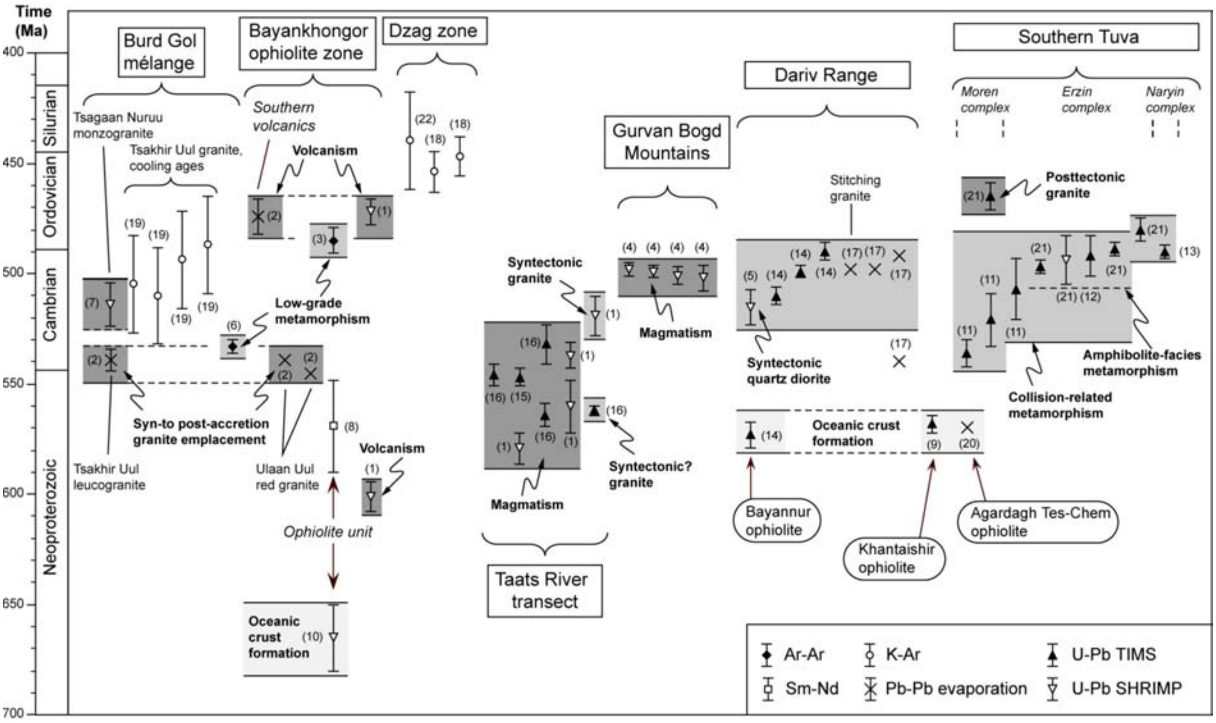

Fig. 13. Synoptic diagram showing isotopic ages obtained in central and western Mongolia, and southern Tuva. Data sources: 1, this study; 2, Buchan et al. (2002); 3, Delor et al. (2000); 4, Demoux et al. (2009a); 5, Dijkstra et al. (2006); 6, Höck et al. (2000); 7, Jahn et al. (2004); 8, Kepezhinskas et al. (1991); 9, Khain et al. (2003); 10, Kovach et al. (2005); 11, Kozakov et al. (1999a); 12, Kozakov et al. (1999b); 13, Kozakov et al. (2001); 14, Kozakov et al. (2002b); 15, Kozakov et al. (2006); 16, Kozakov et al. (2008); 17, Kröner et al. (2001); 18, Kurimoto et al. (1998); 19, Osozawa et al. (2008); 20, Pfänder & Kröner (2004); 21, Sal'nikova et al. (2001); 22, Teraoka et al. (1996). See Fig. 14 for location of areas mentioned.

5.4. Post-accretion Ordovician volcanic activity.

On the 1:200,000 Geological Map, the sheared felsic meta-volcanic rock M290 is located within the late Neoproterozoic-Cambrian schist sequence of the BOZ (Fig. 4). The zircon age of 472 ± 6 Ma obtained for this sample does not support this correlation, and we suggest that this sample belongs to a separate Ordovician volcanic sequence. However, our zircon age is comparable to the zircon age of 474 ± 8 Ma reported for a rhyolite dyke in the Southern volcanics unit (Buchan et al. 2002). Within the ophiolite unit, metamorphic amphiboles from a pillow basalt yielded an Ar–Ar plateau age of 485 ± 6 Ma (Fig. 13; Delor et al. 2000), indicating that parts of the BOZ still underwent deformation at that time. We therefore speculate that early Ordovician punctuated volcanic centres developed on the southern margin of the BOZ in response to prolonged southward subduction. Final amalgamation and stabilization of the region may not have occurred prior to the late Ordovician as indicated by K-Ar ages of about 450 Ma for white micas from pelitic schists of the Dzag zone (Fig. 13;

Teraoka et al. 1996; Kurimoto et al. 1998), suggesting a persistent strain field and crustal deformation at that time.

5.5. Regional correlation with Cambro-Ordovician metamorphic and magmatic events in western Mongolia and southern Tuva.

Remnants of mid-Neoproterozoic to Cambrian oceanic crust are sporadically distributed, from western Mongolia to southern Tuva, along a discontinuous and gently curved belt (Fig. 14). The Khantaishir, Bayannur and Agardagh Tes-Chem ophiolites show a good age correlation for their time of formation at about 570 Ma (Fig. 13; Kozakov et al. 2002b; Khain et al. 2003; Pfänder & Kröner 2004). These ophiolites also display comparable geochemical signatures related to supra-subduction zone environments (Pfänder et al. 2002; Matsumoto and Tomurtogoo 2003; Dijkstra et al. 2006). The BOZ has long been interpreted as part of the same c. 570 Ma old ophiolite belt based on its former Sm–Nd age. However, as mentioned earlier, this ophiolite formed at about 665 Ma (Kovach et al. 2005) and represents a fragment of older oceanic crust. In addition, the BOZ shows distinct chemical features pointing to enriched mantle and intraplate signatures and does not show any subduction-related components (Kovach et al. 2005; Kovalenko et al. 2005). The BOZ also differs from the other ophiolites by its tectonic position. It is sandwiched between two Precambrian complexes and may represent part of an ocean-floored basin, whereas the c. 570 Ma ophiolite complexes show strong relationships with island arc environments.

The ophiolite complexes are broadly distributed along the margin of the presumed Tuva-Mongolian and Dzabkhan microcontinents (Fig. 14). However, recent geochronological data for high-grade gneisses of the Tuva-Mongolian microcontinent do not record Precambrian metamorphic events but show these gneisses to represent deep-seated crustal sections of Cambrian to late Ordovician collisional zones (Fig. 13; Sal'nikova et al. 2001; Kozakov et al. 2002b). In southern Tuva, the Moren, Erzin and Naryn metamorphic complexes are adjacent to the Agardagh Tes-Chem ophiolite (Fig. 14) and underwent high-grade metamorphism between c. 536 and 480 Ma (Kozakov et al. 1999a, 1999b, 2001; Sal'nikova et al. 2001). A post-tectonic granite with a zircon age of c. 465 Ma (Sal'nikova et al. 2001) suggests that these metamorphic complexes were stabilized by the middle Ordovician. In western Mongolia, the Bayannur ophiolite is in tectonic contact with the gneissic basement of the Dariv Range (Fig. 14) and was accreted onto its margin between c. 515 and 498 Ma (Kröner et al. 2001; Dijkstra et al. 2006). During this time interval, metamorphic rocks of the Dariv Range underwent high-grade metamorphism between c. 510 and 490 Ma (Fig. 13; Kozakov et al. 2002b).

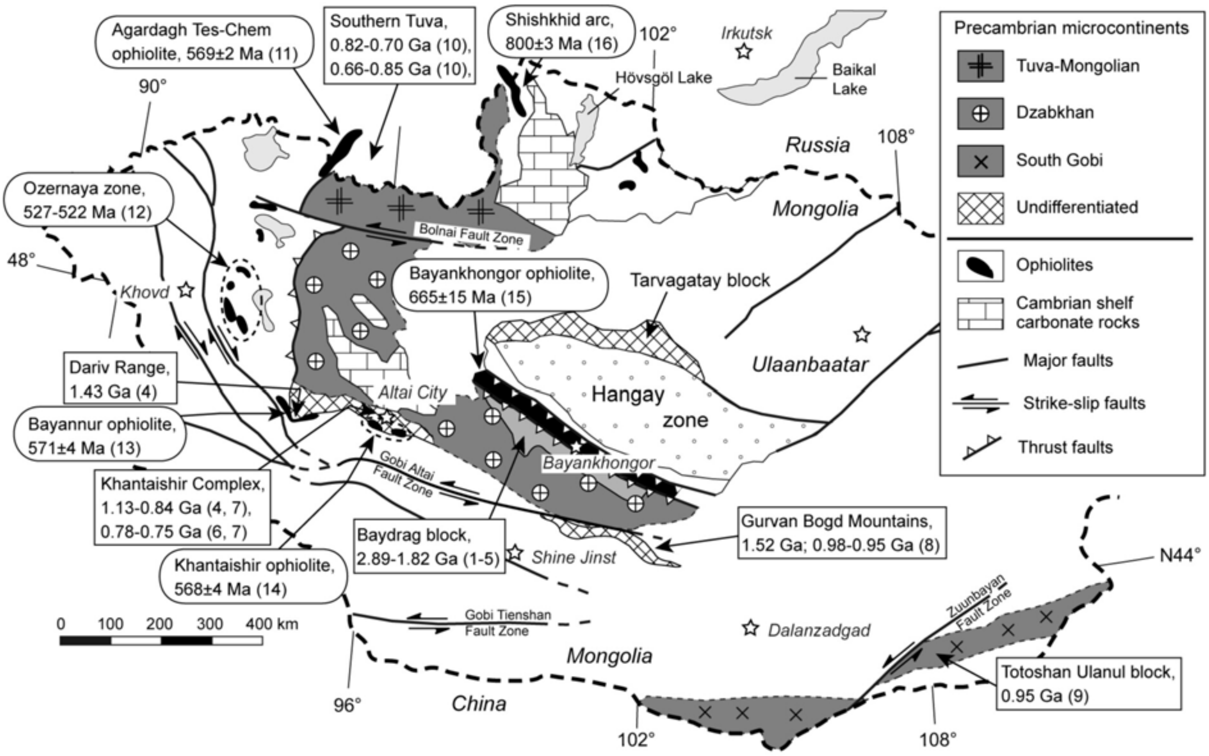

Fig. 14. Simplified lithotectonic map of western and central Mongolia showing location of Precambrian basement and mid-Neoproterozoic to Cambrian ophiolite complexes discussed in the text (modified after Badarch et al. 2002; Buchan et al. 2002). Ages for igneous events shown by Precambrian rocks and time of ocean crust formation for ophiolite complexes are indicated; data sources: 1, Bibikova et al. (1990); 2, Kotov et al. (1995); 3, Kozakov et al. (2007b); 4, Kröner et al. (2001); 5, Mitrofanov et al. (1985); 6, Yarmolyuk et al. (2008a); 7, Zhao et al. (2006); 8, Demoux et al. (2009a); 9, Yarmolyuk et al. (2005); 10, Kozakov et al. (2005); 11, Pfänder & Kröner (2004); 12, Kovalenko et al. (1996); 13, Kozakov et al. (2002b); 14, Khain et al. (2003); 15, Kovach et al. (2005); 16, Kuzmichev et al. (2005).

The Bayankhongor/Baydrag orogenic zone shows a comparable tectono-magmatic history with a phase of accretion between c. 540 and 519 Ma and continuous convergence until about 472 Ma. All data presented above suggest that a large part of the CAOB in western Mongolia and southern Tuva underwent accretion/collision processes at a similar time thus contributing to formation of a stable continental margin by the late Ordovician as proposed by Windley et al. (2007) and Kröner et al. (2007).

Our data are difficult to reconcile with the geodynamic model of Şengör et al. (1993) for the eastern CAOB, which considers the evolution, beginning in the latest Neoproterozoic, of a single and long-lived magmatic arc. The Bayankhongor/Baydrag orogenic zone demonstrates that final amalgamation of three contrasting lithotectonic units did not occur before the late Ordovician. Therefore, it is unlikely that the aforementioned regions underwent subduction-accretion processes along a single and continuous along strike arc front prior to the late Ordovician.

6. Conclusions

Our geochronological results provide new time constraints on the tectonothermal evolution of the Baydrag block prior to 1.8 Ga and on the late Neoproterozoic to Cambrian tectono-magmatic evolution of the Bayankhongor/Baydrag orogenic zone in central Mongolia. The principal results are summarized as follows:

- The Baydrag block underwent a major tectonothermal event in the late Palaeoproterozic characterized by high-grade metamorphism between 1840 and 1826 Ma and coeval with the intrusion of granitic magma at mid-crustal level at 1839 Ma.
- A crystallization age of 1051 Ma for a granite gneiss, together with predominantly Mesoproterozoic detrital zircons for a quartzite lens within the Burd Gol mélange and Neoproterozoic inherited zircons for granitic intrusions, testify to the heterogeneity and long Precambrian history of the Baydrag block.
- The northeastern margin of the Baydrag block was an active margin in the late Neoproterozoic to early Cambrian as indicated by prolonged granitoid activity from 579 to 537 Ma.
- Accretion of the BOZ to the northern active margin of the Baydrag block occurred in the mid-Cambrian as signified by a zircon age of 519 Ma for a syntectonic granite vein from the Taats River transect. This reflects a major phase of deformation at deep crustal levels.
- The region was still converging in the early Ordovician as suggested by punctuated volcanic activity at about 474–472 Ma, developed at the junction between the BOZ and the Baydrag block.

Chapter 3

Middle Palaeozoic evolution of an active continental margin in southern Mongolia: zircon ages and geochemical characteristics of igneous rocks of the Gobi-Altai region

Abstract

SHRIMP and conventional U–Pb zircon ages as well as whole-rock chemical, and Nd isotopic data were determined for predominantly middle Palaeozoic metaigneous rocks from the Gobi-Altai region in southern Mongolia. This area occupies a central position within the eastern part of the Central Asian Orogenic Belt (CAOB). Felsic metavolcanic rocks yielded early Silurian zircon crystallization ages of 443 ± 5 and 441 ± 5 Ma (2σ), whereas the protolith of a granite gneiss yielded a zircon crystallization age of 454 ± 4 Ma (2σ). The early Silurian mafic to intermediate metavolcanic rocks were probably formed by melting of variably depleted sub-arc mantle sources ($\varepsilon_{Nd(t)}$-values of +4.6 to +8.0), overprinted by slab-derived components. The felsic metaigneous rocks display typical crustal geochemical signature and yielded heterogeneous Nd isotopic compositions with initial $\varepsilon_{Nd(t)}$-values of -4.8 to +4.0 that indicate melting of juvenile and older crustal material with mean crustal residence ages dating back to the middle Mesoproterozoic. We suggest that these late Ordovician/early Silurian igneous sequences formed along a mature active Andean-type margin. A metamorphic assemblage, predominantly composed of mafic and felsic granitoid gneisses, is exposed at the southern boundary of the Gobi-Altai. The protolith of a tonalitic gneiss yielded an early Devonian zircon crystallization age of 415 ± 3 Ma (2σ). Early Devonian mafic gneisses yielded high initial $\varepsilon_{Nd(t)}$-values of +6.2 to +8.8 and hence were derived from time-integrated highly LREE-depleted mantle sources. Subduction-related calc-alkaline granodioritic to granitic gneisses were likely formed by melting of predominantly juvenile crustal material with subordinate involvement of old crustal components as indicated by initial $\varepsilon_{Nd(t)}$-values of +2.0 to +4.6 and mean crustal residence ages of c. 0.9–0.7 Ga. We suggest that these rocks were emplacement within the outboard portion of the late Ordovician/early Silurian active continental margin. The combined geochronological and geochemical data suggest that magmatism across an Andean-type margin migrated oceanwards through time by way of subduction zone retreat from the late Ordovician/early Silurian to the early Devonian. Progressive extension of the continental margin throughout the Devonian was possibly related to roll-back of the subducting oceanic lithosphere and culminated in the late Devonian with the formation of a Japan-type arc front associated with a back-arc basin in the Gobi-Altai region.

1. Introduction

Island arc-continent collision is a fundamental process during the evolution of orogenic belts and is also regarded as a significant process during the growth of the continental crust (Tarney & Jones 1994; Rudnick 1995; Jahn et al. 2000a). The Central Asian Orogenic Belt (CAOB; Jahn et al. 2000a), also known as Altaids (Şengör et al. 1993; Şengör & Natal'in 1996) or Central Asian Foldbelt (Zonenshain et al. 1990) is composed of numerous lithotectonic units or terranes and is regarded as one of the largest areas on Earth of continental crust produced during the Phanerozoic (Şengör et al. 1993; Jahn et al. 2000a; Jahn 2004). It extends from the Ural Mountains to the Pacific coast and is sandwiched between the Siberian Craton in the N and the North China (Sino-Korean) and Tarim Cratons in the S (Fig. 1a). The belt formed through subduction-accretion processes within the Palaeoasian Ocean (Zonenshain et al. 1990) and related oceanic basins, from the latest Mesoproterozoic to the late Permian/early Triassic (Şengör et al. 1993; Mossakovsky et al. 1994; Khain et al. 2002; Xiao et al. 2003, 2009a; Yakubchuk 2008). The details of formation of this huge orogenic system are still controversial but most researchers agree that it resulted from the amalgamation of magmatic arc material (island arcs, accretionary prisms, backarc/forearc basins), interspersed with slivers of ophiolitic material and subordinate Precambrian continental fragments (Coleman 1989; Şengör et al. 1993; Mossakovsky et al. 1994; Buslov et al. 2001; Badarch et al. 2002;

Khain et al. 2003; Yakubchuk 2004; Dobretsov & Buslov 2007; Kröner et al. 2007; Windley et al. 2007; Xiao et al. 2008, 2009b; Yakubchuk 2008).

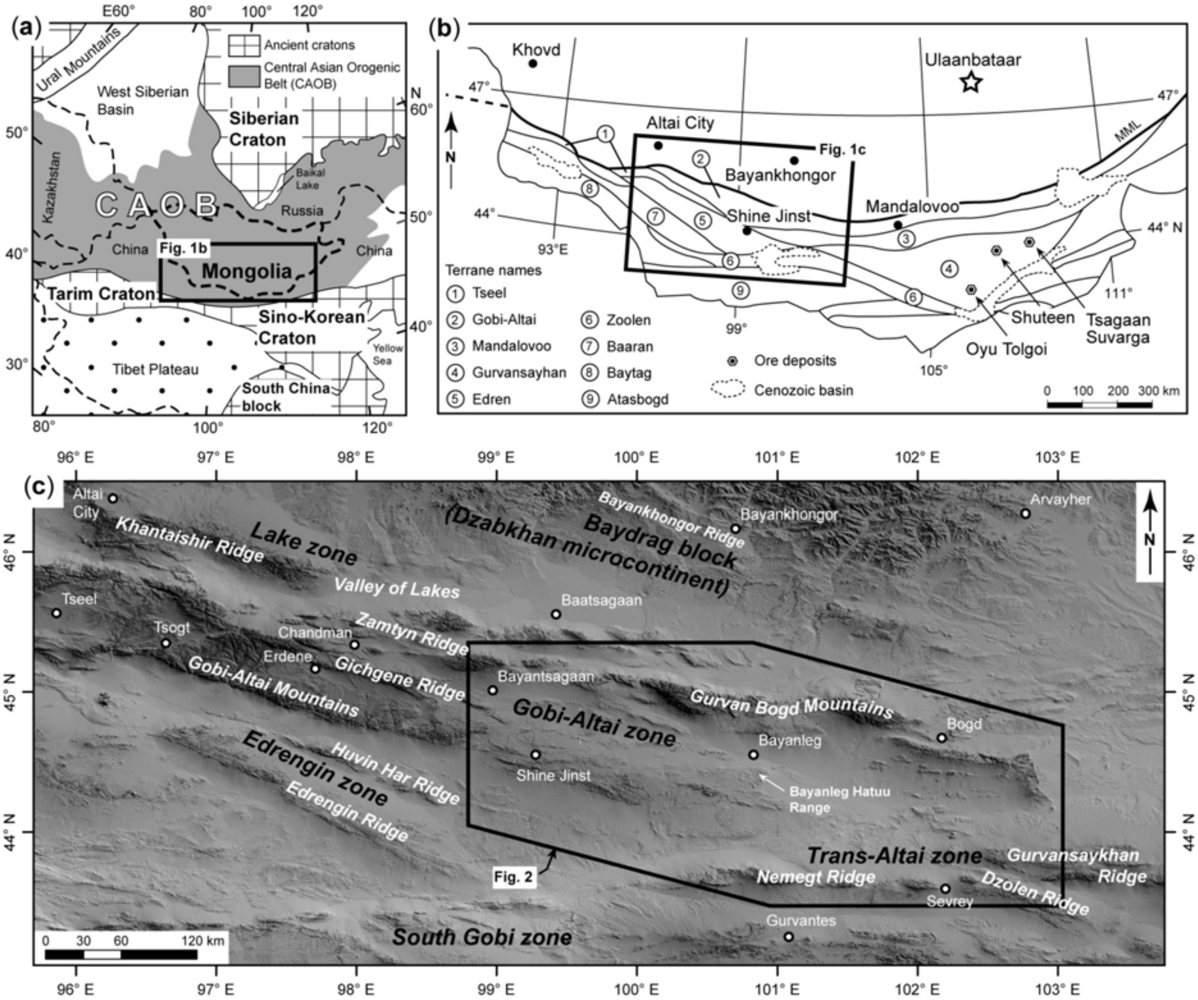

Fig. 1. (**a**) Simplified tectonic subdivision of Central Asia (modified after Jahn et al. 2000a). The Central Asian Orogenic Belt (CAOB), in medium grey, is predominantly composed of late Neoproterozoic to late Palaeozoic folded domains. Inset (Fig. 1b) shows the southern Mongolian segment. (**b**) Tectonostratigraphic terrane map of southern Mongolia; MML: Main Mongolian Lineament; numbers within circles refer to the names of terranes listed in the lower left corner of diagram (adapted from Badarch et al. 2002). (**c**) Grey-scale topographic image (Shuttle Radar Topography Mission) showing the geography of southwestern Mongolia and the location of the lithostratigraphic 'zones' (modified after Dergunov 2001). The study area shown in detail in Fig. 2 is outlined.

Located in a central position within the eastern CAOB (Fig. 1a), the territory of Mongolia records a significant time span of the evolution of this orogenic system (Badarch et al. 2002; Kröner et al. 2007). Traditionally, Mongolia is geologically subdivided into a northern and southern domain, separated by the so-called Main Mongolian Lineament (MML, Tomurtogoo 1997; Badarch et al. 2002; Windley et al. 2007) and interpreted as a regional structural boundary. The northern domain is predominantly composed of Neoproterozoic to early Palaeozoic island arcs and related sedimentary rocks (Kovalenko et al. 1996; Kozakov et al. 2002b), late Neoproterozoic ophiolitic assemblages (Khain et al. 2003; Kovach et al. 2005; Kuzmichev et al. 2005), as well as fragments (microcontinents?) of Precambrian crystalline basement (Kozakov et al. 2007b; Demoux et al. 2009a). The southern domain is dominated by early to late Palaeozoic volcanic and volcaniclastic rocks (Ruzhentsev & Pospelov 1992; Lamb & Badarch 1997, 2001) and Carboniferous to Permian intrusive complexes (Kovalenko et al. 1995; Gerel et al. 2005; Kovalenko et al. 2006; Kozakov et al. 2007a; Kozlovsky et al. 2007; Hanžl et al. 2008; Yarmolyuk et al. 2008c).

During the last decade, systematic geochronological and isotopic studies considerably improved the understanding of crustal growth processes in several parts of the CAOB. On the basis of a compilation of whole-rock Nd isotopic data, Kovalenko et al. (2004) proposed a subdivision of the CAOB into four isotopic provinces. These provinces were interpreted in terms of distinct crustal growth episodes. In Mongolia, these authors recognized two provinces referred to as a northern ‘Caledonian’ province with Nd mean crustal residence ages (t_{DM}) of 1.1 to 0.6 Ga and a southern ‘Hercynian’ domain characterized by younger t_{DM} of 0.8 to 0.5 Ga. On a broad scale, these two isotopic provinces roughly coincide with the two tectonic domains separated by the MML. This led some authors to propose that the MML represented a stabilized accreted margin by Ordovician time (Kröner et al. 2007; Windley et al. 2007) facing a southward-open oceanic realm (present-day coordinates). The southern domain of Mongolia is therefore ideally suited to study the development of the CAOB following the late Cambrian episode of terrane accretion farther N.

Here we present new U–Pb zircon ages, whole-rock major and trace element data, and Nd-isotopic systematics for early Silurian to early Devonian meta-igneous rocks from the Gobi-Altai region, which constitutes the northern segment of the southern domain of Mongolia. These data shed light on the early-middle Palaeozoic geodynamic development of this portion of the CAOB by suggesting likely tectonic settings for the origin of these middle Palaeozoic magmatic sequences.

2. Geological setting

The geological inventory of south-central Mongolia was traditionally subdivided in the Russian literature into distinct tectonic zones with specific lithostratigraphic records and tectonic evolution (e.g. Dergunov 2001 and references therein). Using geological, structural, and palaeontological data, Badarch et al. (2002) and Badarch (2005) proposed an alternative subdivision in terms of tectonostratigraphic terranes. These authors recognized not less than sixteen terranes within the southern Mongolian domain (i.e. south of the MML; Fig. 1b), subdivided into cratonal, metamorphic, island arc, back-arc/fore-arc, accretionary wedge, and ophiolitic terranes. However, recent studies within the southern Mongolian domain suggested that some of their proposed terrane boundaries are ambiguous (Helo et al. 2006; Blight et al. 2008; Demoux et al. 2009b), and we therefore prefer to use the subdivision into ‘zones’ as proposed by earlier studies (e.g. Dergunov 2001). Lithostratigraphic features of the Lake, Gobi-Altai, Edrengin, and Trans-Altai zones (Fig. 1c) are briefly described below.

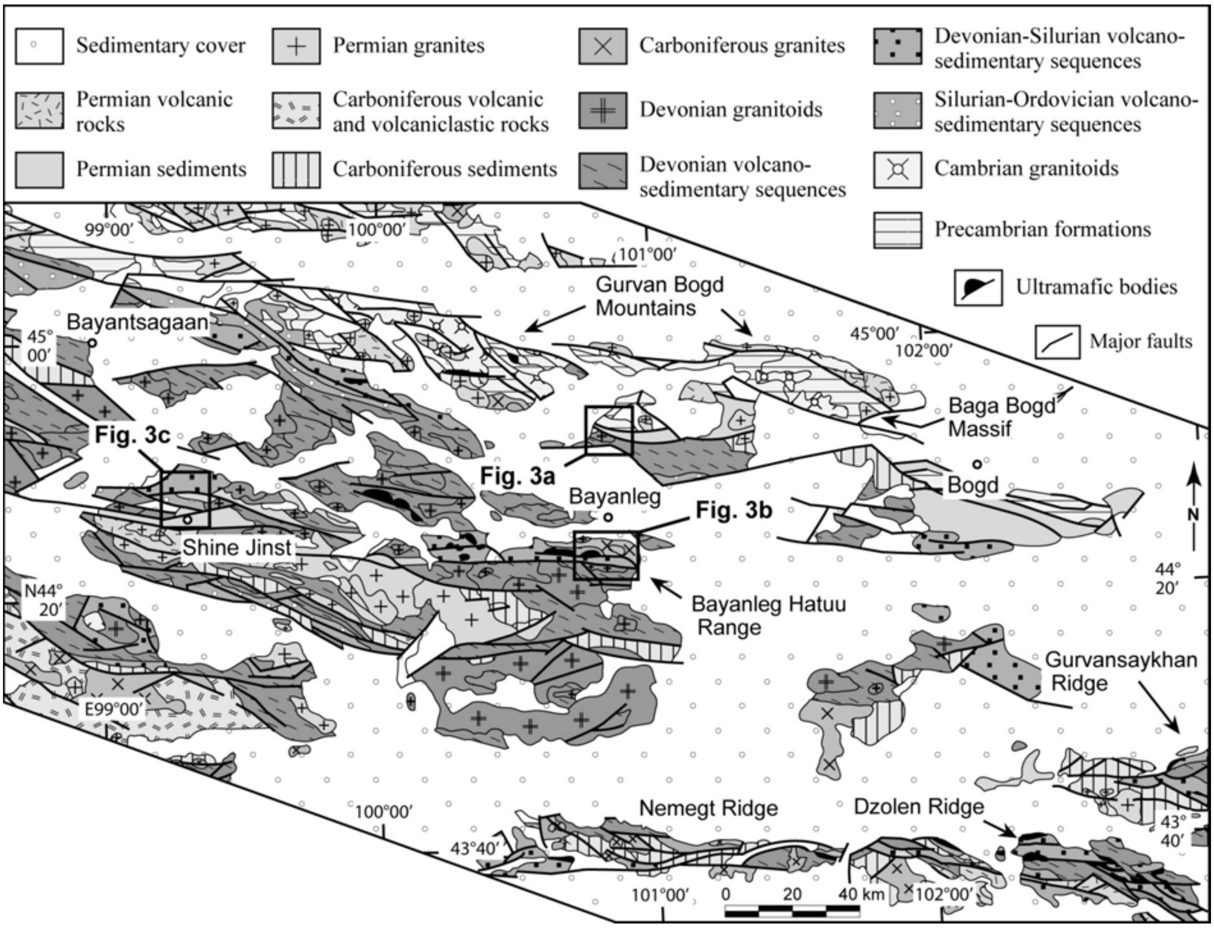

Fig. 2. Geological map of the study area (modified after Tomurtogoo 1998). The areas investigated in this study are outlined (Fig. 3 a, b and c).

Immediately to the N of the MML, the Lake zone (SE domain of the Lake terrane of Badarch et al. 2002) contains volcanic, carbonate and siliciclastic strata of late Neoproterozoic to Cambrian age. S of Altai City (Fig. 1c), the Khantaishir Ridge includes the late Neoproterozoic Khantaishir ophiolite (c. 568 Ma; Gibsher et al. 2001) and the late

Neoproterozoic/early Cambrian Ulanshandin island arc, formed onto an older folded basement (Ruzhentsev & Burashnikov 1996). Major and trace element data suggest that the Khantaishir ophiolite originated within a supra-subduction zone environment via intra-arc spreading (Zonenshain & Kuzmin 1978; Matsumoto & Tomurtogoo 2003). Northwest accretion of the ophiolite/island arc complexes against the passive margin of the Precambrian Dzabkhan microcontinent (Macdonald et al. 2009) is though to have occurred during the early Cambrian and was completed by the middle Cambrian (Ruzhentsev & Burashnikov 1996). Recent geochronological data from the boundary between the Lake and Gobi-Altai zones indicate the presence of a Precambrian basement strip that extends from the Zamtyn Ridge to the Gurvan Bogd Mountains (Fig. 1c). Granitoid gneisses from the latter locality yielded protolith zircon crystallization ages of c. 1.52 to 0.95 Ga (Demoux et al. 2009a), and may represent the southern extension of the Dzabkhan microcontinent (Mossakovsky et al. 1994). This Meso-Neoproterozoic basement underwent a strong thermal pulse during the late Cambrian as manifested by the emplacement of numerous granitoids bodies with zircon crystallization ages of c. 518 to 498 Ma (Hanžl & Aichler 2007; Hrdličková et al. 2008; Demoux et al. 2009a).

The Gobi-Altai zone (Fig. 1c) extends along the southern side of the MML and was subdivided by Badarch et al. (2002) into the Gobi Altai back-arc/fore-arc terrane, the Tseel metamorphic terrane and the Mandalovoo island arc terrane (Fig. 1b). Supracrustal rocks in the Gobi-Altai zone consist of minor Ordovician to Silurian sedimentary sequences and of voluminous sequences of Devonian clastic sediments, shallow marine limestones, and volcaniclastic and volcanic rocks, metamorphosed to greenschist-facies (Ruzhentsev & Pospelov 1992; Lamb & Badarch 1997, 2001; Ruzhentsev 2001; Demoux et al. 2009b). Carboniferous and Permian sediments occur sporadically within narrow basins throughout the area (Lamb & Badarch 1997). Deep crustal rocks predominantly occur in the NW of the Gobi-Altai zone within the Tseel metamorphic complex (Gobi-Altai Mountains) and along the NE flank of the Gichgene Ridge (Fig. 1c). These rocks have zircon crystallization ages of c. 385 to 361 Ma (Bibikova et al. 1992; Kozakov et al. 2002a, 2007a; Kröner et al. 2007, Hrdličková et al. 2008) and are represented by high- to medium-grade granitoid gneisses, amphibolites, micaschists, and migmatites. In the vicinity of Chandman village (Fig. 1c), the Chandman magmatic complex includes calc-alkaline arc-related dioritic to granitic intrusions (Economos et al. 2008) from which a granite body yielded a zircon crystallization age of 345 ± 2 Ma (Hrdličková et al. 2008). Local gneissification of the plutonic bodies argues in favour of a syntectonic emplacement (Economos et al. 2008). The Gobi-Altai zone is bordered to the SW and SE by the Edrengin and Trans-Altai zones, respectively.

The lithostratigraphy within the Edrengin zone (Edren island arc terrane of Badarch et al. 2002) was detailed in the Huvin Har and Edrengin Ridges (Fig. 1c; Ruzhentsev & Pospelov 1992; Lamb & Badarch 1997; Ruzhentsev 2001). The Huvin Har Ridge contains Lower to Upper Devonian clastic sediments, marine limestones, shales, jasper beds, and greywacke flysch that were interpreted as backarc deposits (Ruzhentsev & Pospelov 1992). The Edrengin Ridge is characterized by voluminous volcaniclastic and volcanic rocks. The Devonian volcanic rocks show typical island arc-related geochemical fingerprints and positive initial $\varepsilon_{Nd(t)}$-values of +6.7 to +7.7 (Lamb & Badarch 2001; Yarmolyuk et al. 2008c). The Devonian rocks at both localities are transgressively overlain by early Carboniferous volcanic-terrigenous molasse (Ruzhentsev & Pospelov 1992; Ruzhentsev 2001).

The Trans-Altai zone (Zoolen accretionary wedge and Gurvansayhan island arc terranes of Badarch et al. 2002) shows a complex structure of imbricated tectonic slivers, dismembered blocks, and mélange zones (Zonenshain et al. 1975; Ruzhentsev et al. 1985). Typical sections are best exemplified within the Dzolen and Gurvansaykhan Ridges (Fig. 1c) and consist of volcano-sedimentary and volcanic deposits as well as serpentinized ultramafic mélanges (Zonenshain et al. 1975; Eengin 1978; Ruzhentsev et al. 1985). The lower sequence contains jasper with radiolaria of Silurian-Lower Devonian age (Zonenshain et al. 1975). Volcaniclastic rocks from the Dzolen Ridge yielded zircon crystallization ages of c. 421–417 Ma (Helo et al. 2006), confirming an early Devonian phase of volcanism. The geochemical features and strongly depleted Nd isotopic compositions of mafic to intermediate volcanic rocks point to an origin in a single intra-oceanic island arc/fore-arc environment (Helo et al. 2006; Yarmolyuk et al. 2008c). The late Silurian to late Devonian arc-related assemblages are locally overlain with an angular unconformity by early Carboniferous volcanic-terrigenous deposits (Suyetenko 1973; Ruzhentsev & Pospelov 1992).

The Edrengin and Trans-Altai zones were interpreted as the remains of island arc systems testifying to the existence of a late Silurian to Devonian oceanic realm riming the southern margin of the North Asiatic Caledonian continent (present-day coordinates), and referred to as the South Mongolian ocean basin (Zonenshain 1973; Ruzhentsev & Pospelov 1992).

3. Sample localities

Our study area is located in the Gobi-Altai region (Fig. 1c) where we investigated two low-grade sequences in the N and S of Bayanleg village and a third medium-grade basement in the N of Shine Jinst village (Fig. 2). Geological sketch maps with sample locations are shown in Fig. 3; the GPS coordinates of samples are listed in Appendix A.

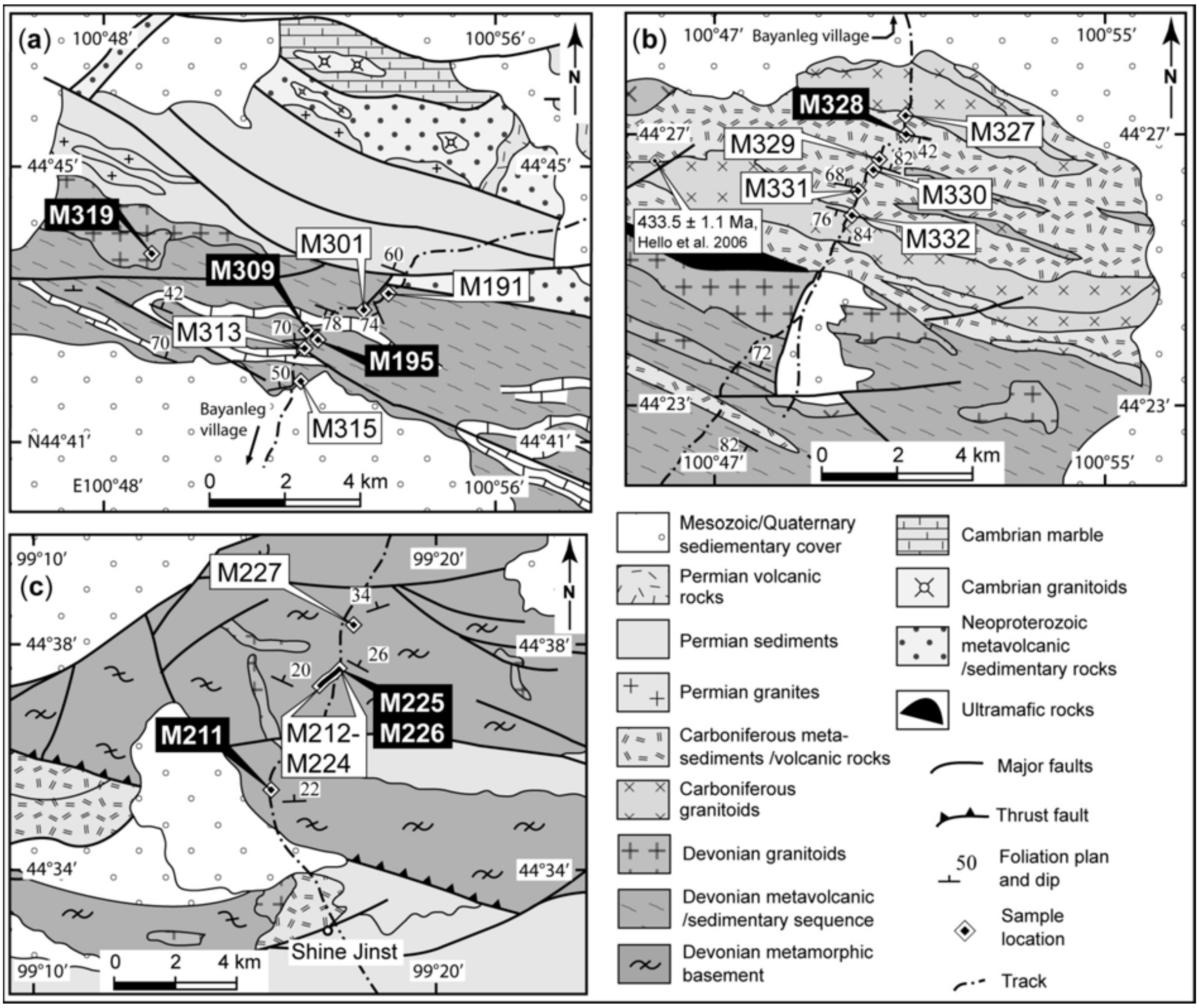

Fig. 3. Geological maps of (**a**) the Halbagant Range, (**b**) the Hulsnii Valley (Bayanleg Hatuu Range) and (**c**) the Shine Jinst area (modified after Geological Map of Mongolia at scale 1:200,000, sheets L-47-XXIX, L-47-XXXIV and L-47-XXXV; Zabotkin 1988). Numbers within black boxes refer to the samples used for U–Pb geochronology.

3.1. Halbagant Range

The Halbagant Range is located S of the Gurvan Bogd Moutains (Fig. 2) which are composed of uplifted crustal fragments that contain granitoid gneisses with early Neoproterozoic and late Cambrian protolith emplacement ages (Demoux et al. 2009a). A section across the Halbagant Range (Fig. 3a) shows a succession of strongly sheared metavolcanic and metasedimentary rocks deformed under greenschist-facies conditions. This volcano-sedimentary sequence is presumed to be early Devonian in age as inferred from the 1:200,000 Geological Map (Zabotkin 1988). About 6 km to the W, the sequence is intruded by a NW–SE trending granitoid pluton, about 4 km in length and 2 km wide, of presumed Devonian age (Zabotkin 1988). The pluton is composed of undeformed granite and granodiorite bodies showing sharp intrusive contacts with the surrounding low-grade metamorphic rocks. It contains numerous decimetre- to metre-sized xenoliths of gabbroic to dioritic composition as well as xenoliths of sheared low-grade metamorphic rocks. To the N, the sequence is in tectonic contact with a gently folded Permian sedimentary sequence. The Permian sediments are composed of sandstones, siltstones, and shales with occasional coal layers and were most likely deposited within an intracontinental basin. The northern part of the section is dominated by sheared massive lava flows of basaltic to dacitic composition which are intercalated with decimetre- to metre-thick limestone and medium- to fine-grained sandstone beds. Towards the S, pyroclastic rocks become prominent in comparison to sheared massive lava flows. The lithologies vary from tuffaceous slates of intermediate composition, minor sheared massive volcanic rocks of mafic to intermediate composition to sheared felsic pyroclastic rocks. These meta-volcanic rocks alternate with sheared limestone beds (Fig. 4a), and fine- to medium-grained, well-sorted turbiditic deposits. The sequence is cut by rare subvertical mafic to felsic dykes. To the S, the number of exotic blocks increases. These blocks (olistoliths?) are composed of metre- to several metre-large limestone blocks and sheared mafic to felsic rocks, embedded in a calc-chlorite-schist matrix. Towards the southern end of the section, the sequence becomes tightly folded by SW-verging isoclinal folds with subhorizontal fold axes. A large exotic block of massive limestone occurs in tectonic contact with the surrounding calc-chlorite-schists (Fig. 4b). The presence of exotic blocks of different lithologies as well as pyroclastic deposits interbedded with large amounts of carbonate and terrigenous clastic sediments suggests a marginal basin or forearc setting.

3.2. Hulsnii Valley (Bayanleg Hatuu Range)

Some 30 km S of the previous locality (Fig. 2), the Bayanleg Hatuu Range is composed of Ordovician to Devonian arc-related volcanic, volcaniclastic and sedimentary rocks and Carboniferous intrusive and extrusive rocks (Fig. 3b). To the S a large granite pluton of presumed late Devonian age intrudes a volcano-sedimentary sequence with a palaeotonlogicaly determined early Devonian age (Zabotkin 1988). We investigated a traverse across this Range following the N–S trending Hulsnii Valley and covering a distance of about 5 km (Fig. 3b). The traverse is described below from N to S.

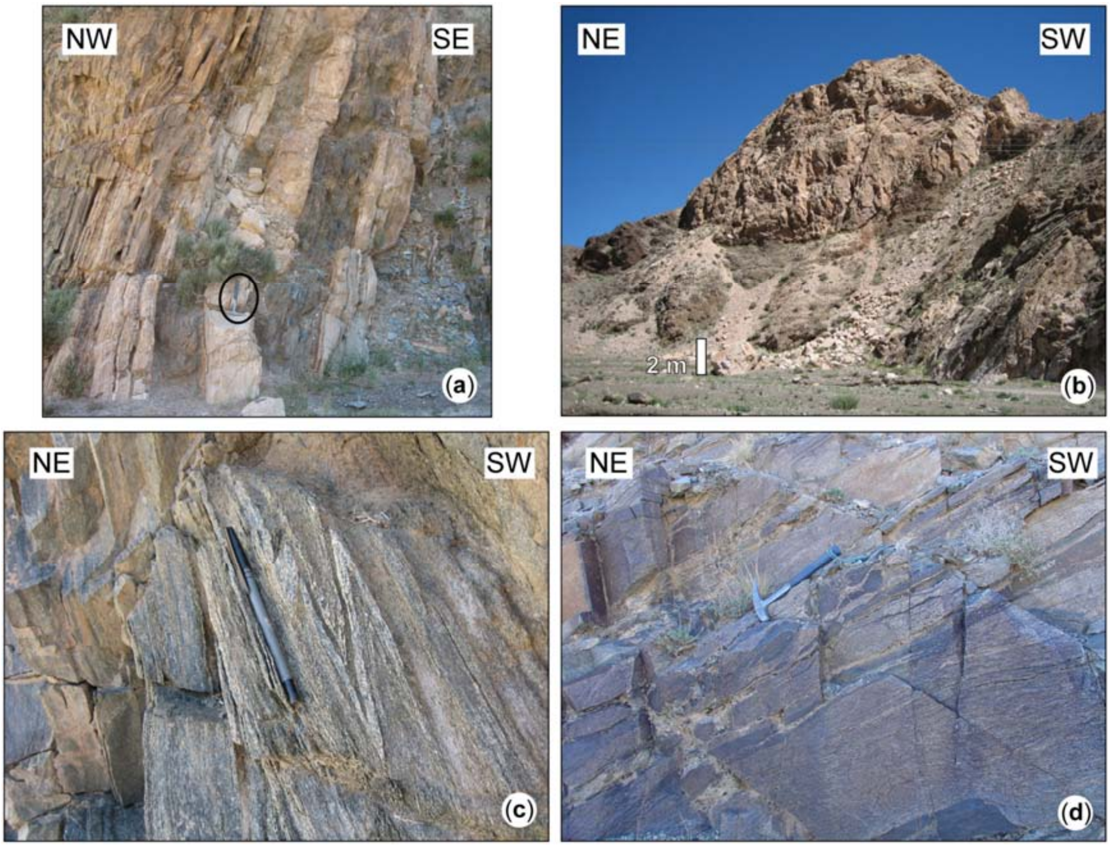

Fig. 4. (**a**) Strongly sheared felsic pyroclastic rocks alternating with sheared limestone beds, Halbagant Range; hammer (circled) for scale. (**b**) Massive limestone block thrust over sheared volcanic-derived schists, Halbagant Range. (**c**) Tight isoclinal folds in quartz-biotite schists, Hulsnii Valley. (**d**) Compositional banding in granodioritic gneisses with amphibolite boudins, metamorphic basement N of Shine Jinst village.

The section begins with undeformed porphyritic hornblende-bearing plutonic rocks of gabbroic composition. These intrusions are presumed to be of Carboniferous age (Zabotkin 1988). These rocks are cut by decimetre-wide and randomly distributed gabbro dykes. The section continues with strongly foliated felsic volcanic rocks sheared under low-grade metamorphic conditions. The age of these rocks is unclear and is shown either as late Silurian-early Devonian or early Carboniferous on the 1:1,000,000 and 1:200,000 Geological Maps, respectively. Intrusive contacts were observed between the Carboniferous intrusions and the sheared felsic schists. Close to the contact, the sheared felsic schists are intruded by mafic and felsic dykes. They consist of minor decimetre-wide coarse-grained granite dykes or several metre-wide coarse-grained gabbro dykes containing cm to several cm large enclaves of sheared volcanic rocks and/or dolomitic limestone. About 100 m southwards, there is a 10 metre-wide ridge of sheared limestone showing conformable lithological contacts with the surrounding low-grade schists. The section continues with a series of strongly sheared quartz-biotite schists and biotite-muscovite schists. To the S, felsic schists of dacitic composition predominate. Across the entire transect, the various lithologies display a consistent penetrative schistosity striking NW−SE and dipping between 42° to 68° NE or SW. The schistosity is locally overprinted by steep and tight isoclinal folds with subhorizontal axes (Fig. 4c). At the end of the transect, a strongly foliated porphyritic granite occurs in sharp contact with the surrounding sheared felsic volcanic rocks. The metagranite is about 800 metres wide and was affected by a steeply N-dipping and E−W striking foliation conformable to the foliation in the surrounding sheared metavolcanic rocks. A Carboniferous age was assigned to this metagranite on the 1:200,000 Geological Map (Zabotkin 1988). However, a Pb–Pb zircon evaporation age of 433.5 ± 1.1 Ma (Helo et al. 2006) was obtained from the same metagranite, sampled about 6 km along strike to the NW of our transect (Fig. 3b).

3.3. Shine Jinst area

The area S of Shine Jinst village (Fig. 3c) is primarily composed of late Permian interbedded sandstone and shale and minor volcaniclastic sediments and felsic volcanic rocks (Lamb & Badarch 2001; Lamb et al. 2008; Johnson et al. 2008). This sequence is thought to have formed within a Permian intracontinental basin (Lamb et al. 2008). Three km to the N of Shine Jinst, a metamorphic terrain is exposed over an area of some 400 km^2 and is in thrust contact with the southern Permian intracontinental basin. The metamorphic rocks are predominantly composed of amphibolite-facies paragneisses, orthogneisses and migmatitic gneisses in some places. According to the 1:200,000 Geological Map (Zabotkin 1988), this metamorphic basement is inferred to be early Devonian in age (Fig. 3c). Along the studied transect, the metamorphic rocks typically consist of strongly foliated and imbricated granitoid gneisses, leucocratic metagranites, amphibolitic boudins (Fig. 4d), and minor paragneisses. These rocks show little or no evidence of migmatization except towards the N where sample M227 was collected. The rocks display a penetrative foliation striking NW−SE and dipping 22° to 36° NE or NW. Original lithological contacts are poorly preserved and lie parallel to the main pervasive fabric because of high-strain ductile shearing. The asymmetric shape of amphibolite boudins suggests a top-to-the S sense of shearing (Fig. 4d). This initial metamorphic fabric is overprinted by decimetre-wide greenschist-facies shear zones gently dipping to the N. These rocks are locally intruded by undeformed pegmatitic veins.

4. Analytical methods

SHRIMP zircon dating. Zircons from samples M309 and M328 were analysed on the Sensitive High-Resolution Ion MicroProbe (SHRIMP II) at the Chinese Academy of Geological Sciences in Beijing, China, whereas zircons from samples M195, M211, and M226 were dated on the SHRIMP II at the Centre of Isotopic Research (CIR) in St. Petersburg, Russia. All zircons were separated at the University of Mainz, using a Frantz magnetic separator and heavy liquid (methylene iodide). Representative zircons were hand-picked under a binocular microscope and mounted on an epoxy resin disc together with chips of the zircon standards CZ3 (Beijing) and Temora 1 (St. Petersburg). The mounts were polished until the interiors of the grains were exposed. Zircons were documented with transmitted and reflected light photomicrography, and the internal structure of the grains was documented using cathodoluminescence (CL) images. CL imaging was performed on a JEOL JXA-8900 RL Superprobe at the University of Mainz (operating conditions were 15 KV accelerating voltage and 12 nA beam current on carbon-coated mounts) and on a CamScan MX2500 scanning electron microscope at the CIR in St. Petersburg (operating at 15 kV and high resolution on a gold-coated mount). CL images reveal the internal structures by imaging high-U (dark) and low-U (bright) domains (Corfu 2003). CL-dark areas of zircon grains were preferably chosen for in-situ SHRIMP analysis.

The SHRIMP II instrumental characteristics were outlined by De Laeter & Kennedy (1998) and Larionov et al. (2004), and the analytical procedures are described in Claoué-Long et al. (1995), Nelson (1997) and Williams (1998). For data collection, 6 scans through the critical mass range were made in Beijing and 4 scans in St. Petersburg. The measured $^{206}Pb/^{238}U$ ratios for the CZ3 standard were normalized to 0.0914, which is equivalent to an age of 564 Ma (Pidgeon et al. 1994) and those for Temora 1 to 0.0668, equivalent to an age of 417 Ma (Black et al. 2003). Primary beam intensity was about 6.4 nA in Beijing and about 4.2 nA in St. Petersburg. The mass-resolution was about 5000 at both instruments, enabling clear separation of isobaric interferences. The uncertainty in the ratio of radiogenic ^{206}Pb over U calculated for all measurements of the CZ3 standard in Beijing was 1.3% and 0.85% for the TEMORA 1 standard in St. Petersburg. Sensitivity for Pb on CZ3 and TEMORA 1 was about 26 cps/ppm/nA in Beijing and about 47 cps/ppm/nA in St. Petersburg. Analyses of unknown samples and standards were regularly alternated to asses the extent of Pb^+/U^+ discrimination. Raw data reduction followed the method described by Nelson (1997, 2006). Corrections for common Pb were made using the ^{204}Pb method, assuming, in the case of ^{204}Pb counts similar to the average ^{204}Pb counts in the standards, that most of the common Pb is surface-related (Kinny 1986) and has the composition of Broken Hill lead. In the case of higher ^{204}Pb counts, the age-related common Pb was corrected following the model Pb compositions of Cumming & Richards (1975). Stern (1997) provided a detailed account of the counting error assessment for SHRIMP analyses. Pooled ages and errors were calculated using the Isoplot program of Ludwig (2003) and are given in Ma at 2σ or 95% confidence levels. The analytical data are reported in Appendix B-3. Errors of individual analyses are based on counting statistics and are given at the 1σ confidence level.

Conventional U–Pb zircon dating. Isotope dilution analyses were carried out at the Max-Planck Institut (MPI) für Chemie in Mainz (Germany). Digestion of two to three zircon grains per aliquot was performed in teflon bombs following Wendt & Todt (1991). Before dissolution, the grains were washed in concentrated HNO_3 and carefully rinsed with ultra-pure water. A mixed ^{205}Pb–^{233}U spike was added prior to dissolution. Dissolution of the grains was achieved with concentrated HF in sealed Teflon vials at 200 °C during one week. After complete dissolution of the grains, chemical separation of Pb and U was performed with HBr chemistry, using 20 µl columns with anion-exchange resin. Pb and U were loaded together on single rhenium filaments with silica gel. The isotopic compositions were measured on a Finnigan-MAT 261 thermal-ionisation mass spectrometer (TIMS) equipped with a secondary electron multiplier (SEM). The measured ratios were corrected for mass fractionation (0.3‰ per a.m.u), blank contribution and common Pb (Stacey & Kramers 1975). Mass fractionation was determined by repeated measurements of the NBS 981 standard solution. Total procedural blanks for Pb were <25 pg. Ages and regression lines were calculated using the Isoplot program of Ludwig (2003). Analytical results are listed in Appendix D-1.

Major and trace element analyses. For each sample, about one kg of rock was crushed into centimetre-size fragments using a hydraulic press; fresh chips were hand-picked and ground in an agate mortar at the MPI in Mainz. Major and some trace elements (Cr, Ni, Co, Ga and V) were determined on glass and powder pellets, respectively, using an X-ray fluorescence Philips MagiXPro spectrometer at the University of Mainz. Loss on ignition (LOI) was determined gravimetrically after heating at 1050 °C for 4 hours. Whole-rock rare earth elements (REE), and selected trace elements (Rb, Sr, Ba, Zr, Hf, Nb, Ta, Th, U and Y) for twenty-seven samples were determined on melted sample powders (glass chips) by laser-ablation inductively coupled plasma mass-spectrometry (LA-ICP-MS) using a ThermoFinnigan Element 2 at the MPI in Mainz (Stoll et al. 2008). The data of the whole-rock samples are shown in Appendix E-2 and the analyses of standard materials are listed in Appendix G-1.

Sm–Nd isotopes. Twenty-seven samples were chosen for Sm–Nd isotopic analysis. Chemical separation of Sm and Nd was carried out at the MPI in Mainz. About 70 mg of whole-rock powder was mixed with a ^{149}Sm–^{150}Nd tracer solution and dissolved in steel-lined Teflon vessels in a mixture of HF-$HClO_4$ for seven days at 180 °C, ensuring complete dissolution of refractory accessory mineral phases. Separation of Sm and Nd was performed using standard chromatographic procedures as described in White & Patchett (1984). Isotopic measurements were carried out at the MPI in Mainz and at the University of Munich, using Finnigan MAT 261 mass spectrometers. The ^{143}Nd/^{144}Nd ratios were corrected for thermal mass fractionation by normalization to ^{146}Nd/^{144}Nd = 0.7219. Repeated measurements of the La Jolla standard solution in Mainz yielded ^{143}Nd/^{144}Nd = 0.511832 ± 14 (2σ, n = 10). Analyses of an in-house Ames-Nd standard in Munich yielded ^{143}Nd/^{144}Nd = 0.512133 ± 12 (2σ, n = 2, equivalent to 0.511837 in La Jolla). Initial $\varepsilon_{Nd(t)}$-values were calculated using the present-day values for a chondritic uniform reservoir (CHUR) with ^{143}Nd/^{144}Nd = 0.512638 and ^{147}Sm/^{144}Nd = 0.1967 (Jacobsen & Wasserburg 1980). Nd model ages (t_{DM}) were calculated according to the single-stage model of DePaolo (1981) and are interpreted in terms of mean crustal residence ages (Arndt & Goldstein 1987). Two samples (M226 and M227) from the Shine Jinst metamorphic basement display unusually low ^{147}Sm/^{144}Nd ratios (e.g. <0.1), which may have resulted from fractionation of Sm and Nd during post-emplacement metamorphism. We can therefore not preclude some modification of the initial Sm/Nd ratios during this later event. However, the budget in REE of rocks that underwent medium- to high-grade metamorphism is considered to remain relatively unchanged (e.g. Condie et al. 1993) and we are therefore confident that the Sm–Nd systematics of the rock samples has not been disturbed significantly during post-emplacement metamorphism. In order to compensate for possible intracrustal fractionation effects, we recalculated the t_{DM} for these two samples using the two-stage model of Liew & Hofmann (1988). The Sm–Nd isotope data are listed in Appendix F-1.

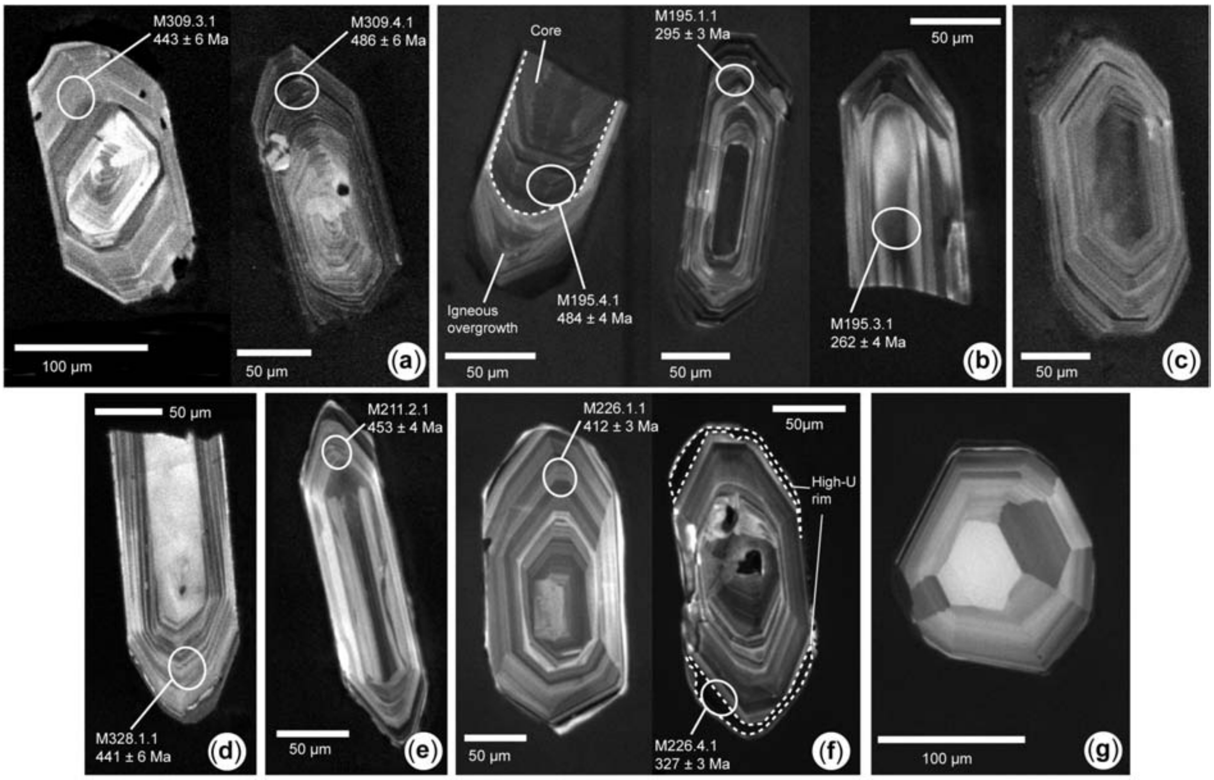

Fig. 5. Cathodoluminescence images of representative zircon grains analyzed in this study. The circles indicate the spots analyzed by SHRIMP. Age uncertainties are given at the 1σ confidence level; spot numbers refer to those listed in Appendix B-3. (**a**) Pyroclastic metarhyolite sample M309, Halbagant Range. (**b**) Rhyolite dyke sample M195, Halbagant Range. (**c**) Undeformed granodiorite sample M319, Halbagant Range. (**d**) Metadacite sample M328, Hulsnii Valley. (**e**) Coarse-grained granite gneiss sample M211, Shine Jinst area. (**f**) Medium-grained tonalitic gneiss sample M226, Shine Jinst area. (**g**) Fine-grained granodioritic gneiss sample M225, Shine Jinst area.

5. Petrography

The volcano-sedimentary sequences exposed within the Halbagant Range and the Hulsnii Valley underwent deformation and shearing at low metamorphic grade as indicated by greenschist-facies metamorphic assemblages (e.g. chlorite, calcite, quartz, epidote). Metabasalts are green in colour, mostly fine-grained, and consist of plagioclase, pseudomorphs of glomerophyric olivine, and relicts of pyroxene, set in a fine-grained intergranular matrix of plagioclase. Secondary minerals include albite, actinolite, epidote, Fe-Ti oxide and calcite. Pyroclastic rocks of intermediate composition such as meta-tuffs are fine-grained and show a slaty cleavage. They are mostly composed of plagioclase and biotite, frequently replaced by secondary calcite and sericite, and chlorite, respectively. The felsic metavolcanic rocks are mostly porphyritic with phenocrysts of K-feldspar variably altered to fine-grained sericite and biotite transformed into chlorite, all set in a fine-grained recrystallized matrix of equigranular quartz and plagioclase. Felsic pyroclastic rocks are medium- to fine-grained and typically show a large proportion of secondary calcite, chlorite and sericite defining the schistosity.

Metamorphic rocks exposed N of Shine Jinst village show a pervasive foliation and exhibit amphibolite-facies mineral assemblages. Mafic boudins are mostly fine-grained amphibolites with a lepidoblastic texture. They are composed of euhedral to subhedral amphibole, plagioclase and minor clinopyroxene, which are present in each sample in variable proportions. The most common felsic rock type is a medium-grained and strongly foliated granitoid gneiss composed of quartz, biotite, plagioclase, hornblende and minor K-feldspar. The most differentiated samples show a high proportion of K-feldspar. Quartz typically shows undulose extinction, and K-feldspar exhibits mostly microcline twinning. Secondary minerals include chlorite, sericite and epidote indicating a greenschist-facies metamorphic overprint.

6. U–Pb zircon geochronology and age interpretations

6.1. Halbagant Range

Sample M309 is a slightly deformed felsic pyroclastic rock collected in the central portion of the presumed early Devonian volcano-sedimentary sequence exposed across the Halbagant Range (Fig. 3a). The rock is composed of 75% clasts, mainly quartz (~ 85%) and plagioclase (~ 15%). Quartz typically shows undulose extinction, and plagioclase is moderately sericitized. The groundmass is fine-grained and mostly composed of recrystallized quartz and white mica. The latter defines the foliation wrapped around the clasts. Secondary minerals include calcite and sericite. Zircons are yellow to light brown, translucent, short-prismatic and idiomorphic. CL images show well-developed igneous oscillatory zoning (Fig. 5a) and the presence of inherited, resorbed cores in some grains. Five zircons were analysed on the Beijing SHRIMP II and provided a cluster of data points (Fig. 6a) with a weighted mean $^{206}Pb/^{238}U$ age of 441 ± 5 Ma (MSWD = 0.78). We interpret this early Silurian age as the time of emplacement of the pyroclastic rock and as currently the best age estimate for the volcano-sedimentary sequence at this locality. One additional grain of identical morphology and internal structure yielded a concordant analysis with a significantly older $^{206}Pb/^{238}U$ age of 486 ± 6 Ma (1σ; Fig. 6a). This older zircon is interpreted as a xenocryst, probably inherited from the surrounding basement rocks.

Sample M195 was collected about 500 m SE of sample M309 from a single 1 m wide rhyolite dyke cross-cutting at high-angle the surrounding low-grade volcano-sedimentary rocks. It consists of quartz, K-feldspar and plagioclase, set in a fine-grained matrix of quartz and plagioclase. Secondary minerals include sericite, epidote and minor calcite. Zircons are colourless to light yellow, mostly short-prismatic and euhedral. The grains have typical igneous oscillatory zoning and occasionally host inherited cores as documented by CL images (Fig. 5b). Eight zircons were analysed on the St. Petersburg SHRIMP II and produced a complex pattern with data scattered along the Concordia curve from c. 483 to 231 Ma (Fig. 6b). At the upper end of the spread, two spot analyses of zircon cores yielded similar results with a weighted mean $^{206}Pb/^{238}U$ age of 483 ± 6 Ma (Fig. 6b). Four spot analyses from magmatic zircon domains yielded a tight data cluster (Fig. 6b) with a weighted mean $^{206}Pb/^{238}U$ age of 293 ± 3 Ma (MSWD = 0.27). Two additional zircons with similar external and internal morphology yielded still younger $^{206}Pb/^{238}U$ ages of 262 ± 4 and 231 ± 2 Ma (1σ; Fig. 6b). At the upper end of the data range, the age of 483 ± 6 Ma is similar to that of the xenocryst from sample M309. We therefore interpret these grains as crystals from early Palaeozoic rocks that were inherited during the ascent and emplacement of the felsic magma. Consequently, we consider the early Permian age of 293 ± 3 Ma as reflecting the time of emplacement of this felsic dyke. However, we do not have a satisfactory explanation for the two younger ages of c. 262 and 231 Ma, which do not correspond to any known geological event in this area. They are unlikely to reflect a metamorphic overprint since the spot analyses were not located on metamorphic rims but in the centre of the grains.

Sample M319 is a coarse-grained, undeformed granodiorite and was collected from the granitoid pluton intruding the late Ordovician low-grade sequence to the W (Fig. 3a). The texture is mainly granoblastic and locally granophyric. The mineral assemblage consists of K-feldspar, plagioclase, quartz, large subhedral hornblende and minor biotite flakes. Feldspar is usually replaced by fine-grained sericite, and biotite is partly replaced by chlorite. Accessory minerals include apatite and zircon. Secondary minerals consist of chlorite and calcite-filled alteration veins. Zircons are transparent with a slight yellowish colour, idiomorphic and mostly long-prismatic with perfect crystal faces. CL images show regular oscillatory zoning typical of igneous growth (Fig. 5c). Irregular cores with convolute zoning are occasionally present and also visible under the binocular, and we excluded such grains for conventional U–Pb analysis. Four aliquots, each consisting of two grains, have been analysed from this sample. These aliquots define a cluster of data plotting close to the Concordia curve (Fig. 6c) with a weighted mean $^{206}Pb/^{238}U$ age of 345 ± 3 Ma (MSWD = 0.37) that we consider as the minimum age of emplacement for this granitoid body. This age indicates that the granitoid body is not Devonian as shown on the 1:200,000 Geological Map (Zabotkin 1988), but early Carboniferous.

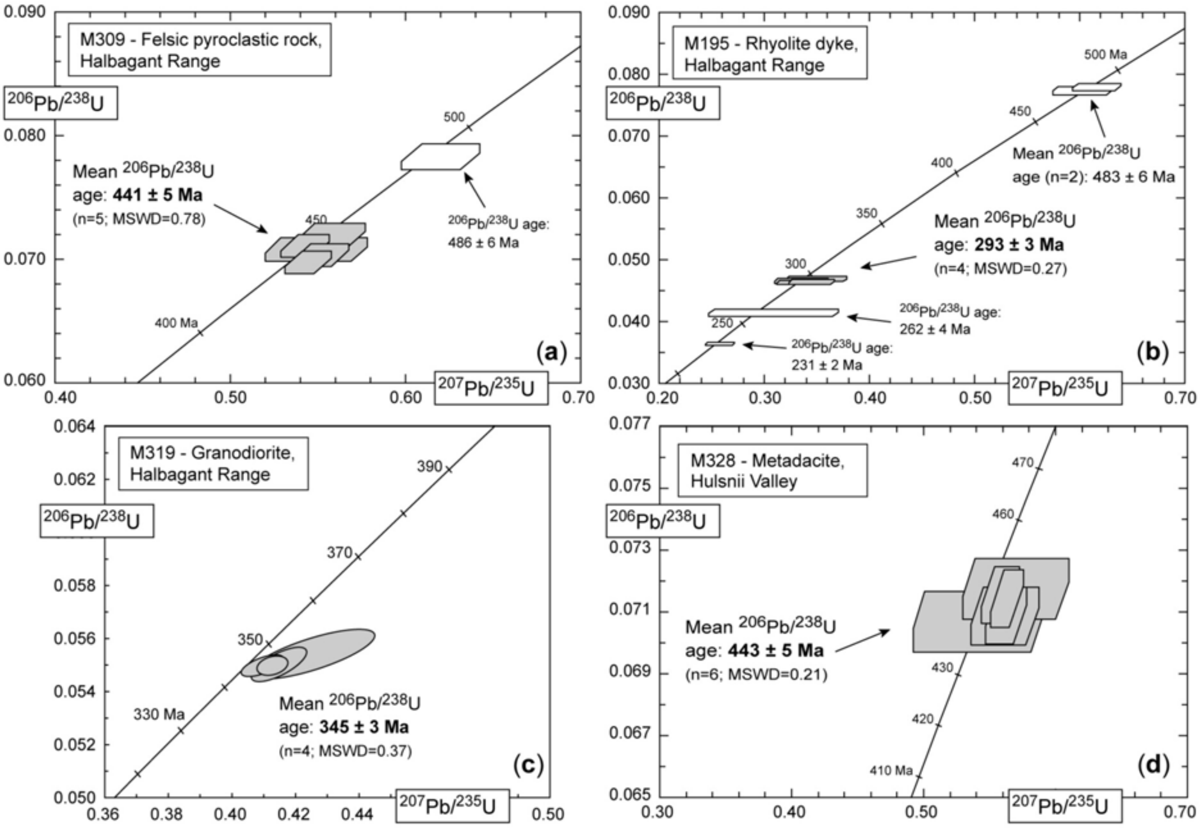

Fig. 6. Concordia diagrams showing the U–Pb data of zircon analysed for samples from the Halbagant Range (**a, b, and c**) and the Hulsnii Valley (**d**). (**a, b, and d**) SHRIMP analyses of single zircons; error boxes are defined by the standard errors in the ^{207}Pb/^{235}U, ^{206}Pb/^{238}U and ^{207}Pb/^{206}Pb ratios. (**c**) TIMS U–Pb zircon analyses. Errors for pooled ages are given at the 2σ confidence level.

6.2. Hulsnii Valley (Bayanleg Hatuu Range)

Sample M328 is a fine-grained felsic gneiss of dacitic composition, collected in the Hulsnii Valley (Fig. 3b). The rock is strongly foliated and composed of quartz, plagioclase, biotite, and minor relicts of anhedral hornblende. The foliation is underlined by biotite flakes and secondary sericite. Secondary minerals include sericite, epidote and minor calcite. The sample contains a homogeneous population of clear, transparent to slightly yellow, euhedral zircons with well-developed magmatic oscillatory zoning (Fig. 5d). Six grains were analysed in Beijing, and the spot analyses yielded overlapping and concordant results (Fig. 6d) with a weighted mean ^{206}Pb/^{238}U age of 443 ± 5 Ma (MSWD = 0.21) that we interpret to reflect the time of emplacement of the dacitic protolith. The entire sequence exposed along the Hulsnii Valley is shown as Carboniferous on the 1:200,000 Geological Map (Zabotkin 1988; see Fig.

3b). However, our zircon age does not corroborate this age assignment and is in better agreement with the early Silurian age reported by Helo et al. (2006) for a metagranite exposed W of our transect (Fig. 3b). This age is also virtually identical to the emplacement age of pyroclastic metarhyolite sample M309 from the previous locality, which probably reflects a single early Silurian volcanic event.

6.3. Shine Jinst area

Sample M211 is a well-foliated and medium-grained granite gneiss collected about 5 km N of Shine Jinst village and belongs to a presumed early Devonian metamorphic basement (Fig. 3c). It is composed of K-feldspar, plagioclase, quartz and relicts of small biotite flakes now preserved as chlorite. Secondary minerals include sericite and epidote. Zircon is the main accessory mineral, and grains are colourless, euhedral and long-prismatic with sharp terminations. CL images document distinct concentric oscillatory zoning (Fig. 5e) characteristic of an igneous origin. Five zircons were analysed on the St. Petersburg instrument and produced a cluster of similar and concordant data points (Fig. 7a) with a weighted mean $^{206}Pb/^{238}U$ age of 454 ± 4 Ma (MSWD = 0.19). We interpret this age to reflect the time of emplacement of the granitic protolith.

Sample M226 is a strongly foliated and coarse-grained orthogneiss of tonalitic composition, collected about 9 km N of Shine Jinst village and also belong to the presumed Devonian metamorphic basement (Fig. 3c). The rock contains plagioclase, quartz, relicts of brownish amphibole and minor biotite and K-feldspar. K-feldspar is partly replaced by sericite and occurs with quartz showing undulose extinction. Amphibole and biotite are mostly replaced by chlorite. Secondary minerals include sericite, minor calcite and epidote. Zircons are clear, long- to short-prismatic and idiomorphic. CL images reveal simple oscillatory zoning, related to magmatic growth, and show no evidence of older cores (Fig. 5f). Some grains display U-rich rims (dark in CL, Fig. 5f) that locally truncate the original igneous structures. Six zircons were analysed in St. Petersburg. Four spot analyses on four different zircons yielded identical results (Fig. 7b) with a weighted mean $^{206}Pb/^{238}U$ age of 415 ± 3 Ma (MSWD = 0.77) that we interpret as the time of emplacement of the granite-gneiss protolith. Analyses of U-rich rims from two separate grains yielded sub-concordant and younger $^{206}Pb/^{238}U$ ages of 380 ± 4 and 330 ± 3 Ma (1σ; Fig. 7b). Considering that these rims are relatively thin (<25 μm), it is possible that the results reflect mixed analyses. On the other hand, these high-U rims may have resulted from late-stage fluid-mineral interaction related to a hydrothermal event with percolation of U-rich fluids (e.g. Hoskin & Schaltegger 2003). This possibility is supported by the presence of undeformed pegmatitic veins locally observed close to this orthogneiss.

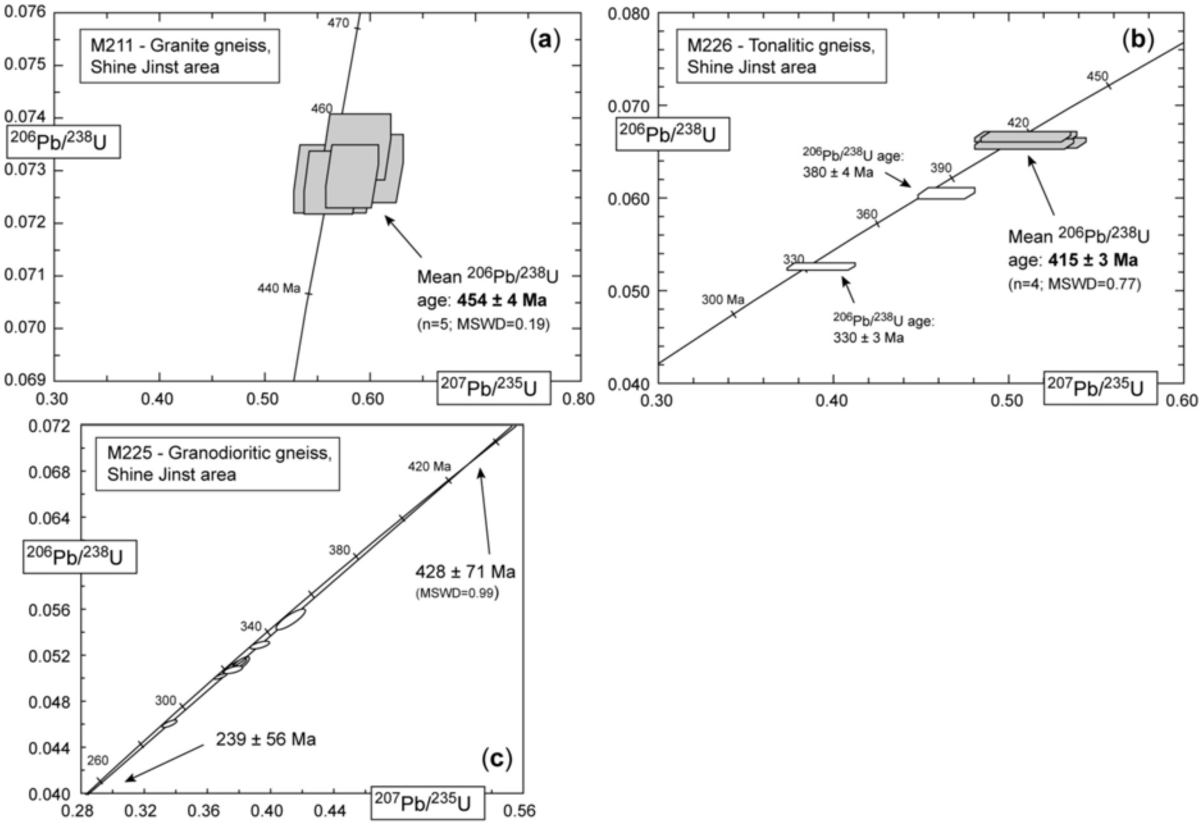

Fig. 7. Concordia diagrams showing the U–Pb data of zircon analysed for samples from the metamorphic basement exposed N of Shine Jinst. (**a, b**) SHRIMP analyses of single zircons; error boxes are defined as in Fig. 6. (**c**) TIMS U–Pb zircon analyses; errors for intercept ages are given at the 2σ confidence level.

Sample M225 is a granodioritic gneiss, also collected from the presumed early Devonian metamorphic basement N of Shine Jinst village (Fig. 3c). The rock is medium-grained and consists of plagioclase, K-feldspar, amphibole, quartz and minor biotite. Zircons are homogeneous in shape, clear, transparent, short-prismatic and idiomorphic. CL images show sector-zoned domains (Fig. 5g) and no inherited cores or metamorphic overgrowth. These zircons were analysed by the conventional U–Pb method. Eight aliquots consisting of two or three grains each are all slightly discordant (Fig. 7c). The data points define a regression line (MSWD = 0.99) yielding an imprecise upper Concordia intercept age of 428 ± 71 Ma and a lower intercept age at 239 ± 56 Ma. The large error in the intercept ages is due to the scatter of data points close to the concordia curve, and the upper intercept age is interpreted as the best estimate for the time of emplacement of the granodioritic protolith. The lower intercept age may be attributed to lead loss related to a regional metamorphic event. This age is identical, within error, to a ^{40}Ar/^{39}Ar plateau age of 295 ± 15 Ma obtained for an amphibolitic gneiss about 8.5 km SE of Shine Jinst village (Lamb et al. 2008), which may date the time of metamorphism of the early Devonian granitoid protoliths.

The zircon crystallization ages obtained for protoliths of granitoid gneisses M225 and M226 confirm that the most common rock type of the metamorphic basement N of Shine Jinst is early Devonian in age as shown on the 1:200,000 Geological Map (Fig. 3c; Zabotkin 1988). Compared to these samples, granite gneiss M211 yielded a much older late Ordovician protolith emplacement age. This sample was collected about 4 km S of the aforementioned sample M225 and may represent the country rock into which the early Devonian granitoids were emplaced or, alternatively, it may belong to a different tectonic sheet as also suggested by contrasting Nd isotopic data (see below).

7. Whole-rock chemical compositions

7.1. Major and trace element data

7.1.1. Sample alteration

Major and trace element abundances of whole-rock samples are listed in Appendix E-2. Most samples underwent greenschist- to amphibolite-facies metamorphism. Mafic and felsic samples from the Halbagant Range contain relatively high LOI values up to 9 wt%, consistent with large amounts of secondary water-bearing minerals as observed in thin section. Samples from the Shine Jinst area and the Bayanleg Hatuu Range have maximum LOI values of 3.7 and 2.2 wt%, respectively (average values of 1.4 and 1.3 wt%, respectively). Major elements such as Si, Na, Ca, and K and the trace elements Rb, Ba, and U are fluid-mobile and easily mobilized during late and/or post-magmatic processes (including hydrothermal alteration and/or metamorphic overprint). Their concentrations may therefore not reflect primary compositions (e.g. Bach et al. 2001). However, high-field strength elements (HFSE) such as Zr, Nb, Ta, Y, Ti, Hf, Th, and the REE are usually considered immobile and less affected by alteration at low- to medium-grade metamorphism (Pearce & Cann 1973; Münker et al. 2004). The discussion of the petrogenesis of the meta-igneous rocks will thus largely be based on these immobile elements, including the Sm–Nd isotopic data.

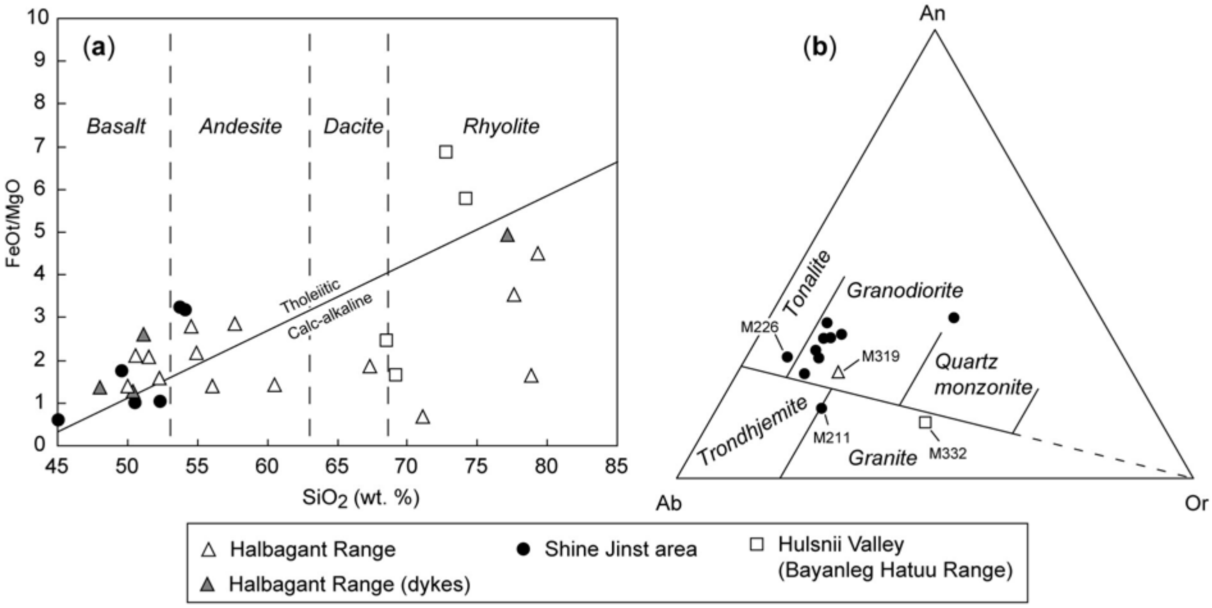

Fig. 8. (**a**) FeOt/MgO vs. SiO_2 diagram showing volcanic rock samples (modified after Miyashiro 1974) and (**b**) Anorthite-Albite-Orthoclase diagram for granitoid samples (granitoid fields after O’Connor 1965) from the Halbagant Range, Hulsnii Valley, and Shine Jinst area. Data were recalculated to anhydrous compositions to facilitate comparison of the samples.

7.1.2. Halbagant Range

The mafic meta-volcanic rocks of the Halbagant Range have SiO_2 contents of 50–60 wt% indicating basaltic to andesitic compositions. Most of the basaltic samples are tholeiitic as can be seen in the FeOt/MgO vs. SiO_2 classification diagram (Fig. 8a), except for the andesitic samples M307 and M315 which show calc-alkaline affinities. All basaltic to andesitic samples are moderately differentiated as indicated by Mg# (Mg-number = 100xMgO/(MgO+FeOt) molar proportion) of 37 to 54 and low Cr and Ni contents (14–200 ppm and 15–112 ppm, respectively). Their TiO_2 contents are high and range from 1.5 to 2.1 wt%, except for the calc-alkaline meta-andesite M307 with a lower content of 0.6 wt%. The Ti/V ratios of basaltic samples range from 34 to 48 and are comparable to those in mid-ocean ridge basalts (MORB; Shervais 1982). Chondrite-normalized REE patterns of representative samples are shown in Fig. 9a. All samples have similar patterns characterized by little enrichments of the light REE (LREE) over to the heavy REE (HREE; Ce_N/Yb_N = 1.6–2.6). The almost flat HREE patterns (Dy_N/Yb_N = 1.1–1.2) resemble MORB patterns and preclude melting in the garnet-stability field. Small negative Eu anomalies (Eu/Eu* = 0.8–0.9) indicate some plagioclase fractionation during melt evolution. Their primitive mantle (PRIMA)-normalized trace-element patterns are slightly to moderately enriched in Th relative to the LREE and show small negative concentration anomalies for Nb and Ti and positive ones for Zr (Fig. 9a).

The intermediate to felsic metavolcanic rocks have calc-alkaline dacitic to rhyolitic compositions (Fig. 8a) with SiO_2 contents of about 64 to 76 wt%. As suspected from petrographic observations, a large scatter is observed for most major elements easily mobilized during alteration processes. This is particularly evident for samples with high porosity such as the pyroclastic rocks (e.g. M309 and M311), which show high LOI and CaO concentrations correlated with low K_2O.

(**a**) Halbgant Range, mafic metavolcanic rocks

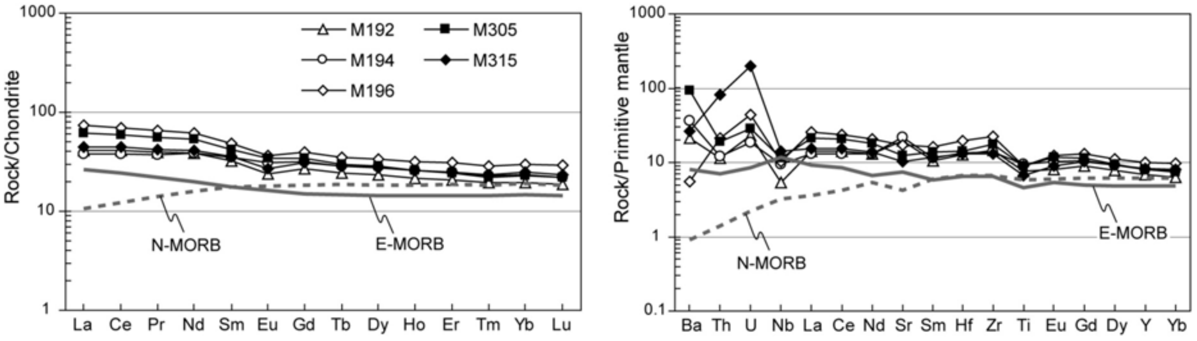

(**b**) Halbgant Range, felsic metavolcanic rocks

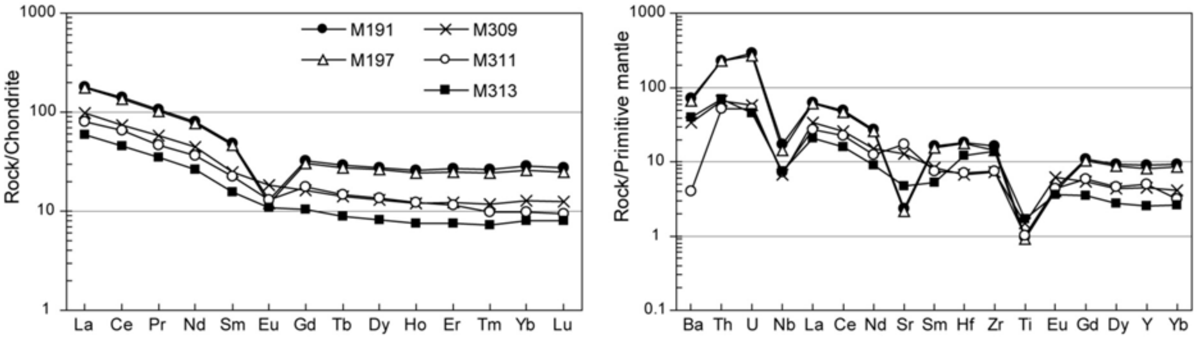

(**c**) Halbagant Range, rhyolite dyke

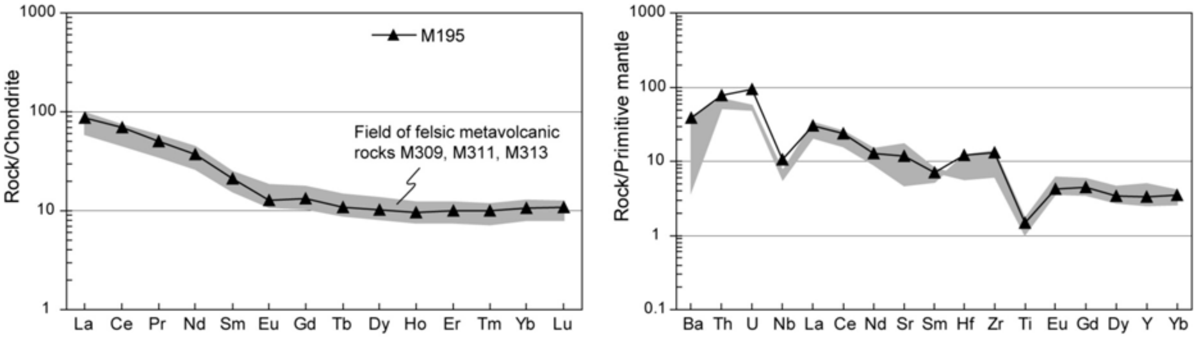

Fig. 9. REE and trace element patterns for representative metavolcanic rocks from the Halbagant Range. Chondrite and primitive mantle normalizing values are from McDonough & Sun (1995) and Sun & McDonough (1989), respectively. Data for E- and N-MORB are from Sun & McDonough (1989).

Pyroclastic metarhyolites M309, M311, and metarhyolite M313 display similarly fractionated REE patterns (Ce_N/Yb_N = 5.7–6.7) with flat HREE distribution (Dy_N/Yb_N = 1.0–1.4) and small negative Eu anomalies (Eu/Eu* = 0.7–0.9)(Fig. 9b). They display typical subduction-related trace-element patterns with enrichments in large ion lithophile elements (LILE) relative to the LREE, well-developed negative anomalies for Nb and Ti, and slightly positive anomalies for Sr compared to neighbouring elements (Fig. 9b). Metarhyolites M191 and M197 are different from the other samples in that they display much higher concentrations of incompatible elements. The large negative anomalies for Sr and Eu (Eu/Eu* = 0.3)(Fig. 9b) are consistent with significant plagioclase fractionation and/or melting of sources with residual feldspar.

The early Permian dyke M195, cross-cutting the late Ordovician metavolcanic rocks, has a rhyolitic, calc-alkaline composition (Fig. 8a) and is metaluminous as indicated by $Al_2O_3/(CaO+Na_2O+K_2O)$ and $Al_2O_3/(Na_2O+K_2O)$ molecular ratios of 0.7 and 1.5, respectively. This sample shows a moderately fractionated REE pattern with a slightly negative Eu anomaly, enrichment of LILE over the LREE and negative Nb and Ti anomalies (Fig. 9c). Overall, this sample has similar trace-element characteristics as the pyroclastic felsic samples M309, M311, and M313 (Fig. 9c).

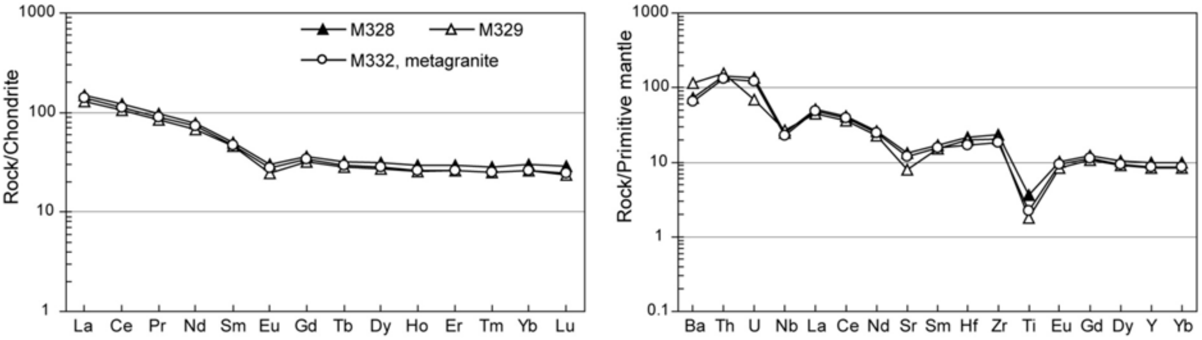

Fig. 10. REE and trace element patterns for representative felsic metaigneous rocks from the Hulsnii Valley, Bayanleg Hatuu Range. Sources of chondrite and primitive mantle normalizing values as in Fig. 9.

7.1.3. Hulsnii Valley (Bayanleg Hatuu Range)

The felsic metaigneous rocks from the Hulsnii Valley range in SiO_2 contents from 65 to 73 wt% and are mostly calc-alkaline in composition (Fig. 8a). Meta-dacite M328 and metarhyolite M329 have very similar trace element concentrations and show moderately fractionated REE patterns (Fig. 10, Ce_N/Yb_N = 4.0–4.3), distinct negative Eu anomalies (Eu/Eu* = 0.6–0.7) and flat HREE patterns. Their PRIMA-normalized trace element patterns show characteristic subduction-related signatures with enrichment in Th, Ba, U and LREE (Fig. 10). Other features include well-developed negative anomalies for Nb, Ti and Sr.

Metagranite M332 has a calc-alkaline composition and is slightly peraluminous as indicated by A/CNK and A/NK ratios of 1.1 and 1.4, respectively. This sample displays broadly similar trace element patterns as the felsic meta-volcanic samples M328 and M329 (Fig. 10).

7.1.4. Shine Jinst area

The amphibolite samples are mostly tholeiitic with two samples showing a transitional tholeiitic/calc-alkaline affinity (Fig. 8a). Their SiO_2 contents range from 45 to 54 wt%. The tholeiitic/calc-alkaline basaltic amphibolites have Ti/V ratios of 18 to 40 which overlap the fields of island arc basalts and MORB (Shervais 1982). Amongst these, amphibolite M212 exhibits very high MgO (17.7 wt%), Cr and Ni (1278 and 598 ppm, respectively) concentrations combined with a high Mg# of 76, indicating that this sample is an olivine cumulate rock and does not represent a melt composition. Interestingly, this sample shows depletion in LREE from Nd to La, whereas the other REE are sub-parallel to those in the associated samples (Fig. 11a). Accumulation of LREE-depleted pyroxene in this sample as could be assumed from the very high Cr concentration (c. 1300 ppm) is unlikely as the Sc concentration is similar to those in the other samples. As olivine discriminates against the REE and particularly the LREE, it also cannot explain the depletion from Nd to La. Yet it can be assumed that the unusual depletion of La to Nd may be due to loss of the LREE during metamorphism. All amphibolite samples display slight to moderate enrichment of the LREE over the HREE (Ce_N/Yb_N = 1.1–3.8) and nearly flat HREE patterns (Fig. 11a).

The extended trace element patterns of all amphibolite samples show slight to moderate depletion in Nb and Th compare to the LREE, whereas fluid-mobile elements such as Ba and U are enriched. Sr concentrations show an erratic behaviour, probably due to the mobility of this element. In summary, the protoliths of the mafic gneisses are apparently chemically little evolved tholeiitic to mildly calc-alkaline subduction-related igneous rocks.

The granitoid gneisses have SiO_2 contents of 67 to 82 wt% and display predominantly granodioritic to granitic compositions (Fig. 8b). All samples are metaluminous as indicated by A/CNK and A/NK ratios of 0.5–1.0 and 1.7–2.1, respectively. At similar degrees of differentiation, most samples display homogeneous major and trace element concentrations. Their REE patterns are sub-parallel with moderate enrichment in LREE over the HREE (Ce_N/Yb_N = 2.5–7.9) and minute negative Eu anomalies (Eu/Eu* = 0.7–0.8). They display well-developed subduction-related features reflected by enrichment in the LILE over the LREE as well as pronounced negative Nb and Ti troughs (Fig. 11b).

(a) Shine Jinst area, amphibolites

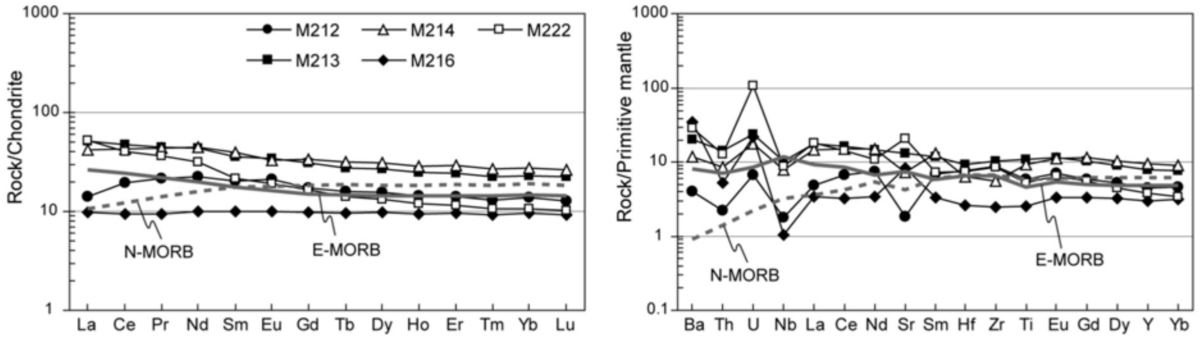

(b) Shine Jinst area, granitoid gneisses

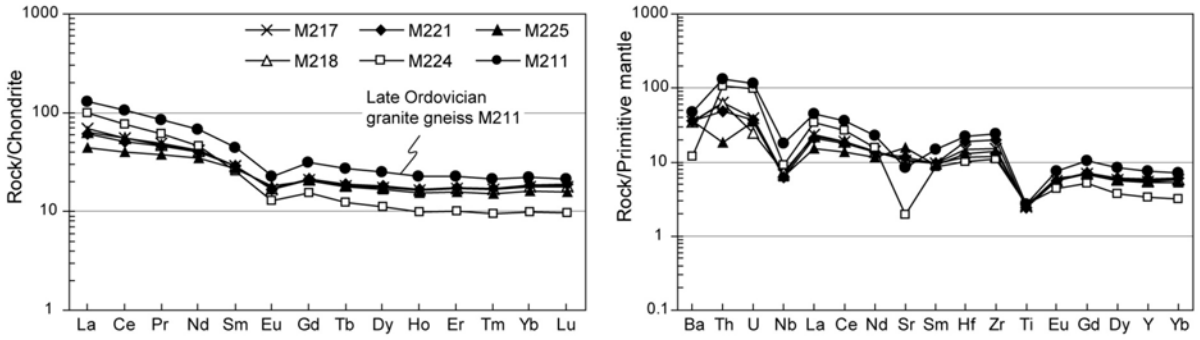

(c) Shine Jinst area, granitoid gneisses

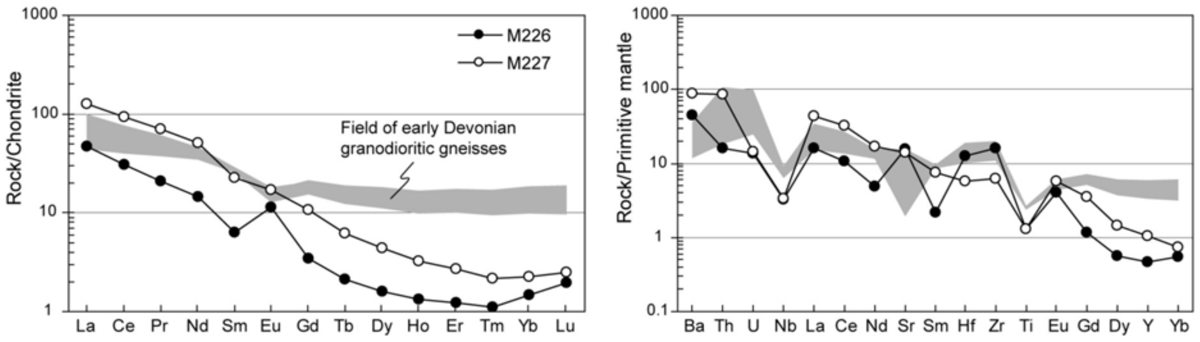

Fig. 11. REE and trace element patterns for representative rocks from the metamorphic basement exposed N of Shine Jinst village. Sources of chondrite and primitive mantle normalizing values as in Fig. 9. Data for E- and N-MORB patterns are from Sun & McDonough (1989).

Samples M226 and M227 show tonalitic and granodioritic compositions in the An–Ab–Or triangular diagram (Fig. 8b). When compared to the other granodioritic gneisses, these two samples are distinguished by lower Nb concentrations (2.5–2.4 ppm) and strongly fractionated REE patterns (Fig. 11c; Ce_N/Yb_N = 18.3–42.2). Both samples show positive Sr and Eu anomalies (Eu/Eu* = 1.1–2.5) consistent with plagioclase accumulation. The concave shape of the HREE for sample M226 (Fig. 11c) suggests significant amphibole fractionation

(Green 1980). In addition, these two samples have fractionated Gd/Er ratios and very low Y (2.3–4.8 ppm) and HREE concentrations (e.g. Yb = 0.29–0.36 ppm), consistent with melting of mafic protoliths with residual garnet.

7.2. Sm–Nd isotopic data

Sm–Nd isotopic analyses for twenty-seven samples are listed in Appendix F-1. For each locality the initial ε_{Nd}-values [$\varepsilon_{Nd(t)}$] were calculated according to the zircon ages presented above, unless stated otherwise. The initial ε_{Nd}-values are plotted in Fig. 12 against ^{147}Sm/^{144}Nd ratios.

The initial Nd isotopic compositions of mafic and felsic metavolcanic rocks from the Halbagant Range were calculated for an age of 441 Ma. The $\varepsilon_{Nd(t)}$-values for mafic samples from this locality are highly positive and range from +4.6 to +8.0 (Fig. 12a). Metabasalts M192 and M194 have the most radiogenic Nd isotopic signatures with strongly positive $\varepsilon_{Nd(t)}$-values of c. +8.0 as in the depleted mantle at c. 450 Ma (Fig. 12a). Metabasalt M305 and metaandesites M196 and M315 display lower $\varepsilon_{Nd(t)}$-values of c. +5.0 (Fig. 12a). These variation in $\varepsilon_{Nd(t)}$ may suggest melting of a heterogenous and variably depleted upper mantle source.

The overall uniformly depleted upper mantle sources for the metabasalts and metaandesites are contrasted by a large variation of positive and negative $\varepsilon_{Nd(t)}$-values of +3.8 to -4.8 in the felsic samples (Fig. 12a). Metarhyolites M191 and M197 have similar and positive $\varepsilon_{Nd(t)}$-values of +3.8 and +4.0 with mean crustal residence ages of c. 0.7 Ga. The other felsic metavolcanic samples display heterogeneous and negative $\varepsilon_{Nd(t)}$-values of -4.8 to -0.9 with mean crustal residence ages of c. 1.3 to 1.0 Ga. These data indicate melting of highly heterogeneous crustal sources comprising juvenile as well as much older crust during the early Silurian igneous event.

The initial Nd isotopic composition of rhyolite dyke M195, cross-cutting the early Silurian volcano-sedimentary sequence, was calculated for an intrusion age of 293 Ma. This sample yielded an $\varepsilon_{Nd(t)}$-value of -2.6 and a mean crustal residence age of c. 1.0 Ga. This indicates the involvement of relatively old and isotopically enriched crustal material during the petrogenesis of this rock. This hypothesis is also supported by zircon xenocrysts in this sample with crystallization ages of c. 486 Ma, which suggest assimilation of early Ordovician material.

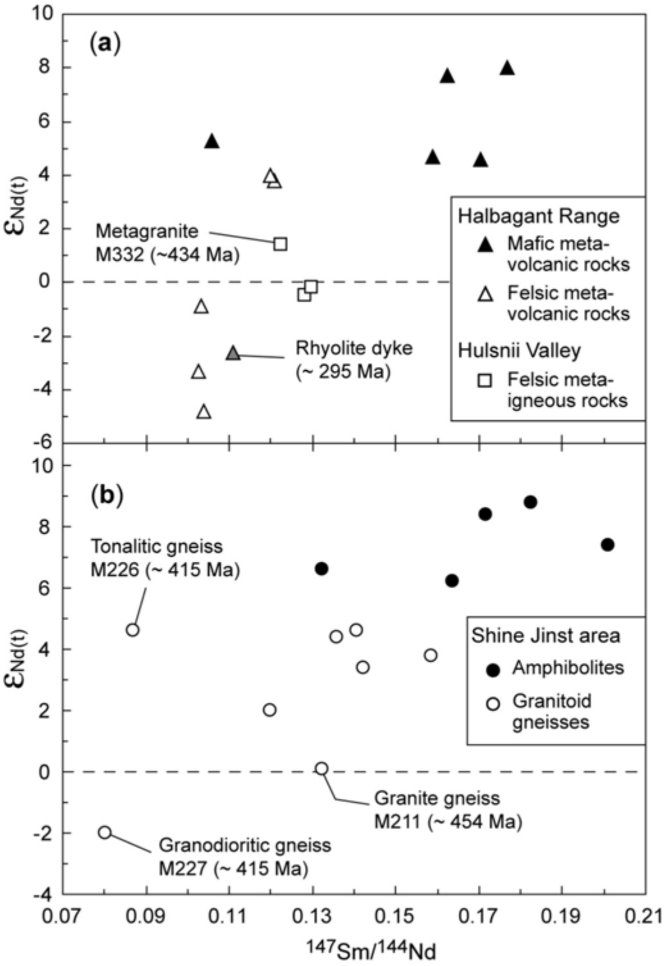

Fig. 12. Initial ε_{Nd}-values vs. $^{147}Sm/^{144}Nd$ ratios for meta-igneous rocks from (**a**) the Halbagant Range and Hulsnii Valley, and (**b**) the Shine Jinst area. The data for the early Silurian mafic metavolcanic rocks (Halbagant Range) and the early Devonian amphibolites (Shine Jinst area) indicate depleted upper mantle sources. The data for the early Silurian felsic metaigneous rocks (Halbagant Range/Hulsnii Valley) indicate mixed sources including juvenile and older crustal material, whereas those for the early Devonian felsic granitoid gneisses (Shine Jinst area) indicate mostly juvenile crustal sources.

The initial Nd isotopic compositions of metadacite M328 and metarhyolite M329 from the Hulsnii Valley were calculated for an emplacement age of 443 Ma. These samples yielded $\varepsilon_{Nd(t)}$-values of -0.5 and -0.2 (Fig. 12a) and mean crustal residence ages of c. 1.1 Ga. As for felsic samples from the Halbagant Range, this indicates melting of a significant amount of older crustal material. The initial Nd isotopic composition of metagranite M332 was calculated for an age of 434 Ma according to the zircon age obtained by Helo et al. (2006) for the same intrusion (Fig. 4c). This sample yielded a $\varepsilon_{Nd(t)}$-value of +1.3 and a mean crustal residence age of c. 0.9 Ga, which again suggests an origin of the granitic protolith from a crustal source comprising juvenile and much older crustal material.

For the amphibolites and granitoid gneisses of the Shine Jinst area (except for sample M211), the initial Nd isotopic compositions were calculated for an emplacement age of 415 Ma. The amphibolites exhibit strongly positive $\varepsilon_{Nd(t)}$-values of +8.8 to +6.2 (Fig. 12b), indicating a highly depleted upper mantle source. The transitional tholeiitic to calc-alkaline amphibolite M222 yielded a $\varepsilon_{Nd(t)}$-value of +6.6 (Fig. 12b) not much different from the values of the tholeiitic amphibolites. This corroborates similar sources and origins for the amphibolite suite of this locality.

The granodioritic gneisses yielded $\varepsilon_{Nd(t)}$-values of +2.0 to +4.6 (Fig. 12b), and their corresponding mean crustal residence ages range from c. 0.9 to 0.7 Ga. This indicates that the gneiss protoliths were mostly derived from juvenile material with little admixture of older crustal material. We note that sample M226 has a low Sm/Nd ratio when compared to typical average crustal values, and it is therefore likely to have experienced post-crystallization modification, probably during the metamorphic event leading to deformation of its protolith. It shows Nd isotopic characteristics comparable to those of the granodioritic gneisses with an $\varepsilon_{Nd(t)}$-value of +4.6 (Fig. 12b) and a mean crustal residence age of c. 0.8 Ga (two-stage Nd model age). The leucocratic metagranite M227 yielded a negative $\varepsilon_{Nd(t)}$-value of -2.0 (Fig. 12b) and a much older mean crustal residence age of c. 1.3 Ga (two-stage Nd model age), indicating input of a significant amount of old crustal material in the generation of the granite protolith. As noted for sample M226, the Sm/Nd ratio is lower than typical average crustal values and suggests post-emplacement alteration during a later metamorphic event.

Granite gneiss M211, with a protolith emplacement age of 454 Ma, also yielded a low $\varepsilon_{Nd(t)}$-value of 0.1 (Fig. 12b) and a relatively old mean crustal residence age of c. 1.1 Ga. As in the early Silurian felsic samples from the Halbagant Range and the Hulsnii Valley, these data suggest input of some juvenile material in the generation of the gneiss protolith, with admixture of a significant amount of older crustal material.

8. Interpretation of geochemical and Nd isotopic data

8.1. Mafic to intermediate metaigneous rocks

Halbagant Range. Early Silurian metabasalt and metaandesite samples from the Halbagant Range display an enrichment in fluid-soluble elements and negative Nb and Ti anomalies as typically found in rocks from subduction-related environments (McCulloch & Gamble 1991; Woodhead et al. 1993). These samples have juvenile Nd isotopic signatures with $\varepsilon_{Nd(t)}$-values covering a range from +4.6 to +8.0 and indicating an origin from moderately to highly depleted mantle sources. Arc-related magmas usually display large trace-element and isotopic variability inherited (1) from the mantle wedge from which they originated by partial melting and (2) from fluids and/or melts released by the subducted oceanic crust and overlying sediments (Woodhead et al. 1993; Pearce & Peate 1995; Münker et al. 2004; Plank 2005). Th/Nb and Th/La ratios may be used as tracers of sediment components in the source of island-arc related magmas (e.g. Johnson & Planck 1999; Plank 2005) because (1) Th and the LREE (e.g. La) are enriched in sediments (Johnson & Planck 1999) and (2) the HFSE (e.g. Nb) and HREE are usually considered to be relatively immobile during subduction metasomatism (Ayers et al. 1997) and are not significantly enriched in pelagic sediments (Plank & Langmuir 1998). Fig. 13 illustrates the behaviour of Th and Nb normalized to the HREE Yb in order to reduce the effect of fractional crystallization and crystal accumulation (Pearce & Peate 1995). Most metavolcanic rocks from the Halbagant Range define a cluster of data (Fig. 13a) with elevated Th/Nb ratios of 0.15–0.26 and Th/La ratios of 0.10–0.11 when compared to N-type MORB (e.g. Th/Nb and Th/La of c. 0.05; Hofmann 1988). This relationship suggests melting of mantle sources with a significant amount of subducted sediment. Metaandesite M315 shows a much higher Th/La ratio of 0.66 and a Th/Nb ratio of 0.70 (Fig. 13a), similar to the value of average arc basalt (e.g. Th/Nb of c. 0.53; McCulloch & Gamble 1991). This suggests an even larger amount of melted sediment as indicated in the other samples.

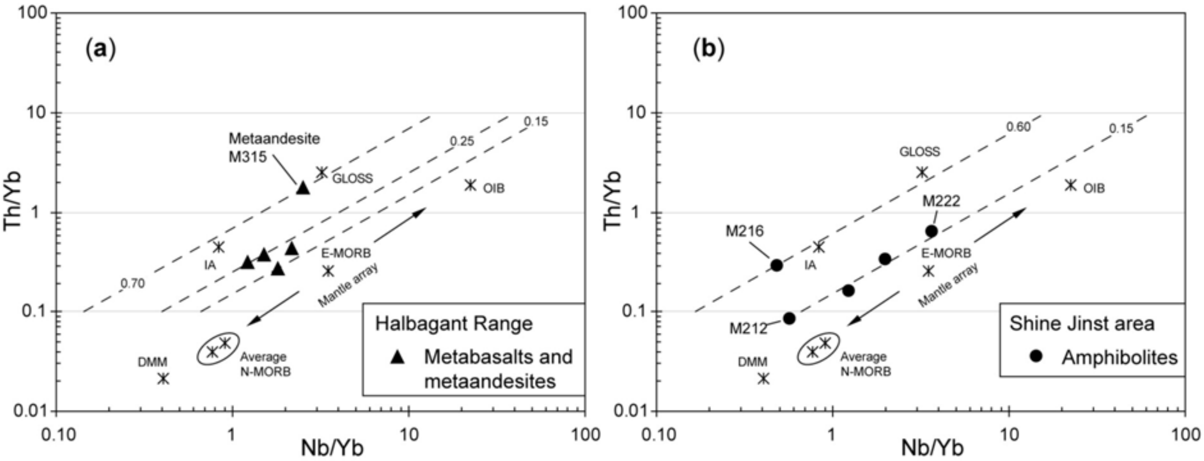

Fig. 13. Th/Yb vs. Nb/Yb ratios for (**a**) early Silurian mafic metavolcanic rocks from the Halbagant Range, and (**b**) early Devonian amphibolites from the Shine Jinst area. E-MORB and OIB data from Sun & McDonough (1989); N-MORB data from Hofmann (1988) and Sun & McDonough (1989); IA data from McCulloch & Gamble (1991); DMM data from Workmann & Hart (2005); GLOSS (global subducting sediment) data from Plank & Langmuir (1998). Dashed lines represent same Th/Nb ratios with values indicated by numbers. The data for both early Silurian and early Devonian mafic metaigneous rocks suggest presence of variable amount of slab-derived components in their depleted upper mantle sources.

Shine Jinst area. Early Devonian tholeiitic to mildly calc-alkaline amphibolite samples from the Shine Jinst area display subduction-related chemical fingerprints such as low Nb relative to La and enrichment of U and Ba relative to the LREE. All amphibolites have high $\varepsilon_{Nd(t)}$-values of +6.2 to +8.8, which provide compelling evidence for an origin from a time-integrated LREE-depleted upper mantle reservoir. Most amphibolites have uniform and low Th/Nb ratios of 0.13–0.17 and Th/La ratios of 0.06–0.10 and define a trend sub-parallel above the N-MORB – OIB array (Fig. 13b). This trend suggests the presence of a small and similar amount of slab-derived component (sediment melt and/or siliceous component of an aqueous fluid) in their mantle source (Pearce & Peate 1995; Leat et al. 2004). Amphibolite M212 has a Nb/Yb ratio of 0.6 and may be interpreted as being derived from an N-MORB-type source that was slightly overprinted by a subduction-related component. By comparison, amphibolite M216 has a similar Nb/Yb ratio of 0.5 but shows a higher amount of sediment as reflected by higher Th/Nb and Th/La ratios of 0.59 and 0.19, respectively.

Tectonomagmatic setting. Finally, certain key elements, with coherent behaviour in specific environments (e.g. the HFSE and to a lesser extent the LREE), have been widely used as tectonic indicators (Wood 1980; Cabanis & Lecolle 1989). However, these ‘tectonic discrimination diagrams’ were established with rocks from modern plate tectonic settings, and caution needs to be exercised when they are applied to ‘ancient’ rocks. The Th–Zr–Nb ternary diagram of Wood (1980) is one of these diagrams for mafic rocks (Fig. 14). The diagram is not intended to assign a specific tectonic setting to the samples of this study but is useful to illustrate some of their geochemical features.

The early Silurian metabasalts and metaandesites from the Halbagant Range plot in the field of mafic rocks from immature (tholeiitic) and mature (calc-alkaline) island arcs (Fig. 14). Most samples are concentrated in the field of tholeiitic basalts, except for metaandesite M315 which plots in the field of calc-alkaline basalts (Fig. 14). The early Devonian amphibolite samples from the Shine Jinst area plot mostly towards the Th apex of the diagram, which corroborates a subduction environment as discussed above (Fig. 14). In summary, the chemical and isotopic evidence for early Silurian and early Devonian mafic metaigneous rocks suggest that an arc component played a significant role in their genesis. The Nd isotopic compositions indicate an absence or only minor involvement of older crust. We speculate that these samples most likely formed through melting of a variably depleted sub-arc mantle at a magmatic arc front.

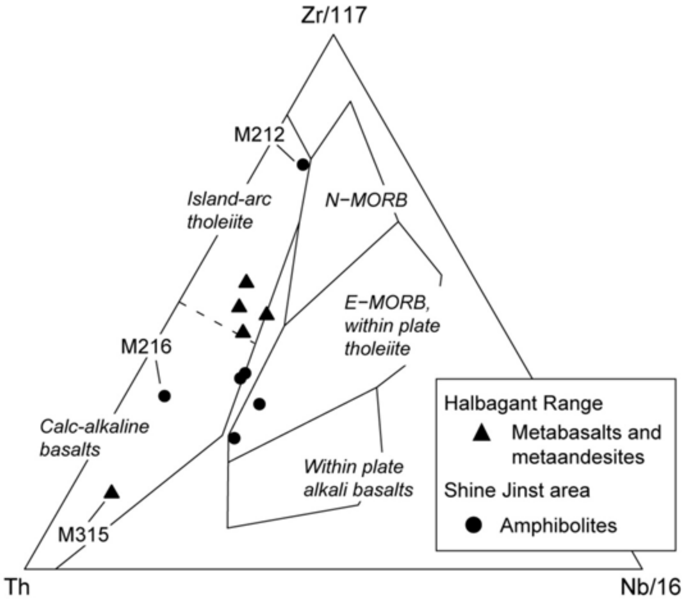

Fig. 14. Th–Zr–Nb ternary diagram (modified after Wood 1980) for mafic meta-igneous rock samples from the Halbagant Range and Shine Jinst area. The data for early Silurian (Halbagant Range) as well as early Devonian (Shine Jinst area) mafic metaigneous rocks suggest predominantly arc-related chemical features.

8.2. Felsic metaigneous rocks

Regardless of their time of emplacement and location in the study area, the felsic metaigneous rocks display typical trace element characteristics of igneous rocks generated at convergent plate margins (Pearce & Peate 1995). The $\varepsilon_{Nd(t)}$-values for the early Silurian and early Devonian felsic metaigneous rocks are shown in a Nd isotopic evolution diagram in Fig. 15. The overall picture emerging from the Nd isotopic data suggest that the rocks of the Halbagant/Bayanleg Hatuu Ranges, on the one hand, and the granitoid gneisses from the Shine Jinst area on the other hand comprise different proportions of an older crustal component, e.g. the Shine Jinst section may represent an oceanward overall more juvenile Andean-type margin, whereas the Halbagant/Bayanleg Hatuu sections are more “cratonic” in composition. Below these inferences are explained in more detail.

Halbagant/Bayanleg Hatuu Ranges. The early Silurian felsic metaigneous rocks of the Halbagant Range and the Hulsnii Valley (Bayanleg Hatuu Range) have ^{147}Sm/^{144}Nd ratios of 0.10 to 0.12 that are comparable to those in mature continental crust (Taylor & McLennan 1985). Their $\varepsilon_{Nd(t)}$-values are heterogeneous and vary from -4.8 to +3.8 (Fig. 15), and their mean crustal residences ages range from c. 1.3 to 0.7 Ga. These data provide evidence for melting of a composite arc crust including juvenile mantle-derived material and much older crustal material with average crustal residence ages up to c. 1.3 Ga. These chemical features are similar to those found in Andean-type arc environments where magma pounding and AFC processes at lower to middle crustal levels produce variable degrees of magma mixing with older crustal material (Wilson 1989). There is as yet no direct evidence that these early Palaeozoic magmatic sequences were emplaced into an older basement, although zircon xenocrysts from the early Silurian pyroclastic metarhyolite M309 and the early Permian rhyolite dyke M195 from the Halbagant Range indicate assimilation of crustal material dating back to the early Ordovician. However, these localities are immediately SW of the Precambrian Gurvan Bogd Mountains (Fig. 2) where geochronological data from the Baga Bogd Massif (Fig. 2) indicate the presence of a Mesoproterozoic basement that underwent a phase of early Neoproterozoic plutonism from c. 983 to 954 Ma (Demoux et al. 2009a). Thus, the early Silurian felsic metaigneous rocks have Nd model ages (c. 1.3–0.7 Ga) similar to the age pattern of the Lake zone basement rocks (c. 1.52–0.95 Ga). The highly variable Nd isotopic compositions and Nd model ages of felsic metaigneous rocks therefore suggest possible derivation from the Meso- early Neoproterozoic Lake zone material, reworked and mixed with variable proportion of juvenile material during the early Silurian orogeny. We speculate that the early Silurian rock assemblages from the Halbagant/Bayanleg Hatuu Ranges were emplaced at an Andean-type continental margin developed on top of the Precambrian Lake zone basement.

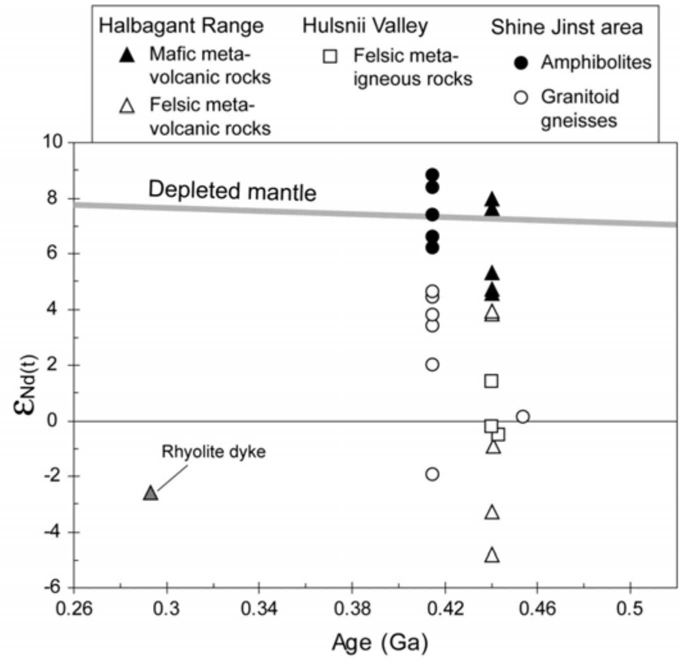

Fig. 15. Nd-isotope evolution diagram showing the data of this study. Depleted mantle line after DePaolo (1981).

Shine Jinst area. The early Devonian metaluminous granitoid gneisses from the Shine Jinst area are predominantly granodioritic in composition and show marked calc-alkaline chemical compositions. Most samples have somewhat higher $^{147}Sm/^{144}Nd$ ratios (i.e. their LREE patterns are less fractionated) than those from the Halbagant/Bayanleg Hatuu Ranges, and comparable to those of average crustal values (Taylor & McLennan 1985). Samples M226 and M227, likely derived from garnet-bearing sources, show very low ^{147}Sm/^{144}Nd ratios of 0.0861 and 0.0801 (Fig. 12b), respectively. For these two samples, the Nd model ages were calculated according to the two-stage isotope evolution model of Liew & Hofmann (1988) in order to compensate for the extreme LREE fractionation.

Most metagranitoid samples (except sample M227) yielded juvenile Nd isotopic systematics (Fig. 15) characterized by $\varepsilon_{Nd(t)}$-values of +2.0 to +4.6 and mean crustal residence ages of c. 0.9 to 0.7 Ga, which provide evidence for melting of a predominantly juvenile arc crust with little admixture of old crustal material. By contrast, metagranite sample M227 yielded Nd isotopic data ($\varepsilon_{Nd(t)}$ of -2.0 and t_{DM} of c. 1.3 Ga) similar to those of the late Ordovician granite gneiss M211 ($\varepsilon_{Nd(t)}$ of 0.1 and t_{DM} of c. 1.1 Ga) from the same locality and to those of the early Silurian felsic metaigneous rocks from the Halbagant/Bayanleg Hatuu Ranges ($\varepsilon_{Nd(t)}$ of -4.8 to -0.2 and t_{DM} of c. 1.3–1.1 Ga). Combined with the chemical characteristics and strongly depleted Nd isotopic data displayed by the mafic gneisses samples from the same locality (see previous section), we propose that the early Devonian protoliths of the granitoid gneisses of the Shine Jinst area represent the lower plutonic portion of the outboard located segment of the late Ordovician/early Silurian Andean-type plate margin.

9. Discussion

A variety of conflicting geodynamic models have been proposed for the Palaeozoic evolution of the CAOB in southern Mongolia (Zonenshain 1967, 1973; Zonenshain et al. 1990; Ruzhentsev & Pospelov 1992; Şengör et al. 1993; Zorin et al. 1993; Dergunov 2001; Ruzhentsev 2001; Badarch et al. 2002). The present study covers areas which have not previously been examined or reported in the literature in great detail. The geochronological and geochemical data presented here enable us to better constraint the likely tectonic setting of the Gobi-Altai region prevalent during the middle Palaeozoic.

Within the northern Gobi-Altai region, Ordovician and Silurian deposits, such as those exposed immediately N of Bayantsagaan (Fig. 2), were traditionally interpreted as intracontinental trough deposits (rift basins) related to rifting of a continental margin (Caledonian North Asian continent), creating several crustal blocks separated by small ocean basins (Ruzhentsev & Pospelov 1992; Dergunov 2001). This assumption was based on the local occurrence of serpentinite blocks in the lower part of thick oligomict terrigenous series and containing rare basaltic interlayers. Alternatively, Lamb & Badarch (1997) interpreted the Ordovician and Silurian sediments as marine turbidites deposited in a shelf or slope environment. However, these authors pointed out that the changes in sedimentation style, grain size, sediment compositions as well as the occurrence of possible angular unconformities may have been the results of tectonic reorganization.

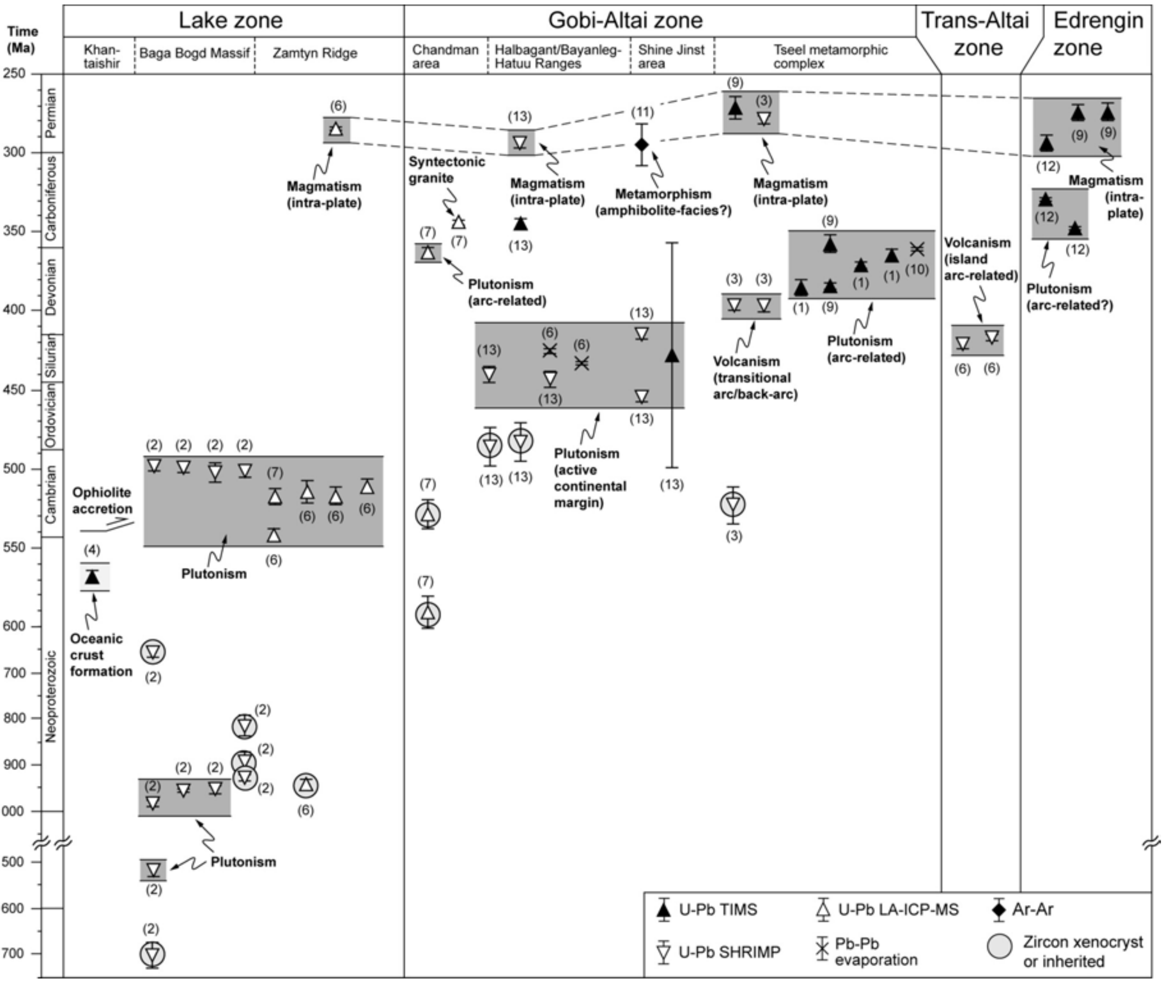

Fig. 16. Synoptic diagram showing U–Pb, Pb–Pb, and Ar–Ar ages from past studies obtained for rock assemblages from the Lake, Gobi-Altai, Trans-Altai and Edrengin zones of south-central Mongolia. Geological time scale according to Gradstein et al. (2004). See Fig. 1c for location of lithotectonic zones indicated. Data sources: (1) Bibikova et al. (1992); (2) Demoux et al. (2009a); (3) Demoux et al. (2009b); (4) Gibsher et al. (2001); (5) Hanžl & Aichler 2007; (6) Helo et al. (2006); (7) Hrdličková et al. (2008); (8) Kozakov et al. (2002a); (9) Kozakov et al. (2007a); (10) Kröner et al. (2007); (11) Lamb et al. (2008); (12) Yarmolyuk et al. (2008b); (13) this study.

Dating of a granite-gneiss (sample M211) and two felsic metavolcanic rocks (samples M309 and M328) indicates that magmatic events occurred within the Gobi-Altai region from c. 454 to 441 Ma (Fig. 16). These results provide first evidence for late Ordovician/early Silurian igneous activity in the region and are in contrast with previous interpretations which suggested that volcanic activity was very limited during this time period. The geochemical and heterogeneous Nd isotopic data for the early Silurian felsic and mafic metaigneous rocks from the Halbagant/Bayanleg Hatuu Ranges suggest that magmatism occurred on older continental crust, likely at an Andean-type continental margin. Moreover, the Nd model ages for felsic rocks argue in favour of the establishment of a late Ordovician/early Silurian active margin on top of the Precambrian Lake zone basement, possibly representing the southern margin of the Dzabkhan microcontinent. These data are supported by Nd isotopic characteristics previously reported for felsic metaigneous from the Bayanleg Hatuu Range which display $\varepsilon_{Nd(t)}$-values of +5.3 to -1.6 and Nd model ages of c. 1.1 to 0.7 Ga (Fig. 16; Helo et al. 2006). Therefore, the combined data set presented here suggests a change in geodynamic setting along the southern margin of the Caledonian North Asian continent during the late Ordovician/early Silurian that evolved from a shelf setting to an active margin setting.

The next igneous event identified within the Gobi-Altai area corresponds to the intrusion of early Devonian metaluminous granitoids at c. 415 Ma (sample M226). The geochemical and Nd isotopic data for the early Devonian mafic and felsic gneisses point to predominantly juvenile sources with minor involvement of early Neoproterozoic crustal material. These data suggest emplacement of the plutonic suites at the outboard portion of the late Ordovician/early Silurian Andean-type margin. Overall, the geochronological and geochemical/isotopic data suggest an oceanward migration of magmatism through time across an Andean-type margin, from the late Ordovician/early Silurian to the early Devonian.

Throughout the Devonian, the Gobi-Altai region accumulated thick sequences of shallow marine fossiliferous limestone, clastic sediments and volcanogenic deposits likely deposited within a marginal basin (Ruzhentsev & Pospelov 1992, Ruzhentsev 2001; Lamb and Badarch 1997, 2001). Volcanic activity within the basin occurred as early as the middle Devonian at c. 397–396 Ma (Demoux et al. 2009b). Middle Devonian metavolcanic rocks from the southern slope of the Gichgene Ridge display geochemical features and heterogeneous Nd isotopic data indicating an origin from mixed sources (including juvenile and Precambrian crustal components) within a transitional arc – back-arc environment (Demoux et al. 2009b). Geochronological data from the Tseel metamorphic complex (southern margin of the Gobi-Altai Mountains, see Fig. 1c) indicate protracted arc-related igneous activity throughout the middle to late Devonian from c. 385 to 357 Ma (Fig. 16; Bibikova et al. 1992; Kozakov et al. 2002a, 2007a; Kröner et al. 2007). Sedimentary facies for Devonian deposits clearly indicate marine conditions (Lamb & Badarch 1997), but there is as yet no evidence for ophiolite-related material (i.e. ultramafic and mafic igneous rocks and deep water sediments) of Devonian age within the Gobi-Altai region. It is therefore unlikely that back-arc extension never reached true ocean width but occurred within thin and submerged continental crust.

The collective evidence presented here suggests that the Gobi-Altai region underwent strong extension throughout the Devonian, likely developed in response to roll-back of the subducting oceanic slab (Collins & Richards 2008). We speculate that the late Ordovician/early Silurian Andean-type margin underwent progressive stretching during the Devonian that was associated with the opening of a continental back-arc basin and culminated with the formation of a Japan-type arc front in the late Devonian.

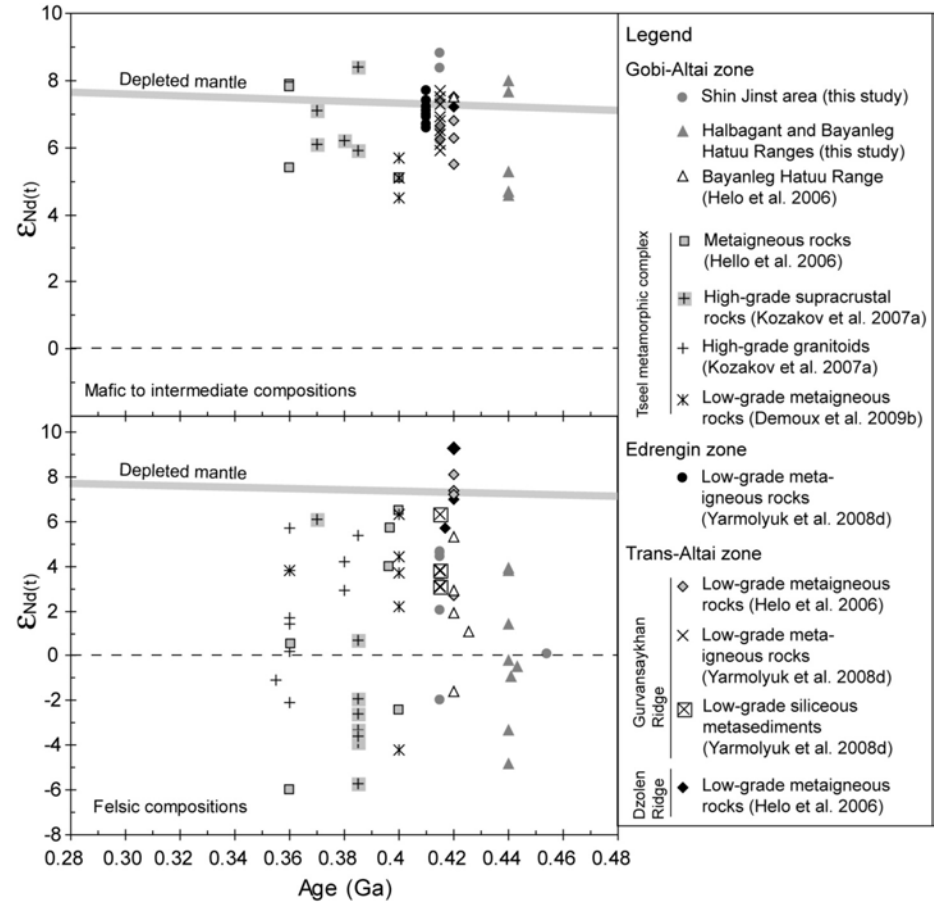

Fig. 17. Nd-isotope evolution diagram for metaigneous and metasedimentary rocks from southern Mongolia; data sources are given in the legend. Location of lithotectonic zones is shown in Fig. 1c. Depleted mantle line after DePaolo (1981).

The Gobi-Altai zone is bordered to the S by the Edrengin and Trans-Altai zones where lithostratigraphic, palaeontological and radiometric data indicate the remains of an arc system that was active at least from the early Silurian (Fig 16; Ruzhentsev & Pospelov 1992; Helo et al. 2006). The mafic and felsic igneous rocks as well as the siliceous sediments (products of erosion of the arc) of these regions display geochemical features and high positive $\varepsilon_{Nd(t)}$ values (Fig. 17; Helo et al. 2006; Yarmolyuk et al. 2008c) that undoubtedly indicate formation within an intra-oceanic arc far from a continental landmass. This indicates that the tectono-magmatic structures identified within the Gobi-Altai zone and the Edrengin/Trans-Altai zones evolved independently throughout the middle Palaeozoic and are unlikely to have belonged to the same subduction zone system.

10. Conclusions

Our geochronological and geochemical data for metaigneous rocks from the Gobi-Altai region shed new light on the geological evolution of southern Mongolia during the middle Palaeozoic.

Zircon crystallization ages of c. 454 to 441 Ma obtained for three felsic metaigneous samples provide the first record of late Ordovician/early Silurian igneous activity in the Gobi-Altai region. Geochemical and Nd isotopic compositions for mafic to felsic metaigneous rocks suggest emplacement at an Andean-type active continental margin. A zircon crystallization age of c. 415 Ma obtained for a tonalitic gneiss indicates another early Devonian magmatic pulse in the Gobi-Altai region. This magmatic phase was characterized by the intrusion of mafic to felsic granitoid bodies likely emplaced at the outboard segment of the aforementioned Andean-type margin as indicated by predominantly juvenile Nd isotopic compositions for mafic to felsic gneisses.

The combined geochronological and geochemical/isotopic data suggest that magmatic activity at an active continental margin migrated oceanward through time from the late Ordovician/early Silurian to the early Devonian. Progressive extension of the active margin culminated with the formation of a Japan-type arc front in the middle to late Devonian, associated with a back-arc basin.

Chapter 4

Devonian arc-related magmatism in the Tseel terrane of southwestern Mongolia: chronological and geochemical evidence

Abstract

The Tseel terrane in the Gobi Desert of SW Mongolia constitutes a composite crustal segment of imbricated sheets of high- and low-grade metamorphic rocks of predominantly middle Palaeozoic age. New sensitive high-resolution ion microprobe (SHRIMP) zircon ages of 396 ± 3 Ma (2σ) and 397 ±3 Ma (2σ) for two calc-alkaline metarhyolite samples indicate arc volcanism during the early Devonian. An undeformed feldspar porphyry cross-cutting the early Devonian low-grade sequence yielded an emplacement age of 279 ± 2 Ma (2σ). Geochemical and Nd isotopic data for low-grade mafic metavolcanic rocks are consistent with melting of moderately depleted upper mantle sources in a transitional arc/back-arc setting. In addition there are high- and low-grade felsic metaigneous rocks with subduction-related chemical signatures and heterogeneous Nd isotopic compositions indicating an origin from mixed sources, including juvenile and Precambrian crustal components. The field observations combined with the geochemical and isotopic data suggest that the Tseel terrane represents a segment of a mature Japan-type arc associated with a juvenile back-arc basin.

1. Introduction

The Central Asian Orogenic Belt (CAOB), also known as the Altaid Tectonic Collage (Şengör et al. 1993), is one of the largest accretionary orogens on Earth. It is bounded by the Siberian Craton to the N and by the Tarim and Sino-Korean Cratons to the S. It extends over more than 5000 km from the Ural Mountains in the W via Kazakhstan, Mongolia, southern Siberia and northern China and reaches the Okhotsk Sea in the E (Fig. 1a). It is composed of a mosaic of magmatic arc assemblages, ophiolitic complexes and Precambrian crustal slivers, amalgamated by subduction-accretion processes from the Neoproterozoic to the late Permian (Şengör et al. 1993; Khain et al. 2002; Xiao et al. 2003; Kröner et al. 2007; Windley et al. 2007). Two major hypotheses have been proposed to account for the development of this huge orogenic system. One model considers duplication of one to three long-lived magmatic arcs via large-scale strike-slip tectonics (Şengör et al. 1993; Şengör & Natal'in 1996; Yakubchuk 2004). The other concept invokes the development of multiple subduction systems and microcontinents, amalgamated by frontal collisions, similar to the present SW Pacific (Coleman 1989; Zonenshain et al. 1990; Mossakovsky et al. 1994; see Windley et al. 2007 for additional references).

In SW Mongolia, the Gobi-Altai region (Fig. 1c) records a significant part of the Palaeozoic history of the CAOB. This region is located S of the Main Mongolian Lineament (MML; Tomurtogoo 1997; Badarch et al. 2002), interpreted as a structural boundary separating Mongolia into a northern and a southern domain (Kröner et al. 2007; Windley et al. 2007). The northern domain is dominated by Precambrian to early Palaeozoic arc-related assemblages, dismembered ophiolite belts and blocks of Precambrian metamorphic basement (Badarch et al. 2002). The southern domain is predominantly composed of middle to late Palaeozoic island arc-related rock assemblages (Badarch et al. 2002; Kröner et al. 2007), including late Palaeozoic fragments of ophiolites (Rippington et al. 2008).

In this paper, we report sensitive high-resolution ion microprobe (SHRIMP) zircon ages and whole-rock geochemical-isotopic data for predominantly low-grade metaigneous rocks from the Tseel terrane in SW Mongolia. The results shed light on the composition and development of a middle Palaeozoic magmatic arc.

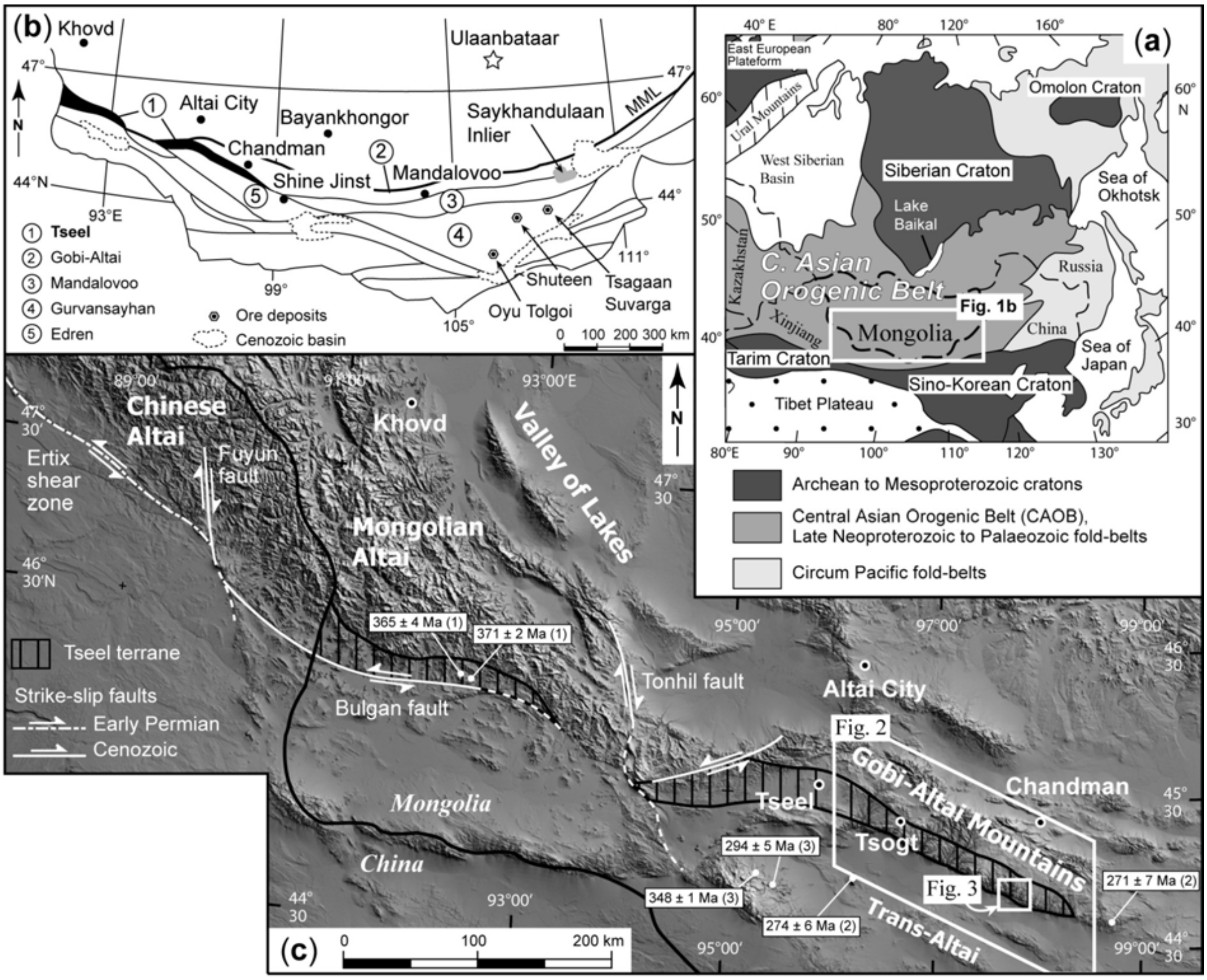

Fig. 1. Maps showing the location and geodynamic context of the Tseel terrane in southwestern Mongolia. (**a**) Outline of the Central Asian Orogenic Belt (modified after Jahn et al. 2000a). Inset (Fig. 1b) shows the southern Mongolian segment. (**b**) Tectonostratigraphic terrane map of southern Mongolia (adapted from Badarch et al. 2002). The Tseel terrane investigated in this study is shown in black; 1–5: names and location of terranes discussed in this paper; MML: Main Mongolian Lineament. (**c**) Grey-scaled digital topographic image (Shuttle Radar, SRTM) showing the Gobi-Altai Mountains (Fig. 2) in southwestern Mongolia and adjacent Mongolian and Chinese Altai Mountains to the NW. The study area in the Gobi-Altai Mountains is also indicated (Fig. 3). Also shown are zircon ages from past studies obtained for high-grade metamorphic rocks from the western block of the Tseel terrane and for granitoid intrusions from the Gobi-Altai and Edren terranes; (1) Bibikova et al. (1992), (2) Kozakov et al. (2007a), (3) Yarmolyuk et al. (2008d).

2. Geological framework

The Tseel terrane (Fig. 1b; Badarch et al. 2002) is composed of two main crustal blocks which extend from the southern flank of the Mongolian Altai in the west towards the Gobi-Altai Mountains in the SE (Fig. 1c). The western block is beyond the scope of this study, but both blocks are interpreted as parts of a single crustal infrastructure as established by lithological, structural and geochronological similarities (e.g. Kozakov et al. 2007a, and references therein). The southeastern block, of interest in this study, is located on the southern side of the Gobi-Altai Mountains in the NW Gobi Desert. It is a NW-trending lithotectonic unit, c. 250 km long and up to 50 km wide (Fig. 1b and 2). It is bounded in the NE by the Gobi-Altai back-arc/fore-arc terrane (Fig. 2a; Badarch et al. 2002). To the NW of the study area (Fig. 2b) the Gobi-Altai terrane is composed of Ordovician siliciclastic sediments and shallow marine Silurian limestones (Lamb & Badarch 1997). Immediately to the N of the study area (Fig. 2b), Devonian rocks predominate and form a wide basin primarily composed of siliciclastic sediments, lower Devonian fossiliferous limestones and interbedded felsic volcanic rocks and pillow basalts, deformed under low-grade metamorphic conditions (Lamb & Badarch 1997). A multigrain U–Pb zircon age of 271 ± 7 Ma was reported for a post-tectonic leucogranite (Kozakov et al. 2007a) cross-cutting the greenschist-facies rocks of this terrane about 70 km WSW of the Tseel terrane (Fig. 1c). In the SW, the Tseel terrane is in tectonic contact with the Edren terrane (Fig. 2a; Badarch et al. 2002) which is predominantly composed of Devonian thin-bedded argillites, fossiliferous limestones, clastic sediments and volcanic rocks, as well as Carboniferous volcanic and sedimentary rocks (Ruzhentsev 2001). These lithologies underwent greenschist-facies metamorphism and intense brittle to ductile deformation (Lamb & Badarch 1997; Badarch et al. 2002). Previous major and trace element data for Devonian volcanic rocks from the Edren terrane were interpreted as evidence for an island arc setting (Lamb & Badarch 2001). Carboniferous to Permian granitoid intrusions cross-cutting the low-grade rock assemblages of this terrane yielded multigrain U–Pb zircon crystallization ages between 348 ± 1 and 274 ± 6 Ma (Fig. 1c; Kozakov et al. 2007a; Yarmolyuk et al. 2008d).

2.1. Tseel terrane

The Tseel terrane is a composite unit made up of fault- or thrust-bounded blocks and/or nappes of low- and high-grade metamorphic rocks showing evidence of a polymetamorphic history (Kozakov et al. 2002a, 2007a). This terrane has long been interpreted as a Precambrian crustal basement because of the occurrence of high-grade and highly deformed rocks (Tomurtogoo 1998). However, several recent geochronological studies have now shown that the crustal domains are predominantly composed of Palaeozoic rocks (e.g. Kozakov et al. 2007a and references therein).

The dominant rock types include supracrustal rocks and tonalitic gneisses, amphibolites, micaschists and syntectonic granitoids. Rare and small boudins of hypersthene-bearing granulite-facies rocks are locally interlayered within migmatitic gneisses and were interpreted as relicts of a major granulite-facies metamorphic event (Kozakov et al. 2002a). Multigrain U–Pb zircon dating yielded ages of 385 ± 5 and 384 ± 2 Ma for the migmatitic gneisses (Fig. 2b; Bibikova et al. 1992; Kozakov et al. 2002a, respectively). The ages were interpreted as dating the peak of high-grade metamorphism. Most granulite-facies rocks were, however, retrograded to amphibolite-facies conditions associated with migmatization and deformation, and coeval emplacement of syntectonic granitoids (Kozakov et al. 2007a). The latter yielded multigrain U–Pb zircon ages of 358 ± 6, 365 ± 4 and 371 ± 2 Ma (Fig. 1c and 2b; Bibikova et al. 1992; Kozakov et al. 2002a) and a Pb–Pb zircon evaporation age of 361 ± 1 Ma (Fig. 2b; Kröner et al. 2007).

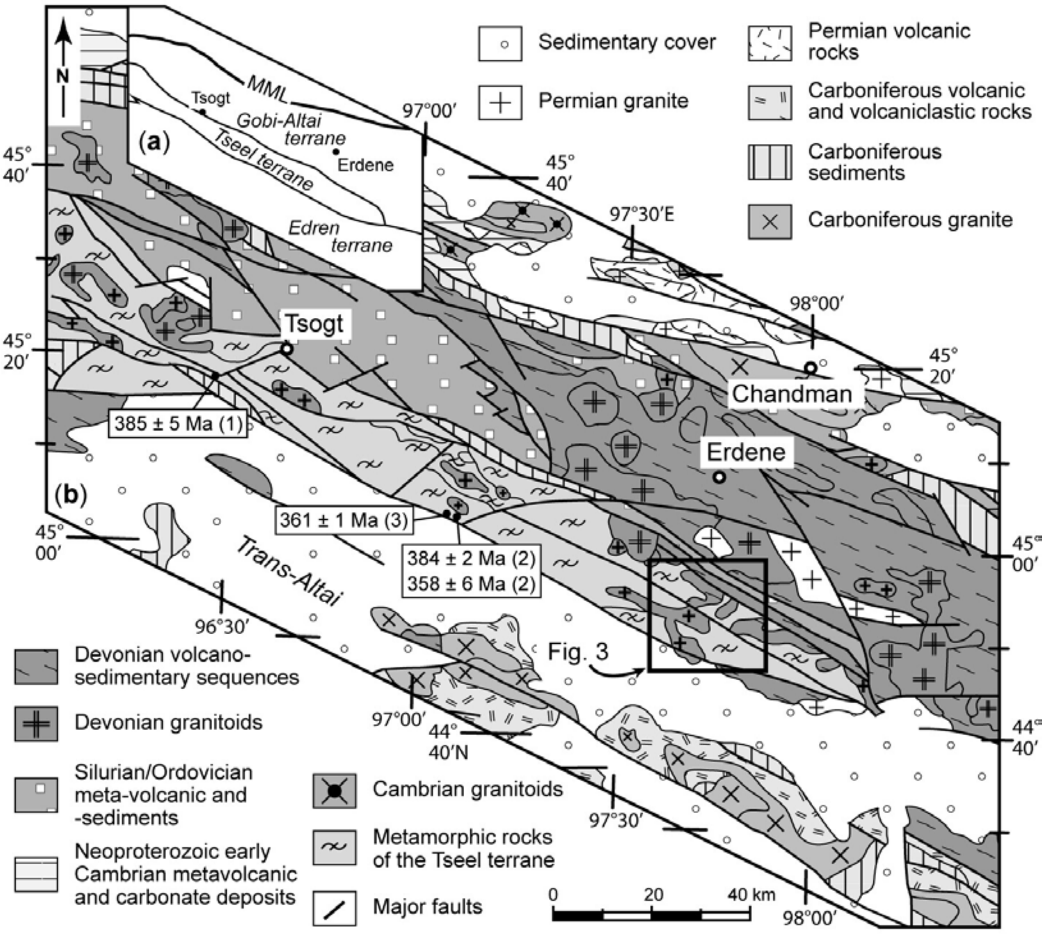

Fig. 2. Geological map of the southeastern Tseel terrane and surrounding areas. (**a**) Simplified map of the terranes bordering the southeastern Tseel terrane (after Badarch et al. 2002). (**b**) Geological sketch map of the southeastern Tseel terrane (modified after Tomurtogoo 1998) showing the location of the study area as also depicted in Fig. 3. Also indicated are zircon ages obtained for high-grade metamorphic rocks from past studies; (1) Bibikova et al. (1992), (2) Kozakov et al. (2002a), (3) Kröner et al. (2007).

Helo et al. (2006) reported major and trace element and Sm–Nd isotopic data for high- and low-grade metamorphic rocks from the eastern part of the Tseel terrrane. These data were interpreted to indicate a composite structure including remnants of a continental arc and oceanic crust. The authors interpreted the data as evidence for a rejuvenated old continental block associated with a back-arc basin.

2.2. Geology of the sampled transect in the Devreh Valley

We focussed on the southeastern block of the Tseel terrane (Fig. 1c) and investigated a traverse following the Devreh Valley which is located at the SE margin of this block (Fig. 2). There are no published geochronological data for this part of the Tseel terrane and therefore all stratigraphic ages mentioned in the following description are derived from the 1:200,000 Geological Map (Fig. 3; Rauzer 1987). The valley traverses the entire sequence of low- to locally high-grade metaigneous rocks (Fig. 3). The section is dominated by low-grade volcano-sedimentary deposits, locally intruded by undeformed feldspar porphyry and dykes of mafic to intermediate composition. To the N, the section is fringed by low-grade Devonian metasediments intruded by a large undeformed granitic batholith of presumed late Devonian age.

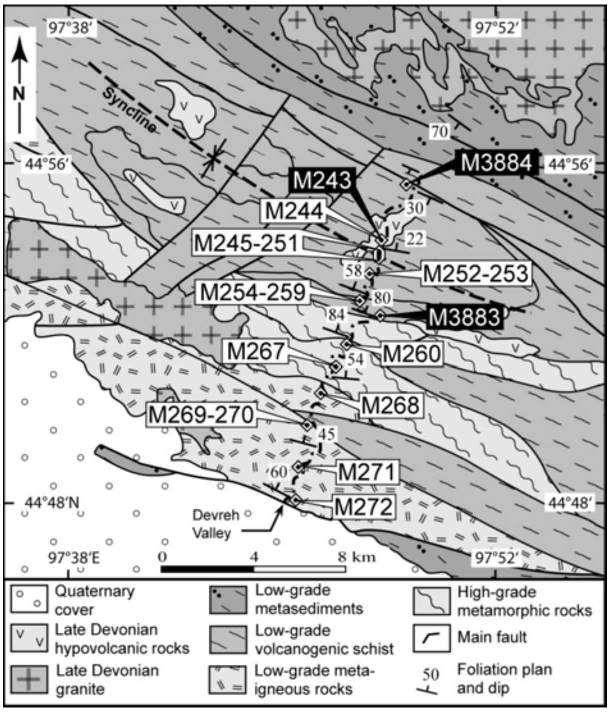

Fig. 3. Geological sketch map of sampled section following the Devreh Valley. Map was drawn on the basis of the Geological Map L47-XXVI (scale 1:200,000; Rauzer 1987), Landsat satellite images, and our own field observations. Localities of samples are indicated. Sample numbers within black boxes refer to those used for geochronology.

From N to S the section is composed of two units of low-grade metamorphic rocks, separated by a unit of higher-grade rocks. The northernmost low-grade unit is situated on the southern limb of a 30 km long and 6 km wide NW–SE-trending syncline (Fig. 3) which can be easily recognized on Landsat satellite images. This unit primarily contains dacitic to rhyolitic pyroclastic rocks interbedded with massive fine-grained dacitic lava flows and siliciclastic sediments. In the N, this unit is intruded by a NE–SW elongated feldspar porphyry body, about 4 km in length and 800 m wide, which is presumed to be late Devonian in age. This intrusion cross-cuts the surrounding low-grade volcano-sedimentary rocks with sharp contacts and does not show evidence of post-emplacement deformation. The foliation within the surrounding low-grade rocks strikes at 100° and dips 22° to the NE. Towards the S, the pyroclastic rocks are interlayered with strongly deformed decimetre thick marble beds. Basaltic metavolcanic rocks are intercalated with felsic volcaniclastic and carbonate/terrigenous sediments. Pyroclastic breccias are locally preserved and occur intercalated with the carbonate/terrigenous sediments. The dip of foliation increases gradually towards the S where the sequence is in contact with a lithologic unit of higher metamorphic grade. The rocks of high metamorphic grade are composed of garnet micaschists, recrystallized felsic gneisses and strongly foliated granitoid gneisses. The metamorphic schists and granitoid gneisses show a penetrative foliation striking 100° and dipping 74° to the NE. Farther S, supracrustal rocks of the second unit of low-grade metamorphism are sheared and display a well-defined foliation striking 100–130° and dipping 45 to 65° NE. This fabric is overprinted by a severe cataclastic deformation. The sequence is dominated by medium-grained felsic pyroclastic rocks interbedded with more massive volcanic horizons and/or volcaniclastic rocks. Intrusive rocks of granodioritic and granitic composition are locally present.

3. Petrography

Localities of our rock samples are shown in Fig. 3, and GPS coordinates are available in Appendix A.

Metabasalt samples M255, M256, M257, and M259 are dark green, fine- to medium-grained, well-foliated and display a granolepidoblastic texture. They are composed of anhedral green pleochroic amphibole, plagioclase, quartz, epidote and Fe-Ti oxides. Most of the plagioclase is strongly sericitized, and the amphibole is mostly replaced by chlorite and calcite. Clinopyroxene occurs as relicts and is almost entirely replaced by amphibole in samples M255, M256, and M257 or was not observed in sample M259.

The dacitic to rhyolitic samples display a crude foliation, underlined by the alignment of biotite, amphibole and secondary muscovite. The mineral assemblage is dominated by plagioclase, quartz, and biotite with minor alkali feldspar and amphibole. Both plagioclase and alkali feldspar show variable degrees of saussuritization or carbonate alteration. The amphiboles are mostly altered to chlorite and minor epidote. The matrix is invariably recrystallized and forms a fine-grained equigranular mosaic of quartz and feldspar. Secondary minerals such as sericite and epidote are present in most samples. Among the pyroclastic rocks there are also fine-grained tuffaceous or medium-grained volcaniclastic rocks. The primary texture is poorly preserved and the rocks commonly contain a large proportion of fine-grained chlorite and biotite, minor carbonate and rare resorbed garnet.

The granitoid gneisses (samples M260 and M267) from the high-grade unit are medium-grained and strongly foliated. The mineral assemblage consists of quartz, plagioclase, amphibole, alkali feldspar, and minor biotite. Alkali feldspar includes microcline and minor microperthite. The foliation is defined at a millimetre to centimetre scale by the preferred orientation of mafic minerals. The plagioclase and alkali feldspar are partly altered to fine-grained white mica and the quartz typically displays undulose extinction.

Undeformed intrusive rocks cross-cutting the low-grade metamorphic sequence are represented by a diorite (sample M244) and a feldspar porphyry (sample M243). The diorite has a microgranular texture and is composed of plagioclase, K-feldspar, amphibole, minor biotite and quartz. Plagioclase is partly altered to fine-grained sericite, whereas amphibole is mostly replaced by chlorite and oxide minerals. Accessory minerals consist of apatite, zircon and opaque oxides. The feldspar porphyry contains 50–60% of subhedral phenocrysts, including K-feldspar (~ 70%) and mafic minerals (~ 30%; biotite ± amphibole). K-feldspar phenocrysts are strongly altered and replaced by a combination of sericite and carbonate; mafic phenocrysts are mostly replaced by chlorite. The fine-grained groundmass consists mostly of plagioclase, quartz, and minor biotite. Accessory minerals include zircon and an opaque phase.

4. U–Pb zircon ages

Zircons from feldspar porphyry sample M243 were analysed on the Sensitive High-Resolution Ion Microprobe (SHRIMP II) at the Centre of Isotopic Research (CIR) in St.

Petersburg, Russia, and zircons from meta-rhyolite samples M3883 and M3884 on the SHRIMP II of the Perth Consortium, Australia. Zircons were separated at Mainz University using conventional procedures including magnetic separation and heavy liquid (methylene iodide). Representative grains were handpicked under a binocular microscope, mounted in epoxy resin together with chips of the zircon standard TEMORA 1 (St. Petersburg) and CZ3 (Perth) and then polished to about half of their thickness. The internal zircon structures were documented by cathodoluminescence (CL) imaging at St. Petersburg (sample M243; CamScan MX2500 scanning electron microscope) and Mainz University (samples M3883 and M3884; JEOL JXA-8900RL microprobe). The SHRIMP II instrumental characteristics were outlined by De Laeter & Kennedy (1998) and Larionov et al. (2004). Details of the analytical procedures are reported in Claoué-Long et al. (1995) and Williams (1998). For data collection, four scans through the critical mass range were made in St. Petersburg and six scans in Perth. The measured ^{206}Pb/^{238}U ratios for the standard TEMORA 1 were normalized to 0.0668, equivalent to an age of 417 Ma (Black et al. 2003) and those for CZ3 to 0.0914, equivalent to an age of 564 Ma (Pidgeon et al. 1994). The primary beam intensity was about 4.3 nA in St. Petersburg and about 2.2 nA in Perth. The mass-resolution was about 5000 at both instruments, and thus allowed clear elimination of isobaric interferences. The average uncertainty of ^{206}Pb*/^{238}U ratio was 0.85% for the standard TEMORA 1 and 1.1% for the standard CZ3. Sensitivity for Pb on TEMORA 1 and CZ3 was about 47 and 25 cps/ppm/nA, respectively. Analyses of samples and standards were regularly alternated to asses the extent of Pb^+/U^+ discrimination. Raw data reduction followed the method described by Nelson (1997, 2006). Corrections for common Pb were made using the ^{204}Pb method, assuming, that for low counts of ^{204}Pb, common Pb is mainly surface-related (Kinny 1986, Nelson 1997) and has the composition of the Broken Hill lead. In the case of higher ^{204}Pb counts, the age-related common Pb was corrected following the model Pb composition of Cumming & Richards (1975). Errors on individual analysis are based on counting statistics, include the uncertainty of the standard analysis, and are given in Appendix B-4 at the 1σ level. Stern (1997) provided a detailed account of the counting error assessment for SHRIMP analyses. Pooled ages were calculated using the Isoplot program of Ludwig (2003); all errors reported in the text correspond to the 95% confidence interval.

Sample M3883 was collected on the southern limb of the syncline affecting low-grade volcano-sedimentary rocks and is a massive metarhyolite interbedded with surrounding volcaniclastic rocks (Fig. 3). The zircons are 100–220 μm long, mostly transparent, slightly yellow, idiomorphic and short-prismatic in shape. Some grains have a brown colour and are subhedral with rounded terminations. CL images reveal simple oscillatory zoning (Fig. 4a) related to magmatic growth (Corfu et al. 2003) and inherited cores in some of the grains. Of seven zircon analyses, six define a cluster of concordant results (Fig. 4a) with a weighted mean ^{206}Pb/^{238}U age of 396.3 ± 3.3 Ma (MSWD = 0.09) that we interpret as the time of emplacement of the rhyolitic magma. One grain with a subhedral habit yielded a concordant but much older ^{206}Pb/^{238}U age of 523 ± 12 Ma (Fig. 4a). This grain is interpreted as a xenocryst, probably inherited from a felsic protolith.

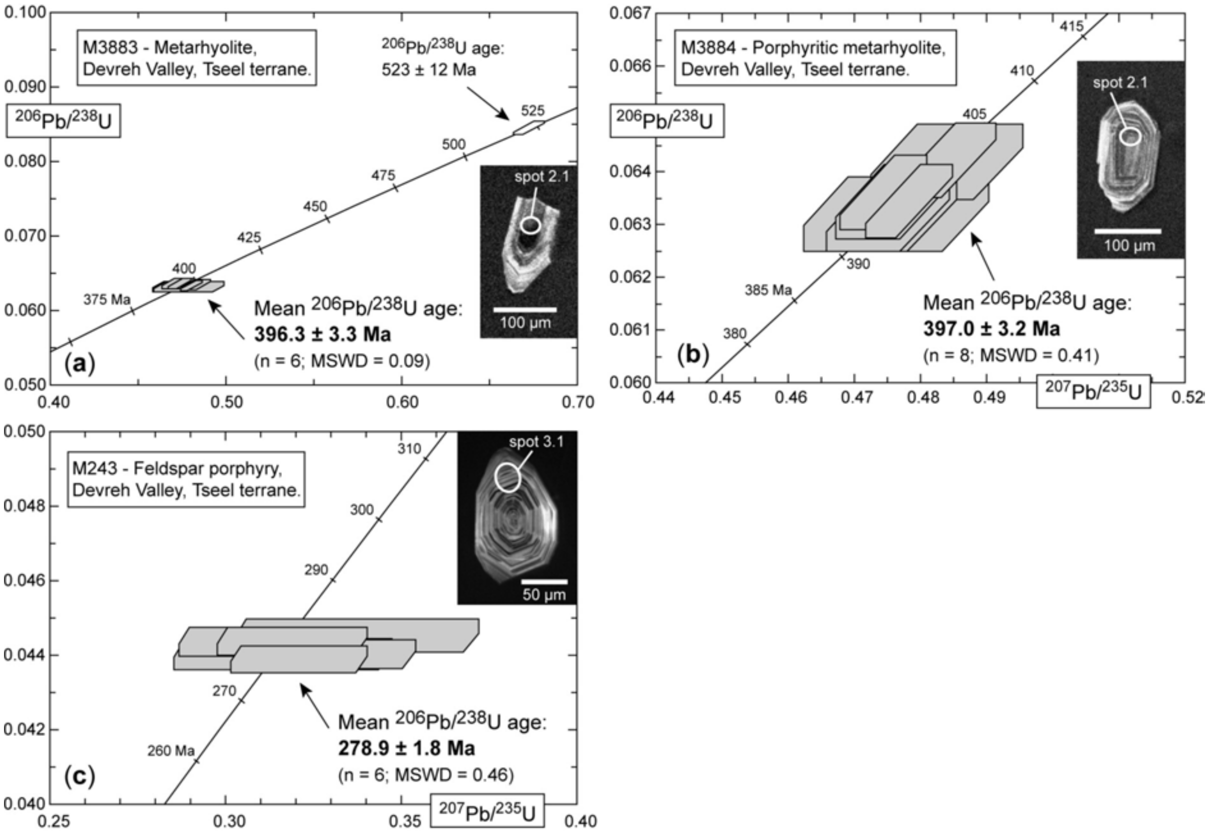

Fig. 4. Concordia diagrams showing SHRIMP analyses of single zircons for rock samples from the Devreh Valley. The error envelopes of the data points include the standard errors for ^{207}Pb/^{235}U, ^{206}Pb/^{238}U and ^{207}Pb/^{206}Pb. All uncertainties are given at the 95% confidence level. Insets are zircon CL images with white circles indicating SHRIMP analytical spots; spot numbers refer to those in Appendix B-4.

Sample M3884 is a porphyritic metarhyolite collected on the northern limb of the syncline in the low-grade unit (Fig. 3). The zircon population is composed of two morphological types. A first type is represented by transparent, colourless, euhedral and long-prismatic grains. A second type is composed of light yellow, translucent, euhedral and short-prismatic grains. The grain size varies from 120 µm to 300µm in length, and CL images document well-defined magmatic oscillatory zoning (Fig. 4b). The analyses of seven zircons from both types of grains define a cluster of concordant data points (Fig. 4b) with a weighted mean $^{206}Pb/^{238}U$ age of 397.0 ± 3.2 Ma (MSWD = 0.41). We interpret this age as the time of emplacement of the rhyolitic magma.

Sample M243 was collected from the presumed late Devonian feldspar porphyry body intruding the early Devonian low-grade volcano-sedimentary rocks (Fig. 3). It contains a large population of perfectly euhedral zircons that are colourless to light yellow with a short- to long-prismatic habitus. The zircons are 140 to 230 μm in length with a few grains up to 300 μm, usually free of cracks or opaque inclusions. CL images reveal well-developed oscillatory magmatic zoning (Fig. 4c) and some grains with dark and rounded inherited cores mantled by oscillatory-zoned overgrowths. Oscillatory-zoned domains of six grains were analysed and yielded a cluster of concordant data points with a weighted mean $^{206}Pb/^{238}U$ age of 278.9 ± 1.8 Ma (MSWD = 0.46; Fig. 4c). This age is interpreted as the time of emplacement of the feldspar porphyry and shows that this intrusion is not of late Devonian but early Permian age.

5. Whole-rock major and trace element data

Twenty four samples were selected for analysis by X-ray fluorescence spectrometry (XRF) using a Philips MagiXPro spectrometer in the Department of Geosciences, Mainz University. Loss on ignition (LOI) was determined after heating the sample powders at 1050 °C for 4 h. From the XRF data set, twelve samples were selected for the analysis of Rare Earth Element (REE) and additional trace-elements by laser ablation of glass beads using an ICP-MS at the Max Planck Institut (MPI) für Chemie in Mainz. For samples with SiO_2 content <56 wt%, glass beads were produced by melting c. 40 mg of rock powder using a Iridium strip heater as described by Stoll et al. (2008). For samples with SiO_2 >56 wt%, the rock powder was mixed with a high purity CaO–MgO powder in order to reduce the melt viscosity and increase the homogeneity of the glass bead. ICP-MS performance and stability were monitored by repeated measurement of basalt BHVO-2 and rhyolite JR-1 whole-rock reference materials. The whole-rock analyses are reported in Appendix E-3 and the data of the reference materials are available in Appendix G-2.

5.1. Sample alteration

All samples were subjected to different degree of metamorphism which may have modified the primary concentration of fluid-mobile elements to variable extents. This is suggested by petrographic observations showing alteration of primary minerals and variable LOI values of 0.4 to 2.7 wt%. Si, Na, Ca, K, Rb, Ba, and U are easily mobilized during late and/or post-magmatic processes including hydrothermal alteration and metamorphic overprinting (e.g. Bach et al. 2001). However, the concentration of the high field-strength elements (HFSE) Zr, Nb, Ta, Y, Ti, Hf, Th, the REE and transition elements such as Cr, Ni and Sc are considered as relatively immobile and little affected during rock alteration and low-grade metamorphic processes (Pearce & Cann 1973; Münker et al. 2004). Thus the discussion on the petrogenesis of the metaigneous rocks will focus on fluid-immobile elements such as the REE and HFSE as well as the Sm–Nd isotopes.

5.2. Mafic metavolcanic rocks

The mafic rocks from the low-grade portion of the transect have c. 48–51 wt% SiO_2 and high FeO^T/MgO ratios classifying them as tholeiitic basalts (Fig. 5a). All metabasalts have high TiO_2 concentrations of 1.8 to 2.2 wt% (Fig. 5b) and show little to moderate degrees of melt fractionation as indicated by MgO concentrations of 8.7 to 5.2 wt% and Mg-numbers (Mg#) of 58 to 43. The chemically most primitive samples M255, M256, and M257 reveal moderately high concentrations of Ni, Cr and Sc due to abundant former olivine and pyroxene (Wilson 1989).

The metabasalts M255, M256 and M257 show moderate enrichment in light REE (LREE) and slightly fractionated heavy REE (HREE) patterns as indicated by chondrite-normalized Dy_N/Yb_N ratios of c. 1.4 (Fig. 6a). Eu/Eu* ratios of 1.0–1.1 indicate absence of Eu anomalies and little or no involvement of plagioclase during melt fractionation. Primitive-mantle normalized trace element patterns (Fig. 6b) are slightly convex and suggest MORB-like mantle sources. The fluid-mobile elements such as Sr, U and Ba that are typically enriched in island arcs relative to the LREE (McCulloch & Gamble 1991) show a systematic depletion. Furthermore, the abundances of the HFSE Nb and Ti follow the smooth trend of neighbouring REE and are not depleted as in basalts from island arcs (McCulloch & Gamble 1991; Pearce & Peate 1995). Metabasalt sample M259 differs from the other metabasalts in that it shows a distinct negative Nb anomaly as found in rocks from island arcs (Fig. 6b). This sample is further characterized by a slight enrichment in LILE and Th over the LREE suggesting melting of subduction-overprinted mantle source.

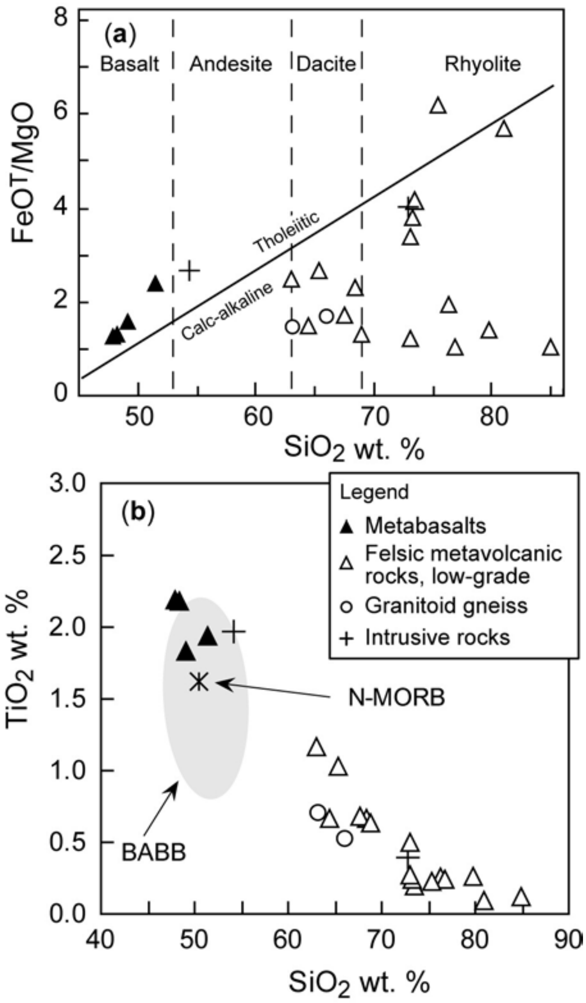

Fig. 5. Harker diagrams for rock samples from the Devreh Valley. (**a**) FeO^T/MgO v. SiO_2 concentrations indicate tholeiitic as well as calc-alkaline arc-related rock series (diagram modified after Miyashiro 1974). (**b**) TiO_2 v. SiO_2 concentrations showing MORB-like and arc-like compositions. Field for back-arc basin basalts (BABB) from Eissen et al. (1991) and Taylor & Martinez (2003); average N-MORB from Hofmann (1988). Data were recalculated to anhydrous compositions to facilitate comparison of the samples.

5.3. Felsic metaigneous rocks

The low-grade felsic metavolcanic rocks have calc-alkaline dacitic to rhyolitic compositions with SiO_2 concentrations of 63–85 wt% (Fig. 5a). The major element data show little or no correlation with SiO_2 as differentiation index (not shown) suggesting different sources and magma differentiation histories.

The samples display sub-parallel REE patterns (except for sample M247; Fig. 6c) with an enrichment in LREE, flat HREE distributions (Dy_N/Yb_N = 0.9–1.2) and negative Eu anomalies (Eu/Eu* = 0.7–0.8). The extended trace element patterns show enrichment of the LILE relative to the LREE and well-developed negative Nb and Ti anomalies (Fig. 6d) consistent with melting of crustal protoliths formed in a subduction environment. The metarhyolite sample M247 shows typical trace elements characteristics of adakitic rocks as defined by Defant & Drummond (1990). It has a high Sr/Y ratio of 81, a strongly fractionated REE pattern (La_N/Yb_N = 36) with a weak negative Eu anomaly (Eu/Eu* = 0.9) and low overall HREE abundances (Fig. 6c). It further displays enrichment of the LILE relative to LREE, well-developed negative Nb and Ti anomalies and a slightly positive Sr anomaly (Fig. 6d).

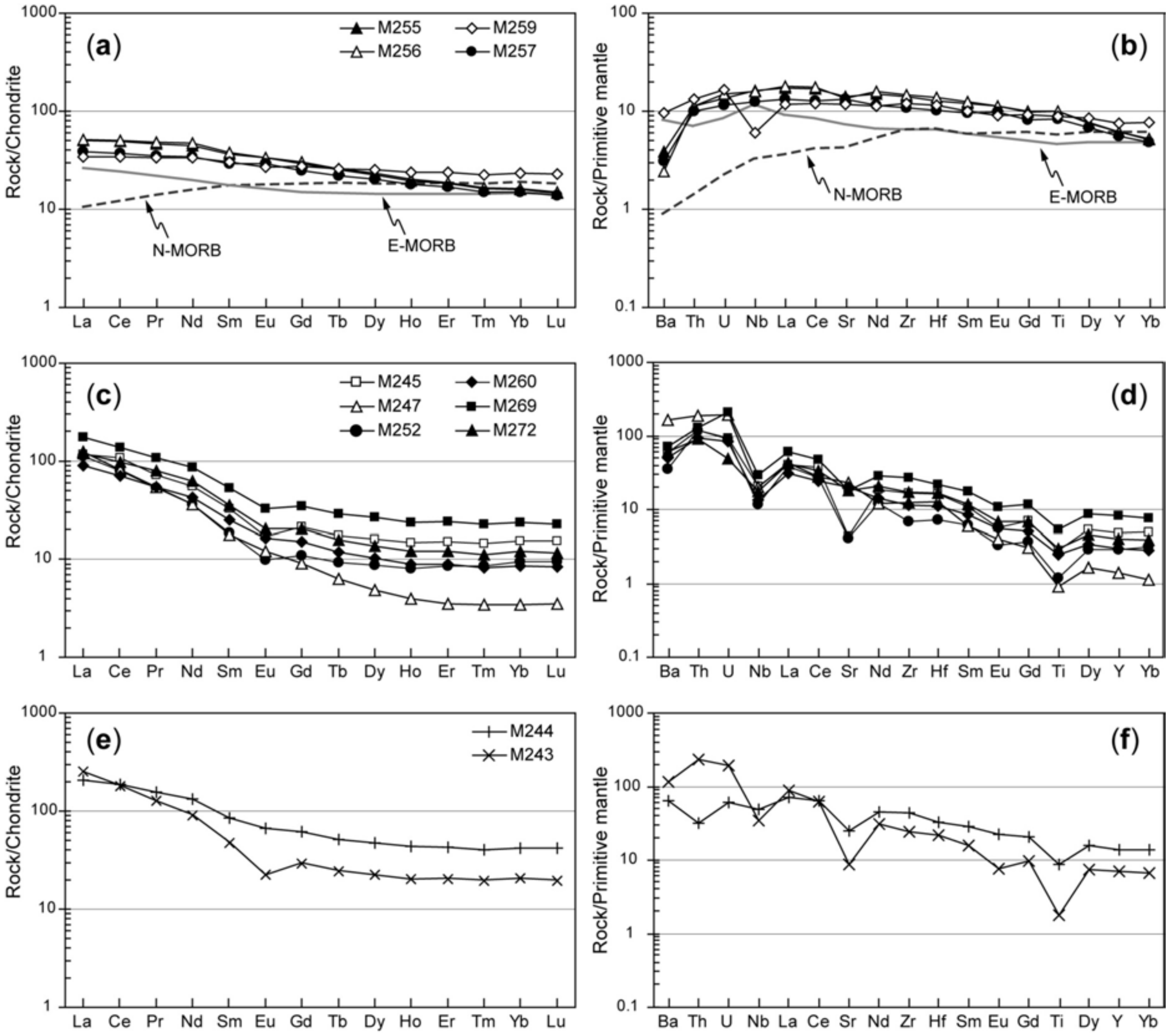

Fig. 6. Chondrite-normalized REE and mantle-normalized trace element patterns for selected rock samples from the Devreh Valley. (**a**–**b**) Mafic metavolcanic rocks; (**c**–**d**) felsic metaigneous rocks from the low- and high-grade (sample M260) units; (**e**–**f**) early Permian intrusive rocks. Chondrite and primitive-mantle normalizing values are from McDonough & Sun (1995) and Sun & McDonough (1989), respectively. E-MORB and N-MORB patterns (Sun & McDonough 1989) are shown for comparison.

The granitoid gneisses M260 and M267 have a calk-alkaline granodioritic composition (Fig. 5a) and sample M260 shows a fractionated REE pattern with a flat HREE distribution and a minute negative Eu anomaly (Fig. 6c). As also indicated for the low-grade felsic igneous rocks, this sample shows well-developed subduction-related signatures such as enrichment in LILE and negative Nb and Ti anomalies (Fig. 6d).

5.4. Undeformed intrusive rocks

Sample M244 is a transitional alkaline-subalkaline diorite with high TiO_2 (2.0 wt%), K_2O (1.2 wt%) and P_2O_5 (1.1 wt%) concentrations as in igneous rocks formed in intra-plate settings (Wilson 1989). The sample has high REE abundances and shows an extended trace element pattern with small negative Nb and Ti anomalies (Fig. 6f) indicating ultimately mantle sources overprinted by subduction processes.

The feldspar porphyry sample M243 has a granitic calk-alkaline composition (Fig. 5a) with a slightly metaluminous affinity as suggested by $Al_2O_3/(CaO+Na_2O+K_2O)$ and $Al_2O_3/(Na_2O+K_2O)$ molecular ratios of 1.0 and 1.2 respectively. The sample shows a fractionated REE pattern (Fig. 6e) with a distinct negative Eu anomaly (Eu/Eu* = 0.6) and well-developed negative anomalies for Nb, Ti, and Sr on the extended trace-element diagram (Fig. 6f).

6. Sm–Nd isotopic data

Sm–Nd isotope analyses were carried out on eleven whole-rock samples, using a Finnigan MAT 261 thermal ionisation mass spectrometer at the MPI für Chemie, Mainz. About 70 mg of rock powder was spiked with a ^{149}Sm–^{150}Nd tracer solution and then dissolved in Teflon bombs in a mixture of $HF–HClO_4$ for about five to seven days at 180 °C. Separation of Sm and Nd was performed with standard chromatographic procedures described in White & Patchett (1984). A rhenium double filament assembly was used for Nd and Sm isotopic measurements. $^{143}Nd/^{144}Nd$ ratios were normalized to $^{146}Nd/^{144}Nd = 0.7219$. Total procedural blanks were <60 pg for Nd and <20 pg for Sm. Repeated measurements of the La Jolla Nd standard solution yielded $^{143}Nd/^{144}Nd = 0.511837 \pm 21$ (2 s.d., N = 8). The error in the $^{147}Sm/^{144}Nd$ ratio is c. 0.3%. Sm–Nd model ages (t_{DM}) were calculated according to the model of DePaolo (1981) and are interpreted as mean crustal residence ages (Arndt & Goldstein 1987). The Sm–Nd isotope data are listed in Appendix F-2 and displayed in Fig. 7.

According to the zircon ages obtained in this study, initial ε_{Nd}-values for low-grade metamorphic rocks were calculated for an age of 400 Ma, and 280 Ma for the intrusive rocks

M243 and M244. For the granodioritic gneiss M260, we accepted an age of 360 Ma as can be inferred from previous zircon age determination on similar lithologies (Kozakov et al. 2002a; Kröner et al. 2007). We note that age uncertainties up to 30 Ma will not significantly change the calculated initial ε_{Nd}-values for felsic rocks.

The positive ε_{Nd}-values in Fig. 7 indicate that the basaltic samples originated from the depleted upper mantle and the felsic metaigneous rocks from juvenile mantle-derived protoliths with short crustal residence times. A single sample (M245) with a negative initial ε_{Nd}-value was formed by melting of much older crustal sources. Nevertheless, a larger data base indicates that the Tseel terrane comprises a significant amount of older crust (see Discussion and Fig. 9).

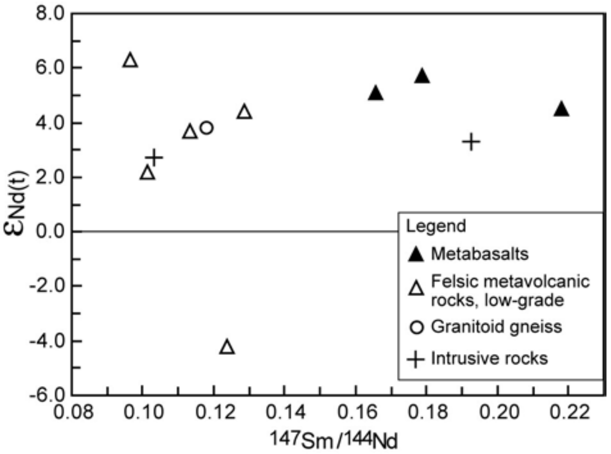

Fig. 7. Initial ε_{Nd}-values v. ^{147}Sm/^{144}Nd ratios for rock samples from the Devreh Valley. The data for the basaltic rocks indicate depleted upper mantle sources and those for the felsic rocks mostly juvenile crustal sources.

In detail, the LREE enriched tholeiitic metabasalt samples M255 and M256 yielded positive initial ε_{Nd}-values of +4.5 and +5.1 (Fig. 7) indicating moderately depleted mantle sources when compared to a value of 7.3 for depleted model mantle at c. 400 Ma. Sample M259, characterized by a negative Nb anomaly as found in rock from subduction zones, yielded an initial ε_{Nd}-value of +5.7 (Fig. 7) indicating slightly more depleted mantle sources although not much different from those of the metabasalts M255 and M256.

The felsic low-grade metavolcanic rocks show a wide range of initial ε_{Nd}-values ranging from 6.3 to -4.2 indicating melting of juvenile sources as well as recycling of much older material as documented by the pyroclastic metadacite sample M245. The corresponding mean crustal residence ages range from 1.4 to 0.5 Ga, the latter being not much older than the magmatic age of c. 0.4 Ga. The granodioritic gneiss M260 from the high-grade portion of the transect yielded a positive initial ε_{Nd}-value of +3.8 and a corresponding mean crustal residence age of 0.6 Ga.

The Permian undeformed mafic and felsic intrusive rocks M244 and M243 yielded positive initial ε_{Nd}-values of +3.3 and +2.7 (Fig. 7) suggesting sources not much different from those involved in the c. 400 Ma arc magmatism.

7. Interpretation of geochemical and isotopic data

7.1. Mafic metavolcanic rocks

The mafic samples have high TiO_2 concentrations of 1.8–2.2 wt% (Fig. 5b), similar to those reported for back-arc basin basalts (BABB, TiO_2 ~ 1.2–2.0 wt%; Eissen et al. 1991; Woodhead et al. 1993; Taylor & Martinez 2003), enriched mid-ocean ridge basalts (E-MORB, TiO_2 ~ 1.8 wt%; Klein 2004) and oceanic island basalts (OIB, TiO_2 >2 wt%). However, the relatively low degree of LREE enrichment ($Ce_N/Yb_N \leq 3.1$) correlated with moderate HREE concentrations and weakly fractionated HREE patterns do not support an origin from an OIB-like mantle source (Fig. 6a).

Their Ti/V ratios of 29 to 42 overlap the range for BABB and MORB with a typical range of 20 to 50 (Shervais 1982). Sample M259 has a negative Nb anomaly as basalts generated in subduction zones (McCulloch & Gamble 1991). Nevertheless, it shows relatively high Zr/Nb (31.0) and low Nb/Yb (1.1) ratios, similar to those of N-MORB (e.g. Zr/Nb = 31.8, Nb/Yb = 0.8; Sun & McDonough 1989) suggesting melting of a subduction-overprinted depleted mantle source. Beside high TiO_2 concentrations, the metabasalts M255, M256, and M257 are characterized by high Nb concentrations (8.9–11.6 ppm). Moreover, their moderate Zr/Nb (13.5–14.5) and high Nb/Yb (3.7–4.6) ratios are consistent with moderately enriched mantle sources.

Th and the LREE (e.g. La) are enriched in sediments (Johnson & Plank 1999) and can therefore be used as tracers of a crustal component subducted as sediment. As Nb concentrations are low in crustal material and pelagic sediments (Plank & Langmuir 1998), the Th/Nb ratio as well as the Th/La ratio may be investigated as evidence for continental material in the basalt sources. Indeed, metabasalt M259 has a high Th/Nb ratio of 0.26 and a Th/La ratio of 0.14 when compared to those reported for N-type MORB (e.g. Th/Nb and Th/La ratios of c. 0.05; Hofmann 1988). This finding suggests melting of a mantle source overprinted by a crustal component probably delivered by a subducting slab. The metabasalts M255, M256, and M257 have low Th/Nb (0.08–0.10) and Th/La (0.08–0.09) ratios, suggesting only a subordinate or no influence of slab-derived component in their mantle source.

Although there is trace element evidence for presence and absence of an enriched old continental component in the mafic rocks, their ε_{Nd}-values of +4.5 to +5.7 are all similar and also lower than in a typical depleted MORB mantle source at c. 400 Ma. This relationship may be explained by a compositionally heterogeneous upper mantle including geochemically depleted and geochemically enriched components (Castillo et al. 2007).

Finally, using immobile HFSE as in the Th–Zr–Nb ternary diagram of Wood (1980), it can be seen that the basaltic rocks, except for sample M259 with subduction-related characteristics, are indistinguishable from E-MORB and also tholeiitic rocks from intra-plate settings (Fig. 8). As mentioned above, the REE do not support OIB-like sources and therefore an origin of the mafic samples from an immature accretionary plate margin in a young back-arc basin is plausible. In summary, the geochemical and isotopic data of the metabasalts are consistent with an origin in a transitional arc/back-arc setting.

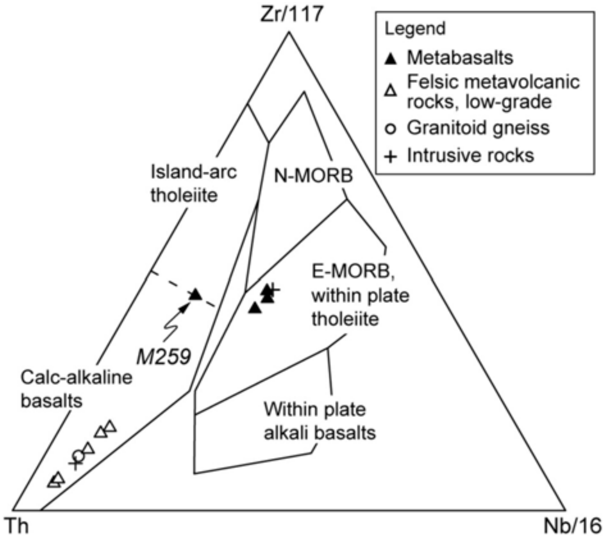

Fig. 8. Th–Zr–Nb ternary diagram (modified after Wood 1980) for rock samples from the Devreh Valley, showing arc and within plate characteristics.

7.2. Felsic metaigneous rocks

The felsic metaigneous rocks exhibit the chemical characteristics of volcanic rocks from mature convergent margin (Pearce & Peate 1995) with distinct enrichment in LREE. The felsic samples show a wide range of ε_{Nd}-values of +6.3 to -4.2 as found in mature Andean-type continental margins where magma ponding and AFC processes at lower crustal levels are important and lead to variable degrees of magma mixing with older crust. Most samples (except sample M245) have positive ε_{Nd}-values and young mean crustal residence ages (t_{DM} <0.8 Ga) providing evidence for melting of arc crust dominated by juvenile mantle-derived material. Sample M245 has a negative ε_{Nd}-value of -4.2 and a significantly older mean crustal residence age of 1.4 Ga clearly indicating an origin from old crustal material. This suggests the presence of discrete long-lived crustal domains within a predominantly juvenile arc crust.

8. Discussion

8.1. Geodynamic setting and evolution of the Tseel terrane

The SHRIMP zircon ages obtained for two low-grade metarhyolite samples indicate a phase of arc volcanism at c. 400 Ma (Fig. 4a and 4b). This was followed by the intrusion of arc granitoids between c. 371 and 358 Ma coeval with amphibolite-facies metamorphism (Bibikova et al. 1992; Kozakov et al. 2002a, 2007a; Kröner et al. 2007). Finally, the c. 279 Ma crystallization age obtained for an undeformed feldspar porphyry (Fig. 4c) cross-cutting the Devonian low-grade rocks suggest that the Devonian arc was already accreted to the southward growing margin (present-day coordinates) of the CAOB prior to the early Permian. The crystallization age of the undeformed feldspar porphyry is similar to previous multigrain zircon ages reported for post-tectonic granitoids intrusive into greenschist-facies rock assemblages of Devonian to Carboniferous ages in the Gobi-Altai and Trans-Altai areas (Fig. 1c; Kozakov et al. 2007a, Yarmolyuk et al. 2008d). These granitoids consistently display positive ε_{Nd}-values (Fig. 9) indicating derivation from isotopically primitive, short-lived crustal sources.

The geochemical data for Devonian metaigneous rocks presented in this study agree with those published earlier for similar lithologies (Helo et al. 2006; Kozakov et al. 2007a). The wide range of ε_{Nd}-values of +6.3 to -4.2 (Nd model ages of 1.4–0.5 Ga) overlap the data set of previous studies (Fig. 9). The overall Nd isotopic data for basaltic rocks suggest that the amount of juvenile crust may have increased with time. For instance, the c. 400 Ma old metabasalts from this study were derived from moderately depleted mantle sources, while the c. 360 Ma old metabasalts reported by Helo et al. (2006) collected some 55 km to the NW have highly positive initial ε_{Nd}-values of almost +8 and lack evidence of subduction-related components. We suggest that these mafic samples account for a marginal back-arc setting and reinforce the assumption of a nascent oceanic basin along the northern portion of the arc.

As previously mentioned, the Nd isotopic data of some felsic metaigneous rocks indicate that they originated from old crustal protoliths (Fig. 9). Palaeoproterozoic and Neoproterozoic crustal fragments are well documented in central Mongolia (Kozakov et al. 2007b; Demoux et al. 2009a) but at the present time there is no geochronological evidence for Precambrian crust in the Tseel terrane.

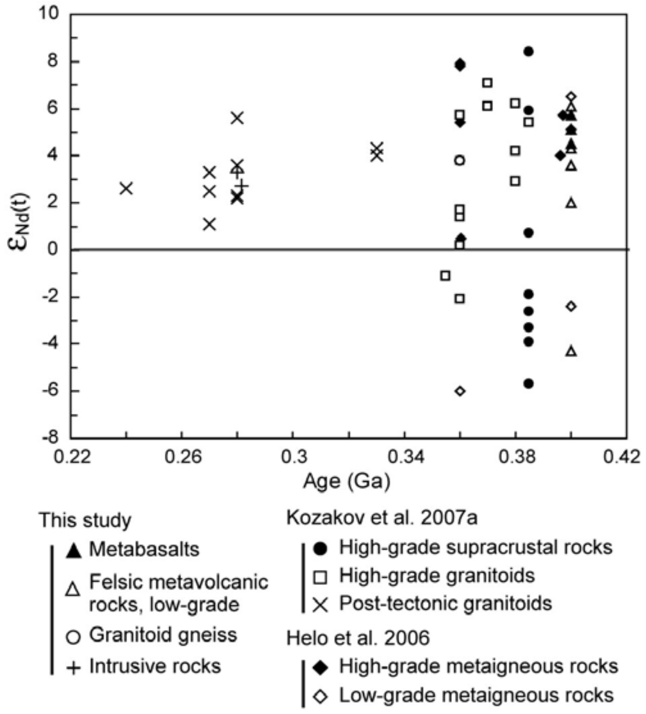

Fig. 9. Nd-isotope evolution diagram for rock samples from the Tseel terrane. Plotted are data from this study, Helo et al. (2006) and Kozakov et al. (2007a). The initial ε_{Nd}-values document a composite lithologic structure for the Tseel terrane, including juvenile mantle-derived as well as older crustal

In summary, the lithological, geochemical and Nd isotopic data indicate that the Tseel terrane is a composite unit made up of a Devonian mature island arc, including predominantly juvenile crustal material and discrete long-lived crustal domains, associated with a juvenile back-arc basin. Moreover, the collective evidence presented here indicates that neither the metamorphism nor the protoliths of the high- and low-grade metamorphic rocks, exposed within the southeastern block of the Tseel terrane, are Precambrian, but Palaeozoic in age. We cautiously suggest that the Gobi-Altai terrane and the southeastern Tseel block formed part of a single crustal infrastructure during the Devonian, as discussed below.

8.2. Regional correlations for southern Mongolia

Early to middle Palaeozoic volcano-sedimentary sequences in southern Mongolia are mainly composed of basaltic lava flows or pillow lavas interbedded with volcaniclastic sandstone, felsic pyroclastic rocks, marine siltstone and limestone, and minor chert (Lamb & Badarch

1997, 2001; Ruzhentsev 2001; Wang et al. 2005). There is only a limited number of radiometric ages for Devonian magmatic rocks (see below), but the age of some sedimentary stratigraphic units is well constrained by paleontological data (e.g. Wang et al. 2005). Provenance studies of Devonian marine sandstones indicate sources dominated by arc-related material with local contribution of components derived from a continental and/or mature island arc (Lamb & Badarch 2001). In addition, the thickness of the units and lithofacies may vary from place to place and indicate fluctuating depositional environments from subaeral to shallow- or deep-marine conditions as documented in the Shine Jinst area (Lamb & Badarch 1997) or the Saykhandulaan Inlier (Fig. 1b; Blight et al. 2008).

Helo et al. (2006) reported chemical data and Nd isotopes for late Silurian rocks from the Gurvansayhan island arc terrane (Fig. 1b; Badarch et al. 2002) which are consistent with an origin in a juvenile intra-oceanic arc. This terrane hosts major porphyry-type deposits such as the Oyu Tolgoi Cu–Au and Tsagaan Suvarga Cu–Mo deposits (Fig. 1b). Emplacement of the arc-related ore-hosting granitoids occurred from c. 411 to 365 Ma (Lamb & Cox 1998; Watanabe & Stein 2000; Perelló et al. 2001). The emplacement of calc-alkaline to high-K calc-alkaline volcano-plutonic complexes (Gerel et al. 2005; Yarmolyuk et al. 2008d) between c. 348 and 307 Ma (Lamb & Cox 1998; Perelló et al. 2001; Yarmolyuk et al. 2008d) suggest persistent igneous activities into the Carboniferous that may have been associated with a long-lived mature island arc.

All these data suggests that the SE domain of Mongolia contains remnants of a Silurian intra-oceanic arc that probably evolved into a mature island arc through the Devonian–late Carboniferous. The available data for the Tseel terrane also support a mature arc setting in the Devonian for the NW domain of southern Mongolia. The geochemical data of mafic metavolcanic rocks and the sedimentary rock facies in SW and SE Mongolia clearly indicate that these portions of the magmatic arc were fringed to the N (present-day coordinates) by an oceanic domain (open ocean or trapped oceanic basin?). However, the heterogeneous sources and lateral variation of sedimentary strata (e.g. Lamb & Badarch 2001) tend to suggest that the geometry along strike of the arc was not straightforward.

All across the southern border of Mongolia, the predominant alkaline chemical affinities of early Permian volcanic and plutonic rocks favour a continental setting (Lamb & Badarch 2001; Gerel et al. 2005; Kovalenko et al. 2006; Kozlovsky et al. 2007; Yarmolyuk et al. 2008d). Permian sedimentary rocks in SW and south-central Mongolia primarily record non-marine depositional environments (Lamb & Badarch 2001; Johnson et al. 2008; Lamb et al.

2008). This suggests that most of the southern domain of Mongolia was amalgamated by the early Permian while the formation of oceanic crust still occurred at that time in northern China (e.g. Hegenshan ophiolite; Miao et al. 2008).

8.3. Large-scale correlations with the Chinese Altai

Along strike, NW of the Tseel terrane, The Chinese Altai Mountains (Fig. 1c) record a long tectono-magmatic history from Cambrian to Permian time (e.g. Xiao et al. 2008 and references therein). These mountains are bounded to the S by the Ertix left-lateral strike-slip fault (Fig. 1c). This shear zone has been correlated in SW Mongolia with the Bulgan fault (Cunningham et al. 1996) which borders the Tseel terrane to the S (Fig. 1c). ^{40}Ar/^{39}Ar mineral dating of various lithologies within the Ertix shear zone record movements from c. 290 to 265 Ma (Laurent-Charvet et al. 2003; Briggs et al. 2007).

Geochronological data of metasediments and felsic metavolcanic rocks document an Ordovician substratum related to an early Palaeozoic active continental margin (Windley et al. 2002; Wang et al. 2006; Sun et al. 2008). Magmatic ages of c. 460–359 Ma for granitoid gneisses indicate intense plutonic activity from the late Ordovician to late Devonian (Windley et al. 2002; Wang et al. 2006; Yuan et al. 2007; Sun et al. 2008). Monazite ages determined by electron microprobe for metasediments record greenschist- to amphibolite-facies metamorphism at 382–377 Ma (Zheng et al. 2007), coeval with the Devonian arc magmatism. Along the southern side of the Chinese Altai, Devonian mafic to felsic metaigneous assemblages have geochemical and Sr–Nd isotopic features supporting an emplacement in an active back-arc basin/island arc (Xu et al. 2003; Niu et al. 2006). An ophiolite-related plagiogranite within one of these back-arc sequences yielded a SHRIMP zircon age of 372 ± 19 Ma, interpreted as the age of oceanic crust formation (Zhang et al. 2003).

Attempting to correlate the Devonian evolution in the Chinese Altai with that of the Tseel terrane is a difficult endeavour since the geology between these two regions is poorly documented and the original rock relationships are largely obscured by late Cenozoic transpressional deformation (Cunningham et al. 2003). To a first approximation, the Chinese Altai and the Tseel terrane display similarities regarding the timing of Devonian magmatic and metamorphic events suggesting that they belonged to the same subduction system. However, it remains uncertain if they constitute the prolongation of a single and continuous along-strike magmatic arc.

9. Conclusions

SHRIMP zircon ages in combination with geochemical data document a phase of arc-related magmatism in the Tseel terrane in the early Devonian at c. 400 Ma. These supracrustal rocks were subsequently deformed under low-grade metamorphic conditions and intruded by an undeformed feldspar porphyry in the early Permian times at c. 280 Ma. Geochemical and isotopic data suggest that 1) the basaltic metaigneous rocks were derived from a moderately depleted mantle source probably within a marginal back-arc environment; 2) the felsic metaigneous rocks have subduction-related chemical features and were formed by melting of predominantly juvenile crustal protoliths and subordinately ancient crustal materials. The field observations and the geochemical and isotopic data suggest that the Tseel terrane represents a portion of a mature island arc/back-arc environment as seen in Japan-type magmatic arcs.

Comparing the geological, chronological, and geochemical data for Devonian rock assemblages from southern Mongolia and the Chinese Altai suggests that these regions may have been part of the same subduction system but it remains uncertain if they belonged to the same and continuous along-strike magmatic arc.

References

Arndt, N.T. & Goldstein, S.L. 1987. Use and abuse of crust-formation ages. *Geology*, **15**, 893–895.

Ayers, J.C., Dittmer, S.K. & Layne, G.D. 1997. Partitioning of elements between peridotite and H2O at 2.0–3.0 GPa and 900–1100 °C, and application to models of subduction zone processes. *Earth and Planetary Science Letters*, **150**, 381–398.

Bach, W., Alt, J.C., Niu, Y., Humphris, S.E., Erzinger, J. & Dick, H.J.B. 2001. The geochemical consequences of late-stage low-grade alteration of lower ocean crust at the SW Indian Ridge: Results from ODP Hole 735B (Leg 176). *Geochimica et Cosmochimica Acta*, **65**, 3267–3287.

Badarch, G., Cunningham, W.D., & Windley, B.F. 2002. A new terrane subdivision for Mongolia: implications for the Phanerozoic crustal growth of Central Asia. *Journal of Asian Earth Sciences*, **21**, 87–110.

Badarch, G. 2005. Tectonics of south Mongolia. *In:* Seltmann, R., Gerel, O. & Kirwin, D.J. (eds). Geodynamics and metallogeny of Mongolia with a spezial emphasis on copper and gold deposits. SEG-IAGOD Field Trip, 14-16 August 2005, 8th Biennal SGA Meeting. *IAGOD Guidebook Series 11: CERCAMS/NHM London,* 119–129.

Bayasgalan, A., Jackson, J., Ritz, J.F. & Carretier, S. 1999. ‘Forebergs’, flowers structures, and the development of large intra-continental strike-slip fault: the Gurvan Bogd fault system in Mongolia. *Journal of Structural Geology*, **21**, 1285–1302.

Berzin, N.A., Coleman, R.G., Dobretsov, N.L., Zonenshain, L.P., Xuchang, X. & Chang, E.Z. 1994. Geodynamic map of the western part of the Paleoasian ocean. *Russian Geology and Geophysics*, **35**, 5–22.

Bibikova, E.V., Baikova, V.S., Gorohovskii, B.M., Gracheva, T.V., Kirnozova, T.I., Kozakov, I.K., Kotov, A.B., Neymark, L.A., Ovchinnikova, G.V., Sumin, L.V. & Shuleshko, I.K. 1990. Early Proterozoic Boundary in the Baidrag Block in Central Mongolia. *Izvestiya Akademii Nauk SSSR, Seriya Geologicheskaya*, **7**, 57–62. (In Russian)

Bibikova, E.V., Kirnozova, T.I., Kozakov, I.K., Kotov, A.B., Neymark, L.A., Gorkhovskiy, B.M. & Shuleshko, I.K. 1992. Polymetamorphic Complexes of the Southern Slope of the Mongolia and Gobi Altai: Results of U–Pb Dating. *Geotectonics*, **26**, 166–172.

Black, L.P., Kamo, S.L., Allen, C.M., Aleinikoff, J.N., Davis, D.W., Korsch, R.J. & Foudoulis, C. 2003. TEMORA 1: a new zircon standard for Phanerozoic U–Pb geochronology. *Chemical Geology*, **200**, 155–170.

Blight, J.H.S, Cunningham, D. & Petterson M.G. 2008. Crustal evolution of the Saykhandulaan Inlier, Mongolia: Implications for Palaeozoic arc magmatism, polyphase deformation and terrane accretion in the Southeast Gobi Mineral Belt. *Journal of Asian Earth Sciences*, **32**, 142–164.

Briggs, S.M., Yin A., Manning, C.E., Chen, Z.L., Wang, X.F. & Grove, M. 2007. Late Paleozoic tectonic history of the Ertix Fault in the Chinese Altai and its implications for the development of the Central Asian Orogenic System. *Geological Society of America, Bulletin,* **119**, 944–960.

Buchan, C., Cunningham, D., Windley, B.F. & Tomurhuu, D. 2001. Structural and lithological characteristics of the Bayankhongor Ophiolite Zone, central Mongolia. *Journal of the Geological Society, London,* **158**, 445–460.

Buchan, C., Pfänder, J., Kröner, A., Brewer, T.S., Tomurtogoo, O., Tomurhuu, D., Cunningham, D. & Windley, B.F. 2002. Timing of accretion and collisional deformation in the Central Asian Orogenic Belt: implications of granite geochronology in the Bayankhongor Ophiolite Zone. *Chemical Geology*, **192**, 23–45.

Buslov, M.M., Saphonova, I.Yu., Watanabe, T., Obut, O.T., Fujiwara, Y., Iwata, K., Semakov, N.N., Sugai, Y., Smirnova, L.V. & Kazansky, A.Y. 2001. Evolution of the Paleo-Asian Ocean (Altai–Sayan Region, Central Asia) and collision of possible Gondwana-derived terranes with the southern marginal part of the Siberian continent. *Geosciences Journal*, **5**, 203–224.

Cabanis, B. & Lecolle, M. 1989. Le diagramme La/10-Y/15-Nb/8: un outil pour la discrimination des series volcaniques et la mise en evidence des processus de melange et/ou de contamination crustale. *Comptes Rendus de l'Académie des Sciences- Series II*, **309**, 2023–2029.

Castillo, P.R., Rigby, S.J. & Solidum, R.U. 2007. Origin of high filed strength element enrichment in volcanic arcs: Geochemical evidence from the Sulu Arc, southern Philippines. *Lithos*, **97**, 271–288.

Chen, B., Jahn, B.M. & Tian, W. 2008. Evolution of the Solonker suture zone: constraints from zircon U–Pb ages, Hf isotopic ratios and whole-rock Nd–Sr isotope compositions of subduction- and collision-related magmas and forearc sediments. *Journal of Asian Earth Sciences*, **34**, 245–257.

Claoué-Long, J.C., Compston, W., Roberts, J. & Fanning, C.M. 1995. Two Carboniferous ages: a comparison of SHRIMP zircon dating with conventional zircon ages and ^{40}Ar/^{39}Ar analysis. *In:* Bergen, W.A., Kent, D.V., Aubrey, M.P. & Hardenbol, J. (eds). Geochronology time scales and global stratigraphic correlation. *SEPM Special Publication*, **54**, 3–20.

Coleman, R.G. 1989. Continental growth of northwest China. *Tectonics*, **8**, 621–635.

Collins, W.J. & Richards, S.W. 2008. Geodynamic significance of S-type granites in circum-Pacific orogens. *Geology*, **36**, 559–562.

Condie, K.C., Boryta, M.D., Liu, J. & Qian, X. 1993. The origin of khondalites: geochemical evidence from the Archean to early Proterozoic granulite belt in the North China craton. *Precambrian Research*, **59**, 207–223.

Corfu, F., Hanchar, J.M., Hoskin, P.W.O. & Kinny, P. 2003. Atlas of zircon textures. *In:* Hanchar, J.M. & Hoskin, P.W.O. (eds). Zircon. Mineralogical Society of America, Washington, *Reviews in Mineralogy & Geochemistry,* **53**, 469–500.

Cowgill, E., Yin, A., Harrison, T.M. & Wang, X.F. 2003. Reconstruction of the Altyn Tagh fault based on U–Pb geochronology: role of back thrusts, mantle sutures, and heterogeneous crustal strength in forming the Tibetan Plateau. *Journal of Geophysical Research*, **108**(B7), 2346.

Cumming, G.L. & Richards, J.R. 1975. Ore lead isotope ratios in a continuously changing earth. *Earth and Planetary Science Letters*, **28**, 155–171.

Cunningham, D. 2005. Active intracontinental transpressional mountain building in the Mongolian Altai: defining a new class of orogen. *Earth and Planetary Science Letters*, **240**, 436–444.

Cunningham, W.D., Windley, B.F., Dorjnamjaa, D., Badamgarov, G. & Sandaar, M. 1996. A structural transect across the Mongolian Western Altai: active transpression mountain building in Central Asia. *Tectonics*, **15**, 142–156.

Cunningham, W.D., Davies, S. & Badarch G. 2003. Crustal architecture and active growth of the Sutai Range, western Mongolia: a major intracontinental, intraplate restraining bend. *Journal of Geodynamics*, **36**, 169–191.

De Laeter, J.R. & Kennedy, A.K. 1998. A double focusing mass spectrometer for geochronology. *International Journal of Mass Spectrometry*, **178**, 43–50.

Defant, M.J. & Drummond, M.S. 1990. Derivation of some modern arc magmas by melting of young subducted lithosphere. *Nature*, **347**, 662–665.

Delor, C., Deroin, J.-P., Maluski, H. & Tomurtogoo, O. 2000. Petrostructural constraints and Ar-Ar dating of the Bayankhongor ophiolites. *In:* Badarch, G. & Jahn, B.M. (eds). IGCP 420 Continental Growth in the Phanerozoic: Evidence from Central Asia, Second Workshop, Abstracts and Excursion Guidebook (Geotraverse through a terrane collage in southern Hangay) July 25–August 3, 1999, Ulaanbaatar, Mongolia. *Geosciences Rennes. Hors series*, **2**, p. 21.

Demoux, A., Kröner, A., Liu, D. & Badarch, G. 2009a. Precambrian crystalline basement in southern Mongolia as revealed by SHRIMP zircon dating. *International Journal of Earth Sciences*, doi:10.1007/s00531-008-0321-4.

Demoux, A., Kröner, A., Hegner, E. & Badarch, G. 2009b. Devonian arc-related magmatism in the Tseel terrane of SW Mongolia: chronological and geochemical evidence. *Journal of the Geological Society, London*, **166**, 459–471.

DePaolo, D.J. 1981. A Neodymium and Strontium Isotopic study of the Mesozoic Calc-Alkaline Granitic Batholiths of the Sierra Nevada and Peninsular Ranges, California. *Journal of Geophysical Research*, **86**, 10470–10488.

Dergunov, A.B. (ed.) 2001. Tectonics magmatism and metallogeny of Mongolia. Routledge, London and New York, 288 p.

Dergunov, A.B., Ryazantsev, A.V., Luneva, O.I. & Rikhter, A.V. 1997. Structure and geological history of the Bayan–Khongor Zone, Central Mongolia. *Geotectonics*, **31**, 132–140.

Didenko, A.N., Mossakovsky, A.A., Pechersky, D.M., Ruzhenstev, S.V., Samygin, S.G. & Kheraskova, T.N. 1994. Geodynamics of the Central-Asian Paleozoic oceans. *Russian Geology and Geophysics*, **35**, 59–75.

Dijkstra, A.H., Brouwer, F.M., Cunningham, W.D., Buchan, C., Badarch, G. & Mason, P.R.D. 2006. Late Neoproterozoic proto-arc ocean crust in the Dariv Range, western Mongolia: a supra-subduction zone end-member ophiolite. *Journal of the Geological Society, London*, **163**, 363–373.

Dobretsov, N.L. & Buslov, M.M. 2007. Late Cambrian-Ordovician tectonics and geodynamics of Central Asia. *Russian Geology and Geophysics*, **48**, 1–12.

Dobretsov, N.L., Buslov, M.M. & Vernikovsky, V.A. 2003. Neoproterozoic to early Ordovician evolution of the Paleo-Asian ocean: Implications to the break-up of Rodinia. *Gondwana Research*, **6**, 143–159.

Economos, R.C., Hanžl, P., Hrdličková, K., Buriánek, D., Said, L.O., Gerdes, A. & Paterson, S.R. 2008. Geochemical and structural constraints on the magmatic history of the Chandman Massif of the eastern Mongolian Altay Range, SW Mongolia. *Journal of Geosciences*, **53**, 335–352.

Eengin, G. 1978. Structure of the sedimentary mantle of the Dzolen Range, Mongolia. *Geotectonics*, **12**, 54–57.

Eissen, J.P., Lefevre, C., Maillet, P., Morvan, G. & Nohara, M. 1991. Petrology and geochemistry of the central north Fiji basin spreadingcenter (southwest Pacific) between 16 degrees and 22 degrees. *Marine Geology*, **98**, 201–239.

Filippova, I.B., Bush, V.A. & Didenko, A.N. 2001. Middle Paleozoic subduction belts: the leading factor in the formation of the Central Asian fold-and-thrust belt. *Russian Journal of Earth Sciences*, **3**, 405–426.

Frost, B.R., Barnes, C.G., Collins, W.J., Arculus, R.J., Ellis, D.J. & Frost, C.D. 2001. A geochemical classification for granitic rocks. *Journal of Petrology*, **42**, 2033–2048.

Gerel, O., Oyungerel, S. & Minjin, C. 2005. Intrusive magmatism of south Mongolia. *In:* Seltmann, R., Gerel, O. & Kirwin, D.J. (eds). Geodynamics and metallogeny of Mongolia with a spezial emphasis on copper and gold deposits. SEG-IAGOD Field Trip, 14-16 August 2005, 8th Biennal SGA Meeting. *IAGOD Guidebook Series 11: CERCAMS/NHM London*, 131–148.

Gehrels, G.E., Yin, A. & Wang, X.F. 2003. Magmatic history of the northeastern Tibetan Plateau. *Journal of Geophysical Research*, **108**(B9), 2423.

Gibsher, A.S., Khain, E.V., Kotov, A.B., Sal'nikova, E.V., Kozakov, I.K., Kovach, V.P., Yakovleva, S.Z. & Fedoseenko, A.M. 2001. Late Vendian age of the Han-Taishiri ophiolite complex in western Mongolia. *Russian Geology and Geophysics*, **42**, 1110–1117.

Gladkochub, D., Pisarevsky, S., Donskaya, T., Natapov, L., Mazukabzov, A., Stanevich, A. & Sklyarov, E. 2006. The Siberian Craton and its evolution in terms of the Rodinia hypothesis. *Episodes*, **26**, 169–174.

Gradstein, F.M., Ogg, J.G. & Smith, A.G. 2004. A Geologic Time Scale 2004. *Cambridge University Press*, pp. 610.

Green, T.H. 1980. Island arc and continental building magmatism–a review of petrogenetic models based on experimental petrology and geochemistry. *Tectonophysics*, **63**, 367–385.

Hanžl, P. & Aichler, J. 2007. Geological survey of the Mongolian Altai at a scale 1:50,000 (Zamtyn Nuruu - 50), final report, 389 p.

Hanžl, P., Bat-Ulzii, D., Rejchrt, M., Košler, J., Bolormaa, K. & Hrdličková, K. 2008. Geology and geochemistry of the Palaeozoic plutonic bodies of the Trans-Altay Gobi, SW Mongolia: implications for magmatic processes in an accreted volcanic-arc system. *Journal of Geosciences*, **53**, 201–234.

Hargrove, U.S., Stern, R.J., Kimura, J.I., Manton, W.I. & Johnson, P. 2006. How juvenile is the Arabian-Nubian Shield? Evidence from Nd isotopes and pre-Neoproterozoic inherited zircons. *Earth and Planetary Science Letters*, **252**, 308–326.

Helo, C., Hegner, E., Kröner, A., Badarch, G., Tomurtogoo, O., Windley, B.F. & Dulski, P. 2006. Geochemical signature of Paleozoic accretionary complexes of the Central Asian Orogenic Belt in South Mongolia: Constraints on arc environments and crustal growth. *Chemical Geology*, **227**, 236–257.

Höck, V., Frank, W., Hejl, E. & Furtmueller, G. 2000. Petrology and cooling history of the Mt. Ushgoeg Range (Central Mongolia). *In:* Badarch, G. & Jahn, B.M. (eds). IGCP 420 Continental Growth in the Phanerozoic: Evidence from Central Asia, Second Workshop, Abstracts and Excursion Guidebook (Geotraverse Through a Terrane Collage in Southern Hangay) July 25–August 3 1999, Ulaanbaatar, Mongolia. *Geosciences Rennes. Hors serie*, **2**, p. 35–37.

Hofmann, A.W. 1988. Chemical differentiation of the Earth: the relationship between mantle, continental crust, and oceanic crust. *Earth and Planetary Science Letters*, **90**, 297–314.

Hoskin, P.W.O & Schaltegger, U. 2003. The composition of zircon and igneous and metamorphic petrogenesis. *In:* Hanchar, J.M. & Hoskin, P.W.O. (eds). Zircon. Mineralogical Society of America, Washington. *Reviews in mineralogy & geochemistry*, **53**, 27–62.

Hrdličková, K., Bolormaa, K., Buriánek, D., Hanžl, P., Gerdes, A. & Janoušek, V. 2008. Petrology and age of metamorphosed rocks in tectonic slices inside the Palaeozoic sediments of the eastern Mongolian Altay, SW Mongolia. *Journal of Geosciences*, **53**, 139–165.

Irvine, T.N. & Baragar, W.R. 1971. A guide to the chemical classification of the common volcanic rocks. *Canadian Journal of Earth Sciences*, **8**, 523–548.

Jacobsen, S.B. & Wasserburg, G.J. 1980. Sm–Nd evolution of chondrites. *Earth and Planetary Science Letters*, **50**, 139–155.

Jahn, B.M. 2004. The Central Asian Orogenic Belt and growth of the continental crust in the Phanerozoic. *In:* Malpas, J., Fletcher, C.J.N., Ali, J.R. & Aitchison, J.C. (eds). Aspects of the tectonic evolution of China. *Geological Society, London, Special Publications*, **226**, 73–100.

Jahn, B.M., Wu, F.Y. & Chen, B. 2000a. Granitoids of the Central Asian Orogenic Belt and continental growth in the Phanerozoic. *Transactions of the Royal Society of Edinburgh: Earth Sciences*, **91**, 181–193.

Jahn, B.M., Wu, F. & Chen, B. 2000b. Massive granitoid generation in Central Asia; Nd isotope evidence and implication for continental growth in the Phanerozoic. *Episodes*, **23**, 82–92.

Jahn, B.M., Capdevila, R., Liu, D., Vernon, A. & Badarch, G. 2004. Sources of Phanerozoic granitoids in the transect Bayanhongor-Ulaanbaatar, Mongolia: geochemical and Nd isotopic evidence, and implications for Phenerozoic crustal growth. *Journal of Asian Earth Sciences*, **23**, 629–653.

Johnson, C. L., Amory, J., Zinniker, D., Lamb, M. A., Graham, S. A., Affolter, M. & Badarch, G. 2008. Accretionary tectonics and sedimentation during late Paleozoic arc collision, China-Mongolia border region. *In:* Draut, A., Clift, P. & Scholl, D. (eds). Formation and applications of the sedimentary record in arc collision zones. *Geological Society of America Special Paper*, **436**, 363–390.

Johnson, M.C. & Plank, T. 1999. Dehydration and Melting Experiments Constrain the Fate of Subducted Sediments. *Geochemistry Geophysics Geosystems*, **1**, 1999GC000014.

Kelty, T.K., Yin, A., Dash, B., Gehrels, G.E. & Ribeiro, A.E. 2008. Detrital-zircon geochronology of Paleozoic sedimentary rocks in the Hangay-Hentey basin, north-central Mongolia: implications for the tectonic evolution of the Mongol-Okhotsk Ocean in central Asia. *Tectonophysics*, **451**, 290–311.

Kepezhinskas, P.K., Kepizhinskas, K.B. & Pukhtel, I.S. 1991. Lower Palaeozoic oceanic crust in Mongolian Caledonides: Sm–Nd isotope and trace element data. *Geophysical Research Letters*, **18**, 1301–1304.

Khain, E.V., Bibikova, E.V., Kröner, A., Zhuravlev, D.Z., Sklyarov, E.V., Fedotova, A.A. & Kravchenko-Berezhnoy, I.R. 2002. The most ancient ophiolite of the Central Asian fold belt: U–Pb and Pb–Pb zircon ages for the Dunzhugur Complex, Eastern Sayan, Siberia, and geodynamic implications. *Earth and Planetary Science Letters*, **199**, 311–325.

Khain, E.V., Bibikova, E.V., Sal'nikova, E.E., Kröner, A., Gibsher, A.S., Didenko, A.N., Degtyarev, K.E. & Fedotova, A.A. 2003. The Palaeo-Asian ocean in the Neoproterozoic and early Palaeozoic: new geochronologic data and palaeotectonic reconstructions. *Precambrian Research*, **122**, 329–358.

Kheraskova, T.N., Didenko, A.N., Bush, V.A. & Volozh, Y.A. 2003. The Vendian-Early Paleozoic history of the continental margin of eastern Paleogondwana, Paleoasian Ocean, and Central Asian Foldbelt. *Russian Journal of Earth Sciences*, **5**, 165–184.

Kinny, P.D. 1986. 3820 Ma zircons from a tonalitic Amitsoq gneiss in the Godthab district of southern West Greenland. *Earth and Planetary Science Letters*, **79**, 337–347.

Klein, E.M. 2004. Geochemistry of the Igneous Oceanic Crust. *In:* Holland, H.D. & Turekian, K.K. (eds). *Treatise on Geochemistry, Elsevier, Amsterdam*, **3**, 433–463.

Kotov, A.B., Kozakov, I.K., Bibikova, E.V., Sal'nikova, E.B., Kirnozova, T.I. & Kovach, V.P. 1995. Duration of regional metamorphic episodes in areas of polycyclic endogenic processes: A U–Pb Geochronological Study. *Petrology*, **3**, 567–575.

Kovach, V.P., Jian, P., Yarmolyuk, V.V., Kozakov, I.K., Kovalenko, V.I., Liu, D.Y. & Terent'eva, L.B. 2005. Magmatism and geodynamics of early stages of the Paleoasian ocean formation: geochronological and geochemical data on ophiolites of the Bayan-Khongor zone. *Doklady Earth Sciences*, **404**, 1072–1077.

Kovalenko, V.I., Yarmolyuk, V.V. & Bogatikov, O.A. 1995. Magmatism, geodynamics and metallogeny of Central Asia. MIKO, *Commercial Herald Publishers*, Moscow, 272 p.

Kovalenko, V.I., Yarmolyuk, V.V., Pukhtel, I.S., Stosch, H., Jagoutz, E. & Korikovsky, S.P. 1996. Igneous rocks and magma sources of the Ozernaya Zone Ophiolites, Mongolia. *Petrology*, **4**, 420–459.

Kovalenko, V.I., Yarmolyuk, V.V., Kovach, V.P., Kotov, A.B., Kozakov, I.K., Sal'nikova, E.B. & Larin, A.M. 2004. Isotope provinces, mechanisms of generation and sources of the continental crust in the Central Asian mobile belt: geological and isotopic evidence. *Journal of Asian Earth Sciences*, **23**, 605–627.

Kovalenko, V.I., Yarmolyuk, V.V., Tomurtogoo, O., Antipin, V.S., Kovach, V.P., Kotov, A.B., Kudryashova, E.B., Sal'nikova, E.B. & Zagornaya, N.Yu. 2005. Geodynamics and crust-forming processes in the early Caledonides of the Bayanhongor Zone, Cental Mongolia. *Geotectonics*, **39**, 298–316.

Kovalenko, V.I., Yarmolyuk, V.V., Sal'nikova, E.B., Kozlovsky, A.M., Kotov, A.B., Kovach, V.P., Savatenko, V.M., Vladykin, N.V. & Ponomarchuk, V.A. 2006. Geology, geochronology, and geodynamics of the Khan Bogd alkali granite pluton in southern Mongolia. *Geotectonics*, **40**, 450–466.

Kozakov, I.K. (ed.) 1993. The early Precambrian in the Central Asian Fold Belt. St. Petersburg, Nauka. (In Russian)

Kozakov, I.K., Kotov, A.B., Kovach, V.P. & Sal'nikova, E.B. 1997. Crustal growth in the geologic evolution of the Baidarik Block, Central Mongolia: evidence from Sm–Nd isotopic systematics. *Petrology*, **5**, 201–207.

Kozakov, I.K., Kotov, A.B., Sal'nikova, E.B., Bibikova, E.V., Kovach, V.P., Kirnozova, T.I., Berezhnaya, N.G. & Lykhin, D.A. 1999a. Metamorphic age of crystalline complexes of the Tuva-Mongolia Massif: The U–Pb geochronology of granitoids. *Petrology*, **7**, 177–191.

Kozakov, I.K., Sal'nikova, E.B., Bibikova, E.V., Kirnozova, T.I., Kotov, A.B. & Kovach, V.P. 1999b. Polychronous Evolution of the Paleozoic Granitoid Magmatism in the Tuva-Mongolia Massif: U–Pb Geochronological Data. *Petrology*, **7**, 592–601.

Kozakov, I.K., Kotov, A.B., Sal'nikova, E.B., Kovach, V.P., Natman, A., Bibikova, E.V., Kirnozova, T.I., Todt, W., Kröner, A., Yakovleva, S.Z., Lebedev, V.I. & Sugorakova, A.M. 2001. Timing of the structural evolution of the metamorphic rocks in the Tuva-Mongolian Massif. *Geotectonics*, **35**, 165–184.

Kozakov, I.K., Glebovitsky, V.A., Bibikova, E.V., Azimov, P.Y. & Kirnozova, T.I. 2002a. Hercynian granulites of Mongolian and Gobian Altai: geodynamic setting and formation conditions. *Doklady Earth Sciences*, **38**, 781–785.

Kozakov, I.K., Sal'nikova, E.B., Khain, E.V., Kovach, V.P., Berezhnaya, N.G., Yakovleva, N.G. & Plotkina, Y.V. 2002b. Early Caledonian crystalline rocks of the Lake zone, Mongolia: Stages and tectonic environments as deduced from U–Pb and Sm–Nd isotopic data. *Geotectonics*, **36**, 156–166.

Kozakov, I.K., Sal'nikova, E.B., Natman, A., Kovach, V.P., Kotov, A.B., Podkovyrov, V.N. & Plotkina, Yu.V. 2005. Metasedimentary complexes of the Tuva-Mongolian Massif: Age, provenances, and tectonic position. *Stratigraphy and Geological Correlation*, **13**, 1–20.

Kozakov, I.K., Sal'nikova, E.B., Yakovleva, S.Z., Plotkina, Yu.V. & Fedoseenko, A.M. 2006. Vendian metamorphism in the accretionary-collisional structure of Central Asia. *Doklady Earth Sciences*, **407**, 192–197.

Kozakov, I.K., Kovach, V.P., Bibikova, E.V., Kirnozova, T.I., Zagornaya, N.Y., Plotkina, Y.V. & Podkovyrov, V.N. 2007a. Age and sources of granitoids in the junction zone of the Caledonides and Hercynides in southwestern Mongolia: geodynamic implications. *Petrology*, **15**, 126–150.

Kozakov, I.K., Sal'nikova, E.B., Wang, T., Didenko, A.N., Plotkina, Yu.V. & Podkovyrov, V.N. 2007b. Early Precambrian crystalline complexes of the Central Asian microcontinent: Age, sources, tectonic position. *Stratigraphy and Geological Correlation*, **15**, 121–140.

Kozakov, I.K., Sal'nikova, E.B., Kovach, V.P., Yarmolyuk, V.V., Anisimova, I.V., Kozlovsky, A.M., Plotnika, Y.V., Myskova, T.A., Fedoseenko, A.M., Yakovleva, S.Z. & Sugorakova, A.M. 2008. Vendian stage in formation of the early Caledonian superterrane in central Asia. *Stratigraphy and Geological Correlation*, **16**, 360–382.

Kretz, R. 1983. Symbols for rock-forming minerals. *American Mineralogist*, **68**, 277–279.

Kozlovsky, A.M., Yarmolyuk, V.V., Kovalenko, V.I., Savatenko, V.M. & Velivetskaya, T.A. 2007. Trachytes, comendites, and pantellerites of the late Paleozoic bimodal rift association of the Noen and Tost ranges, southern Mongolia: differentiation and contamination of peralkaline salic melts. *Petrology*, **15**, 240–263.

Kröner, A., Byerly, G.R. & Lowe, D.R. 1991. Chronology of early Archaean granite-greenstone evolution in the Barberton Mountain land, South Africa, based on precise dating by single zircon evaporation. *Earth and Planetary Science Letters*, **103**, 41–54.

Kröner, A. & Hegner, E. 1998. Geochemistry, single zircon ages and Sm-Nd systematics of granitoid rocks from the Góry Sowie (Owl) Mts., Polish West Sudetes: evidence for early Palaeozoic arc-related plutonism. *Journal of the Geological Society, London*, **155**, 711–724.

Kröner, A., Jaeckel, P., Brandl, G., Nemchin, A.A. & Pidgeon, R.T. 1999. Single zircon ages for granitoid gneisses in the Central Zone of the Limpopo belt, southern Africa, and geodynamic significance. *Precambrian Research*, **93**, 299–337.

Kröner, A., Tomurtogoo, O., Badarch, G., Windley, B.F. & Kozakov, I.K. 2001. New zircon ages and significance for crustal evolution in Mongolia. *In:* Sklyarov, E.V. (ed.). *Assembly and break up of Rodinia supercontinent, Irkutsk*, 142–145.

Kröner, A., Windley, B.F., Badarch, G., Tomurtogoo, O., Hegner, E., Jahn, B.M., Gruschka, S., Khain, E.V., Demoux, A. & Wingate, M.T.D. 2007. Accretionary growth and crust formation in the Central Asian Orogenic Belt and comparison with the Arabian-Nubian-Shield. *In:* Hatcher Jr., R.D., Carlson, M.P., McBride, J.H. & Martínez Catalán, J.R. (eds). *4-D Framework of Continental Crust*. *Geological Society of America, Memoir*, **200**, 181–209.

Kurimoto, C., Tungalag, F., Bayarmandal, L. & Ichinnorov, N. 1998. K–Ar ages of white micas from pelitic schists of the Bayankhongor area, west Mongolia. *Bulletin of the Geological Survey of Japan*, **49** (1), 19–23.

Kuzmichev, A., Bibikova, E.V. & Zhuravlev, D.Z. 2001. Neoproterozoic (~ 800 Ma) orogeny in the Tuva-Mongolia Massif (Siberia): island arc-continent collision at the northeast Rodinia margin. *Precambrian Research*, **110**, 109–126.

Kuzmichev, A., Kröner, A., Hegner, E., Liu, D.Y. & Wan, Y.S. 2005. The Shishkhid ophiolite, northern Mongolia: a key to the reconstruction of a Neoproterozoic island-arc system in central Asia. *Precambrian Research*, **138**, 125–150.

Lamb, M.A. & Badarch, G. 1997. Paleozoic sedimentary basins and volcanic-arc systems of southern Mongolia: New stratigraphic and sedimentologic constraints. *International Geological Review*, **39**, 542–576.

Lamb, M.A. & Badarch, G. 2001. Paleozoic sedimentary basins and volcanic arc systems of southern Mongolia: new geochemical and petrographic constraints. *In:* Hendrix, M.S. & David, G.A. (eds), Paleozoic and Mesozoic tectonic evolution of central Asia: From continental assembly to intracontinental deformation, Boulder, Colorado. *Geological Society of America, Memoir*, **194**, 117–149.

Lamb, M.A. & Cox, D. 1998. New ^{40}Ar/^{39}Ar age data and implications for porphyry copper deposits of Mongolia. *Economic Geology*, **93**, 524–529.

Lamb, M.A., Hanson, A.D., Graham, S.A., Badarch, G. & Webb, L.E. 1999. Left-lateral sense offset of Upper Proterozoic to Paleozoic features across the Gobi Onon, Tost, and Zuunbayan faults in southern Mongolia and implications for other central Asian faults. *Earth and Planetary Science Letters*, **173**, 183–194.

Lamb, M.A., Badarch, G., Navratil, T. & Poier, R. 2008. Structural and geochronologic data from the Shin Jinst area, eastern Gobi Altai, Mongolia: Implications for Phanerozoic intracontinental deformation in Asia. *Tectonophysics*, **451**, 312–330.

Larionov, A.N., Andreichev, V.A. & Gee, D.G. 2004. The Vendian alkaline igneous suite of northern Timan: ion microprobe U–Pb zircon ages of gabbros and syenite. *In:* Gee, D.G. & Pease, V.L. (eds). The Neoproterozoic Timanide Orogen of eastern Baltica. *Geological Society, London, Memoirs*, **30**, 69–74.

Laurent-Charvet, S., Charvet, J., Monie, P. & Shu, L.S. 2003. Late Paleozoic strike-slip shear zones in eastern central Asia (NW China): New structural and geochronological data. *Tectonics*, **22**, 1009, doi:10.1029/2001TC901047.

Leat, P.T., Pearce, J.A., Barker, P.F., Millar, I.L., Barry, T.L. & Larter, R.D. 2004. Magma genesis and mantle flow at a subduction slab edge: the South Sandwich arc-basin system. *Earth and Planetary Science Letters*, **227**, 17–35.

Li, J.Y. 2006. Permian geodynamic setting of northeast China and adjacent regions: closure of the Paleo-Asian Ocean and subduction of the Paleo-Pacific Plate. *Journal of Asian Earth Sciences*, **26**, 207–224.

Liew, T.C. & Hofmann, A.W. 1988. Precambrian crustal components, plutonic associations, plate environment of the Hercynian Fold Belt of central Europe: indications from a Nd and Sr isotopic study. *Contribution to Mineralogy and Petrology*, **98**, 129–138.

Lu, S., Li, H., Zhang, Ch. & Niu, G. 2008. Geological and geochronological evidence for the Precambrian evolution of the Tarim craton and surrounding continental fragments. *Precambrian Research*, **160**, 94–107.

Ludwig, K.R. 2003. User's Manual for ISOPLOT/Ex 3.0. A geochronological toolkit for microsoft excel. *Berkeley Geochronology Center Special Publication*, **4**, 70 p.

Macdonald, F.A., Jones, D.S. & Schrag, D.P. 2009. Stratigraphic and tectonic implications od a newly discovered glacial diamictite cap carbonates couplet in southwestern Mongolia. *Geology*, **37**, 123–126.

Matsumoto, I. & Tomurtogoo, O. 2003. Petrological characteristics of the Hantaishir ophiolite complex, Altai Region, Mongolia: coexistence of podiform chromitite and boninite. *Gondwana Research*, **6** (2), 161–169.

McCulloch, M.T. & Gamble, J.A. 1991. Geochemical and geodynamical constraints on subduction zone magmatism. *Earth and Planetary Science Letters*, **102**, 358–374.

McDonough, W.M. & Sun, S.S. 1995. The composition of the earth. *Chemical Geology*, **120**, 223–253.

Miao, L., Fan, W., Liu, D., Zhang, F., Shi, Y. & Guo, F. 2008. Geochronology and geochemistry of the Hegenshan ophiolitic complex: implications for late-stage tectonic evolution of the Inner Mongolia-Daxinganling orogenic belt, China. *Journal of Asian Earth Sciences*, **32**, 348–370.

Mitrofanov, F.P., Kozakov, I.K. & Palei, I.P. 1981. Precambrian of Western Mongolia and southern Tuva. *Transactions of the joint Soviet–Mongolian scientific-research geological expedition*, **vol. 32**, Nauka Publishing House, Leningrad pp. 90–102. (In Russian)

Mitrofanov, F.P., Bibikova, E.V., Gracheva, T., Kozakov, I.K., Sumin, L.V. & Shuleshko, I.K. 1985. Archean isotopic age of grey tonalitic gneisses in Celedonian structures of central Mongolia. *Doklady Academii Nauk USSR*, **284**, 670–675. (In Russian)

Miyashiro, A. 1974. Volcanic rock series in island arcs and active continental margins. *American Journal of Science*, **274**, 321–355.

Mossakovsky, A.A., Ruzhentsev, S.V., Samygin, S.G. & Kheraskova, T.N. 1994. Central Asian fold belt: geodynamic evolution and history of formation. *Geotectonics*, **27**, 445–474.

Münker, C., Wörner, G., Yogodzinski, G. & Churikova, T. 2004. Behaviour of high field strengths elements in subduction zones: constraints from Kamchatka-Aleutian arc lavas. *Earth and Planetary Science Letters*, **224**, 275–293.

Nelson, D.R. 1997. Compilation of SHRIMP U–Pb zircon geochronology data. 1996. *Geological Survey of Western Australia Record 1997/2*, pp 189.

Nelson, D.R. 2006. CONCH: A Visual Basic program for interactive processing of ion-microprobe analytical data. Computers and *Geosciences*, **32**, 1479–1498.

Nesbitt, H.W. & Young, G.M. 1982. Early Proterozoic climates and plate motions inferred from major element chemistry of lutites. *Nature*, **299**, 715–717.

Niu, H., Sato, H., Zhang, H., Ito, J., Yu, X., Nagao, T., Terada, K. & Zhang, Q. 2006. Juxtaposition of adakite, boninite, high-TiO2 and low-TiO2 basalts in the Devonian southern Altay, Xinjiang, NW China. *Journal of Asian Earth Sciences*, **28**, 439–456.

O'Connor, J.T. 1965. A classification for quartz-rich igneous rocks based on feldspar ratio. *US Geological Survey Prof Paper*, **525-B**, 79–84.

Orolmaa, D., Erdenesaihan, G., Borisenko, A.S., Fedoseev, G.S., Babish, V.V. & Zhmodik, S.M. 2008. Permian-Triassic granitoid magmatism and metallogeny of the Hangayn (central Mongolia). *Russian Geology and Geophysics*, **49**, 534–544.

Osozawa, S., Tsolmon, G., Majigsuren, U., Sereenen, J., Niitsuma, S., Iwata, N., Pavlis, T. & Jahn, B.M. 2008. Structural evolution of the Bayanhongor region, west-central Mongolia. *Journal of Asian Earth Sciences*, **33**, 337–352.

Pearce, J.A. & Cann, J.R. 1973. Tectonic setting of basic volcanic rocks determined using trace element analyses. *Earth and Planetary Science Letters*, **19**, 290–300.

Pearce, J.A. & Peate, D.W. 1995. Tectonic implications of the composition of volcanic arc magmas. *Annual Reviews of Earth and Planetary Sciences*, **23**, 251–285.

Pearce, J.A., Harris, N.B.W. & Tindle, A.G. 1984. Trace element discrimination diagrams for the tectonic interpretation of granitic rocks. *Journal of Petrology*, **25**, 956–983.

Perelló, J., Cox, D., Garamjav, D., Sanjdorj, S., Diakov, S., Schissel, D., Munkhbat, T.O. & Oyun, G. 2001. Oyu Tolgoi, Mongolia; Siluro-Devonian porphyry Cu-Au-(Mo) and high-sulfidation Cu mineralization with a Cretaceous chalcocite blanket. *Economic Geology*, **96**, 1407–1428.

Pfänder, J.A., Jochum, K.P., Kozakov, I.K., Kröner, A. & Todt, W. 2002. Coupled evolution of back-arc and island arc-like mafic crust in the late-Neoproterozoic Agardagh Tes-Chem ophiolite, Central Asia: evidence from trace element and Sr–Nd–Pb isotope data. *Contribution to Mineralogy and Petrology*, **143**, 154–174.

Pfänder, J.A. & Kröner, A. 2004. Tectono-magmatic evolution, age and emplacement of the Agardagh Tes-Chem ophiolite in Tuva, Central Asia: Crustal growth by island arc accretion. *In:* Kusky, T. (ed.). *Precambrian ophiolites and related rocks, Elsevier Science, Amsterdam*, 207–221.

Pidgeon, R.T., Furfaro, D., Kennedy, A.K., Nemchin, A.A. & Van Bronswijk, W. 1994. Calibration of zircon standards for the Curtin SHRIMP II. *In:* Lanphere, M.A., Dalrymple, J.B. & Turrin, B.D.

(eds). Eighth International Conference on Geochronology, Cosmochronology, and Isotope Geology, Berkley. *US Geological Survey Circular*, **1107**, 251.

Pisarevsky, S.A. & Natapov, L.M. 2003. Siberia and Rodinia. *Tectonophysics*, **375**, 221–245

Pisarevsky, S.A., Natapov, L.M., Donskaya, T.V., Gladkochub, D.P. & Vernikovsky, V.A. 2008. Proterozoic Siberia: a promontory of Rodinia. *Precambrian Research*, **160**, 66–76.

Plank, T. 2005. Constraints from Thorium/Lanthanum on sediment recycling at subduction zones and the evolution of the continents. *Journal of Petrology*, **46**, 921–944.

Plank, T. & Langmuir, C.H. 1998. The chemical composition of subducting sediment and its consequences for the crust and mantle. *Chemical Geology*, **145**, 325–394.

Rauzer, A.A. 1987. Geological Map L47-XXVI, 1:200,000. Open file report 4186, Geological Funds of Mongolia, Ulaanbaatar, Mongolia. (In Russian)

Rippington, S., Cunningham, D. & England, R. 2008. Structure and petrology of the Altan Uul Ophiolite: new evidence for a late Carboniferous suture in the Gobi Altai, southern Mongolia. *Journal of the Geological Society*, London, **165**, 711–723.

Rudnick, R.L. 1995. Making continental crust. *Nature*, **378**, 571–578.

Rudnick, R.L. & Fountain, D.M. 1995. Nature and composition of the continental crust: a lower crustal perspective. *Reviews of Geophysics*, **33**, 267–309.

Ruzhentsev, S.V., 2001. The Variscan belt of South Mongolia and Dzungaria. *In:* Dergunov, A.B. (ed.). *Tectonics, Magmatism, and Metallogeny of Mongolia*. Routledge, London, p. 61–94.

Ruzhentsev, S.V. & Pospelov, I.I. 1992. The south Mongolian Variscan fold system. *Geotectonics*, **26**, 383–395.

Ruzhentsev, S.V. & Burashnikov, V.V. 1996. Tectonics of the western Mongolian Salairides. *Geotectonics*, **29** (5), 379–394.

Ruzhentsev, S.H., Badarch, H. & Voznesenskaya, A., 1985. Tectonics of the Trans-Altai Zone of Mongolia (The Gurvansaykhan and Dzolen Ranges). *Geotectonics*, **19**, 276–284.

Sal'nikova, E.B., Kozakov, I.K., Kotov, A.B., Kröner, A., Todt, W., Bibikova, E.V., Nutman, A., Yakopvleva, S.Z. & Kovach, V.P. 2001. Age of Paleozoic granites and metamorphism in the Tuvino-Mongolian Massif of the Central Asian mobile belt: Loss of a Precambrian microcontinent. *Precambrian Research*, **110**, 143–164.

Şengör, A.M.C., Natal'in, B.A. & Burtman, V.S. 1993. Evolution of the Altaid tectonic collage and Paleozoic crustal growth in Eurasia. *Nature*, **364**, 299–307.

Şengör, A.M.C. & Natal'in, B.A. 1996. Paleotectonics of Asia: fragments of a synthesis. *In:* Yin, A. & Harrison, T.A. (eds). *The tectonic evolution of Asia*. New York, Cambridge University Press, p. 486–640.

Shand, S.J. 1951. Eruptive rocks. 4th edition New York John Wiley, pp 488.

Shervais, J.W. 1982. Ti-V plots and the petrogenesis of modern and ophiolitic lavas. *Earth and Planetary Sciences Letters*, **59**, 101–118.

Smelov, A.P. & Timofeev, A.F. 2007. The age of the North Asian Cratonic basement: an overview. *Gondwana Research*, **12**, 279–288.

Stacey, J.S. & Kramers, J.D. 1975. Approximation of terrestrial lead isotope evolution by a two-stage model. *Earth and Planetary Science Letters*, **26**, 207–221.

Stern, R.A. 1997. The GSC sensitive high resolution ion microprobe (SHRIMP): analytical techniques of zircon U–Th–Pb age determinations and performance evaluation. *In:* Radiogenic age and isotope studies, Report 10. *Geological Survey of Canada, Current Research 1997-F*, 1–31.

Stoll, B., Jochum, K.P., Herwig, K., Amini, M., Flanz, M., Kreuzburg, B., Kuzmin, D., Willbold, M. & Enzweiler, J. 2008. An Automated Ir-strip-Heater for LA-ICP-MS Bulk Analysis of Geological Samples. *Geostandards and Geoanalytical Research*, **32**, 5–26.

Sun, S.S. & McDonough, W.F. 1989. Chemical and isotopic systematics of oceanic basalts: implications for mantle composition and processes. *In:* Saunders, A.D. & Norry, M.J. (eds). Magmatism in Ocean Basins. *Geological Society, London, Special Publications*, **42**, 313–345.

Sun, M., Yuan, C., Xiao, W., Long, X., Xia, X., Zhao, G., Lin, S., Wu, F. & Kröner, A. 2008. Zircon U–Pb and Hf isotopic study of gneissic rocks from the Chinese Altai: Progressive accretionary history in the early to middle Palaeozoic. *Chemical Geology*, **247**, 352–383.

Suyetenko, O.D. 1973. Geology of the Hercynian eugeosynclinal trough in southeastern Mongolia. *Geotectonics*, **7** (3), 177–183.

Takahashi, Y., Arakawa, Y., Oyungerel, S. & Naito, K. 2000. Geochronological data of granitoids in the Bayankhongor area, central Mongolia. *Bulletin of the Geological Survey of Japan*, **51**, 167–174.

Tapponnier, P. & Molnar, P. 1979. Active faulting and Cenozoic tectonics of the Tien Shan, Mongolia, and Baykal regions. *Journal of Geophysical Research*, **84**, 3425–3459.

Tarney, J. & Jones, C.E. 1994. Trace element geochemistry of orogenic igneous rocks and crustal growth models. *Journal of the Geological Society, London*, **151**, 855–868.

Taylor, S.R. & McLennan, S.M. 1985. The continental crust: its composition and evolution. *Blackwell Scientific Publications, Oxford*, pp. 312.

Taylor, B. & Martinez, F. 2003. Back-arc basin basalt systematics. *Earth and Planetary Science Letters*, **210**, 481–497.

Teraoka, Y., Suzuki, M., Tungalag, F., Ichinnorov, N. & Sakamaki, Y. 1996. Tectonic framework of the Bayankhongor area, West Mongolia. *Bulletin of the Geological Survey of Japan*, **47** (9), 447–455.

Tomurtogoo, O. 1997. A new tectonic scheme of the Paleozoides in Mongolia. *Mongolian Geoscientist*, **3**, 12–17.

Tomurtogoo, O. (ed.) 1998. Geological map of Mongolia: Mineral Resources Authority of Mongolia, Mongolian Academy of Sciences, Ulaanbaatar, scale 1:100,000, CD-ROM (with English summary).

Tomurtogoo, O. (ed.) 2002. Tectonic map of Mongolia at scale 1:1,000,000. Mineral Resources Authority of Mongolia, Mongolian Academy of Sciences, Ulaanbaatar, CD-ROM with English summary.

Tomurtogoo, O., Takahashi, Y., Nakajima, T., Ichinnorov, N., Oyungerel, S., Minjin, Ch., Bayarmandal, Lh., Teraoka, Y., Kurimoto, C., Tungalag, F., Delgertsogt, B. & Naito, K. 1998. Geological sheet map L-47-XVI, 1:200,000. *Open file report 5232*, Geological Funds of Mongolia, Ulaanbaatar, Mongolia.

Tomurtogoo, O. & Gerel, O. 1999. Geotraverse through a terrane collage in southern Khangay. *In:* Badarch, G., Jahn, B.M. & Tomurhuu, D. (eds). IGCP-420 Continental Growth in the Phanerozoic: Evidence from Central Asia, Second Workshop, Excursion Guidebook, July 25 - August 9, Ulaanbataar, Mongolia, 91 p.

Vassallo, R., Jolivet, M., Ritz, J.F., Braucher, R., Larroque, C., Sue, C., Todbileg, M. & Javkhlanbold, D. 2007. Uplift age and rates of the Gurvan Bogd system (Gobi-Altay) by apatite fission track analysis. *Earth and Planetary Science Letters*, **259**, 333–346.

Vernikovsky, V.A., Vernikovskaya, A.E., Wingate, M.T.D., Popov, N.V. & Kovach, V.P. 2007. The 880-864 Ma granites of the Yenisey Ridge, western Siberian margin: Geochemistry, SHRIMP geochronology, and tectonic implications. *Precambrian Research*, **154**, 175–191.

Wang, T., Zheng, Y., Gehrels, G.E. & Mu, Z. 2001. Geochronological evidence for existence of South Mongolian microcontinent; a zircon U–Pb age of granitoid gneisses from the Yagan-Onch Hayrhan metamorphic core complex on the Sino-Mongolian border. *Chinese Science B*ulletin, **46**, 2005–2008.

Wang, T., Hong, D.W., Jahn, B.M., Tong, Y., Wang, Y.B., Han, B.F. & Wang, X.X. 2006. Timing, petrogenesis, and setting of Paleozoic synorogenic intrusions from the Altai Mountains, northwest China: implications for the tectonic evolution of an accretionay orogen. *Journal of Geology*, **114**, 735–751.

Wang, C., Weddige, K. & Chuluun, M. 2005. Age revision of some Palaeozoic strata of Mongolia based on conodonts. *Journal of Asian Earth Sciences*, **25**, 759–771.

Wang, K.L., O'Reilly, S.Y., Griffin, W.L. & Pearson, N.J. 2006. In situ Os dating of peridotie xenoliths, Tariat, northern Mongolia. *Geochimica et Cosmochimica Acta*, 70(18S), A687.

Watanabe, Y. & Stein, H. J. 2000. Re-Os ages for the Erdenet and Tsagaan Suvarga porphyry Cu-Mo deposits, Mongolia, and tectonic implications. *Economic Geology,* **95**, 1537–1542.

Wendt, J.I. & Todt, W. 1991. A vapour digestion method for dating single zircons by direct measurement of U and Pb without chemical separation. *Terra abstracts,* **3**, 507–508.

White, W. & Patchett, J. 1984. Hf–Nd–Sr isotopic and incompatible element abundance in island arcs: implication for magma origins and crust-mantle evolution. *Earth and Planetary Science Letters*, **67**, 167–185.

Williams, I.S. 1998. U–Th–Pb Geochronology by ion microprobe. *In:* McKibben, M.A., Shanks, W.C. III & Ridley, W.I. (eds). Applications in micro-analytical techniques to understanding mineralizing processes. *Reviews in Economic Geology,* **7**, 1–35.

Wilson, M. 1989. Igneous petrogenesis, a global tectonic approach. Unwin Hyman, London, pp. 466.

Winchester, J.A. & Floyd, P.A. 1977. Geochemical discrimination of different magma series and their differentiation products using immobile elements. *Chemical Geology,* **20**, 325–343.

Windley B.F., Kröner A., Guo J., Qu G., Li Y. & Zhang C. 2002. Neoproterozoic to Paleozoic geology of the Altai orogen, NW China: New zircon age data and tectonic evolution. *Journal of Geology*, **110**, 719–37.

Windley, B.F., Alexeiev, D., Xiao, W.J., Kröner, A. & Badarch, G. 2007. Tectonic models for accretion of the Central Asian Orogenic Belt. *Geological Society, London*, **164**, 31–47.

Wood, D.A. 1980. The application of a Th–Hf–Ta diagram to problems of tectonomagmatic classification and to establishing the nature of crustal contamination of basaltic lavas of the British Tertiary volcanic province. *Earth and Planetary Science Letters*, **50**, 11–30.

Woodhead, J., Eggins, S. & Gamble, J. 1993. High field strength and transition element systematics in island arc and back-arc basin basalts: evidence for multi-phase melt extraction and a depleted mantle wedge. *Earth and Planetary Science Letters*, **114**, 491–504.

Workman, R.K. & Hart, S.R. 2005. Major and trace element composition of the depleted MORB mantle (DMM). *Earth and Planetary Science Letters*, **231**, 53–72.

Xiao, W.J., Windley, B.F., Hao, J. & Zhai, M.G. 2003. Accretion leading to collision and the Permian Solonker suture, Inner Mongolia, China: termination of the central Asian orogenic belt. *Tectonics*, **22**, doi:10.1029/2002TC001484.

Xiao, W.J., Han, C., Yuan, C., Sun, M., Lin, S., Chen, H., Li, Z., Li, J. & Sun, S. 2008. Middle Cambrian to Permian subduction-related accretionary orogenesis of Northern Xinjiang, NW

China: implications for the tectonic evolution of central Asia. *Journal of Asian Earth Sciences*, **32**, 102–117.

Xiao, W.J., Windley, B.F., Huang, B.C., Han, C.M., Yuan, C., Chen, H.L., Sun, M., Sun, S. & Li, J.L. 2009a. End-Permian to middle Triassic termination of the accretionary processes of the southern Altaids: implications for the geodynamic evolution, Phanerozoic continental growth, and metallogeny of Central Asia. *International Journal of Earth Sciences*, doi:10.1007/s00531-008-0407-z.

Xiao, W.J., Windley, B.F., Yuan, C., Sun, M., Han, C.M., Lin, S.F., Chen, H.L., Yan, Q.R., Liu, D.Y., Qin, K.Z., Li, J.L. & Sun, S. 2009b. Paleozoic multiple subduction-accretion processes of the southern Altaids. *American Journal of Science*, **309**, 221–270.

Xu, J.F., Castillo, P.R., Chen, F.R., Niu, H.C., Yu, X.Y. & Zhen, Z.P. 2003. Geochemistry of late Paleozoic mafic igneous rocks from the Kuerti area, Xinjiang, northwest China: implications for backarc mantle evolution. *Chemical Geology*, **193**, 137–154.

Yakubchuk, A. 2004. Architecture and mineral deposit settings of the Altaid orogenic collage: a revised model. *Journal of Asian Earth Sciences*, **23**, 761–779.

Yakubchuk, A. 2008. Re-deciphering the tectonic jigsaw puzzle of northern Eurasia. *Journal of Asian Earth Sciences*, **32**, 82–101.

Yarmolyuk, V.V., Kovalenko, V.I., Sal'nikova, E.B., Kozakov, I.K., Kotov, A.B., Kovach, V.P., Vladykin, N.V. & Yakovleva, S.Z. 2005. U–Pb age of syn- and postmetamorphic granitoids of south Mongolia: evidence for the presence of Grenvillides in the Central Asian Foldbelt. *Doklady Earth Sciences*, **404**, 986–990.

Yarmolyuk, V.V., Kovalenko, V.I., Kovach, V.P., Rytsk, E.Y., Kozakov, I.K., Kotov, A.B. & Sal'nikova, E.B. 2006. Early stages of the Paleoasian Ocean formation: results of geochronological, isotopic, and geochemical investigations of Late Riphean and Vendian-Cambrian complexes in the Central Asian Foldbelt. *Doklady Earth Sciences*, **411**, 1184–1189.

Yarmolyuk, V.V., Kovalenko, V.I., Anisimova, I.V., Sal'nikova, E.B., Kovach, V.P., Kozakov, I.K., Kozlovsky, A.M., Kudryashova, E.A., Kotov, A.B., Plotkina, Yu.V., Terent'eva, L.B. & Yakovleva, S.Z. 2008a. Late Riphean alkali granites of the Zabhan microcontinent: evidence for the timing of Rodinia breakup and formation of microcontinents in the Central Asian Fold Belt. *Doklady Earth Sciences*, **420**,583–588.

Yarmolyuk, V.V., Kovalenko, V.I, Kozakov, I.K., Sal'nikova, E.B., Bibikova, E.V. Kozakov, I.K., Kozlovsky, A.M., Kotov, A.B., Lebedev, V.I., Eengin G. & Fugzan, M.M. 2008b. The age of the Khangay batholith and the problem of batholith formation in central Asia. *Doklady Earth Sciences*, **423**, 1123–1128.

Yarmolyuk, V.V., Kovalenko, V.I., Kozlovsky, A.M., Kovach, V.P., Sal'nikova, E.B., Kovalenko, D.V., Kotov, A.B., Kudryashova, E.A., Lebedev, V.I. & Eengin, G. 2008c. Crust-forming processes in the Hercynides of the Central Asian Foldbelt. *Petrology*, **16**, 679–709.

Yarmolyuk, V.V., Kovalenko, V.I, Sal'nikova, E.B., Kovach, V.P., Kozlovsky, A.M., Kotov, A.B. & Lebedev, V.I. 2008d. Geochronology of igneous rocks and formation of the late Paleozoic south Mongolian active margin of the Siberian continent. *Stratigraphy and Geological Correlation*, **16**, 162–181.

Yuan, C., Sun, M., Xiao, W., Li, X., Chen, H., Lin, S., Xia, X. & Long, X. 2007. Accretionary orogenesis of the Chinese Altai: Insights from Paleozoic granitoids. *Chemical Geology*, **242**, 22–39.

Zabotkin, L.B. 1988. Geological Maps, sheets L-47-XXIV, L-47-XXIX, L-47-XXX, L-47-XXXIV, L-47-XXXV, 1:200,000. Open file report 4276, Geological Funds of Mongolia, Ulaanbaatar, Mongolia. (In Russian)

Zhang, H.X., Niu, H.C., Terada, K., Yu, X.Y., Sato, H. & Ito, J. 2003. Zircon SHRIMP U–Pb dating on plagiogranite from Kuerti ophiolite in Altay, north Xinjiang. *Chinese Science Bulletin*, **48**, 2231–2235.

Zhang, S.H., Zhao, Y., Song, B., Hu, J.M., Liu, S.W., Yang, Y.H., Chen, F.K., Liu, X.M. & Liu, J. 2009. Contrasting Late Carboniferous and Late Permian-Middle Triassic intrusive suites from the northern margin of the North China craton. *Geological Society of America Bulletin*, **121**, 181–200.

Zhao, Y., Song, B. & Zhang, S.H. 2006. The Central Mongolian microcontinent: Its Yangtze affinity and tectonic implications. *In:* Jahn, B.M. & Chung, L. (eds). Abst.-vol., Symposium on continental growth and orogeny in Asia Taipei Taiwan March 19-26, 135–136.

Zheng, C.Q., Kato, T., Enami, M. & Xu, X.C. 2007. CHIME monazite ages of metasediments from the Altai orogen in northwestern China: Devonian and Permian ages of metamorphism and their significance. *The Island Arc*, **16**, 598–604.

Zonenshain, L.P., Kuzmin, M.I. & Natapov, L.M. 1990. *In:* Page, B.M. (ed.). Geology of the USSR: a plate-tectonic synthesis. *American Geophysical Union, Geodynamic Series*, **21**, 242 p.

Zonenshain, L.P. 1967. Tectonics of the folded regions of central Asia (the structural patterns of geosynclinals regions). *Geotectonics*, **1** (6), 356–365.

Zonenshain, L.P. 1973. The evolution of Central Asiatic geosynclines through sea-floor spreading. *Tectonophysics*, **19**, 213–232.

Zonenshain, L.P. & Kuzmin, M.I. 1978. The Khan-Taishir ophiolitic complex of western Mongolia, its petrology, origin and comparison with other ophiolitic complex. *Contributions to Mineralogy and Petrology*, **67**, 95–109.

Zonenshain, L.P., Suyetenko, O.D., Jamyandamba, L. & Eengin, G. 1975. Structure of the axial part of the South Mongolian eugeosyncline in the Dzolen Range. *Geotectonics*, **9** (4), 214–220.

Zorin, Y.A., Belichenko, V.G., Tututanov, E.K., Kozhenvnikov, V.M., Ruzhentsev, S.V., Dergunov, A.B., Filippova, I.B., Tomurtogoo, O., Arvisbaatar, N., Bayasgalan, T., Biambaa, C. & Khosbayar, P. 1993. The South Siberia-Central Mongolia transect. *Tectonophysics*, **225**, 361–378.

Appendix

Appendix A. Sample list and GPS coordinates

Appendix B. SHRIMP II U–Th–Pb isotopic results of single zircons
    Appendix B-1. Chapter 1
    Appendix B-2. Chapter 2
    Appendix B-3. Chapter 3
    Appendix B-4. Chapter 4

Appendix C. Pb–Pb single zircon evaporation results
    Appendix C-1. Chapter 2

Appendix D. U–Pb analytical results for zircon fractions
    Appendix D-1. Chapter 3

Appendix E. Whole-rock major and trace element data
    Appendix E-1. Chapter 1
    Appendix E-2. Chapter 3
    Appendix E-3. Chapter 4

Appendix F. Whole-rock Sm–Nd isotopic results
    Appendix F-1. Chapter 3
    Appendix F-2. Chapter 4

Appendix G. Results of international geo-reference material analyses by LA-ICP-MS
    Appendix G-1. Chapter 3
    Appendix G-2. Chapter 4

Appendix A. Sample list and GPS coordinates

Chapter	Sample	Sub-locality	Age (Ma)[a]	Lithology	Latitude	Longitude
	Baga Bogd Massif					
1	Mo283	Unnamed Valley	498 ± 3[S]	Dioritic gneiss	N44°45'58.8"	E101°44'35.4"
1	Mo286	Unnamed Valley	499 ± 3[S]	Granodioritic gneiss	N44°45'58.8"	E101°44'35.4"
1	Mo380	Unnamed Valley	501 ± 4[S]	Leucocratic granite gneiss	N44°46'11.7"	E101°44'41.0"
1	Mo381	Unnamed Valley	1519 ± 11[S]	Granite gneiss	N44°46'11.7"	E101°44'41.0"
1	Mo385	Borbituutiin Valley	954 ± 8[S]	Light grey augen-gneiss	N44°46'05.3"	E101°41'29.0"
1	Mo387	Borbituutiin Valley	983 ± 6[S]	Dark grey augen-gneiss	N44°46'08.0"	E101°41'31.2"
1	Mo388	Borbituutiin Valley	502 ± 6[S]	Fine-grained leucogneiss	N44°47'03.5"	E101°41'14.1"
1	Mo389	Tsagaanburgas Valley	956 ± 3[S]	Light grey granite gneiss	N44°47'29.8"	E101°37'16.9"
	Baydrag terrane and Bayankhongor ophiolite zone					
2	M179	Taats River	537 ± 6[S]	Granite vein	N45°38'19.4"	E101°20'03.8"
2	M181	Taats River	1839 ± 8[S]	Layered granite gneiss	N45°37'46.7"	E101°14'52.4"
2	M290	NE of Bayanteg	472 ± 6[S]	Felsic metavolcanic rock	N45°44’14.7"	E101°43'32.4"
2	M295	Taats River	579 ± 7[S]	Porphyritic metagranite	N45°46'24.8"	E101°23'31.1"
2	M297	Taats River	601 ± 7[S]	Felsic metavolcanic rock	N45°51'53.7"	E101°24'16.9"
2	M298	Taats River	1051 ± 10[S]	Layered granite gneiss	N45°37'44.6"	E101°14'47.6"
2	M423	Taats River	519 ± 9[S]	Syntectonic granite	N45°40'45.2"	E101°22'52.7"
2	M424	Taats River	569 ± 2[S]	Granite gneiss	N45°50'06.5"	E101°23'04.3"
2	MBYH 13-2	Baydrag terrane	1826 ± 27[S]	Garnet-two pyroxene granulite	N46°16'51.2"	E99°26'34.8"
2	M98/B9	Baydrag terrane	2409 ± 1[E]	Enderbitic gneiss	N46°16'59.2"	E99°28'40.3"
2	M98/B10	Baydrag terrane	1840 ± 1[E]	Metapelite	N46°16'59.2"	E99°28'40.3"
2	M98/B11	Burd Gol mélange		Quartzite	N46°20'57.5"	E99°38'30.6"
2	M99/B13	Dzag Zone		Sandstone	N46°33'37.8"	E100°09'20.6"
	Halbagant Range					
3	M191			Metarhyolite	N44°43'03.0"	E100°53'46.3"
3	M192			Metabasalt	N44°43'03.0"	E100°53'46.3"
3	M193			Metadacite	N44°43'03.0"	E100°53'46.3"
3	M194			Metabasalt	N44°43'03.0"	E100°53'46.3"
3	M195		293 ± 3[S]	Rhyolite dyke	N44°42'30.2"	E100°52'20.3"
3	M196			Metaandesite	N44°42'30.2"	E100°52'20.3"
3	M197			Metarhyolite	N44°42'30.2"	E100°52'20.3"
3	M301			Metabasalt	N44°42'56.2"	E100°53'14.9"
3	M302			Metabasalt	N44°42'58.1"	E100°53'00.6"
3	M304			Metabasalt	N44°42'42.5"	E100°52'37.6"
3	M305			Metabasalt	N44°42'39.6"	E100°52'34.5"
3	M306			Basalte dyke	N44°42'38.0"	E100°52'25.4"
3	M307			Metaandesite tuff	N44°42'40.3"	E100°52'11.8"
3	M308			Basalt dyke	N44°42'40.3"	E100°52'11.8"
3	M309		441 ± 5[S]	Pyroclastic metarhyolite	N44°42'38.2"	E100°52'09.2"
3	M310			Basalt dyke	N44°42'38.2"	E100°52'09.2"
3	M311			Pyroclastic metarhyolite	N44°42'23.5"	E100°52'05.2"
3	M313			Metarhyolite	N44°42'20.1"	E100°52'03.8"
3	M315			Metaandesite	N44°41'55.8"	E100°51'57.1"
3	M319	Hulhiry Valley	345 ± 3[T]	Undeformed granodiorite	N44°43'41.0"	E100°51'02.2"
	Bayanleg Hatuu Range					
3	M325	Hulsnii Valley		Granite dyke	N44°27'31.3"	E100°51'01.2"
3	M327	Hulsnii Valley		Metadacite	N44°27'17.5"	E100°50'56.2"
3	M328	Hulsnii Valley	443 ± 5[S]	Metadacite	N44°27'01.5"	E100°50'56.9"

[a] Superscripts indicate method used to obtain zircon ages as follow: E: evaporation, Pb–Pb; S: SHRIMP, U–Pb; T: TIMS, U–Pb.

Appendix A. (*continued*)

Chapter	Sample	Sub-locality	Age (Ma)[a]	Lithology	Latitude	Longitude
	Bayanleg Hatuu Range					
3	M329	Hulsnii Valley		Metarhyolite	N44°26'37.3"	E100°50'23.2"
3	M330	Hulsnii Valley		Metadacite	N44°26'25.2"	E100°50'13.7"
3	M332	Hulsnii Valley		Metagranite	N44°25'48.8"	E100°49'48.2"
	Shine Jinst area					
3	M211		454 ± 4[S]	Felsic gneiss	N44°35'23.5"	E99°16'00.6"
3	M212			Amphibolite	N44°37'20.1"	E99°17'05.6"
3	M213			Amphibolite	N44°37'20.1"	E99°17'05.6"
3	M214			Amphibolite	N44°37'20.1"	E99°17'05.6"
3	M215			Felsic gneiss	N44°37'20.1"	E99°17'05.6"
3	M216			Amphibolite	N44°37'20.1"	E99°17'05.6"
3	M217			Felsic gneiss	N44°37'20.1"	E99°17'05.6"
3	M218			Felsic gneiss	N44°37'20.1"	E99°17'05.6"
3	M219			Amphibolite	N44°37'20.1"	E99°17'05.6"
3	M220			Felsic gneiss	N44°37'20.1"	E99°17'05.6"
3	M221			Felsic gneiss	N44°37'44.3"	E99°17'33.1"
3	M222			Amphibolite	N44°37'44.3"	E99°17'33.1"
3	M224			Felsic gneiss	N44°37'44.3"	E99°17'33.1"
3	M225		428 ± 71[T]	Felsic gneiss	N44°37'44.3"	E99°17'33.1"
3	M226		415 ± 3[S]	Tonalitic gneiss	N44°37'44.3"	E99°17'33.1"
3	M227			Meta-granite	N44°38'22.9"	E99°18'02.9"
	Tseel terrane					
4	M3884	Devreh Valley	397 ± 3[S]	Metarhyolite	N44°55'25.0"	E97°49'13.0"
4	M243	Devreh Valley	279 ± 2[S]	Feldspar porphyry	N44°54'03.1"	E97°48'13.5"
4	M244	Devreh Valley		Diorite	N44°54'03.1"	E97°48'13.5"
4	M245	Devreh Valley		Pyroclastic metadacite	N44°53'31.4"	E97°48'06.0"
4	M246	Devreh Valley		Pyroclastic metarhyolite	N44°53'31.4"	E97°48'06.0"
4	M247	Devreh Valley		Metarhyolite	N44°53'31.4"	E97°48'06.0"
4	M248	Devreh Valley		Metarhyolite	N44°53'31.4"	E97°48'06.0"
4	M249	Devreh Valley		Pyroclastic metarhyolite	N44°53'31.4"	E97°48'06.0"
4	M250	Devreh Valley		Pyroclastic metarhyolite	N44°53'31.4"	E97°48'06.0"
4	M251	Devreh Valley		Pyroclastic metarhyolite	N44°53'31.4"	E97°48'06.0"
4	M252	Devreh Valley		Pyroclastic metarhyolite	N44°53'21.2"	E97°47'53.6"
4	M253	Devreh Valley		Pyroclastic metarhyolite	N44°53'21.2"	E97°47'53.6"
4	M254	Devreh Valley		Metadacite	N44°52'38.6"	E97°47'33.8"
4	M255	Devreh Valley		Metabasalt	N44°52'38.6"	E97°47'33.8"
4	M256	Devreh Valley		Metabasalt	N44°52'38.6"	E97°47'33.8"
4	M257	Devreh Valley		Metabasalt	N44°52'38.6"	E97°47'33.8"
4	M258	Devreh Valley		Pyroclastic metarhyolite	N44°52'38.6"	E97°47'33.8"
4	M259	Devreh Valley		Metabasalt	N44°52'38.6"	E97°47'33.8"
4	M3883	Devreh Valley	396 ± 3[S]	Porphyritic metarhyolite	N44°52'23.0"	E97°48'14.0"
4	M260	Devreh Valley		Granodioritic gneiss	N44°51'39.5"	E97°46'10.7"
4	M267	Devreh Valley		Granodioritic gneiss	N44°51'10.9"	E97°46'41.0"
4	M268	Devreh Valley		Pyroclastic metadacite	N44°50'32.6"	E97°46'17.9"
4	M269	Devreh Valley		Pyroclastic metadacite	N44°49'39.9"	E97°46'07.8"
4	M270	Devreh Valley		Metarhyolite	N44°49'39.9"	E97°46'07.8"
4	M271	Devreh Valley		Pyroclastic metadacite	N44°48'49.9"	E97°45'38.0"
4	M272	Devreh Valley		Pyroclastic metadacite	N44°48'05.7"	E97°45'23.6"

Appendix B-1. Chapter 1

Appendix B-1. SHRIMP II U–Th–Pb isotopic results for single zircon grains of granitoid gneisses from the Baga Bogd massif

Labels[a]	U	Th	^{204}Pb/^{206}Pb	^{208}Pb/^{206}Pb	^{207}Pb/^{206}Pb	^{206}Pb/^{238}U	^{207}Pb/^{235}U	Age ± 1σ (Ma)		
	(ppm)	(ppm)						^{206}Pb/^{238}U	^{207}Pb/^{235}U	^{207}Pb/^{206}Pb
Mo283[b]										
1.1	1374	35	0.00011	0.0086 ± 15	0.0577 ± 8	0.0804 ± 6	0.640 ± 10	499 ± 4	503 ± 6	520 ± 28
2.1	1622	295	0.00017	0.0740 ± 13	0.0614 ± 6	0.1072 ± 8	0.908 ± 12	656 ± 5	656 ± 6	654 ± 20
3.1	1132	1659	0.00003	0.4443 ± 30	0.0579 ± 8	0.0803 ± 6	0.641 ± 11	498 ± 4	503 ± 7	526 ± 30
4.1	1636	262	0.00003	0.0405 ± 11	0.0567 ± 6	0.0807 ± 6	0.631 ± 8	500 ± 4	497 ± 5	480 ± 22
5.1	668	410	0.00019	0.1957 ± 31	0.0571 ± 12	0.0803 ± 6	0.632 ± 14	498 ± 4	497 ± 9	494 ± 45
6.1	790	183	0.00007	0.0665 ± 15	0.0576 ± 7	0.0802 ± 6	0.636 ± 10	497 ± 4	500 ± 6	513 ± 28
7.1	689	498	0.00011	0.2192 ± 30	0.0578 ± 11	0.0804 ± 6	0.641 ± 13	498 ± 4	503 ± 8	524 ± 40
8.1	781	729	0.00017	0.2994 ± 39	0.0564 ± 14	0.0804 ± 6	0.624 ± 16	498 ± 4	493 ± 10	466 ± 52
9.1	625	235	0.00003	0.1211 ± 32	0.0575 ± 13	0.0803 ± 6	0.637 ± 16	498 ± 4	514 ± 6	580 ± 26
Mo286[b]										
1.1	1100	2357	0.00001	0.6597 ± 17	0.0572 ± 4	0.0762 ± 9	0.601 ± 9	473 ± 5	478 ± 5	499 ± 14
2.1	1348	2993	0.00001	0.6856 ± 16	0.0571 ± 3	0.0776 ± 9	0.611 ± 8	482 ± 6	484 ± 5	497 ± 12
3.1	1672	2627	0.00020	0.4864 ± 15	0.0572 ± 4	0.0785 ± 9	0.619 ± 9	487 ± 6	489 ± 6	501 ± 16
4.1	1406	52	0.00003	0.0107 ± 7	0.0572 ± 4	0.0761 ± 9	0.600 ± 9	473 ± 5	477 ± 5	498 ± 14
5.1	1162	19	<0.00001	0.0057 ± 2	0.0572 ± 3	0.0793 ± 10	0.625 ± 8	492 ± 6	493 ± 5	499 ± 11
Mo380[c]										
1.1	390	214	0.00011	0.1908 ± 19	0.0578 ± 7	0.0803 ± 10	0.640 ± 12	498 ± 6	503 ± 7	524 ± 27
2.1	392	487	0.00017	0.3958 ± 25	0.0573 ± 8	0.0815 ± 11	0.643 ± 13	505 ± 6	504 ± 8	502 ± 31
3.1	1279	339	0.00003	0.0820 ± 4	0.0700 ± 2	0.1535 ± 20	1.481 ± 20	920 ± 11	923 ± 8	929 ± 6
4.1	566	148	0.00003	0.0900 ± 7	0.0688 ± 3	0.1481 ± 19	1.405 ± 20	890 ± 10	891 ± 9	893 ± 10
5.1	332	56	0.00019	0.1174 ± 18	0.0696 ± 8	0.1526 ± 20	1.464 ± 27	915 ± 11	916 ± 11	917 ± 23
6.1	320	36	0.00007	0.0385 ± 11	0.0662 ± 6	0.1347 ± 18	1.229 ± 20	815 ± 11	814 ± 8	813 ± 18
Mo381[c]										
1.1	158	288	0.00020	0.5526 ± 29	0.0948 ± 9	0.2664 ± 35	3.484 ± 60	1523 ± 18	1524 ± 14	1525 ± 18
2.1	290	257	0.00007	0.2797 ± 15	0.0944 ± 5	0.2231 ± 29	2.903 ± 43	1298 ± 15	1383 ± 11	1516 ± 11
3.1	459	97	0.00019	0.0521 ± 13	0.0949 ± 6	0.2436 ± 32	3.188 ± 49	1405 ± 17	1454 ± 12	1527 ± 13
4.1	885	853	0.00062	0.3494 ± 17	0.0942 ± 7	0.1877 ± 24	2.438 ± 39	1109 ± 13	1254 ± 11	1512 ± 14
Mo385[c]										
1.1	427	79	<0.00001	0.0599 ± 8	0.0710 ± 6	0.1548 ± 18	1.517 ± 23	928 ± 10	937 ± 9	959 ± 16
2.1	608	160	0.00001	0.0710 ± 10	0.0707 ± 5	0.1510 ± 18	1.472 ± 22	907 ± 10	919 ± 9	948 ± 16
3.1	435	69	<0.00001	0.0506 ± 7	0.0713 ± 5	0.1584 ± 19	1.557 ± 23	948 ± 11	953 ± 9	965 ± 15
4.1	387	145	0.00002	0.1344 ± 21	0.0707 ± 9	0.1403 ± 17	1.368 ± 25	846 ± 10	875 ± 11	949 ± 26
5.1	264	113	<0.00001	0.1334 ± 16	0.0709 ± 7	0.1590 ± 19	1.554 ± 25	951 ± 11	952 ± 10	953 ± 19
6.1	384	83	<0.00001	0.0678 ± 10	0.0708 ± 6	0.1395 ± 17	1.362 ± 21	842 ± 9	873 ± 9	952 ± 17
Mo387[c]										
1.1	441	193	0.00075	0.0701 ± 27	0.0719 ± 12	0.1631 ± 21	1.617 ± 36	974 ± 12	977 ± 14	984 ± 34
2.1	421	152	0.00008	0.0711 ± 13	0.0718 ± 6	0.1197 ± 16	1.185 ± 19	729 ± 9	794 ± 9	982 ± 17
3.1	749	340	0.00004	0.0699 ± 7	0.0719 ± 3	0.1547 ± 20	1.533 ± 22	927 ± 11	944 ± 9	982 ± 10
4.1	659	241	0.00004	0.0707 ± 7	0.0719 ± 4	0.1484 ± 19	1.471 ± 21	892 ± 11	919 ± 9	984 ± 10
5.1	119	67	0.00010	0.0958 ± 16	0.1042 ± 8	0.3013 ± 40	4.330 ± 70	1698 ± 20	1699 ± 13	1701 ± 14

[a] 1.1 is spot 1 on grain 1, 2.1 is spot 1 on grain 2, etc

[b] U–Th–Pb isotopic data obtained in St. Petersburg

[c] U–Th–Pb isotopic data obtained in Beijing

Appendix B-1. (*continued*)

Labels[a]	U	Th	^{204}Pb/^{206}Pb	^{208}Pb/^{206}Pb	^{207}Pb/^{206}Pb	^{206}Pb/^{238}U	^{207}Pb/^{235}U	Age ± 1σ (Ma)		
	(ppm)	(ppm)						^{206}Pb/^{238}U	^{207}Pb/^{235}U	^{207}Pb/^{206}Pb
Mo388[c]										
1.1	274	113	0.00033	0.0625 ± 35	0.0573 ± 15	0.0806 ± 11	0.637 ± 19	500 ± 6	501 ±12	504 ± 57
2.1	345	235	0.00022	0.0866 ± 25	0.0583 ± 11	0.0807 ± 11	0.648 ± 15	500 ± 6	507 ± 9	541 ± 40
3.1	254	136	0.00024	0.1031 ± 30	0.0577 ± 13	0.0814 ± 11	0.647 ± 17	504 ± 6	507 ±11	519 ± 48
4.1	333	220	0.00024	0.1141 ± 28	0.0568 ± 12	0.0807 ± 11	0.632 ± 16	500 ± 6	497 ±10	483 ± 45
5.1	792	368	0.00007	0.0812 ± 11	0.0577 ± 5	0.0813 ± 11	0.646 ± 10	504 ± 6	506 ± 6	518 ± 18
Mo389[c]										
1.1	419	92	0.00001	0.0631 ± 14	0.0711 ± 8	0.1601 ± 19	1.569 ± 28	957 ± 11	958 ± 11	960 ± 23
2.1	652	75	<0.00001	0.0322 ± 7	0.0708 ± 6	0.1493 ± 18	1.458 ± 23	897 ± 10	913 ± 10	952 ± 19
3.1	676	91	<0.00001	0.0387 ± 6	0.0709 ± 5	0.1468 ± 17	1.436 ± 20	883 ± 10	904 ± 8	956 ± 13
4.1	562	84	<0.00001	0.0478 ± 7	0.0710 ± 5	0.1363 ± 16	1.334 ± 20	824 ± 9	861 ± 8	958 ± 15
5.1	1199	233	<0.00001	0.0562 ± 5	0.0709 ± 3	0.1721 ± 20	1.681 ± 22	1024 ± 11	1002 ± 8	953 ± 10
6.1	446	64	0.00001	0.0450 ± 11	0.0709 ± 7	0.1402 ± 17	1.370 ± 22	846 ± 9	876 ± 9	954 ± 19
7.1	654	77	<0.00001	0.0374 ± 6	0.0710 ± 5	0.1350 ± 16	1.321 ± 19	816 ± 9	855 ± 8	957 ± 14

Appendix B-2. Chapter 2

Appendix B-2. SHRIMP II U–Th–Pb isotopic results for single zircons of metaigneous rocks from the Baydrag block and the Bayankhongor ophiolite zone

Sample[a]	U (ppm)	Th (ppm)	^{206}Pb/^{204}Pb	^{208}Pb/^{206}Pb	^{207}Pb/^{206}Pb	^{206}Pb/^{238}Pb	^{207}Pb/^{235}Pb	^{206}Pb/^{238}Pb age ± 1σ	^{207}Pb/^{235}Pb age ± 1σ	^{207}Pb/^{206}Pb age ± 1σ
MBYH13-2[b]										
1.1	210	51	0.00025	0.0658 ± 24	0.1108 ± 13	0.3142 ± 73	4.800 ± 131	1762 ± 36	1785 ± 23	1813 ± 21
1.2	221	91	0.00050	0.1073 ± 48	0.1111 ± 27	0.3146 ± 129	4.821 ± 242	1763 ± 64	1789 ± 43	1818 ± 44
2.1	190	36	0.00044	0.0498 ± 37	0.1112 ± 24	0.2923 ± 111	4.482 ± 206	1653 ± 56	1728 ± 39	1819 ± 39
6.1	252	52	0.00035	0.0575 ± 48	0.1092 ± 24	0.3072 ± 104	4.625 ± 197	1727 ± 52	1754 ± 36	1786 ± 40
7.1	198	67	0.00048	0.0916 ± 39	0.1146 ± 19	0.3110 ± 85	4.912 ± 165	1746 ± 42	1804 ± 29	1873 ± 30
8.1	252	110	0.00045	0.1269 ± 67	0.1130 ± 34	0.3127 ± 88	4.871 ± 214	1754 ± 43	1797 ± 38	1848 ± 56
10.1	144	50	0.00080	0.1136 ± 89	0.1121 ± 27	0.3200 ± 105	4.947 ± 212	1790 ± 51	1810 ± 37	1834 ± 44
M179[c]										
1.1	463	461	0.00001	0.3021 ± 20	0.0584 ± 6	0.0869 ± 6	0.700 ± 9	537 ± 4	539 ± 6	546± 23
1.2	201	184	0.00005	0.2611 ± 63	0.0579 ± 24	0.0866 ± 7	0.692 ± 31	535 ± 4	534 ± 18	527± 94
2.1	300	440	0.00001	0.4587 ± 39	0.0583 ± 9	0.0870 ± 6	0.699 ± 13	538 ± 4	538 ± 8	540± 34
2.2	258	59	<0.00001	0.0658 ± 11	0.0657 ± 6	0.1310 ± 10	1.187 ± 15	793 ± 6	795 ± 7	798± 19
M181[c]										
1.1	505	384	0.00002	0.2157 ± 8	0.1124 ± 4	0.3225 ± 24	5.000 ± 42	1802 ± 12	1819 ± 7	1839 ± 6
2.1	305	297	0.00002	0.2798 ± 12	0.1125 ± 5	0.3294 ± 25	5.108 ± 47	1836 ± 12	1837 ± 8	1839 ± 8
3.1	183	78	<0.00001	0.1157 ± 11	0.1224 ± 7	0.3424 ± 28	5.778 ± 60	1898 ± 13	1943 ± 9	1992 ± 10
4.1	311	180	0.00031	0.1719 ± 22	0.1039 ± 10	0.2608 ± 20	3.738 ± 48	1494 ± 10	1580 ± 10	1696 ± 17
5.1	466	289	0.00002	0.1660 ± 8	0.1799 ± 5	0.4703 ± 36	11.666 ± 98	2485 ± 16	2578 ± 8	2652 ± 5
6.1	187	147	<0.00001	0.2217 ± 15	0.1224 ± 7	0.3564 ± 29	6.012 ± 62	1965 ± 14	1978 ± 9	1991 ± 10
7.1	130	131	0.00002	0.3037 ± 32	0.1124 ± 12	0.3297 ± 40	5.109 ± 86	1837 ± 19	1838 ± 14	1838 ± 19
8.1	246	46	<0.00001	0.1080 ± 17	0.1125 ± 10	0.2085 ± 23	3.234 ± 49	1221 ± 12	1465 ± 12	1840 ± 17
9.1	101	72	0.00002	0.2095 ± 40	0.1226 ± 18	0.3618 ± 46	6.115 ± 125	1991 ± 22	1992 ± 18	1994 ± 26
10.1	214	122	0.00001	0.1771 ± 21	0.1123 ± 10	0.2949 ± 33	4.568 ± 68	1666 ± 16	1743 ± 12	1838 ± 16
11.1	162	110	0.00004	0.1958 ± 23	0.1125 ± 10	0.3291 ± 39	5.104 ± 81	1834 ± 19	1837 ± 13	1840 ± 17
12.1	308	185	<0.00001	0.1765 ± 17	0.1125 ± 8	0.3113 ± 34	4.828 ± 66	1747 ± 17	1790 ± 12	1840 ± 13
13.1	108	74	<0.00001	0.1916 ± 20	0.2140 ± 13	0.5806 ± 7	17.127 ± 251	2951 ± 30	2942 ± 14	2936 ± 10
14.1	140	62	<0.00001	0.1290 ± 16	0.1812 ± 12	0.4661 ± 56	11.647 ± 167	2467 ± 25	2576 ± 13	2664 ± 11
15.1	130	147	0.00002	9.3138 ± 26	0.2399 ± 14	0.5948 ± 74	19.670 ± 281	3009 ± 30	3075 ± 14	3119 ± 9
M290[b]										
1.1	438	273	0.00012	0.2042 ± 24	0.0568 ± 9	0.0763 ± 10	0.598 ± 13	474 ± 6	476 ± 8	484 ± 37
2.1	1320	938	0.00004	0.2438 ± 11	0.0564 ± 3	0.0758 ± 10	0.590 ± 9	471 ± 6	471 ± 6	470 ± 14
3.1	449	183	0.00027	0.1163 ± 27	0.0569 ± 11	0.0758 ± 10	0.595 ± 15	471 ± 6	474 ± 9	489 ± 44
4.1	452	222	0.00021	0.1612 ± 23	0.0569 ± 9	0.0757 ± 10	0.593 ± 13	470 ± 6	473 ± 8	486 ± 36
5.1	816	393	0.00010	0.1506 ± 13	0.0567 ± 5	0.0762 ± 10	0.595 ± 10	473 ± 6	474 ± 6	478 ± 19
M295[b]										
1.1	460	265	0.00001	0.1996 ± 22	0.0604 ± 7	0.0933 ± 111	0.774 ± 14	575 ± 7	584 ± 8	618 ± 26
2.1	589	370	<0.00001	0.1882 ± 17	0.0591 ± 6	0.0941± 111	0.766 ± 12	580 ± 7	578 ± 7	570 ± 20
3.1	381	225	0.00002	0.1924 ± 26	0.0604 ± 9	0.0939 ± 112	0.782 ± 16	579 ± 7	589 ± 8	628 ± 24
4.1	767	634	0.00001	0.2612 ± 18	0.0591 ± 5	0.0945 ± 112	0.770 ± 12	582 ± 7	582 ± 7	580 ± 17
5.1	514	282	<0.00001	0.1714 ± 20	0.0598 ± 7	0.0943 ± 112	0.777 ± 14	581 ± 7	584 ± 8	597 ± 24

[a] 1.1 is spot 1 on grain 1, 2.1 is spot 1 on grain 2, etc.

[b] U–Th–Pb isotopic data obtained in Beijing.

[c] U–Th–Pb isotopic data obtained in Perth.

Appendix B-2. (*continued*)

Sample	U (ppm)	Th (ppm)	^{206}Pb/^{204}Pb	^{208}Pb/^{206}Pb	^{207}Pb/^{206}Pb	^{206}Pb/^{238}Pb	^{207}Pb/^{235}Pb	^{206}Pb/^{238}Pb age ± 1σ	^{207}Pb/^{235}Pb age ± 1σ	^{207}Pb/^{206}Pb age ± 1σ
M297[b]										
1.1	280	95	<0.00001	0.1741 ± 31	0.0597 ± 11	0.0564 ± 67	0.465 ± 10	354 ± 4	387 ± 7	593 ± 38
2.1	189	144	<0.00001	0.2289 ± 34	0.0601 ± 10	0.0825 ± 98	0.684 ± 15	511 ± 6	529 ± 6	608 ± 36
3.1	167	97	0.00007	0.1988 ± 71	0.0516 ± 25	0.0308 ± 37	0.220 ± 11	196 ± 2	201 ± 9	269 ± 111
4.1	745	195	<0.00001	0.0802 ± 07	0.0707 ± 4	0.1607 ± 191	1.568 ± 22	961 ± 11	957 ± 8	950 ± 11
5.1	195	129	<0.00001	0.1903 ± 33	0.0596 ± 11	0.0739 ± 88	0.608 ± 14	460 ± 5	482 ± 9	589 ± 38
6.1	315	78	<0.00001	0.0742 ± 11	0.0694 ± 6	0.1526 ± 183	1.461 ± 23	916 ± 10	915 ± 10	912 ± 18
7.1	213	142	0.00001	0.1976 ± 30	0.0597 ± 10	0.0804 ± 96	0.662 ± 14	499 ± 6	516 ± 9	593 ± 35
8.1	667	469	0.00011	0.2390 ± 14	0.0600 ± 5	0.0829 ± 108	0.686 ± 11	513 ± 6	530 ± 7	604 ± 17
9.1	307	338	0.00017	0.3420 ± 24	0.0665 ± 8	0.1360 ± 178	1.248 ± 23	822 ± 10	822 ± 11	823 ± 25
10.1	754	303	0.00037	0.1326 ± 21	0.0601 ± 8	0.0884 ± 115	0.732 ± 15	546 ± 7	558 ± 9	606 ± 30
M298[b]										
1.1	995	580	0.00009	0.1708 ± 9	0.0743 ± 4	0.1559 ± 20	1.598 ± 23	934 ± 11	969 ± 9	1051 ± 10
2.1	431	305	0.00011	0.2195 ± 13	0.0743 ± 5	0.1615 ± 21	1.654 ± 26	965 ± 12	991 ± 10	1050 ± 14
3.1	458	253	0.00077	0.1414 ± 30	0.0744 ± 13	0.1589 ± 21	1.630 ± 37	951 ± 12	982 ± 14	1051 ± 35
4.1	1309	635	0.00011	0.1392 ± 8	0.0743 ± 3	0.1454 ± 19	1.490 ± 21	875 ± 11	926 ± 9	1050 ± 9
5.1	2643	325	0.00031	0.0160 ± 8	0.0744 ± 4	0.1781 ± 23	1.827 ± 27	1056 ± 13	1055 ± 9	1053 ± 10
M424[b]										
1.1	213	76	0.00030	0.1089 ± 42	0.0590 ± 17	0.0907 ± 9	0.738 ± 24	560 ± 6	561 ± 14	569 ± 64
2.1	286	139	0.00025	0.1567 ± 39	0.0591 ± 15	0.0837 ± 9	0.682 ± 20	518 ± 5	528 ± 12	570 ± 57
3.1	271	50	0.00028	0.0609 ± 35	0.0590 ± 15	0.0846 ± 9	0.688 ± 20	523 ± 5	532 ± 12	568 ± 57
4.1	193	50	0.00043	0.0874 ± 54	0.0591 ± 23	0.0684 ± 7	0.557 ± 23	426 ± 4	449 ± 15	570 ± 83
M423[b]										
1.1	75	43	0.00060	0.1729 ± 93	0.0564 ± 37	0.0840 ± 9	0.653 ± 44	520 ± 6	510 ± 27	467 ±144
2.1	155	143	0.00055	0.2847 ± 71	0.0584 ± 26	0.0834 ± 9	0.672 ± 32	517 ± 5	522 ± 20	545 ± 99
3.1	216	142	0.00027	0.1925 ± 42	0.0575 ± 16	0.0840 ± 9	0.666 ± 21	520 ± 5	518 ± 13	510 ± 61

Appendix B-3. Chapter 3

Appendix B-3. SHRIMP II U–Th–Pb isotopic results for single zircons of rock samples from the Gobi-Altai, south Mongolia

Labels[a]	U (ppm)	Th (ppm)	^{204}Pb/^{206}Pb	^{208}Pb/^{206}Pb	^{207}Pb/^{206}Pb	^{206}Pb/^{238}U	^{207}Pb/^{235}U	^{206}Pb/^{238}U Age ±1σ	^{207}Pb/^{235}U Age ±1σ	^{207}Pb/^{206}Pb Age ±1σ
M309[c]										
1.1	221	172	0.00007	0.2319 ± 73	0.0563 ± 28	0.0708 ± 9	0.549 ± 29	441 ± 6	444 ± 19	463 ± 111
2.1	265	226	0.00008	0.2582 ± 50	0.0562 ± 17	0.0720 ± 10	0.558 ± 19	448 ± 6	450 ± 12	462 ± 66
3.1	213	159	<0.00001	0.2325 ± 40	0.0554 ± 11	0.0711 ± 9	0.542 ± 14	443 ± 6	440 ± 9	427 ± 45
4.1	835	422	0.00039	0.1491 ± 43	0.0574 ± 18	0.0783 ± 10	0.620 ± 22	486 ± 6	490 ± 14	508 ± 70
5.1	216	169	0.00002	0.2386 ± 45	0.0569 ± 13	0.0704 ± 9	0.552 ± 16	438 ± 6	446 ± 10	488 ± 52
6.1	287	225	<0.00001	0.2460 ± 40	0.0566 ± 11	0.0698 ± 9	0.545 ± 13	435 ± 5	441 ± 9	477 ± 43
M195[b]										
1.1	577	289	0.00224	0.1630 ± 109	0.0541 ± 41	0.0468 ± 4	0.350 ± 29	295 ± 3	304 ± 22	376 ± 184
2.1	354	294	0.00057	0.2570 ± 91	0.0523 ± 34	0.0464 ± 4	0.334 ± 22	292 ± 2	293 ± 17	297 ± 150
3.1	182	87	0.00113	0.1657 ± 263	0.0540 ± 106	0.0415 ± 6	0.309 ± 62	262 ± 4	273 ± 47	372 ± 380
4.1	338	179	0.00028	0.1428 ± 51	0.0573 ± 21	0.0779 ± 6	0.616 ± 23	484 ± 4	488 ± 15	505 ± 79
5.1	284	305	0.00086	0.3474 ± 107	0.0522 ± 39	0.0466 ± 4	0.335 ± 26	294 ± 3	293 ± 19	292 ± 171
6.1	613	517	0.00043	0.2276 ± 70	0.0513 ± 27	0.0365 ± 3	0.258 ± 14	231 ± 2	233 ± 11	256 ± 121
7.1	278	111	0.00024	0.1340 ± 64	0.0565 ± 26	0.0774 ± 6	0.603 ± 29	481 ± 4	479 ± 18	472 ± 102
8.1	355	231	0.00068	0.1945 ± 84	0.0539 ± 33	0.0465 ± 4	0.345 ± 22	293 ± 2	301 ± 16	366 ± 139
M328[c]										
1.1	137	68	0.00003	0.1593 ± 62	0.0576 ± 24	0.0709 ± 9	0.563 ± 26	441 ± 6	453 ± 17	515 ± 93
2.1	225	117	0.00007	0.1511 ± 92	0.0577 ± 39	0.0717 ± 10	0.571 ± 40	447 ± 6	459 ± 26	520 ± 143
3.1	229	32	<0.00001	0.0477 ± 18	0.0567 ± 11	0.0716 ± 9	0.559 ± 14	445 ± 6	451 ± 9	479 ± 44
4.1	246	30	0.00012	0.0374 ± 112	0.0557 ± 49	0.0707 ± 10	0.542 ± 50	440 ± 6	440 ± 32	438 ± 198
5.1	189	34	<0.00001	0.0608 ± 23	0.0576 ± 13	0.0709 ± 9	0.563 ± 16	442 ± 6	454 ± 10	516 ± 51
6.1	327	151	<0.00001	0.1428 ± 26	0.0573 ± 9	0.0714 ± 9	0.564 ± 13	445 ± 6	454 ± 8	502 ± 36
M211[b]										
1.1	248	60	0.00034	0.0772 ± 72	0.0581 ± 30	0.0734 ± 6	0.588 ± 32	457 ± 4	470 ± 20	533 ± 112
2.1	214	75	0.00042	0.1152 ± 56	0.0580 ± 23	0.0729 ± 6	0.583 ± 25	453 ± 4	466 ± 16	530 ± 87
3.1	257	55	0.00068	0.0603 ± 87	0.0563 ± 36	0.0728 ± 6	0.565 ± 38	453 ± 4	455 ± 24	464 ± 140
4.1	428	56	0.00032	0.0391 ± 58	0.0562 ± 25	0.0727 ± 6	0.563 ± 26	453 ± 4	454 ± 17	458 ± 98
5.1	255	69	0.00026	0.0939 ± 90	0.0589 ± 37	0.0730 ± 7	0.592 ± 39	454 ± 4	472 ± 24	562 ± 140
M226[b]										
1.1	338	162	0.00067	0.1387 ± 74	0.0559 ± 30	0.0660 ± 6	0.509 ± 28	412 ± 3	418 ± 19	449 ± 120
2.1	344	173	0.00024	0.1636 ± 76	0.0554 ± 31	0.0668 ± 6	0.051 ± 29	417 ± 3	418 ± 19	428 ± 124
3.1	340	184	0.00030	0.1775 ± 77	0.0565 ± 31	0.0662 ± 6	0.515 ± 29	413 ± 3	422 ± 19	471 ± 121
4.1	1407	617	0.00207	0.1251 ± 63	0.0542 ± 26	0.0526 ± 4	0.393 ± 19	330 ± 3	337 ± 14	380 ± 106
5.1	307	179	0.00046	0.1859 ± 68	0.0553 ± 27	0.0668 ± 6	0.510 ± 26	417 ± 3	418 ± 17	426 ± 108
6.1	1173	497	0.00067	0.1320 ± 44	0.0556 ± 18	0.0607 ± 6	0.465 ± 17	380 ± 4	388 ± 12	436 ± 73

[a] 1.1 is spot 1 on grain 1, 2.1 is spot 1 on grain 2, etc.

[b] U–Th–Pb isotopic data obtained in St. Petersburg.

[c] U–Th–Pb isotopic data obtained in Beijing.

Appendix B-4. Chapter 4

Appendix B-4. SHRIMP II U–Th–Pb isotopic data for single zircons of igneous rocks from the Devreh Valley, Tseel terrane

Labels[*]	U	Th	^{204}Pb/^{206}Pb	4f206	^{208}Pb/^{206}Pb	^{207}Pb/^{206}Pb	^{206}Pb/^{238}U	^{207}Pb/^{235}U	Age (Ma) ± 1σ		
	(ppm)	(ppm)		(%)					^{206}Pb/^{238}U	^{207}Pb/^{235}U	^{207}Pb/^{206}Pb
M243[†]											
1.1	364	319	0.00075	0.014	0.2545 ± 93	0.0505 ± 36	0.0444 ± 4	0.309 ± 22	280 ± 2	273 ± 17	219 ± 160
2.1	257	362	0.00099	0.018	0.4416 ± 140	0.0521 ± 50	0.0440 ± 4	0.316 ± 31	278 ± 3	279 ± 24	290 ± 220
3.1	234	149	0.00084	0.015	0.1785 ± 139	0.0549 ± 56	0.0445 ± 4	0.337 ± 35	281 ± 3	295 ± 26	409 ± 229
4.1	311	444	0.00054	0.010	0.4477 ± 118	0.0541 ± 42	0.0440 ± 4	0.328 ± 26	278 ± 2	288 ± 20	374 ± 176
5.1	437	999	0.00046	0.009	0.7149 ± 105	0.0530 ± 31	0.0439 ± 4	0.321 ± 19	277 ± 2	283 ± 15	329 ± 134
6.1	424	376	0.00026	0.005	0.2842 ± 90	0.0521 ± 34	0.0444 ± 4	0.319 ± 21	280 ± 2	281 ± 16	291 ± 150
M3883[‡]											
1.1	957	688	0.00001	0.000	0.2203 ± 20	0.0538 ± 7	0.0636 ± 7	0.472 ± 9	398 ± 4	393 ± 6	365 ± 31
1.2	1062	917	0.00001	0.000	0.2687 ± 14	0.0540 ± 4	0.0636 ± 7	0.474 ± 7	397 ± 4	394 ± 5	372 ± 16
2.1	1936	1854	<0.00001	0.000	0.2990 ± 13	0.0550 ± 3	0.0633 ± 7	0.480 ± 6	396 ± 4	398 ± 4	413 ± 12
3.1	338	226	0.00006	0.001	0.2077 ± 29	0.0539 ± 11	0.0632 ± 7	0.470 ± 11	395 ± 4	391 ± 8	369 ± 45
4.1	875	1353	0.00001	0.000	0.4881 ± 24	0.0552 ± 6	0.0635 ± 7	0.483 ± 8	397 ± 4	400 ± 5	418 ± 25
5.1	1356	559	0.00004	0.001	0.1308 ± 9	0.0577 ± 4	0.0845 ± 9	0.672 ± 90	523 ± 6	522 ± 5	518 ± 14
6.1	847	1183	0.00244	0.039	0.4008 ± 55	0.0549 ± 22	0.0632 ± 7	0.479 ± 21	395 ± 4	397 ± 14	409 ± 89
M3884[‡]											
1.1	1225	1711	<0.00001	0.000	0.4262 ± 16	0.0541 ± 4	0.0636 ± 7	0.475 ± 7	397 ± 4	394 ± 4	377 ± 16
1.2	1293	1713	<0.00001	0.000	0.3947 ± 15	0.0547 ± 4	0.0634 ± 7	0.479 ± 7	396 ± 4	397 ± 5	401 ± 16
2.1	375	276	0.00002	0.000	0.2305 ± 29	0.0547 ± 11	0.0642 ± 7	0.484 ± 12	401 ± 4	401 ± 8	402 ± 44
3.1	453	537	<0.00001	0.000	0.3717 ± 23	0.0548 ± 5	0.0642 ± 7	0.485 ± 7	401 ± 4	401 ± 5	403 ± 20
4.1	1359	2382	0.00069	0.011	0.5343 ± 22	0.0545 ± 7	0.0634 ± 7	0.476 ± 9	396 ± 4	395 ± 6	390 ± 30
5.1	287	480	0.00001	0.000	0.5163 ± 36	0.0546 ± 8	0.0632 ± 7	0.475 ± 9	395 ± 4	395 ± 6	396 ± 33
6.1	350	369	0.00002	0.000	0.3316 ± 39	0.0547 ± 14	0.0632 ± 7	0.477 ± 14	395 ± 4	396 ± 10	401 ± 58
7.1	464	509	0.00005	0.001	0.3399 ± 26	0.0547 ± 8	0.0632 ± 7	0.476 ± 9	395 ± 4	396 ± 7	400 ± 34

Uncertainties for isotopic ratios refer to the last significant digits. 4f206 is the percentage of common ^{206}Pb, based on measured ^{204}Pb and Broken Hill lead (M3883, M3884) or model Pb composition of Cumming & Richards (1975) for age of rock (M243).

[*] 1.1 is spot 1 on grain 1, 2.1 is spot 1 on grain 2, etc.

[†] U–Th–Pb isotopic data obtained in St. Petersburg.

[‡] U–Th–Pb isotopic data obtained in Perth.

Appendix C-1. Chapter 2

Appendix C-1. ^{207}Pb/^{206}Pb isotopic data from single grain zircon evaporation of rock samples of the from Baydrag block, the Burg Gol mélange and the Dzag zone

Sample number	Zircon colour and morphology	Grain number	Mass scans[a]	Evaporation temperature (°C)	Mean ^{207}Pb/^{206}Pb ratio[b] and 2σ (mean) error	^{207}Pb/^{206}Pb age and 2σ (mean) error (Ma)
M98/B9	Dark red, long-prismatic, rounded terminations	1	121	1600	0.155743 ± 60	2410.0 ± 0.7
		2	99	1597	0.155634 ± 69	2408.8 ± 0.8
		3	88	1598	0.155588 ± 66	2408.3 ± 0.7
Mean of 3 grains		1-3	308		**0.155663 ± 38**	**2409.1 ± 0.4**[c]
M98/B10	Dark red-brown, spherical and multifaceted	1	66	1598	0.112333 ± 85	1837.5 ± 1.4
		2	77	1599	0.112413 ± 44	1838.8 ± 0.7
		3	121	1599	0.112406 ± 52	1838.7 ± 0.8
		4	71	1601	0.112785 ± 56	1844.8 ± 0.9
Mean of 4 grains		1-4	335		**0.112473 ± 34**	**1839.8 ± 0.6**[c]
M98/B11	Clear to yellow-brown, short- to long-prismatic, well rounded terminations, pitted surfaces	1	54	1596	0.073119 ± 88	1017.3 ± 2.4
		2	104	1598	0.075156 ± 33	1072.7 ± 0.9
		3	66	1594	0.083927 ± 140	1290.9 ± 3.2
		4	74	1600	0.086450 ± 64	1348.3 ± 1.4
		5	88	1598	0.088338 ± 104	1389.8 ± 2.3
		6	44	1596	0.090463 ± 148	1435.3 ± 3.1
		7	74	1599	0.092029 ± 63	1468.0 ± 1.3
		8	54	1599	0.094556 ± 37	1519.2 ± 0.7
		9	85	1598	0.097585 ± 43	1578.5 ± 0.9
		10	86	1598	0.109368 ± 86	1788.9 ± 1.4
		11	59	1593	0.110774 ± 70	1812.2 ± 1.1
		12	116	1600	0.121715 ± 55	1981.5 ± 0.8
		13	125	1589	0.125255 ± 94	2032.4 ± 1.3
M99/B13	Mostly dark red-brown, oval to ball-round, but stubby, near idiomorphic grains also occur	1	103	1599	0.108301 ± 40	1771.0 ± 0.7
		2	44	1596	0.108843 ± 90	1780.1 ± 1.5
		3	82	1597	0.109067 ± 23	1783.9 ± 0.4
		4	88	1598	0.111406 ± 46	1822.5 ± 0.8
		5	82	1599	0.121778 ± 53	1982.4 ± 0.8
		6	82	1592	0.121760 ± 52	1982.2 ± 0.8
		7	87	1596	0.125070 ± 55	2029.8 ± 0.8
		8	65	1594	0.133348 ± 77	2142.5 ± 1.0

[a] Number of ^{207}Pb/^{206}Pb ratios evaluated for age assessment.

[b] Observed mean ratio corrected for nonradiogenic Pb where necessary. Errors based on uncertainties in counting statistics.

[c] Error based on reproducibility of internal standard.

Appendix D-1. Chapter 3

Appendix D-1. U–Pb analytical results for zircon fractions analysed by TIMS for two samples from the Gobi-Altai, south Mongolia

Sample[a]	U_{tot}/ Pb_{rad}	^{206}Pb/ ^{204}Pb[b]	Atomic ratios[c]						Corr.
			^{206}Pb/^{238}U	± 2σ	^{207}Pb/^{235}U	± 2σ	^{207}Pb/^{206}Pb	± 2σ	coef.[d]
M319 Granodiorite									
1, lp. [2]	14.7	520	0.05502	53	0.4148	71	0.05468	50	0.72
2, lp. [2]	14.0	697	0.05498	33	0.4096	55	0.05403	37	0.64
3, sp. [2]	14.7	312	0.05542	78	0.4253	160	0.05567	251	0.27
4, lp. [2]	14.8	235	0.05498	77	0.4128	40	0.05445	250	0.25
M225 Granodioritic gneiss									
2, sp. [2]	15.8	1031	0.05284	28	0.3921	50	0.05381	32	0.64
3, sp. [3]	16.7	2113	0.05139	31	0.3792	34	0.05353	12	0.94
4, sp. [3]	17.0	984	0.05116	52	0.3800	47	0.05384	11	0.97
5, sp. [2]	17.8	1097	0.05008	20	0.3670	32	0.05315	17	0.79
6, sp. [2]	16.7	1955	0.05067	27	0.3751	50	0.05369	35	0.60
8, sp. [2]	15.4	886	0.05509	74	0.4118	77	0.05421	44	0.84
9, sp. [3]	17.2	1949	0.05101	51	0.3761	62	0.05347	26	0.89
12, sp. [3]	19.6	2072	0.04594	26	0.3346	39	0.05284	25	0.76

Sample[a]	Apparent ages (Ma)					
	^{206}Pb/^{238}U	± 2σ	^{207}Pb/^{235}U	± 2σ	^{207}Pb/^{206}Pb	± 2σ
M319 Granodiorite						
1, lp. [2]	345.2	3.3	352.3	5.1	399.2	20.3
2, lp. [2]	345.0	2.0	348.6	3.9	372.3	15.6
3, sp. [2]	347.7	4.8	359.9	16.0	439.1	97.3
4, lp. [2]	345.0	4.7	350.9	11.5	389.7	102.0
M225 Granodioritic gneiss						
2, sp. [2]	332.0	1.7	335.9	3.7	363.2	13.5
3, sp. [3]	323.0	1.9	326.5	2.5	351.1	5.1
4, sp. [3]	321.6	3.2	326.9	3.5	364.4	4.7
5, sp. [2]	315.0	1.3	317.4	2.4	335.2	7.1
6, sp. [2]	318.6	1.6	323.4	3.7	358.0	14.9
8, sp. [2]	345.7	4.5	350.2	5.6	379.9	18.4
9, sp. [3]	320.7	3.2	324.2	4.6	349.0	11.2
12, sp. [3]	289.5	1.6	293.1	3.0	321.7	10.8

[a] lp: long prismatic; sp: short prismatic; number of grains per aliquots in brackets.

[b] Measured ratios.

[c] Corrected for fractionation, blank, spike and common Pb.

[d] Correlation coefficient.

Appendix E-1. Chapter 1

Appendix E-1. Major and trace element analyses of granitoid gneisses from the Baga Bogd massif

Sample	Mo283	Mo286	Mo380	Mo381	Mo385	Mo387	Mo389
Lithology[a]	Meta-D	Meta-GD	G-gneiss	G-gneiss	G-gneiss	G-gneiss	G-gneiss
Age (Ma)	498 ± 3	499 ± 3	501 ± 4	1519 ± 11	954 ± 8	983 ± 6	956 ± 3
SiO_2	55.30	64.08	68.41	64.11	78.73	71.36	71.35
TiO_2	1.65	0.99	0.48	0.83	0.15	0.27	0.11
Al_2O_3	15.99	16.76	14.78	18.55	10.74	14.1	14.32
Fe_2O_3t	7.99	4.67	2.80	6.23	1.42	2.08	1.53
MnO	0.12	0.07	0.03	0.12	0.04	0.03	0.02
MgO	4.06	1.29	0.70	1.14	0.09	0.28	0.16
CaO	6.24	2.74	1.69	0.66	0.56	1.00	0.96
Na_2O	2.26	3.79	2.90	1.57	1.79	2.71	2.91
K_2O	3.05	4.23	4.90	4.13	5.61	6.27	6.36
P_2O_5	0.94	0.37	0.16	0.05	0.18	0.07	0.07
LOI	1.40	0.77	0.83	1.75	0.52	0.38	0.71
Total	99.02	99.76	97.68	99.14	99.83	98.55	98.52
CIA[b]	46.6	51.5	52.9	69.2	51.7	51.9	51.6
A/CNK[c]	0.9	1.1	1.1	2.2	1.1	1.1	1.1
A/NK[d]	2.3	1.6	1.5	2.6	1.2	1.3	1.2
Rb	203	276	229	222	190	358	275
Sr	864	606	259	101	96	95	87
Ba	1056	1162	943	631	367	557	301
Zr	293	364	275	200	110	151	85
Nb	31	28	17	18	5	9	4
Th	14	39	47	17	9	30	24
Pb	22	43	53	34	38	50	54
Cr	77	3	7	61	bd	4	3
Ni	29	5	6	25	4	bd	4
Y	26	20	14	35	19	37	24
V	118	46	27	97	bd	16	6
Sc	15	7	3	13	3	3	3
Co	26	6	2	19	bd	3	2
Cu	21	6	bd	23	6	bd	6
Zn	124	96	55	85	16	37	24
Ga	22	22	21	24	16	19	22
La	82	74	53	29	18	36	19
Ce	163	154	91	61	27	68	35
Pr	21	17	11	8	2	10	8
Nd	71	58	38	31	15	30	18
Sm	4	8	8	10	3	8	4

Major and trace elements were measured by XRF and are in wt% and ppm, respectively

Fe_2O_3t: total iron as Fe_2O_3; LOI: loss on ignition; bd: below detection limit

[a] D, diorite; GD, granodiorite; G, granite

[b] CIA: molecular ratio $100*[Al_2O_3/(Al_2O_3+CaO+Na_2O+K_2O)]$

[c] A/CNK: molecular ratio $Al_2O_3/(CaO+K_2O+Na_2O)$

[d] A/NK: molecular ratio $Al_2O_3/(K_2O+Na_2O)$

Appendix E-2. Chapter 3

Appendix E-2. Major and trace element abundances for rock samples from the Gobi-Altai, south Mongolia

Locality	Halbagant Range												
Sample	M191	M192	M193	M194	M195	M196	M197	M301	M302	M304	M305	M306	M307
Lithology[a]	Meta-R.	Meta-B.	Meta-D.	Meta-B.	R. dyke	Meta-A.	Meta-R.	Meta-B.	Meta-B.	Meta-A.	Meta-B.	B. dyke	Meta-A. tuff
SiO_2	74.26	50.83	64.59	50.67	73.13	54.92	76.21	47.99	51.82	50.07	45.46	47.00	54.28
TiO_2	0.21	1.64	0.88	2.08	0.32	1.95	0.20	2.09	1.54	2.13	1.97	2.21	0.58
Al_2O_3	12.78	16.56	14.19	13.51	9.61	13.22	12.26	13.46	16.30	13.52	14.95	15.21	11.72
$Fe_2O_3^t$	2.11	9.68	6.24	13.61	2.19	10.43	0.98	14.23	11.00	12.09	10.76	9.72	4.27
MnO	0.03	0.16	0.11	0.19	0.37	0.15	0.01	0.18	0.16	0.18	0.17	0.10	0.14
MgO	0.08	5.47	2.99	5.89	0.40	3.27	0.25	6.07	4.58	3.91	6.94	3.35	2.67
CaO	0.20	7.61	2.45	8.72	4.45	9.83	0.36	7.57	3.05	6.28	7.10	8.39	11.13
Na_2O	2.04	4.89	2.47	3.38	3.10	1.12	2.26	2.97	5.41	3.22	2.48	3.09	4.28
K_2O	6.27	0.11	1.87	0.02	1.13	0.03	5.63	0.02	0.17	0.06	0.63	1.72	0.49
P_2O_5	0.05	0.21	0.21	0.23	0.05	0.35	0.03	0.24	0.25	0.31	0.36	1.10	0.15
LOI	1.50	2.25	3.37	2.24	4.97	4.17	1.57	3.89	4.59	6.20	8.79	6.24	9.54
Total	99.5	99.4	99.4	100.5	99.7	99.4	99.8	98.7	98.9	98.0	99.6	98.1	99.3
Mg#[b]	–	53	–	46	–	38	–	46	45	39	56	41	55
FeO^t/MgO	23.7	1.6	1.9	2.1	4.9	2.9	3.5	2.1	2.2	2.8	1.4	2.6	1.4
XRF													
Cr	14	179	182	60	16	b.d.	12	89	52	14	172	88	200
Ni	3	64	61	41	9	15	2	42	22	21	112	45	29
V	7	291	116	329	31	326	5	350	309	479	246	201	105
Sc	3	35	16	38	6	28	b.d.	40	36	38	31	22	22
Ga	19	18	16	20	8	22	17	20	16	17	18	21	12
LA-ICP-MS													
Rb	167	2	–	0.5	44	1.0	164	–	–	–	12	–	–
Sr	49	417	–	458	245	359	45	–	–	–	263	–	–
Ba	506	150	–	254	271	38	458	–	–	–	651	–	–
Y	40	31	–	36	15	46	37	–	–	–	37	–	–
Zr	181	164	–	153	145	253	159	–	–	–	197	–	–
Hf	5.57	3.90	–	4.11	3.71	6.01	5.38	–	–	–	4.40	–	–
Ta	1.19	0.27	–	0.45	0.55	0.49	1.14	–	–	–	0.53	–	–
Nb	12.1	3.8	–	6.8	7.5	7.2	10.2	–	–	–	8.1	–	–
U	6.12	0.48	–	0.39	1.96	0.92	5.61	–	–	–	0.60	–	–
Th	19.5	0.98	–	1.02	6.55	1.80	19.2	–	–	–	1.62	–	–
La	42.7	9.8	–	9.0	20.5	17.5	41.5	–	–	–	14.6	–	–
Ce	86.8	25.3	–	23.1	42.2	42.5	83.4	–	–	–	36.5	–	–
Pr	9.93	3.69	–	3.47	4.67	6.02	9.55	–	–	–	5.15	–	–
Nd	36.6	17.9	–	17.6	17.1	28.1	35.1	–	–	–	24.5	–	–
Sm	7.16	4.73	–	5.13	3.12	7.13	6.83	–	–	–	6.16	–	–
Eu	0.73	1.35	–	1.75	0.72	2.07	0.67	–	–	–	1.95	–	–
Gd	6.48	5.39	–	6.25	2.66	7.89	6.09	–	–	–	6.85	–	–
Tb	1.05	0.88	–	1.03	0.39	1.27	0.99	–	–	–	1.08	–	–
Dy	6.81	5.72	–	6.88	2.52	8.31	6.49	–	–	–	6.99	–	–
Ho	1.41	1.17	–	1.40	0.52	1.72	1.31	–	–	–	1.41	–	–
Er	4.27	3.32	–	3.99	1.59	4.92	3.95	–	–	–	3.93	–	–
Tm	0.66	0.48	–	0.57	0.25	0.71	0.60	–	–	–	0.55	–	–
Yb	4.56	3.16	–	3.74	1.71	4.77	4.16	–	–	–	3.70	–	–
Lu	0.67	0.46	–	0.55	0.27	0.71	0.61	–	–	–	0.54	–	–
Th/Nb	1.61	0.26	–	0.15	0.88	0.25	1.88	–	–	–	0.20	–	–
Th/La	0.46	0.10	–	0.11	0.32	0.10	0.46	–	–	–	0.11	–	–

Major and trace element concentrations in wt% and ppm, respectively. $Fe_2O_3^t$ and FeO^t, total iron as Fe_2O_3 and FeO, respectively. LOI: loss on ignition; b.d.: below detection.

[a] A.: andesite, B.: basalt, D.: dacite, Pyrocl.: pyroclastic, R.: rhyolite.

[b] Mg# = Mg-number = molar 100xMgO/(MgO+FeO^t); FeO^t = 0.8998x$Fe_2O_3^t$. Mg# as differentiation index is meaningful only for mafic rocks and was not calculated for felsic rocks.

Appendix E-2. (*continued*)

Locality	Halbagant Range							Shine Jinst area			
Sample	M308	M309	M310	M311	M313	M315	M319	M211	M212	M213	M214
Lithology[a]	B. dyke	Meta-R. Pyrocl.	B. dyke	Meta-R. Pyrocl.	Meta-R.	Meta-A. Pyrocl.	Grano-diorite	Granite gneiss	Amph.	Amph.	Amph.
SiO_2	48.29	73.12	44.07	64.48	74.67	51.44	63.28	72.43	43.25	52.61	49.03
TiO_2	1.71	0.32	2.00	0.22	0.37	1.45	0.60	0.60	1.28	2.35	1.99
Al_2O_3	16.26	7.05	15.12	8.15	9.60	14.42	15.82	11.83	11.28	14.83	14.38
$Fe_2O_3^t$	10.09	1.35	11.31	0.61	2.26	8.51	4.07	3.89	11.32	12.10	12.12
MnO	0.14	0.08	0.16	0.14	0.04	0.11	0.06	0.08	0.19	0.23	0.19
MgO	7.14	0.27	7.40	0.81	1.23	5.53	2.57	1.69	17.70	3.37	6.31
CaO	7.59	6.67	7.49	13.27	1.76	5.33	3.60	1.64	9.33	7.31	10.13
Na_2O	3.11	1.66	2.58	2.81	2.43	3.46	4.58	3.39	1.01	4.10	3.65
K_2O	1.17	1.59	1.32	0.17	2.26	1.32	2.23	1.53	0.30	0.60	0.73
P_2O_5	0.30	0.03	0.33	0.09	0.04	0.24	0.19	0.17	0.15	0.33	0.23
LOI	3.09	6.04	6.74	8.51	3.50	7.01	2.93	1.95	3.72	1.47	1.09
Total	98.9	98.2	98.5	99.3	98.2	98.8	99.9	99.2	99.5	99.3	99.9
Mg#[b]	58	–	56	–	–	56	–	–	76	36	51
FeO^t/MgO	1.3	4.5	1.4	0.7	1.7	1.4	1.4	2.1	0.6	3.2	1.7
XRF											
Cr	217	32	192	37	82	195	49	25	1278	b.d.	222
Ni	93	4	118	7	18	86	38	12	598	2	94
V	212	35	220	19	55	186	80	63	194	238	336
Sc	25	8	27	12	8	24	10	9	31	28	38
Ga	18	7	17	4	10	18	18	14	12	20	20
LA-ICP-MS											
Rb	–	38	–	3.1	52	56	–	51	9	10	7
Sr	–	271	–	363	99	215	–	180	38	274	151
Ba	–	236	–	28	274	184	–	336	28	139	82
Y	–	20	–	22	12	38	–	35	20	36	43
Zr	–	81	–	82	154	148	–	272	98	114	61
Hf	–	2.08	–	2.16	3.73	4.03	–	6.86	2.33	2.86	1.93
Ta	–	0.37	–	0.44	0.42	1.08	–	0.83	0.09	0.50	0.36
Nb	–	4.8	–	5.2	5.3	10.0	–	12.8	1.3	7.4	5.6
U	–	1.19	–	1.09	0.94	4.13	–	2.44	0.14	0.50	0.37
Th	–	5.59	–	4.43	5.89	7.04	–	11.2	0.19	1.22	0.72
La	–	23.2	–	18.9	14.2	10.7	–	30.8	3.3	12.1	10.0
Ce	–	45.3	–	39.8	27.8	27.2	–	65.3	11.9	29.2	26.3
Pr	–	5.39	–	4.34	3.26	3.89	–	7.96	1.98	4.17	4.10
Nd	–	20.3	–	16.6	12.0	18.8	–	31.4	10.2	19.8	20.5
Sm	–	3.66	–	3.34	2.31	5.25	–	6.63	3.02	5.27	5.80
Eu	–	1.03	–	0.73	0.61	1.52	–	1.29	1.19	1.93	1.86
Gd	–	3.22	–	3.48	2.08	6.12	–	6.32	3.44	6.14	6.75
Tb	–	0.50	–	0.53	0.32	1.03	–	0.99	0.57	1.00	1.14
Dy	–	3.18	–	3.33	2.00	6.80	–	6.28	3.84	6.57	7.64
Ho	–	0.66	–	0.66	0.41	1.40	–	1.26	0.78	1.35	1.58
Er	–	1.95	–	1.83	1.21	3.95	–	3.69	2.25	3.87	4.66
Tm	–	0.29	–	0.24	0.18	0.58	–	0.53	0.32	0.56	0.67
Yb	–	2.04	–	1.57	1.28	3.96	–	3.58	2.24	3.72	4.46
Lu	–	0.31	–	0.23	0.20	0.58	–	0.53	0.31	0.55	0.65
Th/Nb	–	1.17	–	0.85	1.10	0.70	–	0.88	0.15	0.17	0.13
Th/La	–	0.24	–	0.23	0.42	0.66	–	0.36	0.06	0.10	0.07

Appendix E-2. (*continued*)

Locality	Shine Jinst area										
Sample	M215	M216	M217	M218	M219	M220	M221	M222	M224	M225	M226	M227
Lithology[a]	Felsic gneiss	Amph.	Felsic gneiss	Felsic gneiss	Amph.	Felsic gneiss	Felsic gneiss	Amph.	Felsic gneiss	Felsic gneiss	Granite gneiss	Granite gneiss
SiO_2	66.82	51.20	68.58	66.18	53.30	67.02	67.63	49.64	80.98	67.02	71.91	75.82
TiO_2	0.54	0.55	0.54	0.57	2.22	0.51	0.53	1.13	0.59	0.56	0.28	0.28
Al_2O_3	14.48	17.93	14.43	15.00	14.97	14.94	14.86	13.99	6.67	14.56	14.70	12.44
$Fe_2O_3^t$	4.38	7.28	4.35	5.00	11.69	4.50	4.49	7.55	2.13	5.52	2.56	2.47
MnO	0.08	0.15	0.09	0.10	0.23	0.09	0.08	0.13	0.02	0.10	0.03	0.03
MgO	1.67	6.36	1.42	1.94	3.32	1.67	1.77	6.86	0.42	2.00	0.66	0.63
CaO	3.39	8.86	3.89	4.21	7.11	4.33	4.30	16.18	5.48	4.34	3.35	2.53
Na_2O	4.20	3.90	4.14	3.72	4.52	3.90	3.98	2.02	0.89	3.64	4.61	3.94
K_2O	1.44	1.53	1.27	1.62	0.61	1.45	1.31	0.50	1.60	1.15	0.80	1.16
P_2O_5	0.10	0.07	0.10	0.11	0.35	0.10	0.11	0.21	0.07	0.13	0.06	0.05
LOI	0.93	1.69	1.12	1.26	1.26	1.22	1.08	1.42	0.89	1.00	0.94	0.77
Total	98.0	99.5	99.9	99.7	99.6	99.7	100.1	99.6	99.7	100.0	99.9	100.1
Mg#[b]	–	63	–	–	36	–	–	64	–	–	–	–
FeO^t/MgO	2.4	1.0	2.8	2.3	3.2	2.4	2.3	1.0	4.6	2.5	3.5	3.5
XRF												
Cr	9	58	4	12	b.d.	12	9	639	55	13	5	3
Ni	4	53	4	9	4	6	6	286	10	4	2	2
V	88	188	75	101	224	91	94	186	46	49	31	38
Sc	13	37	13	15	28	15	15	35	7	10	5	4
Ga	14	12	14	15	19	14	14	13	6	8	13	11
LA-ICP-MS												
Rb	–	25	35	42	–	–	39	8	37	34	15	33
Sr	–	174	221	228	–	–	242	442	41	326	326	294
Ba	–	240	245	248	–	–	252	201	82	249	314	609
Y	–	13	25	26	–	–	27	17	15	24	2.12	5
Zr	–	27	168	133	–	–	225	95	122	158	179	70
Hf	–	0.81	4.53	3.58	–	–	5.85	2.30	3.11	3.98	3.84	1.79
Ta	–	0.05	0.36	0.41	–	–	0.30	0.37	0.51	0.36	0.08	0.12
Nb	–	0.7	4.8	5.3	–	–	4.5	6.2	6.4	4.5	2.32	2.4
U	–	0.45	0.81	0.51	–	–	0.78	2.25	2.05	0.73	0.28	0.31
Th	–	0.44	5.48	5.25	–	–	4.12	1.07	9.12	1.55	1.35	7.19
La	–	2.3	16.2	15.1	–	–	14.5	12.3	23.4	10.5	11.1	30.4
Ce	–	5.8	33.8	33.6	–	–	31.4	24.9	47.1	24.5	18.8	57.4
Pr	–	0.88	4.51	4.36	–	–	4.26	3.36	5.64	3.49	1.95	6.49
Nd	–	4.6	18.9	18.5	–	–	18.3	14.6	20.9	15.8	6.56	23.1
Sm	–	1.47	4.25	4.25	–	–	4.24	3.18	3.78	4.01	0.95	3.37
Eu	–	0.56	0.93	0.97	–	–	0.93	1.08	0.73	1.02	0.67	0.96
Gd	–	1.96	4.19	4.21	–	–	4.28	3.31	3.04	4.04	0.69	2.12
Tb	–	0.34	0.65	0.67	–	–	0.68	0.51	0.44	0.64	0.08	0.23
Dy	–	2.41	4.29	4.37	–	–	4.44	3.26	2.75	4.08	0.42	1.07
Ho	–	0.52	0.90	0.91	–	–	0.92	0.65	0.54	0.84	0.07	0.18
Er	–	1.53	2.71	2.77	–	–	2.80	1.85	1.60	2.50	0.21	0.43
Tm	–	0.23	0.41	0.42	–	–	0.42	0.26	0.23	0.38	0.03	0.05
Yb	–	1.54	2.84	2.93	–	–	2.96	1.70	1.57	2.58	0.27	0.36
Lu	–	0.23	0.44	0.44	–	–	0.46	0.25	0.24	0.39	0.05	0.06
Th/Nb	–	0.59	1.14	1.00	–	–	0.92	0.17	1.42	0.34	0.58	2.98
Th/La	–	0.19	0.34	0.35	–	–	0.28	0.09	0.39	0.15	0.12	0.24

Appendix E-2. (*continued*)

Locality	Hulsnii Valley, Bayanleg Hatuu Range					
Sample	M325	M327	M328	M329	M330	M332
Lithology[a]	Granite dyke	Meta-D.	Meta-D.	Meta-R.	Meta-D.	Meta-granite
SiO_2	65.37	68.49	66.21	73.28	72.08	70.22
TiO_2	0.29	0.73	0.79	0.39	0.41	0.48
Al_2O_3	18.70	13.42	14.11	13.58	13.51	13.79
$Fe_2O_3^t$	2.17	3.90	5.39	2.63	3.20	2.87
MnO	0.03	0.07	0.09	0.03	0.06	0.06
MgO	0.86	2.14	1.97	0.41	0.42	1.11
CaO	3.91	4.91	2.01	1.23	1.75	1.64
Na_2O	5.36	3.28	4.04	4.10	3.91	3.24
K_2O	2.20	1.90	1.76	2.99	3.54	4.25
P_2O_5	0.20	0.17	0.16	0.06	0.07	0.10
LOI	0.77	0.79	0.69	0.92	0.42	1.82
Total	99.9	99.8	97.2	99.6	99.4	99.6
Mg#[b]	–	–	–	–	–	–
FeO^t/MgO	2.3	1.6	2.5	5.8	6.9	2.3
XRF						
Cr	7	96	40	5	4	9
Ni	7	33	22	5	4	7
V	18	70	90	17	18	45
Sc	5	11	18	9	10	8
Ga	19	16	17	17	17	15
LA-ICP-MS						
Rb	–	–	78	77	–	71
Sr	–	–	279	167	–	249
Ba	–	–	513	812	–	462
Y	–	–	44	39	–	40
Zr	–	–	266	231	–	206
Hf	–	–	6.74	6.08	–	5.19
Ta	–	–	1.22	1.28	–	1.15
Nb	–	–	17.6	19.0	–	16.5
U	–	–	2.83	1.43	–	2.57
Th	–	–	12.0	13.3	–	11.3
La	–	–	35.5	30.5	–	33.1
Ce	–	–	74.2	64.7	–	69.1
Pr	–	–	8.95	7.85	–	8.34
Nd	–	–	35.7	31.2	–	33.4
Sm	–	–	7.45	6.75	–	6.94
Eu	–	–	1.70	1.40	–	1.55
Gd	–	–	7.23	6.38	–	6.69
Tb	–	–	1.15	1.02	–	1.06
Dy	–	–	7.65	6.70	–	6.96
Ho	–	–	1.60	1.39	–	1.43
Er	–	–	4.76	4.20	–	4.21
Tm	–	–	0.70	0.62	–	0.61
Yb	–	–	4.83	4.16	–	4.20
Lu	–	–	0.71	0.57	–	0.61
Th/Nb	–	–	0.39	0.70	–	0.69
Th/La	–	–	0.34	0.43	–	0.34

Appendix E-3. Chapter 4

Appendix E-3. Major and trace element abundances for rock samples from the Devreh Valley, Tseel terrane

Sample	M243	M244	M245	M246	M247	M248	M249	M250	M251	M252	M253	M254
Rock type*	Fsp porph.	Diorite	Meta-D. Pyrocl.	Meta-R. Pyrocl.	Meta-R.	Meta-R.	Meta-D. Pyrocl.	Meta-R Pyrocl.	Meta-R Pyrocl.	Meta-R Pyrocl.	Meta-R Pyrocl.	Meta-D.
SiO_2	72.84	54.29	68.93	76.34	73.37	73.25	73.13	84.98	81.04	79.68	76.79	68.49
TiO_2	0.39	1.97	0.63	0.26	0.20	0.24	0.50	0.12	0.09	0.26	0.24	0.67
Al_2O_3	13.99	15.43	13.89	12.52	14.97	14.88	13.29	8.46	10.60	9.67	14.72	14.70
$Fe_2O_3^T$	2.21	11.37	5.92	2.12	1.40	1.58	4.12	0.71	0.58	2.60	1.34	3.94
MnO	0.05	0.22	0.41	0.08	0.03	0.03	0.48	0.16	0.05	0.62	0.05	0.07
MgO	0.50	3.84	4.12	0.98	0.30	0.37	3.00	0.62	0.09	1.66	1.13	1.54
CaO	1.51	6.83	1.06	1.93	1.43	1.99	1.12	0.98	0.57	1.85	0.42	3.03
Na_2O	3.96	3.76	2.67	3.93	4.42	4.69	0.89	2.70	3.00	1.37	0.75	4.03
K_2O	4.49	1.24	2.24	1.79	3.82	2.90	3.38	1.26	3.96	2.25	4.51	3.31
P_2O_5	0.07	1.06	0.12	0.05	0.05	0.06	0.08	0.02	0.02	0.05	0.04	0.22
LOI	0.8	2.7	2.2	1.2	0.8	0.8	1.9	1.4	0.7	0.8	1.9	1.0
Mg#†	–	40	–	–	–	–	–	–	–	–	–	–
FeO^T/MgO	4.0	2.7	1.3	2.0	4.1	3.8	1.2	1.0	5.7	1.4	1.1	2.3
XRF												
Cr	17	53	69	26	31	21	46	5	2	23	14	35
Ni	3	30	47	3	2	3	31	2	b.d.	16	2	17
V	26	167	87	31	17	20	73	9	4	35	22	57
Sc	2	25	12	3	3	3	8	3	4	5	5	8
Ga	16	22	18	12	22	20	13	7	8	10	15	17
LA-ICP-MS												
Rb	131	21	71	–	161	–	–	–	–	81	–	–
Sr	186	527	92	–	485	–	–	–	–	87	–	–
Ba	805	446	414	–	1149	–	–	–	–	248	–	–
Y	32	64	22	–	6	–	–	–	–	13	–	–
Zr	273	488	188	–	139	–	–	–	–	76	–	–
Hf	6.73	10.07	5.02	–	3.89	–	–	–	–	2.26	–	–
Ta	2.05	1.85	0.97	–	1.32	–	–	–	–	0.73	–	–
Nb	24.5	34.7	14.6	–	14.2	–	–	–	–	8.43	–	–
U	4.09	1.20	1.98	–	4.04	–	–	–	–	1.91	–	–
Th	19.8	2.70	10.1	–	15.9	–	–	–	–	10.3	–	–
La	60.5	49.0	27.8	–	29.4	–	–	–	–	26.4	–	–
Ce	112	114	66.4	–	49.8	–	–	–	–	48.3	–	–
Pr	11.9	14.4	6.60	–	4.98	–	–	–	–	4.88	–	–
Nd	41.9	60.7	25.1	–	16.5	–	–	–	–	16.5	–	–
Sm	7.10	12.7	4.84	–	2.64	–	–	–	–	2.72	–	–
Eu	1.27	3.73	0.96	–	0.67	–	–	–	–	0.55	–	–
Gd	5.87	12.2	4.20	–	1.81	–	–	–	–	2.17	–	–
Tb	0.89	1.85	0.63	–	0.23	–	–	–	–	0.34	–	–
Dy	5.54	11.7	3.98	–	1.20	–	–	–	–	2.14	–	–
Ho	1.11	2.37	0.81	–	0.22	–	–	–	–	0.44	–	–
Er	3.30	6.83	2.39	–	0.56	–	–	–	–	1.36	–	–
Tm	0.49	0.99	0.36	–	0.08	–	–	–	–	0.21	–	–
Yb	3.33	6.81	2.48	–	0.55	–	–	–	–	1.54	–	–
Lu	0.48	1.03	0.38	–	0.09	–	–	–	–	0.23	–	–
Th/Nb	0.81	0.08	0.69		1.12					1.22		

Major element concentrations in wt%, trace element in ppm. Major elements are recalculated to anhydrous composition.

$Fe_2O_3^T$ and FeO^T, total iron as Fe_2O_3 and FeO, respectively. LOI: loss on ignition. b.d.: below detection; (–) not analyzed.

[*] B. = basalt, D. = dacite, Fsp porph. = feldspar porphyry, Gd. = granodioritic, Pyrocl. = pyroclastic, R. = rhyolite.

[†] Mg# = Mg-number = molar 100 x $MgO/(MgO+FeO^T)$; $FeO^T = 0.8998 \times Fe_2O_3^T$.

Mg# as differentiation index is meaningful only for mafic rocks and was not calculated for felsic rocks.

Appendix E-3. *(continued)*

Sample	M255	M256	M257	M258	M259	M260	M267	M268	M269	M270	M271	M272
Rock type[*]	Meta-B.	Meta-B.	Meta-B.	Meta-R. Pyrocl.	Meta-B.	Gneiss Gd.	Gneiss Gd.	Meta-D. Pyrocl.	Meta-D. Pyrocl.	Meta-R.	Meta-D. Pyrocl.	Meta-D. Pyrocl.
SiO_2	48.30	47.82	49.07	73.03	51.46	66.11	63.26	65.27	63.08	75.41	67.58	64.49
TiO_2	2.19	2.20	1.83	0.27	1.95	0.55	0.71	1.03	1.17	0.22	0.68	0.66
Al_2O_3	15.28	15.04	16.29	15.03	14.67	15.07	14.04	15.14	15.82	12.97	15.24	14.10
$Fe_2O_3^T$	11.97	12.28	11.37	1.74	13.78	4.87	6.40	5.40	6.02	1.53	6.12	6.17
MnO	0.17	0.17	0.16	0.03	0.22	0.09	0.10	0.14	0.11	0.05	0.16	0.11
MgO	8.22	8.72	6.39	0.46	5.15	2.59	3.93	1.83	2.17	0.22	3.23	3.77
CaO	11.26	10.86	11.68	2.08	9.25	4.62	5.91	3.91	4.83	0.68	1.30	5.57
Na_2O	2.27	2.57	2.95	4.75	2.85	4.05	3.04	4.07	3.92	2.77	4.59	2.93
K_2O	0.13	0.11	0.09	2.52	0.49	1.96	2.46	2.80	2.53	6.10	0.98	2.08
P_2O_5	0.21	0.22	0.17	0.08	0.18	0.11	0.13	0.40	0.34	0.05	0.12	0.13
LOI	0.7	0.8	0.5	0.5	0.5	1.2	0.9	0.8	1.2	0.4	2.3	1.8
Mg#[†]	58	58	53	–	43	–	–	–	–	–	–	–
FeO^T/MgO	1.3	1.3	1.6	3.4	2.4	1.7	1.5	2.7	2.5	6.2	1.7	1.5
XRF												
Cr	299	301	225	4	37	36	103	24	13	3	86	106
Ni	177	156	81	2	16	18	25	14	8	2	42	28
V	306	315	347	22	395	102	149	75	109	15	96	127
Sc	33	36	40	4	42	14	24	7	11	3	14	18
Ga	19	19	20	21	20	17	18	18	20	14	18	16
LA-ICP-MS												
Rb	0.55	0.36	0.26	–	9	56	–	–	119	–	–	47
Sr	297	283	282	–	248	425	–	–	380	–	–	380
Ba	27	17	21	–	67	348	–	–	503	–	–	423
Y	28	28	25	–	34	14	–	–	37	–	–	18
Zr	157	166	121	–	134	127	–	–	302	–	–	190
Hf	3.90	4.28	3.16	–	3.54	3.47	–	–	6.71	–	–	5.11
Ta	0.78	0.77	0.60	–	0.29	0.74	–	–	1.37	–	–	0.73
Nb	11.6	11.4	8.92	–	4.31	9.61	–	–	21.1	–	–	12.6
U	0.28	0.32	0.24	–	0.35	1.74	–	–	4.38	–	–	1.04
Th	0.96	0.96	0.86	–	1.13	7.89	–	–	11.0	–	–	7.63
La	11.9	12.2	9.13	–	8.14	21.3	–	–	41.3	–	–	28.5
Ce	30.2	31.1	22.6	–	21.1	43.4	–	–	84.2	–	–	60.0
Pr	4.27	4.47	3.25	–	3.10	5.06	–	–	9.97	–	–	7.40
Nd	20.4	21.6	15.7	–	15.4	19.3	–	–	39.1	–	–	28.3
Sm	5.37	5.58	4.31	–	4.47	3.73	–	–	7.84	–	–	5.19
Eu	1.90	1.88	1.65	–	1.53	0.93	–	–	1.84	–	–	1.16
Gd	5.84	6.01	4.90	–	5.51	3.03	–	–	6.93	–	–	4.08
Tb	0.91	0.93	0.79	–	0.92	0.43	–	–	1.04	–	–	0.57
Dy	5.52	5.72	5.02	–	6.25	2.51	–	–	6.51	–	–	3.36
Ho	1.07	1.11	0.98	–	1.31	0.49	–	–	1.29	–	–	0.65
Er	2.92	2.98	2.69	–	3.82	1.41	–	–	3.87	–	–	1.92
Tm	0.40	0.41	0.37	–	0.56	0.20	–	–	0.56	–	–	0.28
Yb	2.54	2.60	2.40	–	3.76	1.39	–	–	3.80	–	–	1.93
Lu	0.36	0.37	0.34	–	0.56	0.21	–	–	0.55	–	–	0.28
Th/Nb	0.08	0.08	0.10		0.26	0.82			0.52			0.60

Appendix F-1. Chapter 3

Appendix F-1. Sm–Nd isotopic data for rock samples from the Gobi-Altai, south Mongolia

Sample	Rock type	Age (Ma)	Sm (ppm)	Nd (ppm)	^{147}Sm/^{144}Nd	^{143}Nd/^{144}Nd$_{(0)}$	$\varepsilon_{Nd(t)}$	t_{DM1}[a] (Ga)	t_{DM2}[b] (Ga)
Halbagant Range									
M191*	Metarhyolite	440	7.31	36.61	0.1208	0.512614 ± 12	3.8	0.72	–
M192	Metabasalt	440	4.45	16.58	0.1624	0.512931 ± 8	7.7	§	–
M194*	Metabasalt	440	5.03	17.23	0.1766	0.512989 ± 12	8.0	§	–
M195	Rhyolite dyke	293 ± 3	3.13	17.07	0.1109	0.512340 ± 13	-2.6	1.04	–
M196	Metaandesite	440	6.88	26.20	0.1587	0.512769 ± 8	4.7	§	–
M197*	Metarhyolite	440	6.95	35.08	0.1198	0.512619 ± 12	4.0	0.70	–
M305	Metabasalt	440	4.00	22.90	0.1057	0.512646 ± 9	5.3	0.58	–
M309	Pyroclastic metarhyolite	441 ± 5	3.46	20.26	0.1032	0.512324 ± 11	-0.9	1.00	–
M311	Pyroclastic metarhyolite	440	2.86	16.63	0.1038	0.512122 ± 10	-4.8	1.28	–
M313	Metarhyolite	440	2.04	12.04	0.1025	0.512195 ± 14	-3.3	1.16	–
M315	Pyroclastic metaandesite	440	4.93	17.51	0.1703	0.512797 ± 14	4.6	§	–
Hulsnii Valley									
M328	Metadacite	443 ± 5	7.58	35.74	0.1282	0.512414 ± 6	-0.5	1.12	–
M329	Metarhyolite	443	6.70	31.20	0.1298	0.512436 ± 6	-0.2	1.10	–
M332	Porphyritic metagranite	434	6.75	33.38	0.1223	0.512493 ± 6	1.3	0.92	–
Shine Jinst area									
M211	Granite gneiss	454 ± 4	6.87	31.37	0.1324	0.512453 ± 8	0.1	1.11	–
M212	Amphibolite	415	3.13	10.37	0.1826	0.513051 ± 11	8.8	§	–
M213	Amphibolite	415	5.16	19.06	0.1635	0.512863 ± 8	6.2	§	–
M214*	Amphibolite	415	5.61	19.76	0.1716	0.512998 ± 11	8.4	§	–
M216	Amphibolite	415	1.44	4.34	0.2011	0.513027 ± 12	7.4	§	–
M217*	Felsic gneiss	415	4.24	18.88	0.1359	0.512700 ± 12	4.4	0.69	–
M218	Felsic gneiss	415	4.30	18.48	0.1406	0.512721 ± 6	4.6	0.69	–
M221	Felsic gneiss	415	4.29	18.25	0.1423	0.512665 ± 10	3.4	0.82	–
M222*	Amphibolite	415	3.17	14.52	0.1322	0.512800 ± 13	6.6	0.48	–
M224*	Felsic gneiss	415	4.15	20.93	0.1199	0.512532 ± 12	2.0	0.84	–
M225	Felsic gneiss	415	4.14	15.79	0.1585	0.512730 ± 13	3.8	0.88	–
M226	Tonalitic gneiss	415 ± 3	0.94	6.56	0.0868	0.512573 ± 12	4.6	0.58	0.75
M226, repeat analysis			1.01	7.09	0.0861	0.512565 ± 14	4.4	0.58	0.76
M227*	Felsic gneiss	415	3.06	23.13	0.0801	0.512220 ± 13	-2.0	0.94	1.26

^{143}Nd/^{144}Nd$_{(0)}$, measured ratio, within-run uncertainty is given at 2σ level and refer to the last significant digits.

* Isotopic measurements carried out in Munich; other samples were analysed in Mainz.

[a] t_{DM1}, Nd model ages calculated according to the single-stage model of DePaolo (1981).

§ Sm/Nd too high for meaningful model age calculation.

[b] t_{DM2}, Nd model ages calculated according to the two-stage model of Liew & Hofmann (1988) for rock samples with Sm/Nd ratios <0.1, see text for explanations.

Appendix F-2. Chapter 4

Appendix F-2. Sm–Nd isotopic data for rock samples from the Devreh Valley, Tseel terrane

Sample	Rock type	Age (Ma)	Sm (ppm)	Nd (ppm)	$^{147}Sm/^{144}Nd$	$^{143}Nd/^{144}Nd_{(0)}$ *	$\varepsilon_{Nd(t)}$ †	t_{DM} ‡ (Ga)
M243	Feldspar porphyry	279	7.15	41.88	0.1032	0.512605 ± 17	2.7	0.62
M244	Diorite	280	24.29	76.27	0.1926	0.512802 ± 7	3.3	§
M245	Pyroclastic metadacite	400	5.15	25.14	0.1239	0.512233 ± 10	-4.2	1.37
M247	Metarhyolite	400	2.63	16.51	0.0965	0.512696 ± 8	6.3	0.47
M252	Pyroclastic metarhyolite	400	2.76	16.46	0.1013	0.512499 ± 12	2.2	0.75
M256	Metabasalt	400	7.54	20.89	0.2182	0.512925 ± 6	4.5	§
M257	Metabasalt	400	4.47	16.31	0.1657	0.512818 ± 14	5.1	§
M259	Metabasalt	400	4.45	15.04	0.1789	0.512884 ± 6	5.7	§
M259	Repeat analysis	400	4.56	15.19	0.1815	0.512900 ± 16	5.9	§
M260	Granodioritic gneiss	360	3.77	19.28	0.1182	0.512650 ± 9	3.8	0.64
M269	Pyroclastic metadacite	400	8.33	39.12	0.1288	0.512683 ± 12	4.4	0.66
M272	Pyroclastic metadacite	400	5.30	28.30	0.1132	0.512607 ± 9	3.7	0.67

* $^{143}Nd/^{144}Nd_{(0)}$ = measured ratio; within-run uncertainty is given at the 2σ level and refers to the last significant digits.

† $\varepsilon_{Nd(t)}$, initial ε_{Nd}-values calculated with the parameters of Jacobsen & Wasserburg (1980).

‡ t_{DM}, depleted mantle model age (Ga), calculated according to DePaolo (1981).

§ Sm/Nd too high for meaningful model age calculation.

Appendix G-1. Chapter 3

Appendix G-1. Results obtained by LA-ICP-MS measurements on glass beads for reference material JR-1 and BHVO2

	JR1, 6 beads, n = 18				BHVO2, 4 beads, n = 12			
	Mean	RSD %[a]	Ref. val.[b]	rec. %[c]	Mean	RSD %[a]	Ref. val.[b]	rec. %[c]
Rb	249	10.3	258	97	9.1	3.1	9.11	100
Sr	33	4.0	28.5	117	389	2.7	396	98
Ba	48	3.0	47.5	101	131	2.4	131	100
Y	41	3.0	41.5	100	25	2.2	26	98
Zr	95	2.3	98.8	96	170	2.9	172	99
Hf	4.70	2.9	4.69	100	4.41	3.1	4.36	101
Ta	1.73	2.3	1.75	99	1.19	3.5	1.14	104
Nb	15.5	1.4	15.6	99	17.9	2.2	18.1	99
U	8.61	2.3	8.83	97	0.41	4.7	0.403	102
Th	27.0	2.2	27.1	99	1.25	3.5	1.22	102
La	19.8	0.7	19.3	103	15.4	1.9	15.2	101
Ce	46.1	1.3	45.7	101	36.8	2.4	37.5	98
Pr	5.92	0.9	5.88	101	5.20	2.1	5.35	97
Nd	23.6	0.0	23.6	100	24.8	1.8	24.5	101
Sm	5.76	1.3	5.74	100	6.13	2.0	6.07	101
Eu	0.27	2.0	0.267	103	2.05	3.0	2.07	99
Gd	5.64	2.0	5.85	96	6.25	2.0	6.24	100
Tb	0.96	2.1	0.98	98	0.92	2.1	0.92	100
Dy	6.37	2.0	6.3	101	5.43	2.1	5.31	102
Ho	1.33	2.2	1.3	102	1.00	1.9	0.98	102
Er	4.17	2.7	4.11	102	2.59	1.8	2.54	102
Tm	0.66	2.9	0.66	101	0.34	2.3	0.33	102
Yb	4.83	2.4	4.74	102	2.08	2.3	2.0	104
Lu	0.73	3.2	0.721	101	0.29	2.7	0.274	104

[a] RSD: relative standard deviation = 100 * σ / mean [%]

[b] Ref. val.: reference values compiled from the GeoRem database (http://georem.mpch-mainz.gwdg.de/)

[c] rec. %: recovery

Appendix G-2. Chapter 4

Appendix G-2. Data for reference materials JR-1 and BHVO-2 obtained by LA-ICP-MS measurements on glass beads

	JR-1; 6 beads n = 18				BHVO-2; 1 bead, n = 3			
	Mean	RSD%[a]	Ref. val.[b]	rec.%[c]	Mean	RSD%[a]	Ref val.[b]	rec.%[c]
Rb	252	6.8	258	98	9.4	0.8	9.1	103
Sr	32	5.3	29	112	403	1.3	396	102
Ba	48	1.8	48	102	135	0.3	131	103
Y	41	2.0	42	99	25.7	2.1	26.0	99
Zr	94	1.9	99	95	171	1.9	172	99
Hf	4.73	2.7	4.69	101	4.51	1.4	4.36	103
Ta	1.73	1.5	1.75	99	1.25	2.1	1.14	110
Nb	15.4	1.6	15.6	98	18.5	2.4	18.1	102
U	8.75	2.9	8.83	99	0.44	3.0	0.403	109
Th	27.2	2.5	27.1	100	1.30	2.5	1.22	106
La	19.8	1.0	19.3	102	15.6	0.8	15.2	103
Ce	46.1	1.0	45.7	101	38.0	0.9	37.5	101
Pr	5.92	0.6	5.88	101	5.36	0.8	5.35	100
Nd	23.6	0.0	23.6	100	25.4	1.0	24.5	104
Sm	5.75	0.8	5.74	100	6.30	1.6	6.07	104
Eu	0.271	2.5	0.267	102	2.14	1.3	2.07	103
Gd	5.63	1.2	5.85	96	6.37	1.2	6.24	102
Tb	0.95	1.0	0.98	97	0.94	1.1	0.92	102
Dy	6.33	1.4	6.30	101	5.55	1.3	5.31	104
Ho	1.33	1.6	1.30	102	1.02	1.5	0.98	104
Er	4.16	2.0	4.11	101	2.63	1.0	2.54	104
Tm	0.66	2.2	0.66	100	0.34	1.4	0.33	104
Yb	4.83	2.2	4.74	102	2.14	0.1	2.0	107
Lu	0.72	2.5	0.72	101	0.29	1.0	0.27	108

[a] RSD: relative standard deviation = 100 x σ / mean [%]

[b] Ref. val.: reference values compiled from the GeoRem database (http://georem.mpch-mainz.gwdg.de/)

[c] rec.%: recovery